Bangor University

DOCTOR OF PHILOSOPHY

Development of a power based angle of arrival system for tracking of bee utlilising a miniature vibration energy harvester for a battery-less transmitter

Shearwood, Jake

Award date:
2020

Awarding institution:
Bangor University

Bangor University

DOCTOR OF PHILOSOPHY

Development of a power based angle of arrival system for tracking of bee utlilising a miniature vibration energy harvester for a battery-less transmitter

Shearwood, Jake

Award date:
2020

DEVELOPMENT OF A POWER BASED ANGLE OF ARRIVAL SYSTEM FOR TRACKING OF BEES UTILISING A MINIATURE VIBRATION ENERGY HARVESTER FOR A BATTERY-LESS TRANSMITTER

Jake Shearwood

School of Electronic Engineering

Bangor University

A thesis submitted in partial fulfilment for the degree of

Doctor of Philosophy

March 2020

"According to the laws of aerodynamics, the bumblebee can't fly either, but the Bumblebee doesn't know anything about the laws of aerodynamics, so it goes ahead and flies anyway."

- Igor Sikorsk

ABSTRACT

The thesis presents the adaption of radio telemetry technology to allow for the tracking of the world's most economically beneficial insect, the honeybee. Currently no technology is available to efficiently enable the long-term evaluation of navigation loss of bees exposed to potentially harmful pesticides such as neonicotinoids. The research aims at developing a self-sustained radio tracking device which can be attached to insects as small as the honeybee. The research presented within the thesis acts as a proof of principle for long range autonomous tracking of bees using a modified radio telemetry.

To allow for compatibility of radio telemetry tags with smaller tags were designed and fabricated which implements a micro-generator that harvests electrical energy from the bee's body vibrations which powers radio-wave transmission from a miniaturized antenna attached to the bees' thorax. The use of lead zirconate titanate (PZT) allowed for sufficient power generation to replace the battery, whilst an increased operation frequency in comparison to current state of the art allowed for sufficient antenna size reduction. Both factors contributed to a significant weight reduction allowing for compatibility with honeybees. The successful transmission of the self-powered radio telemetry tags is shown whilst outlining the effects of the battery replacement and increased frequency on the link budget of the system.

A review of localisation systems for radio telemetry systems was performed in which alternative methods were investigated to allow for autonomous localisation of the radio telemetry tag with a single receiver. A compact phased array antenna affords angle of arrival (AOA) estimation and bee localisation through a received signal strength indicator approach (RSSI). The phased array antenna is capable of scanning +/-50° in azimuth and elevation. Additionally, a reflection type phase shifter capable of a 360° phase shift was designed and fabricated. Initial tests of the system were conducted in controlled environments and highlighted the system's ability to detect and determine the AoA of a tagged bee within a 20m range. Further tests demonstrated the systems unobtrusive nature when monitoring the foraging times of tagged bees whilst recording their initial flight trajectories. Commercial applications of the system are shown in which the system is mounted within a polytunnel to monitor plant visitations and pollinator services on strawberry plants.

To overcome the 20m detection range and achieve long range tracking of tagged bees the receiver unit was integrated to a drone in which the AOA estimate is

autonomously fed into the control system of a drone, allowing for continuous position updates. The drone interprets the estimate in which a bearing is calculated before the drone autonomously moves towards the position of the AoA estimate. The experimental results show proof of concept towards autonomous tracking of tagged bees.

ACKNOWLEDGMENTS

continuously made me smile throughout this journey and has helped me maintain a healthy work-life balance.

PUBLICATIONS

J. Shearwood, D. Man Yuen Hung, P. Cross and C. Palego, "Energy harvesting powered devices for Honeybee health monitoring", in International Microwave Workshop Series on Advanced Materials and Processes, Pavia, 2017.

J. Shearwood, D. Hung, S. Preston, P. Cross and C. Palego, "Honeybee Localization Using an Energy Harvesting Device and Power Based Angle of Arrival Estimation", in IMS 2018, Philadelphia, 2018.

J. Shearwood, S. Williams, N. Aldabashi, P. Cross, B.M. Freitas, C. Zhang and C. Palego, "Localization and Tracking Bees Using a Battery-less Transmitter and an Autonomous Ariel Vehicle", in IMS 2020, Los Angeles, 2020.

CONTENTS

Chapter 1.Introduction

1.1 Motivation

Recent studies have reported catastrophic declines in flying insect biomass, but are unable to fully identify the drivers of such decline [1]. The consequent loss of ecosystem pollination function is critical to human society [2, 3], and the need to fully understand pollinator spatial use at a landscape scale is critical. For example, to maintain or increase levels of crop pollination requires a continuous supply of pollinators, of which bumblebees and honeybees play a significant role [4]. A decrease in pollinator services could potentially reduce crop yields by up to 40% [5]. The transformation of the landscape from species rich habitats to agriculturally productive fields is considered a key factor in insect decline [6]. In order to fully establish how pollinators, interact in the environment, it is critical that we are able to follow their movements across considerable distances. However, current tracking technology is restrictive due to a number of technical and logistical challenges including high cost and transportability of equipment, detectability of insects in a range of landscapes (such as hilly terrain), practical implications of transporting cumbersome tracking technology and limited range of detection. This study aimed to develop a new portable and efficient system capable of long-range tracking of bees.

1.2 Literature review

1.2.1 Importance of insect tracking

A 75% decline in total flying insect biomass has been observed over the past 27 years[1, 7, 8]. Consequently, global efforts to better understand how such insects behave within their natural habitat have focussed on bee telemetric and colony health monitoring approaches [9]. For honeybees, the widespread use of insecticides such as neonicotinoids have been linked to such declines in population. Insecticides interfere with receptors in the central brain of insects, significantly affecting their cognitive functions and ability to navigate [10, 11]. Fig 1.1 displays the continuous decline in insect biomass per day outlining the huge decrease in insect mass over the past 27 years.

(a)

(b)
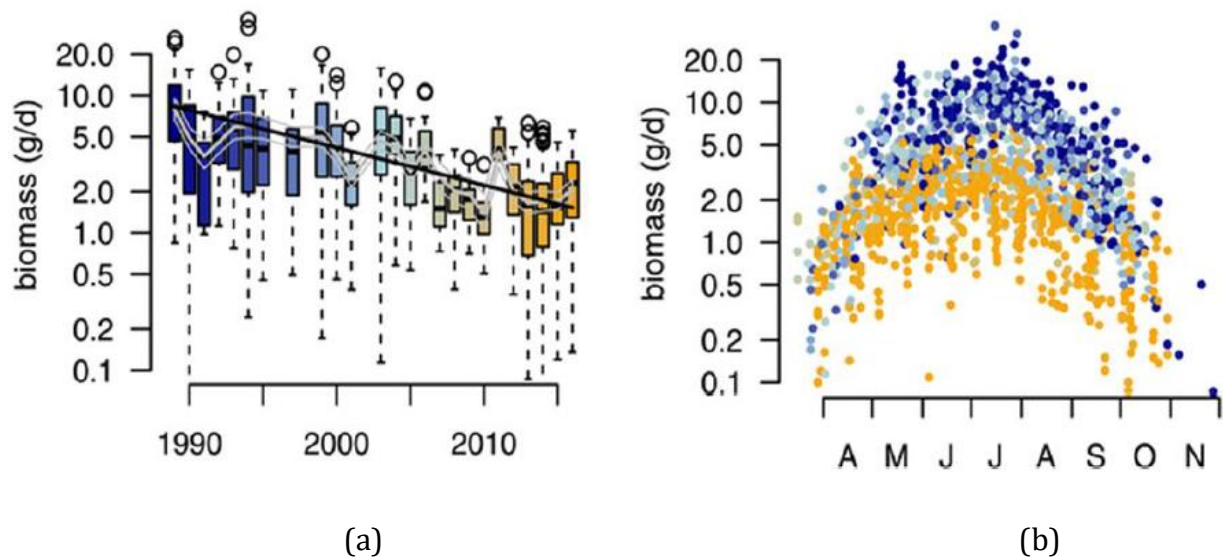
Figure 1.1: (a) shows the distribution of insect biomass (grams per day) captured over all traps in each year. (b) Monthly distributions of insect mass outlining the biggest decreases in warmer months where pollination mostly occurs [1].

Honeybees can forage up to several kilometres from the hive, and communicate information about forage source location to others in the colony via the waggle dance [12, 13, 14]. To decode the information transmitted during the waggle dance and navigate to the proposed location requires a substantial cognitive processing [15]. Navigation via the waggle dance has shown to be processed via flight vectors, which are related to the position of the sun [15]. Navigation has also been demonstrated through the memory of distinct landmarks such as the hive, feeding site or previously communicated locations via waggle dances. The locations are stored as a reference point within the bees' spatial surroundings. The reference points are then used to assist navigation to their destination [16]. This is outlined in Fig 1.2 which demonstrates the concept of spatial memory for navigation in the honeybee.
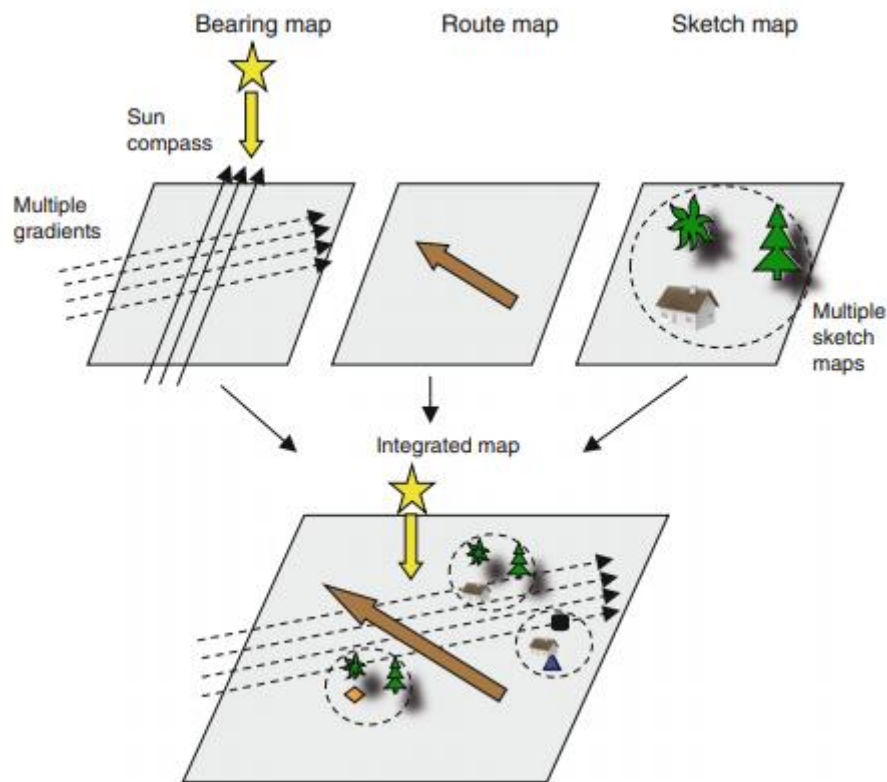
Figure 1.2: Concept of spatial memory for navigation in the honeybee [16]. Bearing maps are generated by relating landscape features (gradients) to the sun compass. Sketch maps are predicted to be placed into a bearing map, in which snapshots memories of landmarks are placed within the bees projected map. Route maps combine both bearing and sketch map features. They are continuously interchanged when one or more features are missing, such as multiple clouds interrupting the sun compass.

A study in 2014 proved that honeybees exposed to non-lethal doses of neonicotinoids significantly affected their ability to return to the hive. The probability to correctly turn when reaching a landscape structure was reduced, and return flights to the hive were less direct [10]. Neonicotinoids are widely used in agriculture to protect crops from insect pests [17]. Neonicotinoids initially stimulate the insects receptor and cause a depolarizing blockade (neuromuscular blocking agent) later leading to death as a result of paralysis [18]. Neonicotinoid concentrations within nectar and pollen of treated plants are often too low to cause direct mortality to bees [19], however continuous foraging on treated crops will likely lead to long term exposure [10].

Neonicotinoids appear to be compromising to bee cognitive function [20, 21, 22, 23] and there is now an urgent need to understand bee foraging behaviour and navigation when exposed to various concentrations of neonicotinoid impacted environments.

1.2.2 Harmonic radar

Applications to study high altitude migration of insects were developed during the 1970's via the use of scanning radar [24]. In the 1990's, radar-based research allowed for increased observation capabilities from the introduction of Vertical Looking Radar (VLR) and harmonic radar. VLR can be used to study high altitude migration of insects, whilst harmonic radar can observe and monitor low altitude foraging flight [25]. Consequently, research became increasingly focussed on flight behaviour and the environmental variables impacting insect flight behaviour. Studies using harmonic radar have shown how healthy honeybees forage in comparison to those exposed to neonicotinoids [10, 26, 27, 28].

Harmonic radar can be separated in two categories: fixed ground-based systems and a handheld portable system, as depicted in Figure 2.3. For more sophisticated and long range studies there is a ground-based radar system capable of achieving a detection range of 1km providing the system is used in flat terrain , however, due to the stationary design, the system cannot cover the entire foraging range of bees due to the limited detection range of the harmonic radar and its inability to detect bees that fly above the vertical beam width of the parabolic antenna [29]. A simpler handheld version can be used, but the detection range is limited to 60m [30]. The portable system is powered using a 12V battery and can be easily placed inside a small backpack. Whilst ground-based harmonic radar have output powers of the order of tens of kilowatts [24], the output of the portable harmonic radar is approximately 0.1W, contributing to the reduced detection range.

The harmonic radar tag consists of a wire antenna attached to a Schottky diode in parallel with an inductive loop, which is responsible for re-emitting the original waveform to the second harmonic of the signal, thus, differentiating the reflected signal from the tag from cluttered environments, whilst weighing between 6-10mg [31]. The significantly low tag weight highlights an advantage of using harmonic radar to track insects, since as the power comes from the radar itself there is no requirement for an on-board battery allowing for substantial miniaturisation [32]. Harmonic radar tracking tags have also been achieved via a microstrip design where a patch antenna is used instead of a wire antenna [33]. A comparison between a traditional harmonic radar transceiver and microstrip transceiver is formed in Fig 2.4. A microstrip design can be continuously

attached to the honeybee throughout their lifespan whilst monopole designs have to be attached and removed before and after flights.

(a)   (b)

(c)
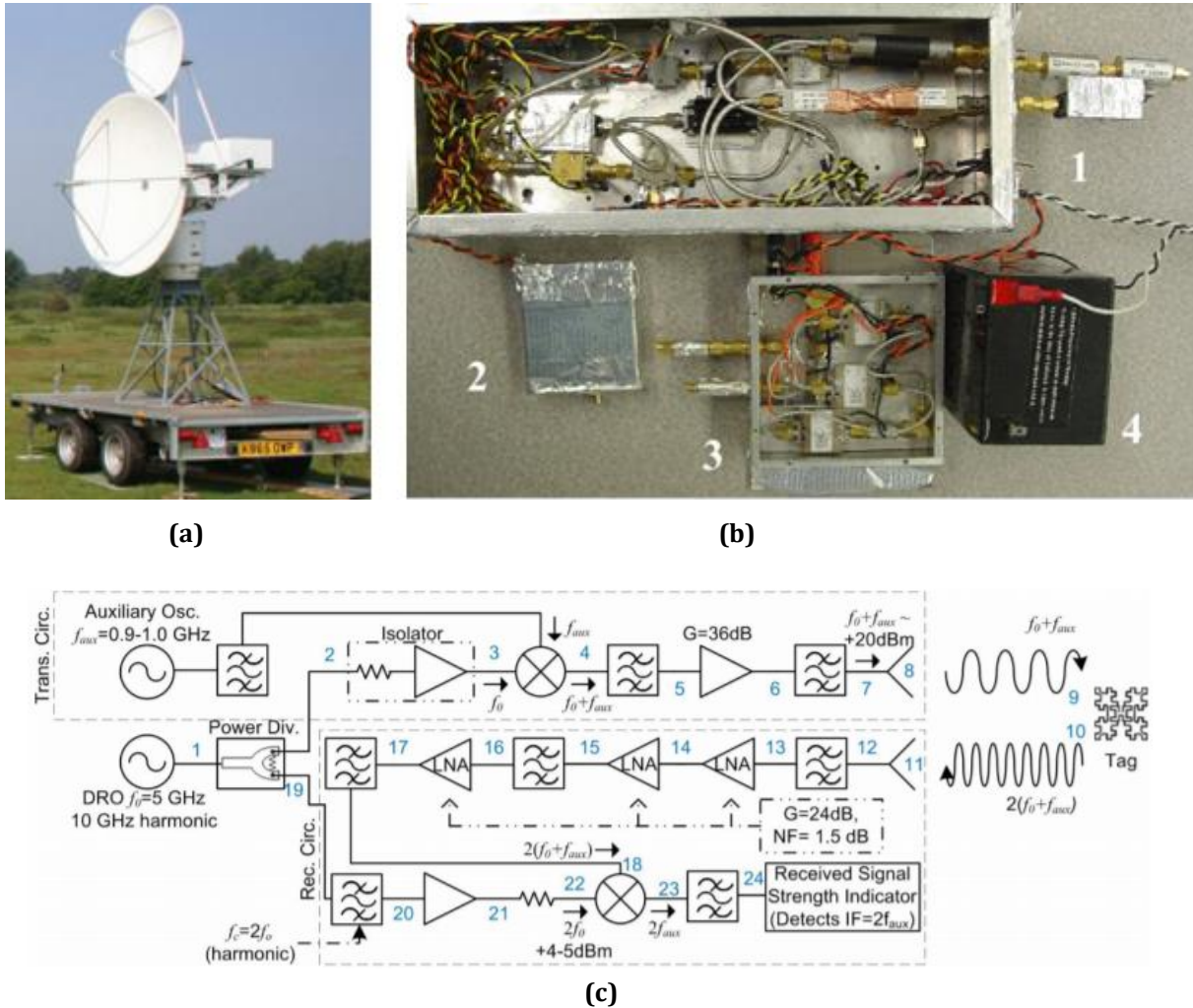
Fig 1.3: (a) Ground-based harmonic radar system from Rothamsted, UK [24]. The larger of the two antennae is used for transmitting a signal at 9.4 GHz, whilst the smaller antenna is responsible for capturing signals returned from the tagged insect. (b) Portable harmonic radar system minus antennae [30]. In numbered order it consists of transmitter, mixing circuit, oscillator, low-noise block and 12V battery. (c) Schematic of the insect tracking system [30].

<div align="center">(a)   (b)</div>
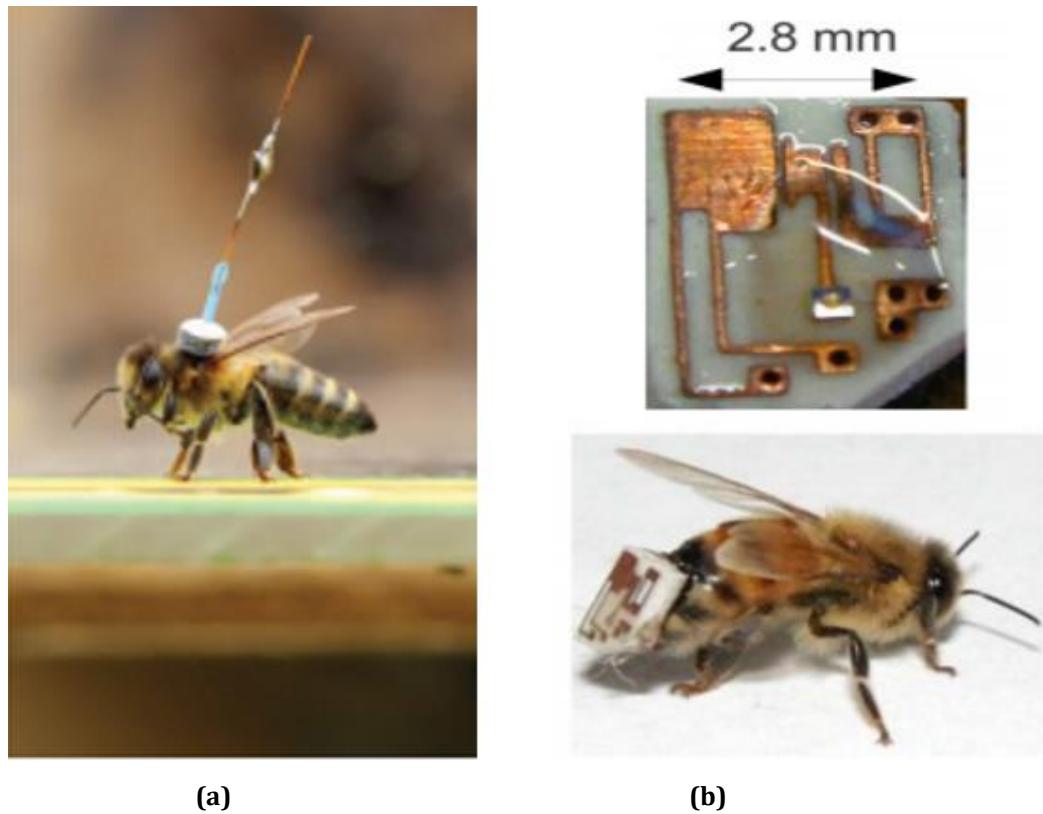
Figure 1.4: (a) A honeybee carrying a harmonic radar transceiver designed for use with traditional ground-based systems operating at 9.4 and 18.8 GHz [24]. (b) Microstrip design of harmonic radar transceiver to decrease the height of the tag [33].

Commercially available radars of interest to entomologists are available in two forms, which can be distinguished via the temporal characteristics of the signal transmission. Frequency Modulated Continuous Wave (FMCW) radars emit a 'chirp', in which the frequency increases with time. The tags distance can then be calculated by comparing the outgoing and incoming signal frequency. As the time frame between increasing the frequency is known the transmitted and received can be correlated to determine the distance from the tag. FMCW radars have been implemented for insect tracking, facilitating increased insect detection precision. Due to the costs involved with generating a high powered 'chirp' across a large frequency range, such devices are difficult to obtain [34]. By contrast, pulsed radar, which emit short bursts of high power radiation, estimate distance via the time delay between transmitted and received signals [35, 36, 37]. Attempts to improve the detection range and sensitivity have seen the inclusion of a pseudorandom code positioning technique to cancel local leakage of the transmitted signal, via the use of advanced signal processing. The leakage is cancelled via the autocorrelation function of the pseudorandom code [38]. The measured sensitivity of the

transceiver is 120 dBm, which is 27 dBm lower than the noise floor [38]. Further challenges include operational frequency as two frequency bands are required. Finding suitable frequencies that satisfy existing regulations has been a particular hindrance for the use of harmonic transponders [39]. The ISM band operating at fundamental frequencies of 2.45, 5.8 and 5.9 GHz have been applied [30, 40], whilst the possibility of using millimetre wave frequency have been explored [41, 42]. Due to the higher path loss associated with higher frequencies only short-range applications have been considered. Maritime radar with a fundamental frequency of 9.4 GHz have been widely adopted for insect tracking [32 ,38].

Traditional radar can be described using the radar equation [39], which can be more accurately characterised using Friis' transmission equation for the forward and return path of the signal [39]. Due to the transceiver's frequency conversion stage, harmonic radar cannot be described via the traditional radar equation, as the harmonic frequency is not accounted for. The transceiver consists of three functions which are harmonized and independent. Firstly, the transceiver is responsible for capturing the transmitted signal and efficiently delivering the signal to the next function which is the frequency conversion. The purpose of the frequency conversion is to deliver a maximum second harmonic power to the transmitting stage. Finally the transmitting stage is responsible for efficiently radiating the generated second harmonic signal back to the receiver [43].

The transceiver comprises a frequency doubler and antenna [44]. The frequency doubler consists of a nonlinear element which is typically a Schottky diode [30], whilst the antenna is responsible for the communication between Tx/Rx, and therefore must be matched to the fundamental and harmonic frequency. Similar design constraints of electrically small antennas can be closely linked to the design of harmonic transceivers. An antenna of small size, good efficiency and broad bandwidth is theoretically impossible to achieve [45]. This is because improving the bandwidth for an electrically small antenna can only be achieved by establishing a TE and TM mode through volume utilisation of the antenna or by reducing efficiency [45]. This leads to designs focussing on meeting small size and good efficiency or small size and broad bandwidth for electrically small antennas. For harmonic transceivers, the impedance characteristics of the diode affect the required matching. Typically, a more complex matching system will increase antenna size, resulting in an improvement in the bandwidth and efficiency of the antenna [46].

We can quantify the tag from a system point of view where we examine the cross-sectional area. The harmonic cross-sectional area of the tag can be quantified by:

$$\sigma_h = \frac{P_{dth}G_{dh}}{W_{df}} \; m^2 \tag{1.1}$$

Where σ_h is the harmonic cross section of the tag; $P_{dth}G_{dh}$ is the effective isotropic radiated power (EIRP) emitted from the tag at the harmonic frequency in Watts. W_{df} is the power density incident upon the tag at the transmitted frequency given in Watts per square meter. Ultimately, we can use the above equation to generate a single parameter to characterise the transceiver performance. As the harmonic cross-section rapidly degrades with power density, it is important to maintain a high transmitted power to achieve maximum range [38].

The radar range equation for harmonic radar shows that the received signal is inversely proportional to the fourth power of the range between Tx/Rx and transceiver [47]. The range law can also be applied to higher harmonics, however this requires the inclusion of a multiplication factor $\left(\frac{\lambda}{n}\right)^2$, where n is an integer which represents the harmonic [48]. Thus, for practical radar and achieving maximum detectable range utilising the second harmonic is required.

The power density incident upon the tag S_t can be calculated by considering the power input into the antenna P_t, radiating through an antenna of gain G:

$$S_t = \frac{P_t \, G}{4\pi \, R^2} \tag{1.2}$$

Where R is the separation between transmitter and tag. Assuming the tag is within the main beam of the antenna, the tag will scatter the incident power in multiple directions at the harmonic frequency as shown in Equation 1. As the scattered source is of finite size, the power density must decay as $1 \, /4\pi R^2$ away from the tag [47]. From this we can determine that the power density of the second harmonic signal reflected back to the receive antenna is:

$$S_r = \frac{P^t G^2 \sigma_h}{(4\pi R^2)^2} \tag{1.3}$$

Using the reflected signal back to the receiver we can define the received power as:

$$Pr = A_e S_r \tag{1.4}$$

Where A_e is the maximum effective aperture of the antenna which describes how much power is captured from a given plane wave. We can further describe the effective aperture with the following equation:

$$A_e = \frac{D\lambda^2}{4\pi} \tag{1.5}$$

D can be defined as aperture efficiency which compares the ratio of maximum directivity vs actual directivity and λ is the wavelength. The effective aperture defined above does not account for the effect of losses in the antenna. This can be solved by considering the gain of the antenna instead of the aperture. For conventional radar, the received power can now be:

$$P_r = \frac{P_t G^2 \lambda^2 \sigma}{(4\pi^3) R^4} \tag{1.6}$$

Whilst the equation is suitable for conventional radar it cannot be applied for harmonic radar as multiple factors are excluded such as the second harmonic wavelength, antenna gain at second harmonic and the gain of the transceiver at fundamental and harmonic frequency. We can write harmonic radar power received as:

$$P_{rh} = P_t G_t G_r \left(\frac{\lambda_f}{4\pi R}\right)^2 G_{df} G_{dh} \sigma_h \left(\frac{\lambda_h}{4\pi R}\right)^2 \tag{1.7}$$

The equation is used to determine the maximum possible received power and assumes a lossless system. Multiple factors such as impedance mismatch, polarisation mismatch between the antennas, attenuation of the signal due to propagation effects or multipath can cause partial cancellation of the received power.

The equation now considers the fundamental frequency λ_f and the harmonic frequency λ_h. The gain of the transmitter/receiver at fundamental frequency G_t and receiver gain at harmonic frequency G_r whilst also accounting for the gain of the transceiver at receiving and transmitting stages respectively G_{df}, G_{dh}. Defining the sensitivity of the radar system as P_{min}, the maximum detection range R_{max} can be expressed as:

$$R_{max} = \frac{1}{4\pi} \left(\frac{P_t G_t G_r G_{df} G_{dh} \sigma_h \lambda_f^2 \lambda_h^2}{P_{min}}\right)^{\frac{1}{4}} \tag{1.8}$$

Furthermore, by determining the above factors, the radar system can be analysed to determine if sufficient range can be achieved to make the radar system functional.

Despite offering larger operational ranges, harmonic radar is limited by the terrain within which it can successfully operate. Conventional harmonic radar systems, as used in a vast majority of harmonic radar studies, implement a parabolic dish antenna with a very high gain and a half power beam width of 1.8 degrees [34, 49, 50, 51]. Hence, when the insect flies outside of the beam width the gain drastically reduces, significantly impacting the detection range. Alternatively, vegetation such as hedges, bushes and trees provide barriers to the system as signals are heavily attenuated, further reducing the maximum achievable range [31], [32].

Consequently, studies can only take place on flat and open terrain. To overcome this limitation. various Rx/Tx designs have been explored to provide highly accurate spatial resolution, whilst allowing for operation in hilly terrains [36], [52]. Designs have incorporated 1.5-degree half power beam widths in azimuth and a much broader beam width of 24 degrees in the elevation plane [53]. To achieve a higher beam width, fewer elements with an antenna array are used, leading to a slightly reduced gain in the Tx and Rx. Referring to the range equation previously derived, the maximum achievable range decreases with a lower antenna gain for Tx and Rx. Whilst these systems have successfully operated in hilly terrains the maximum achievable range was reported to be 500m [52], giving limited coverage of a bee's entire foraging range (typically 3km) [29], providing researchers with limited understanding of how bees interact with their extensive environment.

1.2.3 Radio Frequency Identification

RFID enables users to uniquely identify objects via wireless communication [54]. The main usage of RFID has been for long-term identification of a large number of individuals [9]. An RFID system consists of a tag and interrogator which communicate between one another via an encoded radio frequency signal. When a tagged object enters the read-zone, the interrogator queries the tag to transmit stored data for identification. This principle is demonstrated in Figure 1.5. RFID systems can be designed to operate with either active or passive tags. The effective signal range between interrogator and tag will vary with the frequency selection, power output of the antenna and the size of the tag [54]. Active tags consist of an on-board battery and have been used on larger insects to achieve detection ranges of up to 30m, however, they are normally around 1-5m [55].
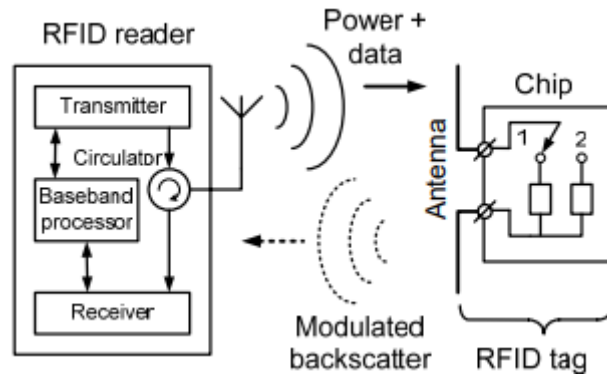
Figure1.5: Operation of a passive RFID system. Signal is transmitted from the receiver in which the tag will transmit a signal back to the reader [56].

For smaller insects, a passive tag is favourable as power is derived from the interrogators transmitted signal, obviating the need for a battery. These tags have a small detection range as they only operate within the near field, via magnetic coupling and have a maximum operational range of a few centimetres and weigh 0.9 – 4mg [57, 58]. The near field region is commonly given as:

$$r = \frac{\lambda}{2\pi} \qquad (1.9)$$

Where r is the separation between tag and reader and λ is the wavelength.

For studies implemented for bee monitoring, interrogators are usually placed at the entrance of the hive to monitor in-and-out movements from hives to feeding stations [57]. As well as bee monitoring, RFID studies have been applied to ants [59], beetles [60] and other subterranean insects [61]. Several studies utilising RFID have investigated honeybee and bumblebee parameters such as: activity patterns; foraging behaviour; homing ability effect of neonicotinoids on survival rates as well as forming comparisons between flight activity and homing ability of the Asian and European honeybee [20, 21, 62, 63].

Three typical frequencies are used while tagging insects and the choice of frequency is contingent upon the requirements of the study. The most important factors to consider are the size of the tags and the maximum detectable range, so that the position of the antenna at the entrance to the feeder or hive can be correctly placed [64]. Figure 1.6 outlines a typical RFID system used in bee monitoring studies.

Some studies employ high frequency (13.56 MHz) radio signals to activate tags which measure approximately $1mm^2$ [65]. The reading distance depends on the tag and reader, as they operate within the near field. The tag and reader are coupled mainly

through magnetic field distances up to 4mm [57, 58, 66]. Laser light activated tags have also been proposed which increase the detection range to 10mm. The tags must read a 1.5mm diameter laser beam therefore detection success can be low due to misalignment between the tag and reader [67]. Further advances have led to detection ranges of 3cm, achieved by using ultra-high-frequency (860-960MHz) tags, however these tags used are usually larger [68]. Further attempts to increase reading distance have explored the use of a booster antenna to increase RF coupling and have demonstrated bumblebees being detected up to 1.5m away with a tag weight of 81mg [69].

(a)   **(b)**
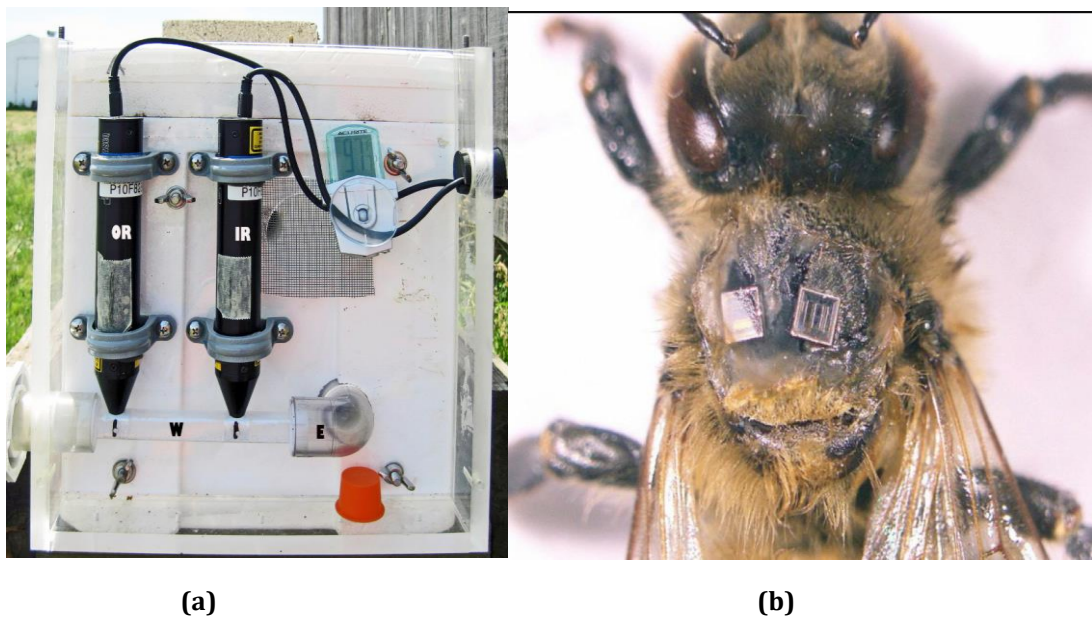
Figure 1.6: (a) RFID reader monitoring the entrance to honeybee hive. Due to a detection range of a few centimetres the readers have to precisely be placed to ensure no misalignment. Two readers are present to determine leaving or entering the hive by comparing which reader lastly identified the honeybee (b) tagged honeybee with 13.56 MHz RFID tag attached [64].

Multiple studies have examined the success rate of the RFID systems to ameliorate parameters such as reader capacity, tag type, experimental set up, duty cycle and power of the transmitted signal. Recent systems have demonstrated nearly 100% success in reading tag where required [58]. Such studies have outlined significant improvements compared to previous studies which demonstrated detection success rates of between 80 – 90% [70, 71].

RFID tags allow unique identification of individuals and at a reduced cost while allowing for continuous monitoring for the entirety of a bees' lifespan. Studies covering larger spatial scales are beyond most research budgets due to the high costs associated with readers [9]. Whilst time stamps allow for identification at hives and feeders, the path taken between these points remains unknown.

1.2.4 Radio telemetry

Radio telemetric techniques have been implemented for more than 50 years for applications involving the study of local movements and habitat of various animals [72, 73, 74]. They have been used for biotelemetric applications [75] , becoming an important technique for wildlife telemetric applications [9]. As depicted in Figure 1.7, radio telemetry comprises three principal components: an active battery-powered tag to send a pulsed signal to a receiver, an antenna system, and a receiver system to detect the transmitted signal. The frequency of these signals is usually VHF; 30 – 300MHz, resulting in very large antennae when the tags are attached to insects. This is due to the low operational frequency of the tag which results in a large wavelength. Active transmitters can typically achieve a maximum range of 500m over flat terrain, facilitating unique identification of individuals [76]. Ranges of between 100 – 400m are reported in studies [76, 77]. Tracking ranges have further increased with the use of helicopters [78] and light aircraft [79] however, the studies have focused on long-range migration for larger species. Continuous bearing estimation ensures the helicopter or light aircraft can maintain its proximity within the detection range between tag and receiver.

(a)   (b)   (c)
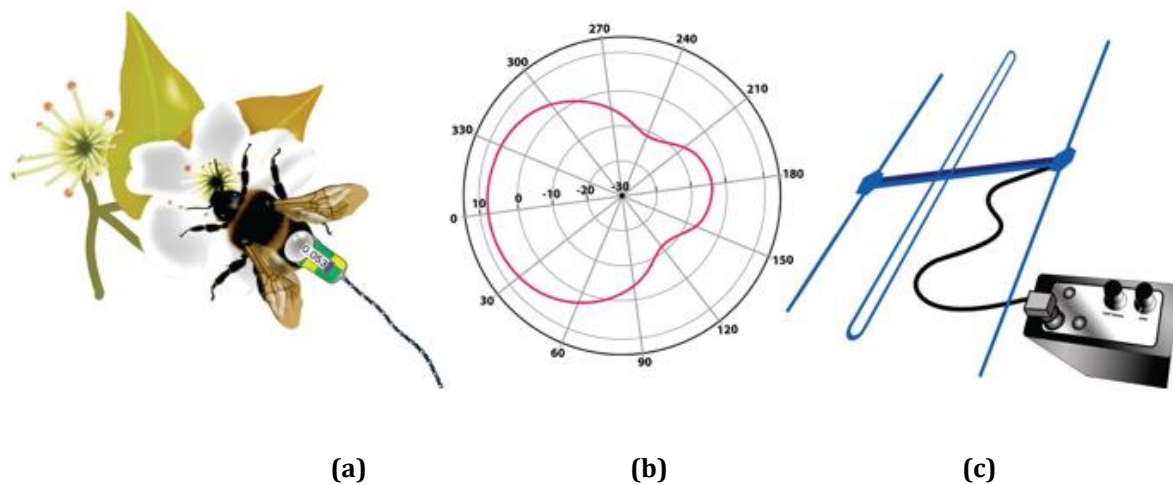
Figure 1.7: Fundamental elements for radio telemetric studies. (a) A tagged bee attached with a radio telemetric transmitter, which emits a radiofrequency signal at known time intervals. (b) A directional antenna. The received radio signal will be at its strongest when the main beam of the antenna is directly facing the bee emitting the RF signal. (c) A receiver unit connected to the directional antenna. The user can manually sweep the antenna from side to side to determine the bearing in which the signal is coming from [9].

The limitation associated with radio telemetric studies highlights the key trade-off between transmitter weight vs power and battery life [9], [80]. The power can be related to battery size which has a direct correlation with the weight of the tag. To achieve higher transmitted power or longer tag duration, a larger tag is required [9]. Unlike passive studies, where tags are generally low cost, active tags cost approximately £130 each [81, 82], whilst having a limited operational lifetime of between 7 -21 days depending on the set duty cycle of the tag [83]. The lightest commercially available tags are around 200mg in weight, limiting the technology to the largest species of tropical bee.

The last decade has seen numerous radio telemetry studies performed using commercially available radio telemetric tags and tracking systems for beetles [84], dragonflies [85], crickets [86] and bees [83, 87]. The first radio telemetry study on bees was performed on carpenter bees in 2008 where their role in crop pollination was explored [87]. Since then, the movement behaviour studies of tropical orchid bees [83], bumblebees [88] and Asian Hornets have been performed [89].

A general rule of thumb states that if the tag weighs more than 10-12% of body weight, it can also adversely affect flight behaviour [88]. This has been observed when 200mg transmitter where attached to bumblebees, and the bee weight vs transmitter weight varied from 44 – 100%, causing significant physical hindrance and energetic costs to the bee. Transmitters have been used to attempt to locate Asian Hornet nests where insect flight was hindered and could only be achieved with a small percentage of tagged hornets [90]. Several studies have used 0.3 g transmitters on orchid bees however they were unable to conclude how flight performance was affected via transmitter load, as researchers were unable to visually confirm the difference between the flights of tagged bees compared to natural flight [83]. Figure 1.8 shows the huge size of commercially available radio telemetric tags when attached to a bumblebee and orchid bee.

(a)   (b)
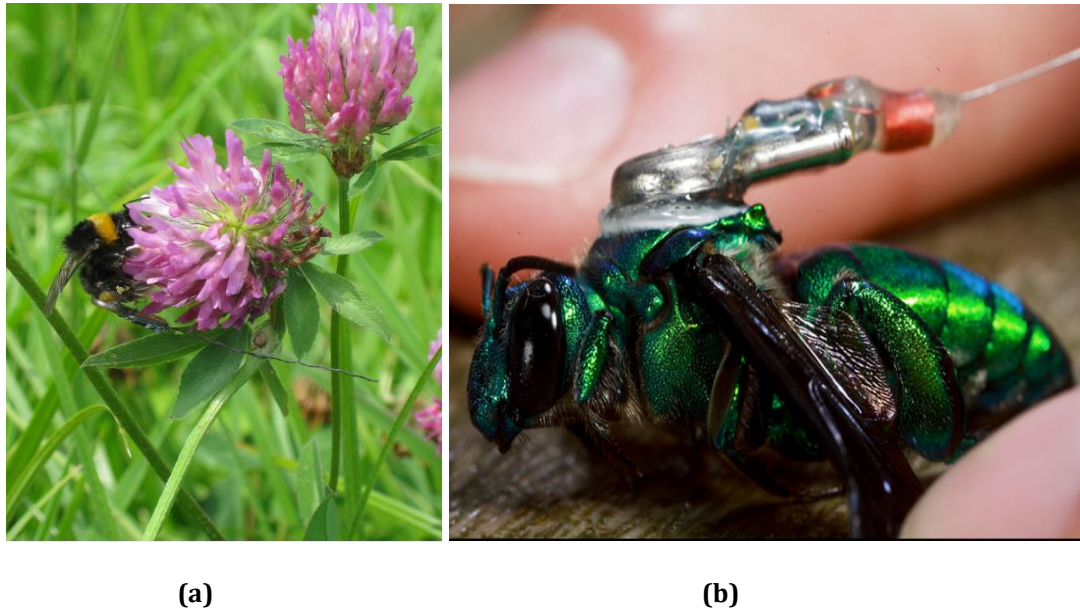
Figure 1.8: Commercially available radio telemetry tags used to study flight behaviours of (a) bumblebees [88]. (b) Tropical orchid bee [83].

Orchid bees are known to be strong flyers [91], therefore it was concluded that their ability to carry such high payloads was not surprising. As the battery comprises the bulk of the transmitter weight, current technology does not permit attaching active radio telemetry transmitters to smaller insects such as honeybees due to the tag's weight.

1.2.5 Alternative tracking methods

Whilst harmonic radar, RFID and radio telemetry approaches are the most common approaches for studying the spatial interaction of insects within their environment, several alternative methods can also be used. These include homing experiments [92, 93], microsatellite approaches [94], acoustic tracking [95], theoretical models [96] and Light Detection and Ranging (LIDAR) [97, 98].

The use of MEMS microphones to record the sound and using signal processing have been used to track bees entering and leaving the hive with high accuracy [99]. Bees also communicate through sound therefore systems which monitor acoustic frequencies emitted from the hive have been implemented to monitor the overall health of the hive and accurately predict swarming behaviour, since there is a known frequency which can be correlated to swarming [100].

Several techniques have focussed on measuring minimum movement rather than focusing on long-range movements. LIDAR, which uses light to measure reflectance of an

object, has been implemented to monitor honeybees' movements up to a distance of 90m [101]. Whilst proven to be an effective method, LIDAR does not allow for the identification of multiple individuals. Genetic microsatellite approaches have been implemented for quantifying foraging range and nest density [94]. The use of opalith tags (small coloured tag usually used for Queen identification within a hive) on individuals have allowed for visual observation to track marked individuals across a study site [102], however, such studies have proven to be onerous and time consuming.

Theoretical models have been developed to predict the maximum foraging ranges of insects. The use of algorithms to predict the maximum foraging range through the correlation of flight range vs body size [96] or by the analysis of optimal foraging theory considering the energy budget of the insect have been implemented to estimate maximum foraging range [103]. Furthermore, maximum foraging range has also been determined via the use of homing experiments. Insects with a natural ability to bring resources back to their hive/nest are exposed to unfamiliar environments and visual observations are performed to observe the insect's ability to return home [92]. Such studies have investigated honeybees [92], solitary bees [104]and bumblebees [93].

Further studies have explored the use of global tracking of animals [105, 106], however the transmitters needed for such systems are relatively large and limited to species weighing 300 g and above. The implementation of solar cells to power the transmitter has reduced tag mass to 5 g allowing for tracking of small birds [107]. Whilst such systems are attractive for long-range tracking, the spatial resolution of such systems is limited to large scale movements such as migrations [9].

1.2.6 Self-powered radio telemetry tags

Current radio telemetry systems have demonstrated potential for monitoring larger insect interactions, however, size constraints have limited the technology to larger insects due to the size of the battery [108]. As explored for satellite technology, the use of self-powered tags greatly reduce the weight of the transmitter [107]. Such an approach could be adapted for radio telemetry and allow for further miniaturisation to the tags in order to be implemented on smaller insects.

Whilst self-powered radio frequency tags have been investigated [109, 110, 111], they have mostly been limited to larger animals. Applications of self-powered transmitters for smaller insects are yet to be developed. Energy harvesting from small

insects such as moths [112] and beetles [113] have been explored, however, studies were aimed at proof of concept. Insect energy harvesters have the potential to replace the battery in traditional radio telemetry circuitry, allowing for small structures which could be adapted to bumblebees and honeybees. Figure 1.9 and 1.10 shows the design and practical implementation of an electromagnetic generators capable of scavenging energy from Moth flight.

The use of a cantilever beam mounted to the thorax of the insects demonstrated the ability to capture energy through the vibration of the thorax during flight. Energy harvesting from moth flight is based on the concept of magnetic induction driven by moving magnets. Moving magnets, a core, a support structure, and stationary windings are used to create the resonant generator. The magnets (~240 mg), which provide the mass along with the support structure and core provide the resonant frequency which is tuned to the wing beat frequency of the moth (~5g). The moving magnets, core and windings create the AC generator (~1.28g).
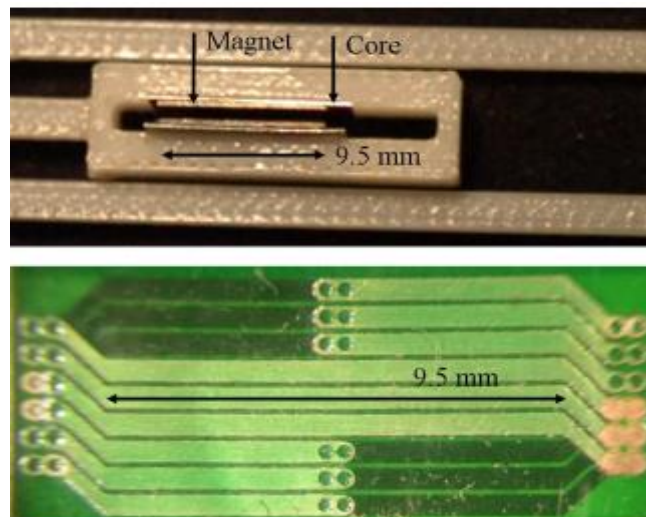
Figure 1.9: Fabricated electromagnetic generator to be used to harvest energy from Moth flight [112].

Figure 1.10: Fabricated energy harvester attached to *Manduca Sexta* [112].

Unlike Moths, where the wing beat frequency is consistent, beetles have a varying wing beat frequency ranging between 85 – 105 Hz, meaning conventional resonant structures will only work when the beetles wing beat frequency matches the resonant frequency of the harvester [113]. The use of a piezoelectric cantilever, in which the tip was directly excited by the thorax of the beetle demonstrated non-resonant energy harvesting from insect flight, as demonstrated in Figure 1.11.
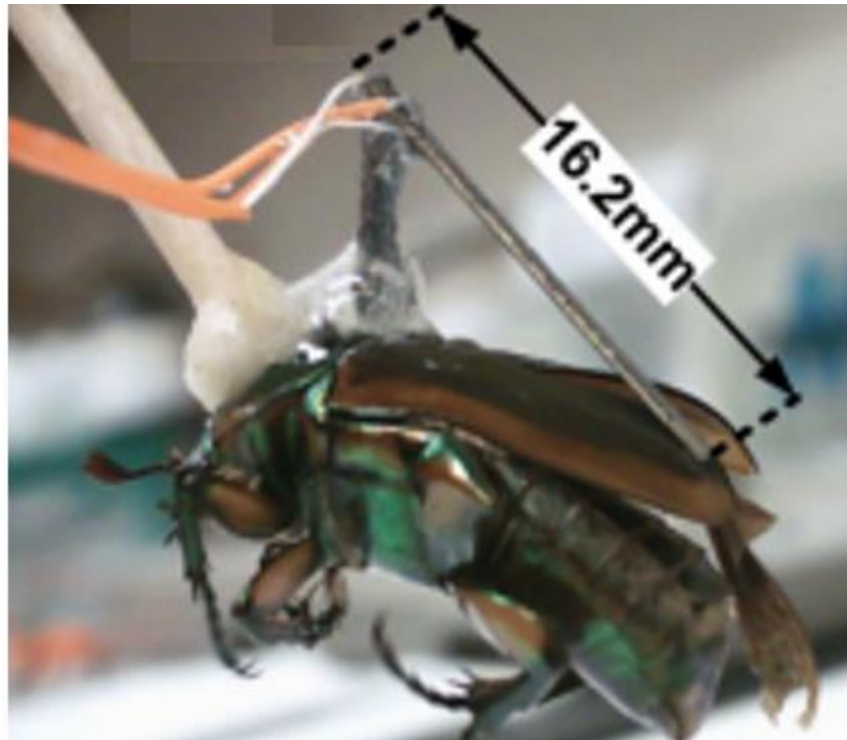
Figure 1.11: Piezoelectric energy harvester prototype mounted to beetle [113].

Flexible piezoelectric material, such as Polyvinylidene fluoride (PVDF), has been successfully implanted into fish and used to power acoustic telemetry systems up to a range of 100m [114]. PVDF allows for superior flexibility in terms of attachment capability, whilst providing minimal impedance to natural movements, however, the power generation is considerably lower compared to piezoelectric ceramic counterparts, due to their much lower mechanical to electrical energy conversion efficiency [115].

Further studies have also explored the possibility of using energy harvesting as a method to further improve battery life [110]. The use of ceramic piezoelectric materials to harvest energy from the flight of birds and use the energy stored as a secondary power source has been explored, however such approaches are unable to reduce tag weight and size. This principle is shown in Figure 1.12.

(a)

(b)
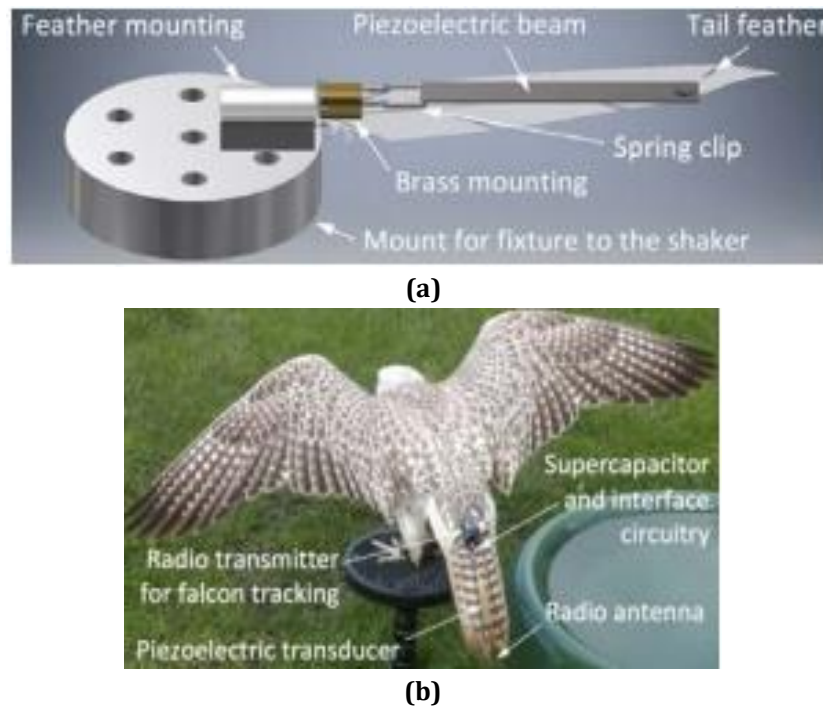
Figure 1.12: (a) Design of the piezoelectric cantilever to harvest energy from tail feather. (b) Piezoelectric energy harvester and radio telemetry system attached to falcon [110].

Whilst only a few studies have explored the possibility of harvesting energy from insect and animal flight for powering radio telemetry tags, several studies have been conducted in closely related fields which could pave the way for the future studies of self-powered radio telemetry tags. Examples of such systems include RFID tags using an electrostatic MEMS-based Vibration Energy Harvester [116] and a self-powered RFID tag using triboelectric-electromagnetic hybrid nanogenerator, which can convert biomechanical energy into electrical energy. Based on the combination of triboelectrification and electrostatic induction energy can be harvested from ambient mechanical sources [117]. Additionally, a piezoelectric harvester which converts mechanical energy found from vibrations in everyday life to electrical energy to power an RFID tag [109].

1.2.7 Radio telemetry tracking systems

The majority of radio telemetry studies discussed thus far have used manual tracking with a handheld receiver or via the use of aircraft or vehicle mounted antenna. Such approaches require a large amount of physical labour which limits tracking to restricted times whilst also limiting sample size, due to the continuous need to be user operated [9]. The use of an automated system would allow for data to be continuously

collected without the presence of a user, as well as removing all tracking errors that can be associated with the operator [131].

Automated systems occur either as data loggers or tracking systems. Whilst both act autonomously, they are differentiated by the information they collect, which is shown in Figure 1.13. Automated tracking systems have become available over the past 10 years, and are typically used to compute bearings of signal from radio telemetric transmitters and continuously track their movements [118]. Automated data loggers however, are unable to perform such tasks as they operate on a presence/absence design which is commonly associated with small scale radio telemetry studies [119]. Data loggers have also been available and used since the start of wildlife telemetry [120]. The set-up of a multiple receiver with overlapping detection ranges would allow for the insect to be tracked in quadrants determined by the location of the receiver. Whilst the technique can accurately locate the quadrant in which the insect lies, the cost associated with the design is high due to the need of multiple receivers, whilst providing minimal special resolution compared to triangulation designs [9].

(a)   (b)
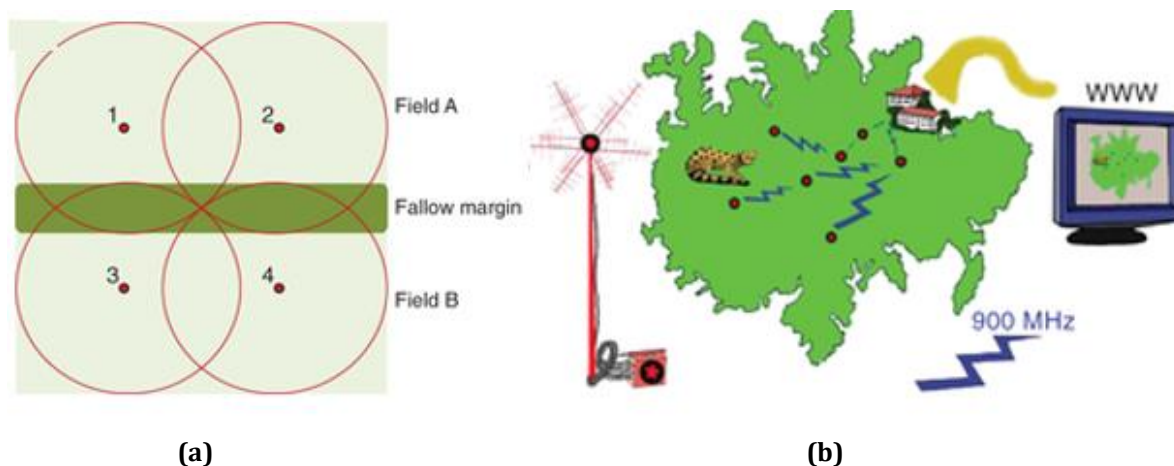
Figure 1.13: (a) Presence/absence design in which the location of the signal can be estimated from the use of multiple receivers, all with overlapping detection range. [9]. (b) Automated triangulation design principle, in which multiple towers are present within an area. The tower is equipped with directional 6 Yagi antenna, set at fixed angles, and calculates a bearing based on the received signal strength. Multiple bearings allow for triangulation of the signal [118].

The use of triangulation designs has increased precision in obtaining spatial locations of tag. Such systems use multiple antennae, to continuously record signals from at least two receiver stations [121]. The use of omnidirectional antennae to provide near uniform coverage allows for bearing estimation based on a Received Signal Strength Indicator (RSSI) at each receiver, however, the sole use of RSSI to estimate position with multiple receivers can lead to errors in position estimation, due to multipath effects [122].

Directional antennas have also been used, but require multiple researchers in different locations to estimate the position in which they will find the intersection point [123].

The two approaches implement different ranging techniques. Researchers using directional antennas to determine an intersection point implement an angle of arrival technique whilst omnidirectional antennae implement a received signal strength approach. Other localization techniques calculate position based on the time difference between receiving signals at known locations, although currently no study has been conducted using this approach for radio telemetry. To implement such a system all receivers would need to be highly synchronised and running off the same time signal. Any small error in time synchronisation would likely lead to elevated estimation errors [124].

Angle of arrival utilises a directional antenna [124] or non-uniform omnidirectional antenna , or by measuring the phase difference of a received signal in an antenna array or multiple antennae [125]. Radio telemetry studies typically utilise a Yagi antenna which is manually rotated to determine the location by comparing received signal strengths [126]. The maximum or minimum value can be used to determine location. Once a reference angle is established, an angle between the signal source and reference can be obtained. Since the bearing is typically calculated by the user, human error is introduced decreasing the accuracy of the bearing estimation. Autonomous systems have been developed with estimation accuracy of +/-5° [125]. Such systems are vulnerable to dense environments as multipath can lead to errors in bearing estimation.

Received signal strength is based on the fact that signal strength decays with distance. From the Friis transmission formula we can state that the signal strength decays with the square of the distance [39]. With known parameters such as the gain of transmitting and receiving antenna, power transmitted and power received, the distance in which the signal travelled can be derived. Adapting Equation 1.6 to consider only forward path, we can define the Friis transmission formula thus:

$$P_r = \frac{G_t G_r \lambda^2}{(4\pi R)^2} P_t \qquad\qquad (1.10)$$

The formula addresses the fundamental question of how much power is received by a radio antenna. This is referred to as the maximum possible received power because there are many multiple factors that can reduce the power received. A fluctuating received power can affect the accuracy of position estimation. Fluctuation factors include:

impedance mismatch at either transmitter or receiving antenna, propagation effects which can cause depolarisation or attenuation and multipath effects [39].

Whilst many guides on triangulation for radio telemetry recommend plotting three bearings and estimating the tag location to be the intersection point [127], there are several methods that can also be applied to provide position estimates. The use of two receivers can be used to estimate location based on geometric, arithmetic, and best biangulation techniques. Adding an additional receiver allows for estimation via a maximum likelihood estimator, whilst four receivers are required for Andrews and Huber [128] that weight bearings based on their contribution to the estimation, making them particularly useful in noisy environments where multiple signals are present [129].

Recently, unmanned aerial vehicles have been introduced into radio telemetric studies, focussing on tracking movements of large animals [130, 131, 132]. Due to system complexity and costs involved in larger UAV's, only a single drone is used to perform localisation, thus limiting the system to a single receiver [130]. Directional antennas have been mounted to a UAV in which the drone would slowly rotate 360° until an angle of arrival estimation was obtained [130]. Such an approach is unsuitable for insect tracking as measurements take approximately 14 seconds each by which time the insect has moved outside the detection range of the system [130] . Figure 1.14 depicts a UAV equipped with a radio telemetry system to allow for real time localisation of radio-tagged animals.
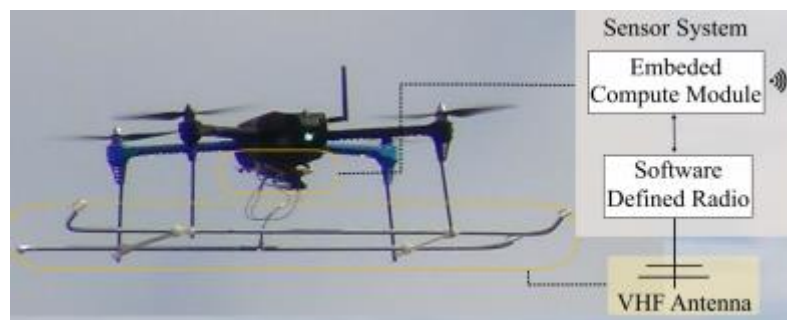
Figure 1.14: UAV equipped with VHF antenna, radio receiver and embedded computer module to allow for real time localisation and tracking of radio-tagged animals [133].

UAV tracking of birds have been successfully demonstrated on small birds using a two-point phased array antenna system [132]. Two monopole antennas are mounted to a rail on the drone in which it performs a full rotation. The position is obtained via determining the phase shift between an observed gain pattern and the expected Fourier series radiation pattern model. Whilst the UAV approaches discussed show promising

applications, further work is required to allow for tracking of smaller insects, including faster positional updates to maintain 500m range [76].

The current research proposed aims at further understand the global decline in honeybee colonies by igniting efforts to better the spatial interaction of bees within their environment. To date no available technology exists to effectively enable the long-term evaluation of navigation loss of bees exposed to potentially harmful pesticides such as neonicotinoids

1.3 Aims and Objectives

The project aimed to design and fabricate a self-powered transmitter capable or being attached to even the smallest species of bees, whilst designing a system capable of localisation of the tag and autonomously tracking the signal across the entire foraging range. The specific objectives for the project are listed below:

- Develop a self-powered radio telemetry tag, which is powered via vibration of the thorax during flight. Current systems are bulky and operate at frequency where the antenna is much larger than the insect. The design must account for the payload capabilities of the bee, whilst generating maximum power to increase the link budget [Chapter 2]
- Replace the traditional user-scanned direction antennas with an electronically scanned phased array antenna. In conjunction with a receiver unit the antenna will be utilised to accurately estimate the location of the bee. Proof of principle will be established from monitoring bees entering and leaving their hive. [Chapters 3 and 4].
- Demonstrate proof of concept for long-range tracking capability by mounting the tracking system onto a UAV. The data collected can be fed directly into the UAV's control system to continuously update the UAV's position based on the received bearing.

1.4 Applications

The development of a radio telemetry system capable of tracking an insect across their entire foraging range has a vast range of applications for an ecologist as well as many potential commercial applications.

The use of the technology could provide vital insights into long-term evaluation of bee exposed to potentially harmful pesticides along with various other factors that could be negatively impacting bee populations. Evidence could be obtained for academic studies or commercially to evaluate the effects of pesticides on pollinators before being released onto the market.

The system could also be modified for the use on Asian Hornets which are known to pose a huge threat to honeybee population. Locating and destroying nests are currently a big problem in Europe and the ability to tag and track a captured Asian Hornet back to their nest would be a hugely beneficial tool to the people tracking down the nests.

The system has potential to also be used commercially to monitor crop pollination. By monitoring the foraging activity of multiple hives within a field, the spatial positioning of the hives can be studied to provide maximum pollination efficiency to that crop, thus increasing crop yield or reducing the number of bees required for successful pollination.

1.5 Thesis Outline

Chapter two focusses on the development of battery-less radio telemetry tags capable of being attached to the honeybee. This chapter reviews the design of a non-resonant energy harvester suitable for harvesting energy from a bees' vibrating thorax, whilst generating sufficient energy to power an on-board transmitter.

Chapter three reports the design of a phased array antenna capable of scanning +/-50° in azimuth and elevation plane, to replace traditional user scanned Yagi antennae. Beam steering is achieved via the integration of phase shifters into the feeding network of a microstrip antenna array. The theory underpinning the design of phased array antennae is discussed alongside simulated and measured results.

Chapter four demonstrates the implementation of the phased array antenna and self-powered tracking tags to estimate the position based on a RSSI approach. A detailed description of the system is given whilst presenting experimental results outlining the system successfully monitoring bumblebees and honeybees leaving and entering their nests/hives, respectively.

Chapter five assess the capability of autonomous tracking, in which the entire tracking system is mounted to a UAV in which it is programmed to autonomously move

towards bearings calculated via the RSSI estimations. System design, limitations and obtained results are reported.

Chapter six concludes the results presented within this thesis, outlining the key achievements and findings throughout the work conducted. Current results are analysed to outline future work to further improve capabilities of tracking insects over large ranges.

1.6 Key contributions of work

The key original contributions of the work presented herein are:

- The development of a self-powered radio telemetry tag, which is considerably smaller in mass and volume in comparison to commercially available technology. The radio telemetry tag is the first of its kind capable of successfully operating on honeybees.

- The design, fabrication and testing of a phased array antenna and receiver unit, capable of autonomously determining the bearing of the tag based on the received signal strength. The contribution allows for the removal of a human operator of the telemetry system, allowing for increased tracking resolution, as the scanning time can be significantly increased, whilst eliminating any human error associated with bearing estimation.

- The successful demonstration of monitoring the foraging activities of bumblebees in a polytunnel, which to the authors knowledge is the first of its kind.

- Proof of concept of long-range autonomous tracking, utilising a UAV to detect the bee bearing and continuously update its position to remain with the detection range of the tag.

Chapter 2. Design and development of self-powered radio telemetry tag

This chapter outlines the theory and methodology behind the design and fabrication of a piezoelectric energy harvester powered radio telemetry tag, which scavenges energy from vibrations caused from flight before being converted to an RF signal and radiated through a transmitting antenna. Design steps, optimisation and results obtained will be discussed herein.

2.1 Energy harvesting sources for insects

As the bulk mass of radio telemetry tags is due to the mass of the battery cell, the replacement of battery with a compact energy harvester has the potential to significantly reduce the overall mass of the tag. An energy harvester is defined as a device that captures and converts small amounts of energy from one or more surrounding sources into electrical energy. Energy harvesting has been extensively used as an alternative to the conventional battery [1, 2, 3].

Energy harvesting from ambient energy sources to generate low levels of electrical power is defined as micro energy harvesting, generating power outputs ranging from mW to μW. To generate mW to μW power outputs, a great variety energy sources can be exploited from the environment such as mechanical vibrations, thermal energy, friction sources, sun light and chemical or biological sources. Figure 2.1 shows the average power density levels that can be achieved from a variety of ambient sources.
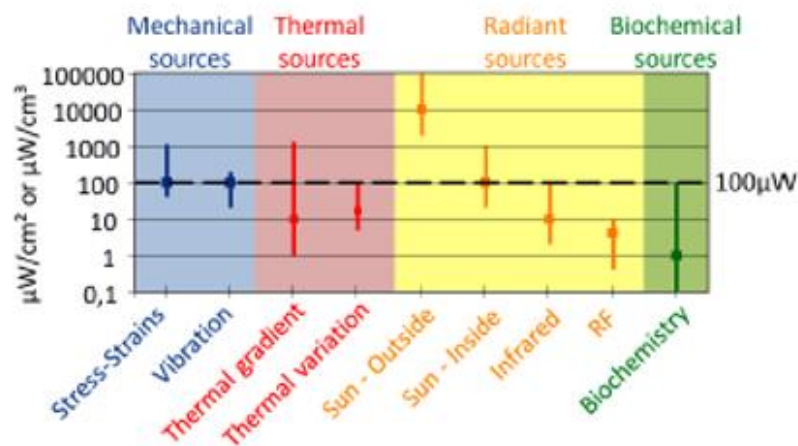
Figure 2.1: Potential EH sources including average power density levels [137].

As device miniaturisation is critical to achieve significant weight reduction when replacing the battery two transduction mechanisms were considered due to their inherently high efficiency and miniaturisation potential: vibration and photovoltaic energy transducers. In order to convert mechanical vibrational energy to electrical energy various transduction mechanisms were considered such as electromagnetic, electrostatic, and piezoelectric energy harvesting. Electromagnetic and piezoelectric harvesting from insect flight have previously been reported in literature [4, 5]. As vibrations are continuously present during insect flight, scavenging energy from mechanical vibrations would allow for perpetual power generation during flight. The use of solar cell technology offers greater power density although the power generation would be dependent upon ambient light, restricting the conditions under which sufficient power can be generated. PV cells are additionally inconvenient for use with insects as the small size of the insect dictates the size of the PV cell, thus, resulting in low power generation.

Piezoelectric materials are able to directly transform mechanical strain into an electric field [138]. Electromagnetic energy harvesting relies on a moving magnet inside a coil which the oscillating motion induces a varying magnetic flux inside the coil, producing a voltage [139]. Finally, electrostatic energy harvesting generates a charge from the relative motion between plates which form a variable capacitor [140]. Table 2.1 summarises the advantages and challenges associated with the electromechanical transducers.

Table 2.1: Summary of the advantages and disadvantages of various vibration energy harvesting mechanisms

Transduction mechanism	*Advantages*	*Disadvantages*
Electromagnetic	• No external voltage source required • No need for active material	• Large form factor due to need for coils and magnet • Difficult to integrate into small devices
Electrostatic	• Compatible with MEMS • Relatively high voltage output	• External voltage source required
Piezoelectric	• Straightforward fabrication • High voltage output meaning simple rectification circuitry • Favourable scaling of power as dimensions shrink	• Depolarisation issue • Brittleness in certain material

As electrostatic devices require an external voltage, they were deemed unsuitable for the application of solely replacing a battery for radio telemetry tags. Due to the higher power density potential, simple configuration and high integration potential, piezoelectric energy harvesting from bee flight was preferred.

2.1.1 Piezoelectric energy harvesting

The piezoelectric effect has reciprocal properties. Firstly, the direct piezoelectric effect, in which an electrical charge is generated, that is proportional to the applied mechanical stress. Alternatively, when an electric field is applied to the material, a displacement proportional to magnitude of the electric field is produced. This is known as the converse piezoelectric effect. The direct piezoelectric effect forms the basis of vibrational energy harvesting as it allows materials to convert surrounding mechanical vibrations into electrical energy. Figure 2.2 shows the general principle for converting mechanical vibrations into electrical energy.
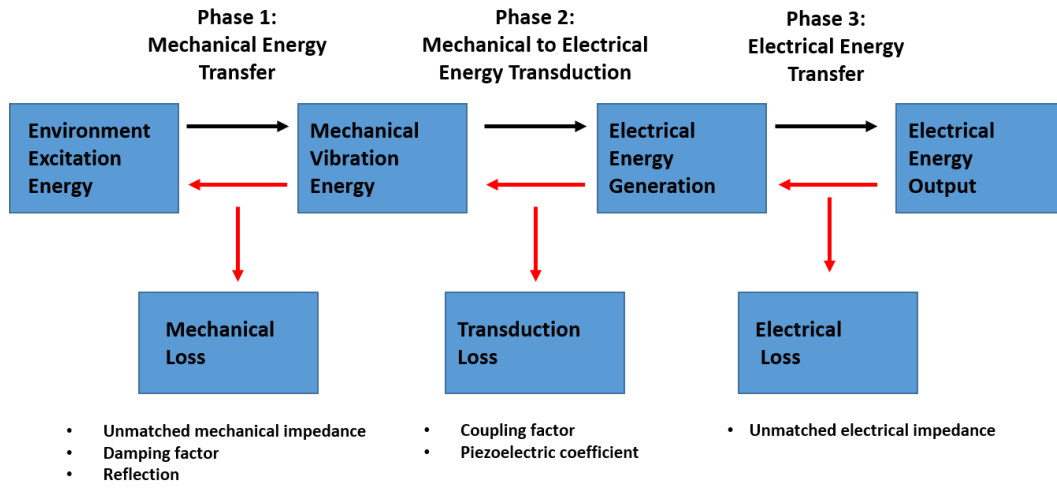
Fig 2.2: General principle of the energy flow of a piezoelectric generator

The following two equations can be used to describe the piezoelectric effect.

Direct piezoelectric effect:

$$D_i = d_{ij}\sigma_j + \varepsilon_{ii}^T E_i \tag{2.1}$$

Converse piezoelectric effect:

$$S_j = s_{ij}^E \sigma_j + d_{ij} E_i \tag{2.2}$$

Where i and j take the values 1 or 3 and are tensor notations. The electrical displacement (D_i), is dependent upon the piezoelectric charge coefficient (d_{ij}), the mechanical stress (σ_j), the permittivity of the material under constant stress (ε_{ii}^T) and the electric field (E_i). Alternatively, for the converse piezoelectric effect the mechanical strain (S_j) is dependent upon the elastic compliance of the material under a constant electric field (s_{ij}^E), the mechanical stress (σ_j), piezoelectric charge coefficient (d_{ij}) and the electric field (E_i).

To further describe values i and j, Figure 2.3 shows a schematic diagram of a piezoelectric transducer in which axis 3 represents the polarisation of the piezoelectric material. Two common coupling modes are used for piezoelectric transducers which are '33' and '31' modes, which are depicted in Figure 2.4. In '33' mode the compressive force is applied along the polarisation direction which collects charge along the electrodes' surface. Alternatively, for '31' mode the strain applied to the material is perpendicular to the polarisation.
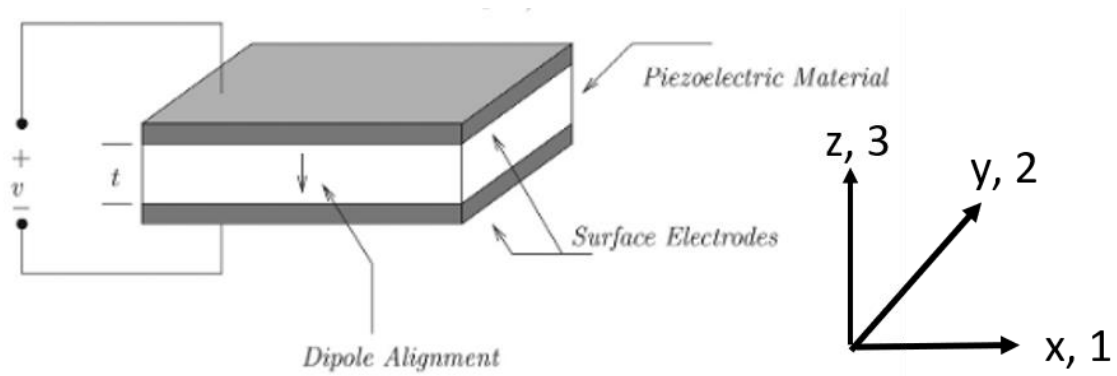
Fig 2.3: Schematic diagram of piezoelectric transducer [141]
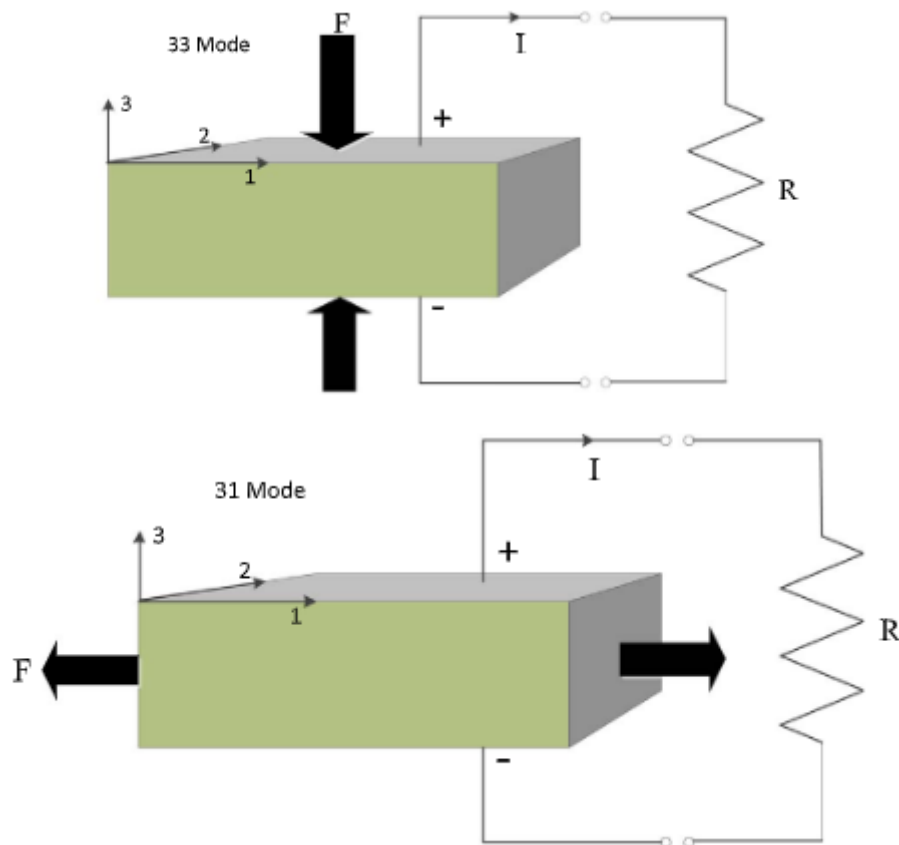
Fig 2.4: Demonstration of '33' and '31' modes for piezoelectric materials [142]

Piezoelectric transducers generally take up the form of unimorph, bimorph or multilayer structures as shown in Figure 2.5. Various cantilever shapes have been proposed in order to increase the maximum excitation amplitude [143]. An advantage of using bimorph and multilayer structures are that they can be individually wired allowing control over series and parallel connections. Whilst the power output remains the same, the ratio of current/voltage can be modified to fit the required application.
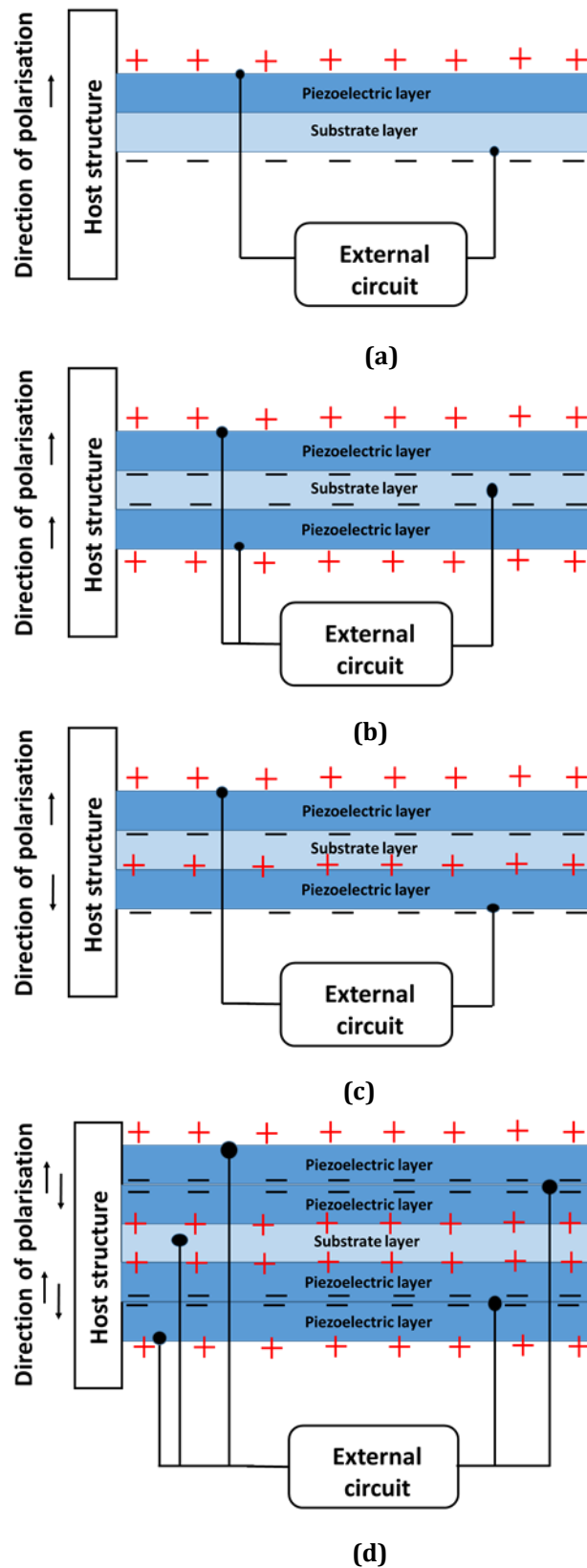
Fig 2.5: Configurations for various piezoelectric harvesters: (a) unimorph, (b) parallel poled bimorph, (c) series pole bimorph and (d) parallel poled multilayer bimorph.

Reviewing the cantilever shown in Figure 2.4, the top and bottom layer contain an electrode, therefore the electric field in axis 1 and 2 becomes zeros, and equations 2.1 and 2.2 can be rewritten as:

Direct piezoelectric effect:

$$D_3 = d_{31}\sigma_1 + \varepsilon_{33}^T E_3 \tag{2.3}$$

Converse piezoelectric effect:

$$S_1 = s_{11}^E \sigma_1 + d_{31}E_3 \tag{2.4}$$

If there is no stress applied to equation 2.3, it simply becomes the constitutive equation linking flux density D to electric field E via the permittivity of the material. Consequently, for equation 2.4, if there is no piezoelectric coupling or the electric field is negligible, the equation becomes Hook's law. This states that the strain of the piezoelectric material is proportional to the stress providing conditions are within the elastic limit of the material.

Besides the piezoelectric charge coefficient and permittivity of the material another import property of piezoelectric materials is the electromagnetic coupling coefficient (K_{ij}). This property is used to assess the effectiveness of the piezoelectric material to convert mechanical vibrational energy into electrical energy, which is shown in equation 2.5 below:

$$K_{Direct} = \sqrt{\frac{Generated\ electrical\ energy}{Input\ mechanical\ energy}} \tag{2.5}$$

Alternatively, for the converse piezoelectric effect we can define electromagnetic coupling efficiency as:

$$K_{Converse} = \sqrt{\frac{Geenrated\ mechanical\ energy}{Input\ electrical\ energy}} \tag{2.6}$$

The electromagnetic coupling coefficient for both the converse and direct piezoelectric effect are equal providing they are both excited in the same mode.

The piezoelectric effect was first demonstrated by Pierre and Marie Curie in the 1880's using natural materials such as crystals of tourmaline, quartz, topaz, cane sugar, and Rochelle salt [137]. Since then various man-made materials have been developed such as ceramics (lead zirconate titanate (PZT) and barium titanate (BaTiO3)), thin and

thick films (PZT) and polymers (polyvinylidenefluoride (PVDF)). Table 2.2 summarises common piezoelectric materials and their properties including piezoelectric charge coefficient, permittivity, electromagnetic coupling efficiency and Curie temperature. Curie temperature can be defined as the maximum temperature before the material loses its piezoelectric properties.

Table 2.2: Properties of some piezoelectric materials

Material	d_{31} (pm/V)	$\varepsilon_{33} / \varepsilon_0$	K_{31}	T_c (°C)	Ref
Quartz	2.3	4.4	-	-	[144]
PZT	-190 to -265	1800 to 3800	0.32 to 0.44	230 to 350	[145]
BTO	-79	1900	0.21	120	[146]
PVDF	20	12	0.11	150	[113]

$\varepsilon_0 = 8.854 \; x10^{12}$, permittivity of empty space

T_c = Curie temperature

For energy harvesting applications, piezoelectric materials with a high electromagnetic coupling coefficient are preferred. For most applications, a higher dielectric constant is also preferred as it lowers the source impedance of the piezoelectric generator. Piezoelectric materials often have high impedances resulting in high voltage/low current outputs.

From Table 2.2 we can see that PZT has a higher electromagnetic coupling coefficient, which has made it more popular in comparison to other piezoelectric materials. Whilst PVDF offers superior flexibility compared to the more brittle PZT, the electromagnetic coupling coefficient is significantly lower and for applications including harvesting energy from insect flight would yield insufficient power. A further advantage of PZT over its polymer counterpart is its ease of optimisation for specific applications as it can easily be manufactured in various shapes and sizes [113].

PZT is a combination of lead titanate and lead zirconate which has a perovskite structure as depicted in Figure 2.6a. When mechanically deformed a dipole is created as the titanate and zirconate deviate from the neutral position which is the centre of the cell. The deviation of the dipoles will then create an electric charge on the surface of the

electrodes. For ceramic materials, a poling process must first be performed to force them to have piezoelectric properties. This process consists of applying a strong DC field to the material in which all the individual dipoles are aligned in the same direction. After removing the field most of the dipoles will remain orientated as shown in Figure 2.6b, c and d, which allows the material to be piezoelectrically active.
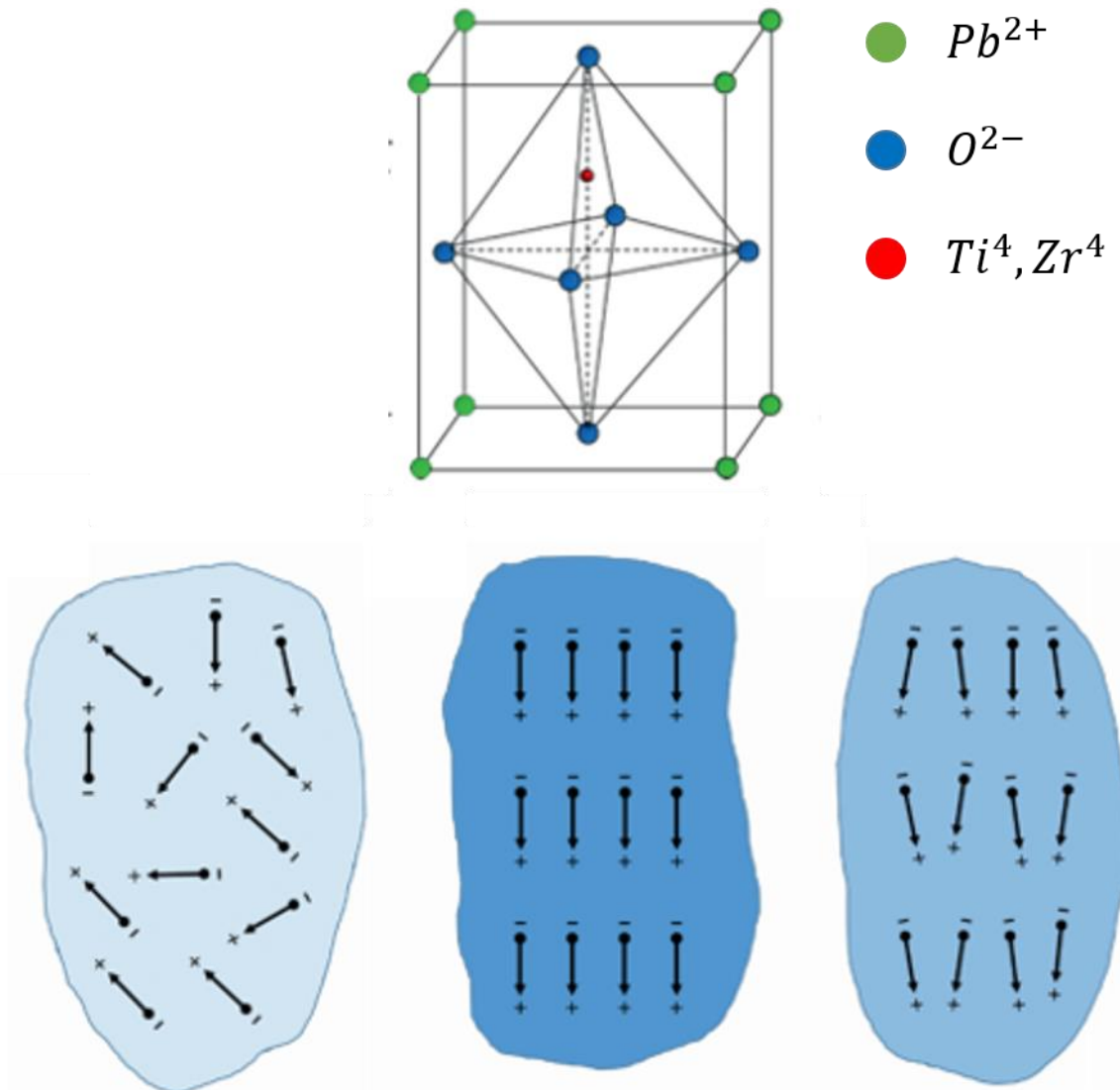
Fig 2.6: (a) Perovskite PZT unit cell, Poling process of piezoelectric materials showing (b) randomly orientated domains, (c) during and (d) after poling process [147].

We can model the vibration energy harvesting system as a simple spring-mass model of a linear inertial-based generator. Assuming that we have a linear system where the mechanical damping of the cantilever is proportional to the velocity and the stiffness is proportional to the displacement, we can understand the mechanical energy to electrical energy conversion. Figure 2.7 illustrates a basic schematic model of a system where m is

the mass, k is the stiffness whilst d_e and d_m are the mechanical and electrical damping coefficients, respectively.

As depicted in Figure 2.7 an external force excites an internal frame in which the mass, stiffness and damping coefficients are located. We can define the external vibrations with an amplitude of Y_o and a vibration frequency of ω as:

$$y(t) = Y_0 Sin(\omega t) \tag{2.7}$$

We can define the model with the use of a differential equation as described in equation 2.8:

$$m\ddot{z}(t) + (d_e + d_m)\dot{z}(t) + kz(t) = -m\ddot{y}(t) \tag{2.8}$$
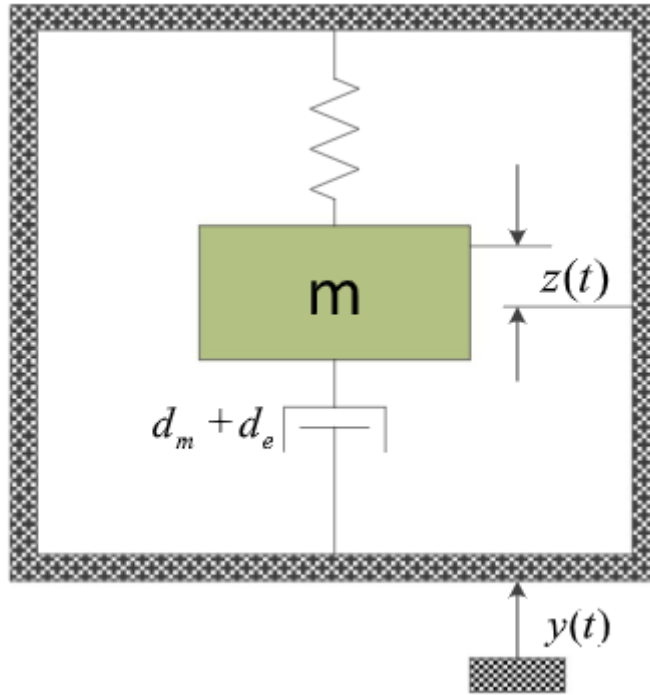
Fig 2.7: (a) Schematic diagram of linear vibration based generator [148].

Where z corresponds to the spring deflection and y is the input displacement. The solution for the differential equation for the mass displacement in relation to the inertial frame is:

$$z(t) = \frac{\omega^2}{\sqrt{(\frac{k}{m}-\omega^2)^2+(\frac{(dm+de)\omega}{m})^2}} Y_0 \sin(\omega t - \varphi) \tag{2.9}$$

In which φ is the phase angle and expressed as:

$$\varphi = tan^{-1}(\frac{(d_e+d_m)\omega}{k-\omega^2 m}) \tag{2.10}$$

For resonant systems, the maximum power output can be achieved when the frequency of external vibrations matches the natural frequency (ω_n) of the spring mass system. Thus, we can substitute z(t) from equation 2.9 into equation 2.8 giving the energy dissipated within the damping:

$$P_d = \frac{m\varsigma_T Y_0^2 (\frac{\omega}{\omega n})^3 \omega^3}{(1-(\frac{\omega}{\omega n})^2)^2+(2\varsigma_T(\frac{\omega}{\omega n}))^2} \tag{2.11}$$

Where ς_T is the total damping ratio. We can further expand on Equation 2.11 to find the power converted to electrical energy, which is equal to the power the electrical induced damping absorbs. This is given by:

$$P_{OUT} = \frac{m\varsigma_e Y_0^2 (\frac{\omega}{\omega n})^3 \omega^3}{(1-(\frac{\omega}{\omega n})^2)^2+(2\varsigma_T(\frac{\omega}{\omega n}))^2} \tag{2.12}$$

Finally, assuming that $\omega = \omega_n$, the converted power can be simplified to equal:

$$P_{OUT} = \frac{m\varsigma_e Y_0^2 \omega_n^3}{4\varsigma_T^2} \tag{2.13}$$

Whilst the model is fairly accurate for electromagnetic conversion, it must be changed somewhat for piezoelectric conversion. Firstly, the relationship between mechanical and electrical systems for piezoelectric harvesters is not always linear. Secondly, the damping is not always linear to velocity. Whilst the model presented is unable to provide complete precision, important conclusions can be drawn which can be extrapolated to piezoelectric systems.

To describe the power output more accurately for piezoelectric conversion, a transducer operating in '33' mode can be described by the following differential equations:

$$m\ddot{z}(t) + (d_e + d_m)\dot{z}(t) + kz(t) - \theta_v(t) = -m\ddot{y}(t) \tag{2.14}$$

$$\theta_{\ddot{z}}(t) + C_p\dot{v}(t) + \frac{1}{R_l} v(t) = 0 \tag{2.15}$$

Equation equations 2.14 and 2.15 are Newton's equation of motion for a single degree-of-freedom system and applying Kirchhoff laws to the circuit with a resistive load R_l respectively. V(t) is the voltage across the piezoelectric material, C_p is the capacitance of the piezoelectric material and θ is the electromechanical coupling coefficient (equations 2.5 and 2.6), which are equal providing they are excited in the same mode. Using Laplace transforms, the electrical power output extracted can be expressed as:

$$P_{OUT} = \frac{m\varsigma_m \alpha \kappa^2 \Omega^2 \omega^4}{\omega n((1-(1+2\varsigma_m\alpha)\Omega^2)^2+((2\varsigma_m+(1+\kappa^2)\alpha)\Omega- \alpha\Omega^3)^2)} \qquad (2.16)$$

Where $\Omega = \omega/\omega_n$, $\kappa^2 = \frac{\theta^2}{(\kappa C_p)}$ which represents the electromechanical coupling coefficient and $\alpha = \omega_n C_p R_l$ which represents the time constant.

Equivalent circuit models can additionally be used for analysis and design of piezoelectric systems. From the systems' transfer functions, we can derive experimental parameters. Using standard elements for mechanical and electrical systems we can define the difference between the two domains as where the mechanical force is considered as the electrical voltage and the velocity is equivalent to the current. Figure 2.8 displays the equivalent models for piezoelectric cantilevers for mechanical and electrical domains, which are excited at the tip of the beam. Whilst most piezoelectric energy harvesters are excited via a vibrating host structure, directly exciting the tip has been successfully demonstrated to harvest energy from insect flight [113]. Table 2.3 summarises the electromechanical analogies.

(a)   **(b)**
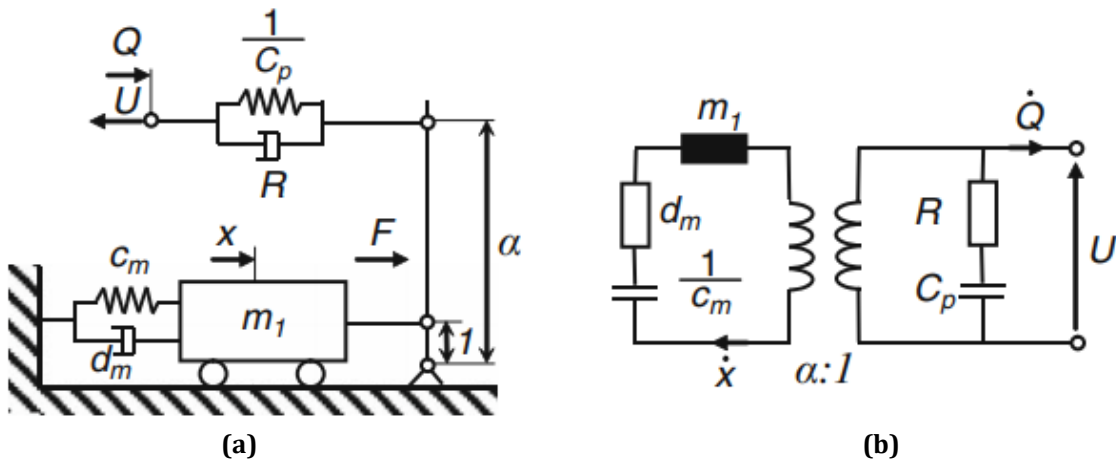
Fig 2.8: Equivalent circuit model for piezoelectric transducer in (a) mechanical domain (b) electrical domain [149].

Table 2.3: Summary of electromechanical analogies

Mechanical representation	Electrical representation
Force	Voltage
Velocity	Current
Mass	Inductance
Spring	1/Capacitance
Damper	Resistance

The parameters in the mechanical model are C_m, d_m and m_1, which represent the modal stiffness, damping and mass, respectively. For the electrical circuit, a resistor and shunted capacitance C_p are introduced to represent the dielectric losses. A transformer with ratio α: 1 is used to represent mechanical to electrical energy conversion efficiency. The models shown in figure 2.8 can be further linked by describing them as a two-port network in which the dynamic behaviour can be characterised by an admittance matrix. The two port variables for the system are the velocity $v = dx/dt$ and the electric current dQ/dt. The matrix is expressed as:

$$\begin{pmatrix} Q \\ Z \end{pmatrix} = \begin{pmatrix} Y_{11} & Y_{12} \\ Y_{21} & Y_{22} \end{pmatrix} \begin{pmatrix} V \\ F \end{pmatrix} \tag{2.17}$$

Where Y_{11} is the short-circuit input impedance, which describes the ratio between amplitudes of current and voltages in absence of mechanical force, F. Y_{12} and Y_{21} describe the electromechancial conversion for force and voltage excitation respectively. Y_{22} describes the ratio of amplitudes of mechanical force and vibrations in absence of electrical voltage.

$$Y_{11} = \frac{j\omega Q}{V}\bigg|_{F=0} = \frac{(\kappa^2)^2}{j\omega m_1 + d_m + c_m/(j\omega)} + \frac{1}{R + 1/(j\omega C_p)} \tag{2.18}$$

$$Y_{12} = Y_{21} = \frac{j\omega z}{V} = \frac{\kappa^2}{j\omega m_1 + d_m + c_m/(j\omega)} \tag{2.19}$$

$$Y_{22} = \frac{j\omega Q}{F}\bigg|_{V=0} = \frac{1}{j\omega m_1 + d_m + c_m/(j\omega)} \tag{2.20}$$

The model is useful in terms of describing the behaviour of the transducer when subjected to input vibrations, however, it does not include energy harvesting functions such as rectification and storage. Figure 2.9 outlines a piezoelectric energy harvesting system with storage circuit. Typically, a 4-diode bridge configuration is used to perform the AC/DC conversion and a storage capacitor is used to collect the energy. The energy stored is calculated via:

$$E = \frac{1}{2}CV^2 \tag{2.21}$$
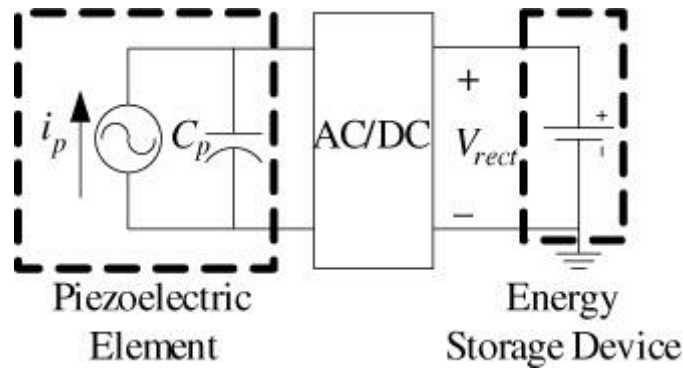
Fig 2.9: Piezoelectric harvester accompanied with AC/DC converter and energy storage device [150].

Whilst the instant energy harvested power is approximated by:

$$P = \Delta E/\Delta t \tag{2.22}$$

One of the most important factors of an energy harvesting circuit is the maximum achievable power output obtained when an external load resistance matches the impedance of the piezoelectric generator. Figure 2.10 shows an updated equivalent circuit model including an external load resistor. Using Kirchhoff's law, the current and admittance of the virtual port can be evaluated using Equations 2.23 and 2.24.

$$Isc = \frac{\kappa^2 \, (j\omega d_m + C_m)}{j\omega m_1 + d_m + \frac{C_m}{j\omega}} \, \dot{y} \tag{2.23}$$

$$Y_L = \frac{1}{R_{LOAD}} + j\omega \left(C_p \frac{(\kappa^2)^2}{C_m + j\omega(d_m + j\omega m_1)} \right) \tag{2.24}$$

When maximum current flows over the load and minimum over the virtual port, maximum power transfer is achieved. For optimal cases Y_L (jω, R_{LOAD}) is zero. Solving this equation for ω gives optimal load as function of frequency. This can be inverted and used to identify the optimal load of the system as a function of frequency.

Figure 2.10a demonstrates the implementation of an equivalent circuit model simulation in ADS (C1 = 570 nF, L1 = 1 H and R1 = 6.9366 Ω), which models a piezoelectric energy harvester and load resistor. The power output vs load resistance is then shown in b, outlining maximum power is achieved when an external load resistance matches the impedance of the piezoelectric generator.
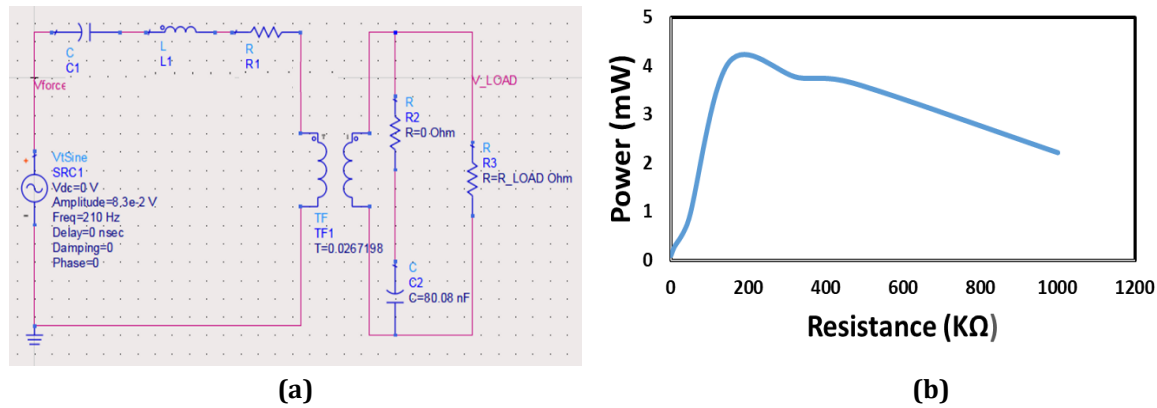
Fig 2.10: (a) Electrical equivalent circuit model, (b) comparison of load resistance vs power output

2.1.2 Piezoelectric energy harvesting from bee flight

Figure 2.7 outlined the schematic model indirectly excited from a vibration source. When analysing the power output of this system vs excitation frequency a response as demonstrated in Figure 2.11 would be observed. When the resonant frequency of the structure matches that of the vibrations, maximum power output is achieved. Power outputs of orders of magnitude lower can be present for systems where resonant frequency does not match the vibration frequency. In our target application, which involves harvesting energy from bee flight, the frequency is dependent upon environmental variables and the individual insect, providing a constantly changing vibrational frequency. A resonant device would not be a practical solution. Instead a broadband energy harvesting solution from insect flight is required.
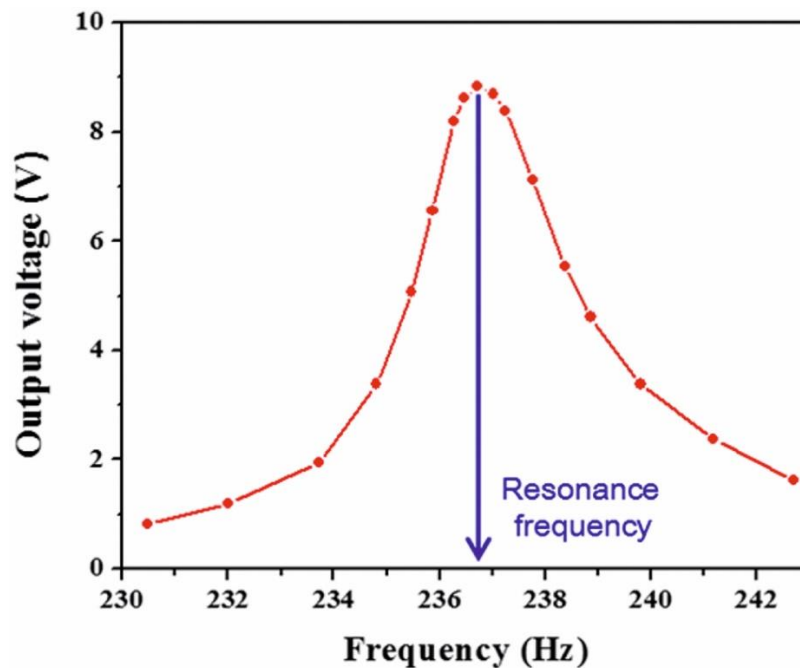
Fig 2.11: Resonant piezoelectric harvester showing frequency dependence to maximise power output [147].

When an external force is directly exciting the tip of the piezoelectric generator, we can redefine Figure 2.7 as:
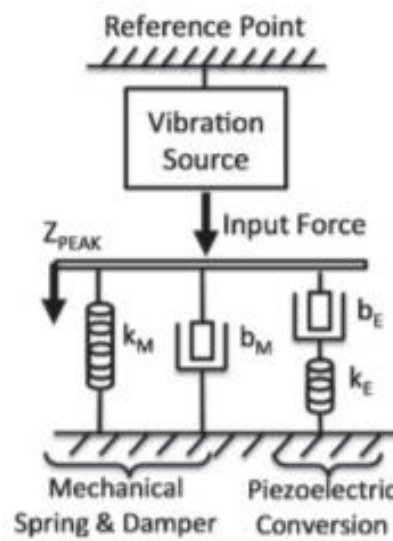
Fig 2.12: Piezoelectric Schematic for harvesting energy directly from a force [113].

Since an external force is directly exciting the beam, a constant deflection of the beam is present. Providing the amplitude of the vibrations for the change in frequency remains consistent, a non-resonant piezoelectric energy harvester can be achieved. Several non-resonant piezoelectric energy harvesters have been reported, where unlike resonant systems, they are capable of efficiently harvesting energy from vibrations of varying frequency [20, 21]. This was demonstrated experimentally when a 31.8 x 10 x 0.38mm piezoelectric series poles bimorph [145], was directly excited at the tip of the beam. Recreating the circuit diagram shown in figure 2.10b, the voltage was measured across a match load resistor to determine the power. Figure 2.13 demonstrates the experimental set up and the power output of a non-resonant energy harvester assuming consistent tip displacement for varying frequencies. Using a function generator and vibration generator the frequency of the generator could be controlled. Limitations in the experimental design lead to only a relatively small span of frequencies being covered, as the increase or decrease in frequency resulted in a smaller/larger force being applied to the tip of the beam.

Another advantage of non-resonant energy harvester for insect harvesting applications is that the weight of the harvester can be significantly reduced as there is no need for a proof mass at the end of the beam. Whilst for resonant systems and when being

excited by vibrating host structure, a proof mass maximises displacement of the beam at its resonant frequency, it would hinder beam displacement when directly excited.
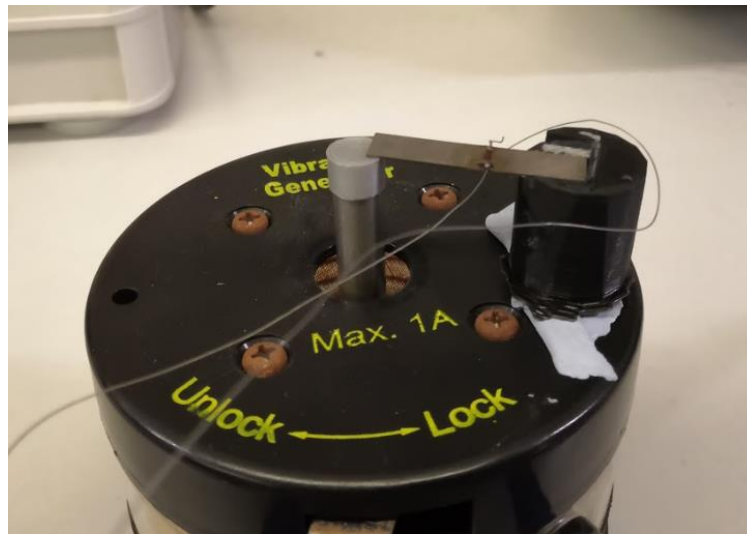
(a)
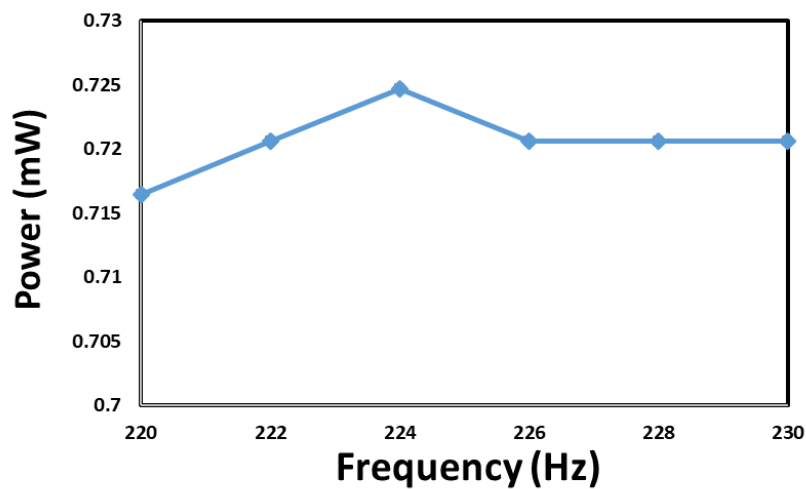
(b)

Fig 2.13: (a) experimental design (b) power output vs frequency for a non-resonant energy harvester.

2.2 Energy harvester design and tag testing

As previously discussed, the broadband frequency range of bee flight suggests the need to design a non-resonant energy harvester. Various other design considerations had to be addressed, such as:

- Bees are also known to carry up to 110% of their body weight [9], this determines the maximum weight of the harvester, circuitry and antenna.
- The tag placement may further reduce the maximum weight of the tag as it can affect the bees centre of gravity. Honeybees weigh around 100 mg, meaning, in theory, they can carry up to 110 mg.

- The energy harvester must be small and compact, whilst providing sufficient power to the transmitting antenna to maximise detection range. It must also be non-obtrusive to the wings to allow for flight.
- Optimal circuitry must be identified to maximise power transfer and storage over short transmission periods ($\sim$1s).

Firstly, the optimal placement of the piezoelectric energy harvester was determined, which required analysing the anatomy of a bee, whilst determining a continuous vibration source, and providing minimal physical hindrance of flight capability.

Allowing to test energy generation capabilities from bee flight, the piezoelectric beam was cut to have a width of 1mm to allow for specific placements on various parts of the bee such as its wings and thorax. The experiment would allow for identification of the optimal placement of the energy harvester to maximise power output whilst minimising physical hindrance to the bees' ability to fly. In order to cut the shape, careful considerations to the properties of the piezoelectric material had to be considered. Reactive-ion etching, ultrasonic machining, milling, nanosecond and femtosecond laser ablation were all possibilities, however, to minimise mechanical and thermal damage to the material, femtosecond laser ablation was chosen. A 200μm beam size was chosen to ablate a straight line along the material for separation, without exceeding the Curie temperature. Figure 2.14 shows the result of PZT cutting with the femtosecond laser.

The beam size was chosen after careful consideration, in order to minimise the material ablated during the cutting whilst additionally allowing for successful separation of the material after cutting. The femtosecond laser was unable to cut through the brass shim due to its relatively low power, meaning the material had to be carefully snapped off after the cutting process. Increasing the beam size allowed for easier material separation, however, smaller beam sizes allowed for increased yield of piezoelectric bimorphs. 200 μm was a suitable trade-off to maximise yield and allow for successful separation after cutting.
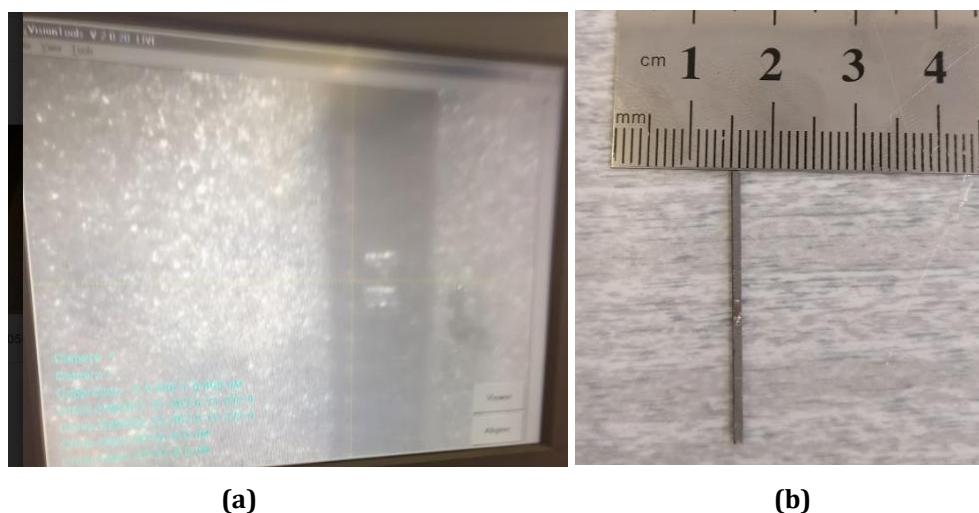
Fig 2.14: (a) 200 μm ablation of piezoelectric material to achieve cutting of the material (b) 31.8mm x 1mm piezoelectric bimorph after cutting

A small holder was 3D printed to maintain one end of the PZT cantilever firmly in place (figure 2.13a), whilst the bee directly excited the other end. The 3D printed enclosure was then mechanically clamped at the same height to the bee so that the piezoelectric beam was continuously held at the same height of the bees' thorax. To test the power generation of the larger scale device (~3:1) the following protocol was established:

- Immobilization of the honeybee by controlled hypothermia at -10° for two minutes.

- Attachment of a 0.5mm diameter tungsten probe to the thorax of the bee using Dymax-208-CTH-F to tether the bee.

- Placement of the tip of the piezoelectric beam against the bees and measure output across the optimal load resistor.

To successfully attach the tungsten rod to the bee, it was critical to have the bee remain still so that the glue could successfully dry on the thorax without spreading to the wing base. Chilling the bee for two minutes, lowers the internal temperature of the bee essentially sending the bee to sleep. Once removing the bee from the cold temperature, it slowly wakes up before returning to normal "pre-hyperthermia" behavior after a few minutes. This gives a short period of time to attach the tungsten rod and the glue to dry.

A 0.5mm tungsten rod was chosen as the small diameter provided minimal hinderance/dampening of the thorax vibrations. The tungsten rod, when clamped in place, was additional sturdy enough to withstand forces generated from flight to hold the bee in the same place allowing for the tip of the piezoelectric material to be continuously

rested against the thorax. Dymax-208-CTH-F was chosen to attach the tungsten rod to the thorax of the bee as its strong adhesion meant the bee could not separate itself from the rod. Superglue can additional be used with the same success, however, care must be taken when applying the glue to avoid the wing base.

By measuring the voltage across a load resistor and determining the power, an external resistor value could be identified in which maximum power transfer occurred. This was performed by trial and error, in which a 100k load provided maximum power for the 31.8 x 1 x 0.38mm piezoelectric beam. For other beam dimensions, another optimal load would need to be determined.

The experimental set up is depicted in Figure 2.15a, whilst 2.15b demonstrates the measured voltage output across an optimal load of 100KΩ.

(a)

(b)
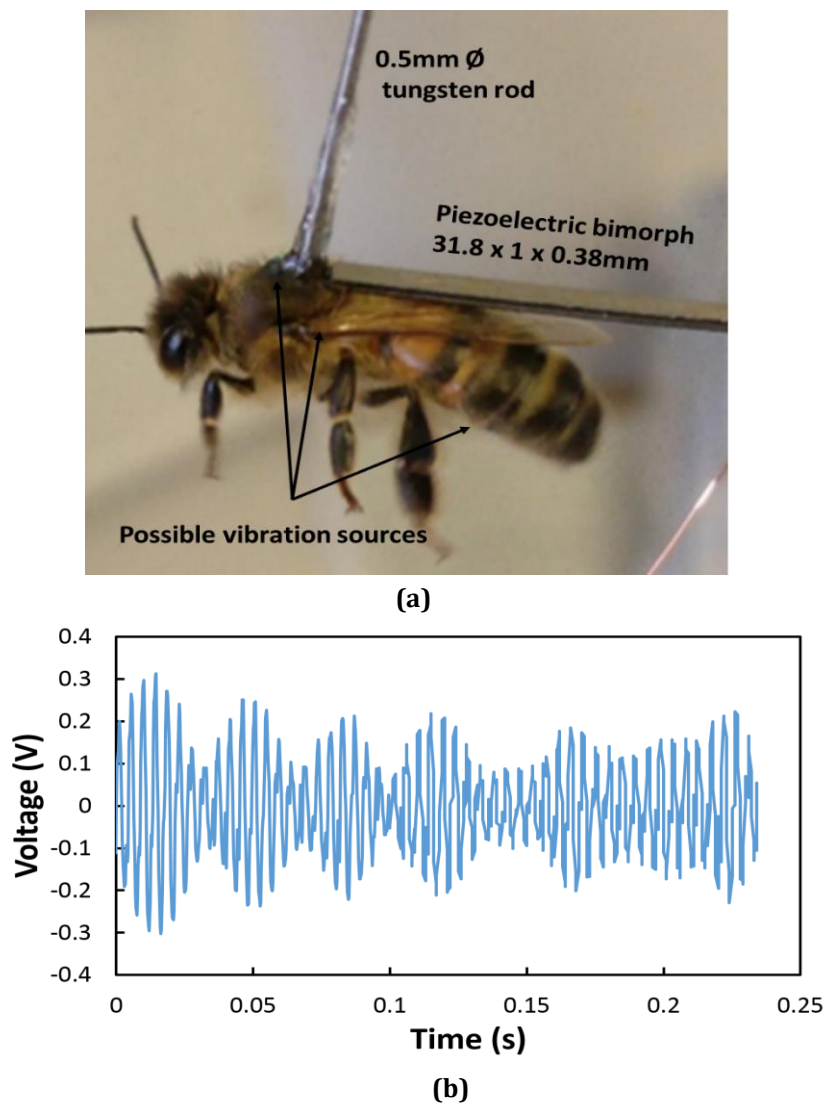
Fig 2.15: Experimental procedure for harvesting energy from tethered honeybee flight. (a) Tethered bee with tip of piezoelectric beam resting against the thorax (b) Measured output voltage across optimum load

Multiple placements of the beam were trialed such as the bee's legs, thorax, wings and abdomen. Only the wings and thorax provided continuous displacement during flight. This identified the optimal harvesting location (thorax) for the energy harvester as minimal hindrance to the bees' flight ability was achieved whilst providing continuous deflection to the beam. The power output across the load continuously varied as a result of the force provided to the tip of the beam, thus, effecting the maximum possible deflection of the piezoelectric beam. Table 2.4 summarises the Pk-Pk voltage measured across multiple honeybees or the same honeybee over time. The maximum power measured was 3.6μW signaling maximum force from the thorax was applied to the tip of the beam. Multiple factors such as tiredness and unwillingness to fully fly when tethered to the tungsten beam contributed to lower observed power:

Table 2.4: Summary of the Pk-Pk voltages measured across the same honeybee over a few minute intervals between flight

Reading number	Pk-Pk voltage	Power across load
1	0.2V	0.4μW
2	0.45V	2.03μW
3	0.6V	3.6μW
4	0.5V	2.5μW

The experiment conducted in Figure 2.15 investigated the energy costs to bees caused by the additional weight of energy harvester. By taking the Fast Fourier Transform (FFT) of the output from the piezoelectric beam during honeybee flight, the change in frequency due to physical constraints over a small time period was observed. Since the magnitude of the signal is related to the force produced by the thorax, the results in Figure 2.16 outline the need to pursue device miniaturization for minimal energy expenditure whilst carrying the device.
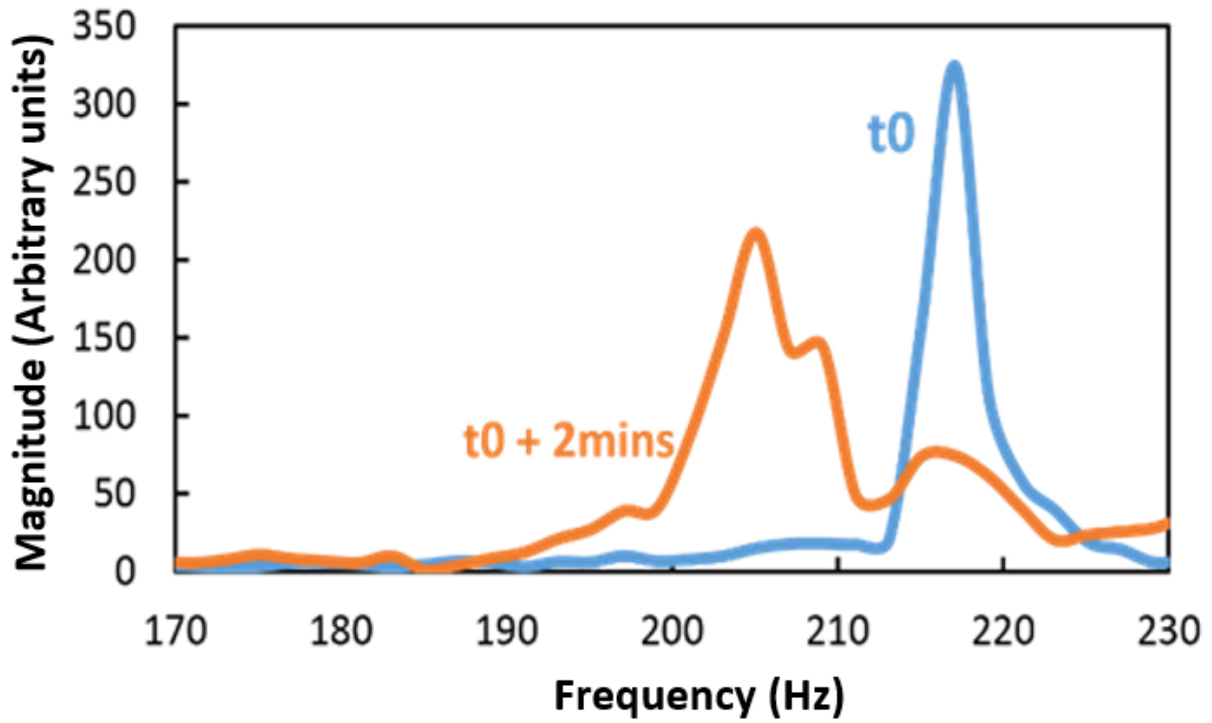
Fig 2.16: Spectrum of the piezoelectric beam output signal, outlining both frequency and amplitude changes due to physical tiredness of the honeybee.

We can see over a small period (2 minutes) the magnitude and frequency of the vibrations significantly decrease, which would in turn minimize power generation. This outlines the need to pursue aggressive weight reduction and device miniaturization.

To enable device miniaturization whilst maximizing the achievable power output, we developed an analytical model capable of predicting power generation from the piezoelectric beam. As proposed in [113], using a non-resonant energy harvesting equation, 2.16 can be rewritten so we can express the power generated from the direct force as:

$$P_{Direct-force} = \frac{9}{64} \frac{E_p d_{31}^2}{\varepsilon} \; \omega_{ACT} \; K_{SPRING} \; Z_{PEAK}^2 \tag{2.25}$$

Where K_{SPRING} is the stiffness of the beam and Z_{PEAK} is the maximum deflection of the beam. Using COMSOL Multiphysics, a finite elements' model replicating the experiment in Figure 2.15 was created in order to predict the power generated as shown in Figure 2.17.
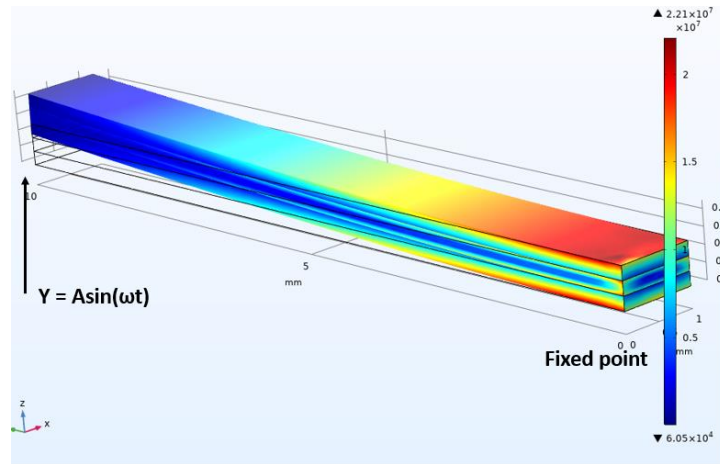
Fig 2.17: Finite element model of 16 x 0.2 x 0.38mm piezoelectric bimorph.

It was found in [153] that the force produced by a tethered honeybees was 3.65 mN. The force applied to the tip of the beam is defined in Equation 2.7 where the amplitude is equal to 3.65mN and the frequency was selected to be 218Hz, in order to match the output presented in Figure 2.15b. Using stationary analysis in COMSOL, the maximum displacement of the beam was determined and applied to Equation 2.25. The combination of stationary analysis to determine the maximum beam displacement and applying the result to the analytical model (Equation 2.25) yielded a predicted power output of 3.66μW, whilst the experimental measurement yielded a 3.6μW power generation across the load resistor. The results suggest that device optimization can be performed through simulation to maximize the power output of the energy harvester.

It was important to optimise the beam analytically due to time and cost restraints associated with the piezoelectric material and its fabrication into custom sizes. Optimal beam dimensions for harvesting maximum power from the bee's thorax can be identified and analysed, accelerating the optimisation process. As the thickness between layers could not be altered uniformly, parameter sweeps of varying beam lengths and widths were conducted, and the maximum deflection with a force of 3.65 mN at 240 Hz was determined. Calculating the change in spring constant for each beam dimension and applying the results to Equation 2.25, the following relationships between beam dimensions and width were determined:
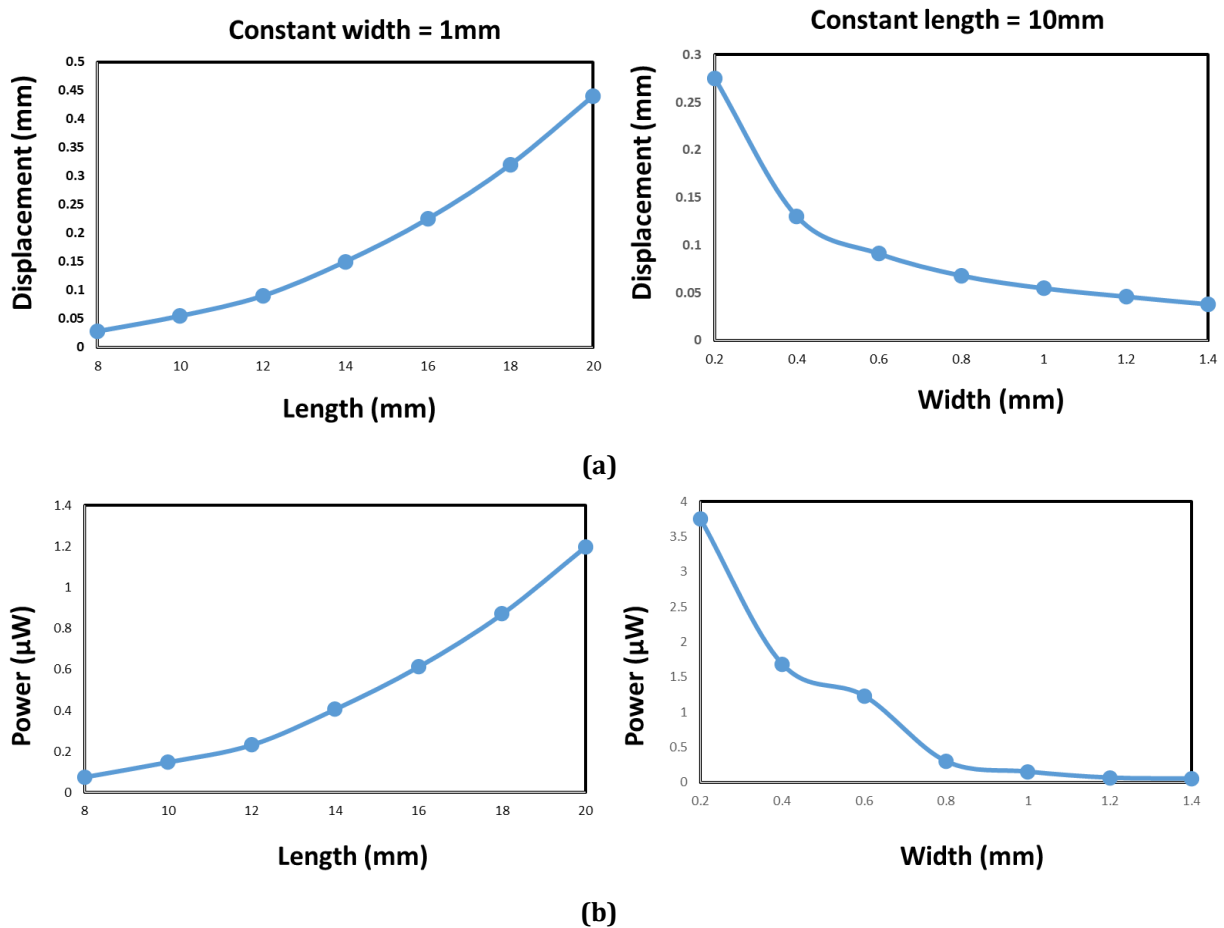
Fig 2.18: Relationship between beam width and length vs (a) beam displacement and (b) power generation

To maximise power generation, it was necessary to maximise the length and minimise the width of the cantilever. However, it is important to keep some structural stiffness to the beam; if it is not too brittle it will be broken by regular flight and foraging activities. It was found that 16 x 0.2 x 0.38 mm cantilever provided an adequate solution to the trade-off between structural integrity and power generation with an expected power across an optimal load of 3.6 µW. Figure 2.19 outlines the fabricated device.
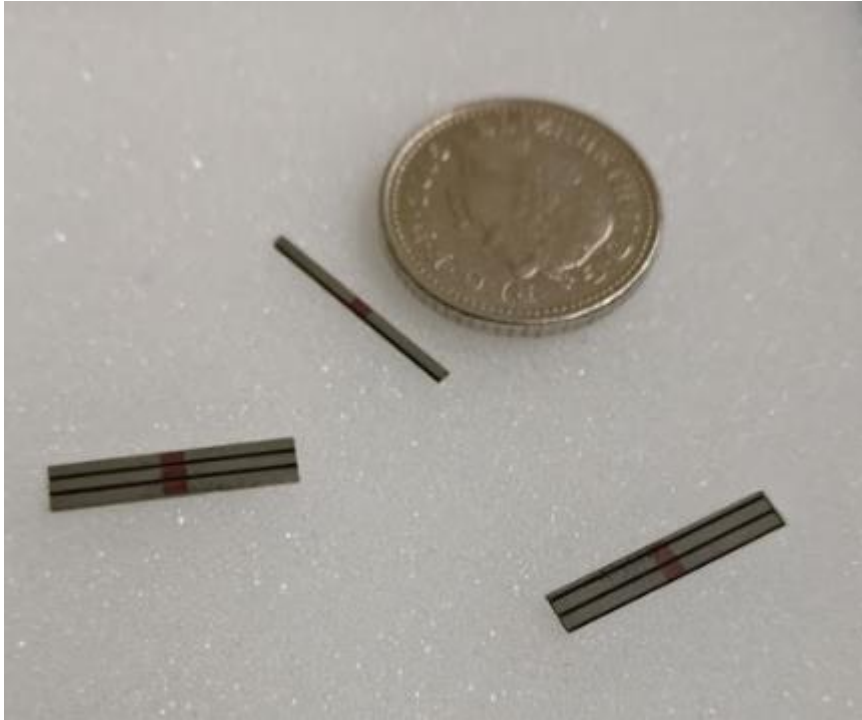
Fig 2.19: Fabricated 16 x 0.2 x 0.38mm piezoelectric harvester after femtosecond laser cutting. Ablation of the material between adjacent beams can be observed and separation is achieved via snapping the connected brass shim.

The final criteria in the design of the energy harvester was to provide optimal circuitry to maximise power transfer and storage over short transmission periods ($\sim$1s). The energy storage circuit consisted of a full wave rectifier and storage capacitor. Schottky diodes [154], were chosen due to their low forward voltage drop, whilst different capacitors C_s were considered for energy storage. The energy accumulated on the capacitor is determined via Equation 2.21, whilst over a small time period the instant energy harvesting power can be approximated by Equation 2.22. Figure 2.20a shows the experimental set up to determine optimal energy storage conditions, whilst 2.20b and 2.20c show the energy accumulation and power over 1 and 30 second periods.
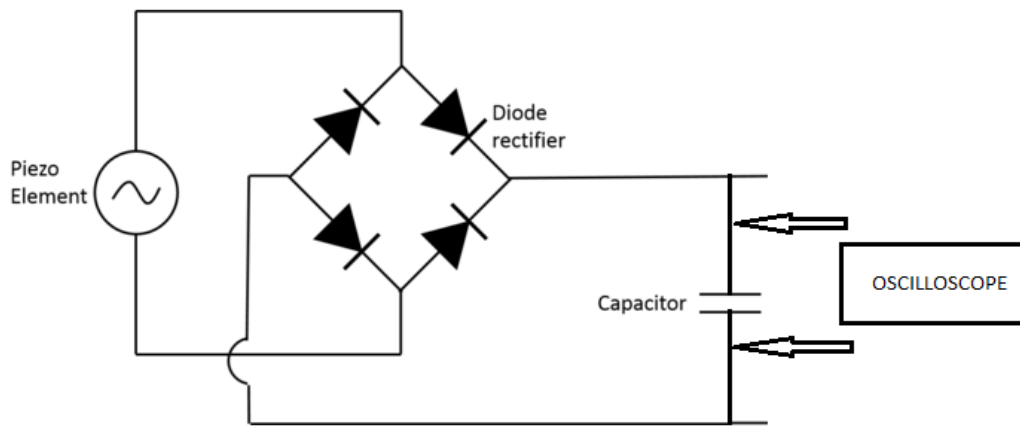
(a)
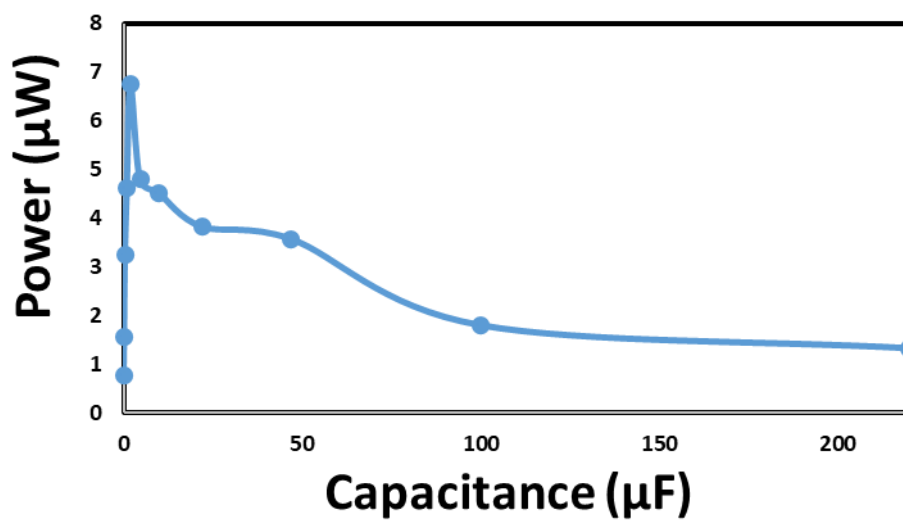
(b)
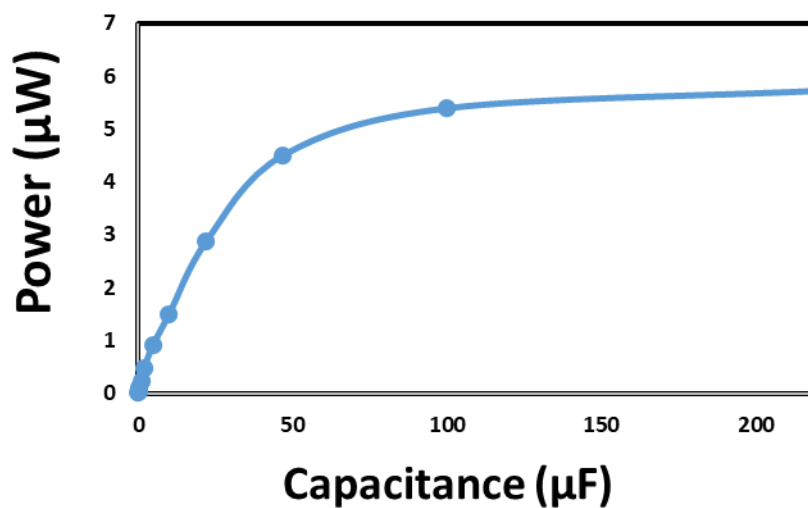
(c)

Fig 2.20: (a) circuit diagram to determine maximum power generation and storage over a short period of time [148] (b) energy accumulation and power over short period of time (1 second) (c) energy accumulation and power over longer period of time (30 seconds).

While large values of capacitors have a larger energy capacity, they are favourable to store energy for later use as observed in Figure 2.20c, however for energy storage over shorter time periods, smaller capacitors are favourable as depicted in Figure 2.20b, where a 1 µF capacitor is the optimal value for short-term energy storage.

Once the energy was stored it was converted into an RF signal, radiated through a transmitting antenna. As continuous transmission provides limited power, the concept from current radio telemetry tags which transmits short pulses of RF signals in intervals was applied to our system. Current tags utilise a pulsing circuit to emit a signal every X seconds depending on the application [155]. They reply on this approach to save energy, thus maximising battery life and the operational lifetime of the tag. For our application, the purpose was to accumulate as much power as possible over a 1 second period to transmit in pulse through a radiating antenna.

A pulsing circuit was achieved via the use of the smallest commercially available components and a transistor (T1), capacitor (C1) and resistor (R1). The pulse width was determined from the RC time constant. Capacitor value of 1 µF and a 500kΩ resistor were chosen to ensure a pulse occurred every second, with an interval long enough for localisation of the signal to be successfully performed.
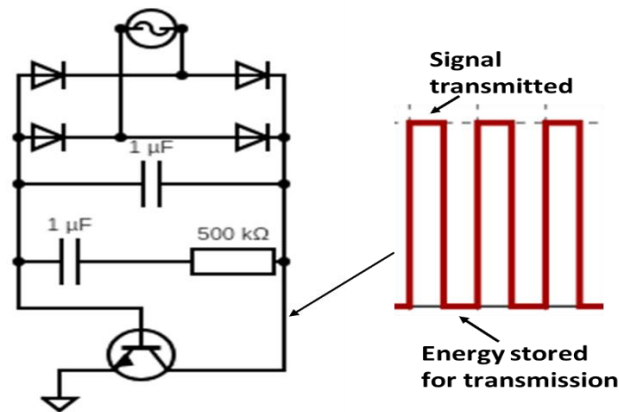
Fig 2.21: Circuit diagram of pulsing unit of radio telemetry tag

The signal was then radiated through a transmitted antenna at 5.8 GHz, which was chosen after careful consideration of the antenna size and link budget of the system. The frequency allowed for significant reduction in antenna size reducing the tag size and weight, whilst allowing for the signal to be detected at a sufficient range for tracking capabilities. The antenna was designed to be as small, lightweight, and isotropic as possible in order to 1) reduce physical hindrance to the bee; and 2) minimize transmitter

circuitry complexity to cope with continuous direction changes during flight. The possibility of integrating the antenna and energy harvester was explored for weight minimization using CST microwave studio. The high dielectric constant of the energy harvester leads to low antenna radiation efficiency and very small bandwidth. The requirement for a high radiation efficiency, alongside challenges to fabricate the device, resulted in the design being unsuitable for the transmitting antenna.

Adding an additional thin layer of Fr4 to reduce the effective dielectric constant led to similar results, as shown in Figure 2.22. An attempted design of a PIFA antenna with a PZT substrate outlining the low achievable efficiency is demonstrated.

(a)

(b)

(c)
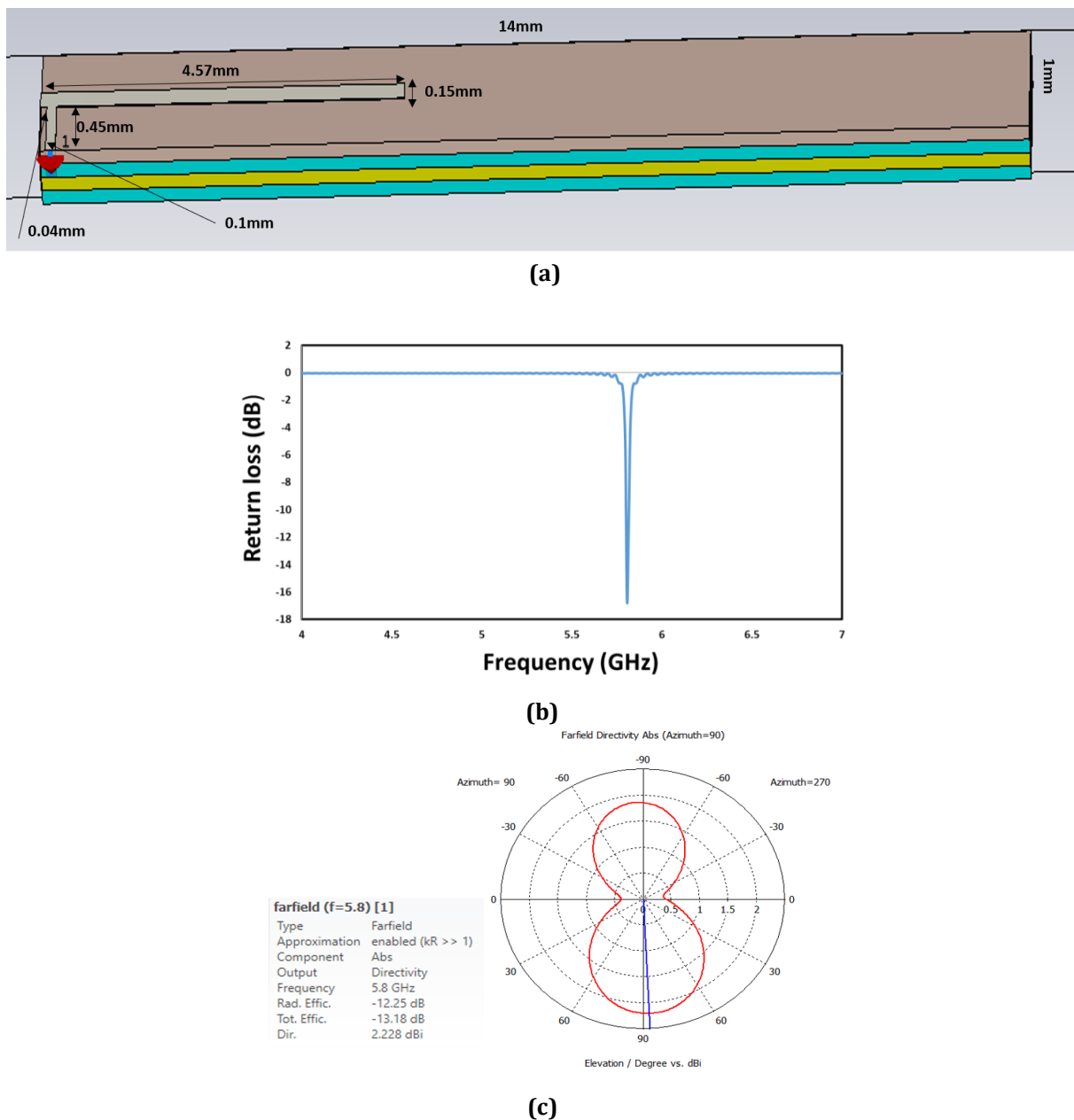
Fig 2.22: Simulation results of PIFA antenna using brass shim as ground plane. (a) Simulation model, (b) antenna return loss and (c) radiation pattern and efficiency

The antenna itself consists of 4 substrate layers and a silver PIFA antenna with 35μm thickness. The substrate layers are two 14 x 1 x 0.13 mm PZT-5A (ε_r = 1800) with a brass shim in between. The brass shim is additionally used as the ground plane for the PIFA antenna. The top substate layer is 0.13mm thick FR-4 (ε_r = 1800). The dimensions of the antenna are shown in below:

A simple monopole configuration with a thin wire was considered sufficiently lightweight and omnidirectional for the application. A 3D model of the proposed tag and bee were generated in which a quarter wavelength monopole is implemented as the transmitting antenna. This is shown in figure 2.22a, whilst the simulated impedance match of the transmitting antenna is shown in figure 2.22b. Additionally the electromagnetic effects of the bee and proximity of the energy harvester were studied to find that whilst a slight shift in resonance occurred, acceptable return loss performance was achieved at 5.8 GHz. The simulated radiation pattern of the monopole is shown in figure 2.22c.

For the simulation, a CAD model of a bee was imported into CST microwave studio. The material of the bee was chosen to be water, which closely resembles the dielectric properties of the bee itself. The purpose of the simulation was to evaluate the frequency shift of the antenna resonance with and without the bee present. The circuit board consisted of 1.6mm thick FR-4, with each component modelled as ABS (Acrylonitrile butadiene styrene). The piezoelectric beam was modelled as a bimorph consisting of PZT-5A – Brass – PZT-5A, each 14mm x 0.2mm x 0.13mm in dimensions. The circuit board was then placed on the centre of the bee's thorax before a 14mm long copper wire with 0.25mm radius was attached on the copper trace on the circuit board.

(a)   **(b)**
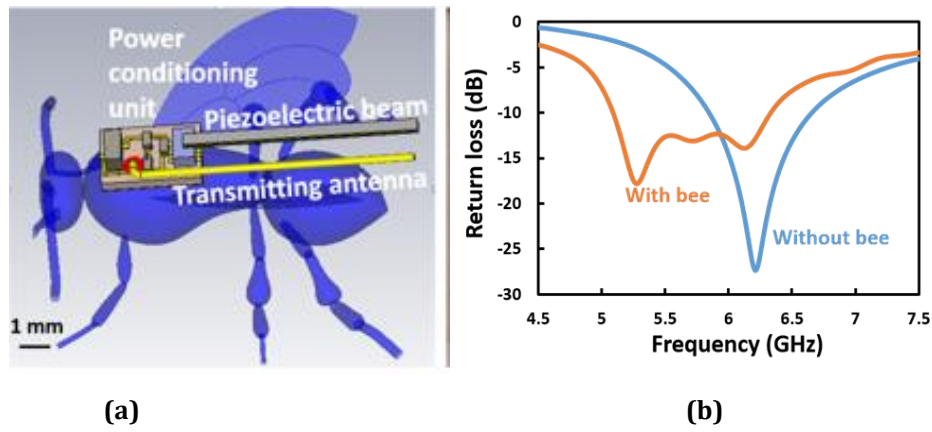
Fig 2.23 (a) transmitter tag component breakdown, (b) simulated return loss for transmitting antenna with and without bee

(c)
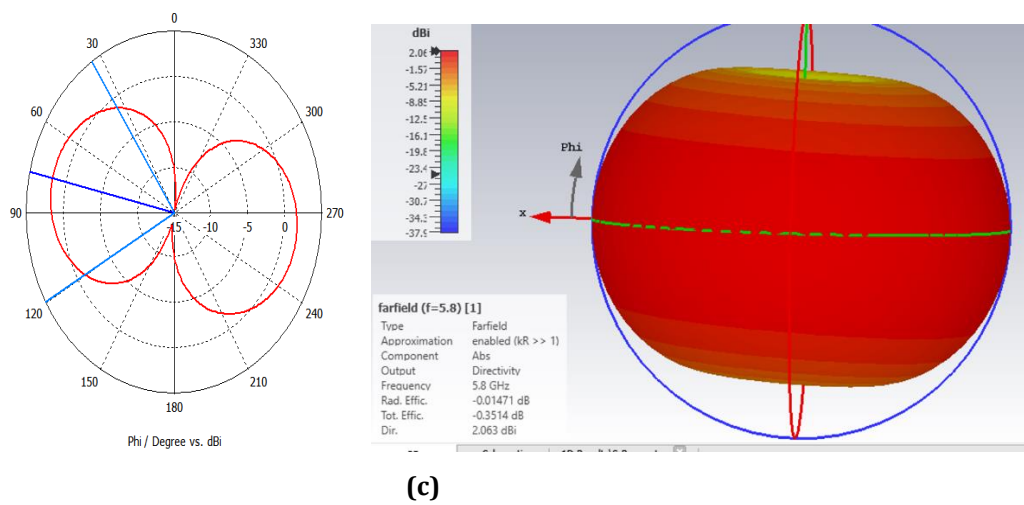
Fig 2.24: Radiation pattern of monopole antenna.

For the initial prototype, the discussed circuitry was integrated onto a 0.8mm thick circuit board and fabricated in house. Using EAGLE, the PCB layout of the circuit was designed and converted to a Gerber file, in which a mask was generated using PCB transfer paper. The mask was applied to the circuit board by heating to 180 °C before removing the transfer paper. Etching used ferric chloride, allowing for creation of the PCB board as the fabricated tag is shown in Figure 2.25.
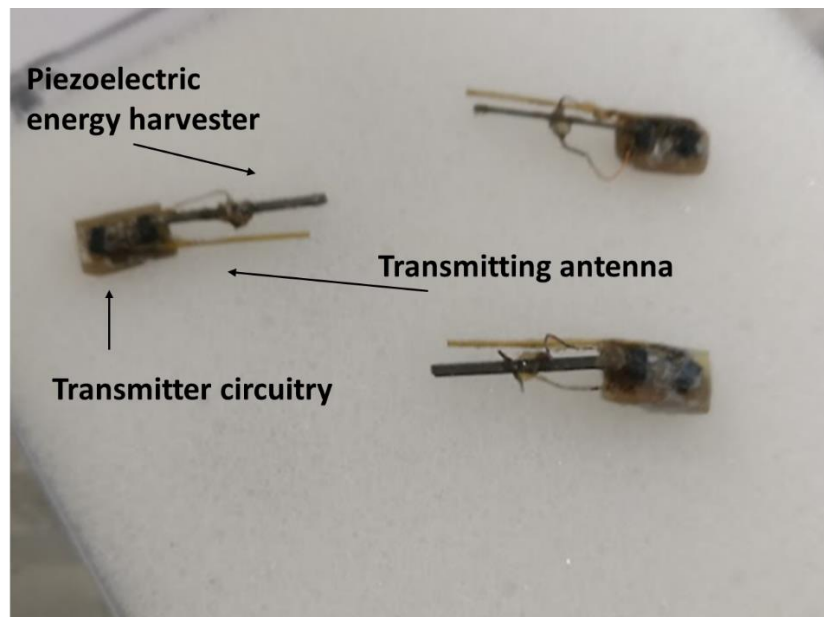
Fig 2.25: Fabricated self-powered radio telemetry tag

The fabricated tag weight (80mg) with a 5% tolerance varied substantially due to an inability to precisely control the solder paste, resulting in more solder on some tags than others. We tested the tag on three types of bees, the honeybee (*Apis mellifera*) (~100mg), bumblebee (Bombus spp.) (~200mg) and a carpenter bee (Xylocopa spp.) (~240mg) (Figure 2.26).
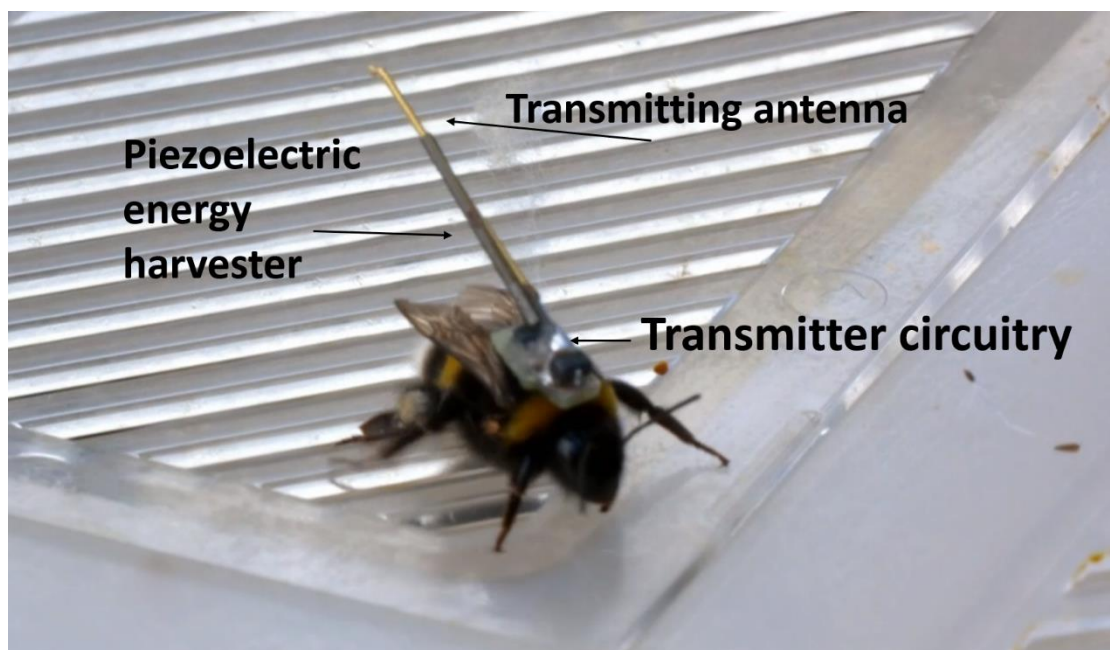
Fig 2.26: Fabricated tag attached to bumblebee

Unhindered flight was possible with bumblebees and carpenter bees; however, honeybees were unable to fly. To determine the maximum tag weight under which honeybees could fly, dummy tags were 3D printed with various weights and aspect ratios and attached to insects as shown in Fig. 2.27. An opalith tag was originally attached to the

thorax of the bee before later gluing on test structure. By varying the length of the cantilever between 10mm - 14mm and adding small blocks of solder along the cantilever structure, the size and weight ($\sim$ 20mg – 40mg) of the test structures could be altered.

The results of tests outlined a maximum tag weight of 35mg (Appendix A). For tag miniaturization a thin (50μm) and flexible FR4-substrate was chosen, which reduced weight and physical hindrance whilst enabling easier attachment of the tag to the bee's thorax. The use of a flexible material decreased circuit volume from 9.6mm^3 to 0.6mm^3, whilst reducing tag weight to ~30mg. Additional individual Schottky diodes, were implemented to replace the rectifier chip allow for further decrease of overall volume of the circuit. The same fabrication procedure as the previous tag was performed, in which figure 2.28 outlines the fabricated tag.
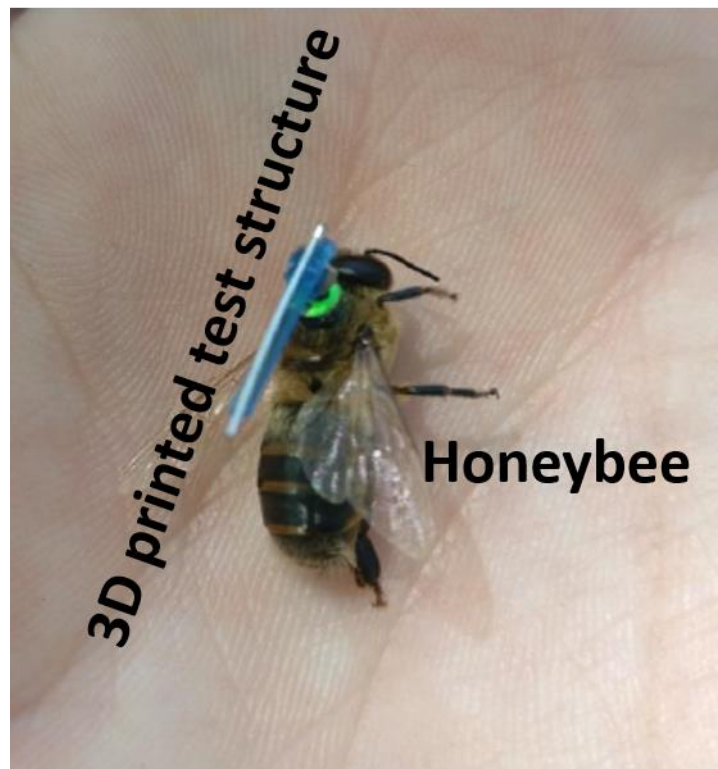
Fig 2.27: Fabricated 3D printed test structure to evaluate flight performance under various tag weights

(a)

(b)   **(c)**
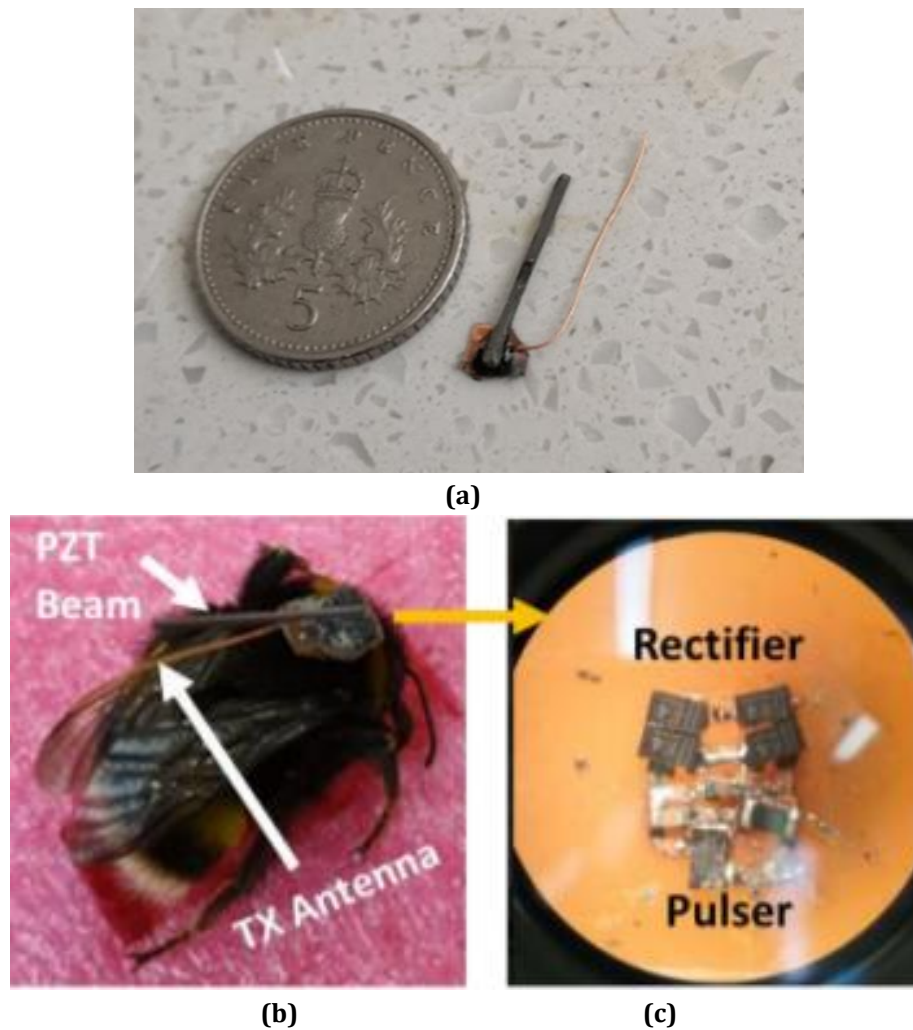
Fig 2.28: (a) Fabrication of flexible circuit board with components soldered with EH. (b) Flexible circuit board and energy harvester attached to bumblebee. (c) Microscope image of fabricated tag

The return loss of the tag with and without the bee were measured and the power output of the tag (figure 2.30) when excited by vibration was determined. Due to the practical difficulty of tagging a tethered bee, a vibration generator was used instead to produce the signal. Due to the 1 µF capacitor specifically implemented to maximise power generation for 1 second periods for the bee, we can assume similar transmission power between the bee and vibration generator. Figure 2.28a shows the measurement setup of the tag, in which a small wire was attached to the SMA connector, which can additionally be connected to a VNA. For measurement purposes of the return loss, the antenna was manually probed with an SMA connector when attached to the vibration generator and bee. Measuring between 5GHz and 7 GHz, figure 2.28b and c show the measured results with and without the bee, respectively.

We can additionally observe a validation of the simulated model in which the presence of the bee causes a shift in frequency, whilst providing satisfactory return loss

at 5.8 GHz. The simulation and experimental results highlighted the requirement of a carefully designed antenna, as a large frequency shift it observed when attached to the bee. The repeatability of the 5.8 GHz antenna was deemed to be consistent providing the antenna geometry could be accurately cut to the same dimensions during fabrication. Capacitance introduced via soldering was observed to cause a slight shift in resonance, however, this a return loss greater than -10 dB at 5.8 GHz could always be maintained. The fixing of the tag to the bee additionally effected the repeatability. It was important to ensure the tag was well mounted on the bee and the movements of the bees' body in any way could not cause any bending to the antenna structure. Any bending in the antenna structure, substantially shifted the frequency of the antenna.

Fig 2.29: Return loss analysis of fabricated transmitting antenna

(a)

(b)
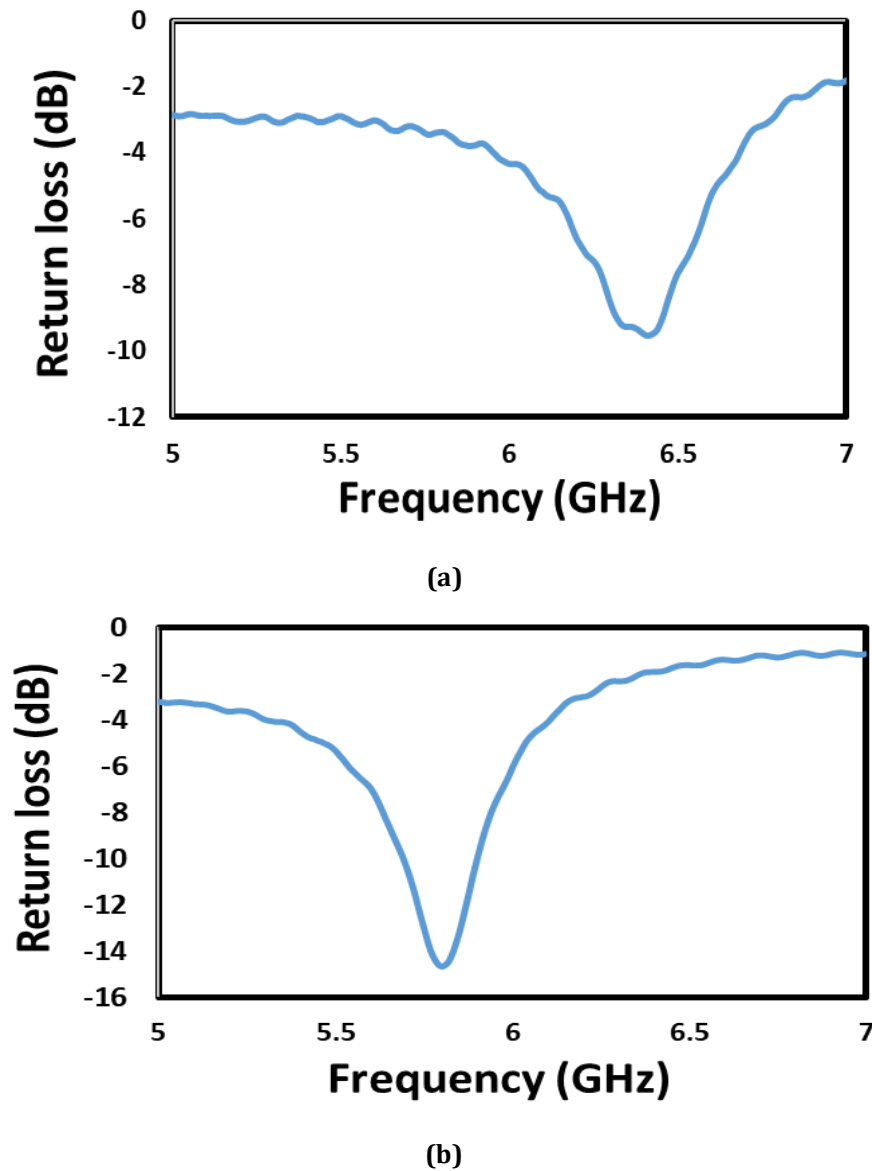
Fig 2.30: (a) measured return loss without bee attachment (b) with bee attachment

We assumed the antenna gain matched the simulated value, which was 1.8 dBi. This was then used to calculate the transmitted power. Figure 2.31a shows the set up in which piezoelectric harvester was directly excited by a vibration generator. Placing a receiving antenna 35 centimetres away from the tag and using a receiving antenna with 3 dBi gain, the received power could be analysed a with spectrum analyser (figure 2.31b). Using friis transmission formula (equation 1.8) we calculated the transmitted power to be -25 dBm.

(a)
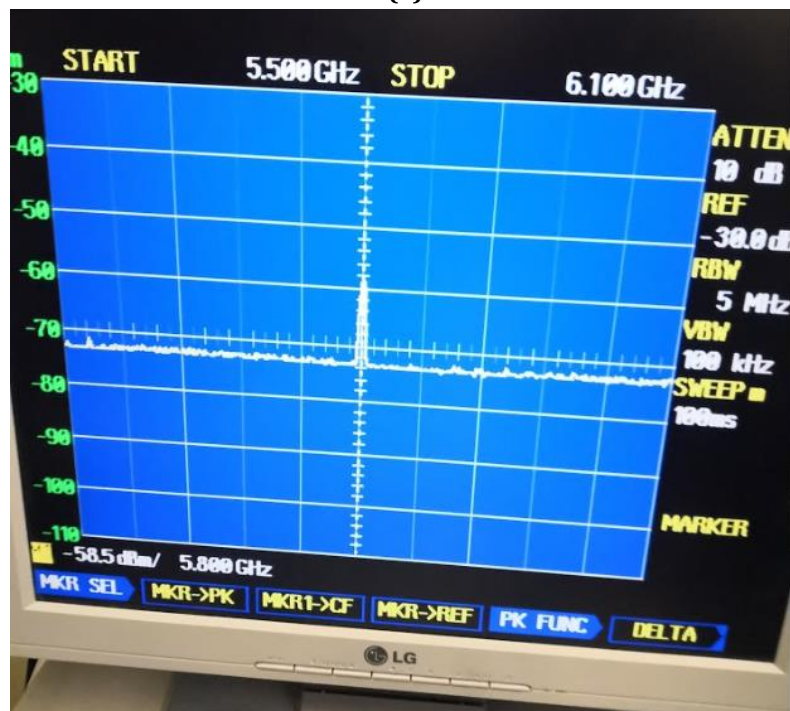
(b)

Fig 2.31: (a) Experimental set up to measure transmitted power. (b) Spectrum analyser showing receiver power with a separation of 35 centimetres [156]. The received signal strength was measured at -58.5 dBm.

This chapter compares current energy harvesting techniques from vibration sources in which piezoelectric materials were identified due to their ease of fabrication, high voltage output and simple structure. Fundamental concepts of piezoelectric harvesting have been discussed whilst the need for a non-resonant harvester has been proposed. The design, fabrication and measurements of the self-powered tag have been presented in which the tag is capable of transmitting a signal of -25 dBm at 5.8 GHz.

Chapter 3. Design and fabrication of phased array antenna

The chapter addresses the theory, design, fabrication, and measurements of a phased array antenna to be used to determine the position of the radio telemetry tag presented in Chapter 2. Location is estimated by the implementation of an angle of arrival (AOA) method to determine the direction of the signal from the received signal strength.

3.1 Localisation systems

Multiple methods have been developed and implemented to estimate the position of an emitting RF source. Current radio telemetry approaches for insect-tracking have implemented either angle of arrival techniques [132] or autonomous systems have been developed which utilise multiple receivers to estimate position based on received signal strength indicator (RSSI) [157]. Table 3.1 summarises positioning systems based on current measurements.

Table 3.1: Positioning systems for RF signals based on available measurements for radio telemetry

Positioning scheme	Measured quantity	Brief description
Received signal strength	Power and range based	Measurement of received power at multiple receivers to determine location
Angle of arrival	Angle based	Usually implements antenna array, which is scanned to determine direction of signal propagation
Time difference of arrival	Time and range difference based	Measured the time difference of arrival at multiple elements or receivers to determine location
Phase difference of arrival	Phase based	Measures phase at each antenna element to determine direction of arrival.

Received signal strength measurements are the simplest to implement as they are always available in every wireless device. They assume that the further away the signal is from the receiver, the weaker the signal will be. Typically, the change in dB between two or more receivers are used to determine range estimation. Due to multipath,

reflection and refraction commonly causing unwanted attenuation with RF signal propagation, readings are frequently erroneous.

Angle of arrival typically implement a beamforming antenna array which are used to electronically steer the main radiation lobe. The signal strength can be measured and compared at all angles scanned to determine the angle of arrival. A single antenna system can be implemented to determine the direction of the signal, whilst multiple antennae can be implemented to find an intersection point providing increased localisation accuracy. Conventional antenna arrays can be implemented to determine angle of arrival; however, they require mechanical scanning or user scanning. Mechanical scanning is suitable for a single plane, although they are often difficult to implement in azimuth and elevation planes. User scanning can easily scan all angles of interest but with reduced precision due to poor operator skill. The disadvantages of angle of arrival techniques are that they are susceptible to multipath providing false estimations, as well as the position estimation degrading as the tag moves further away from the receiver.

Electromagnetic waves propagate through free space at the speed of light. Due to this property, time difference of arrival techniques can characterise the position of the tag when the distance between three or more receivers are known. By comparing the time difference between receivers and knowing that the signal travels at the speed of the light, a distance difference between each receiver is determined. This is plotted as a set of hyperbolic lines, with a position is estimated via the intersection point. Time difference of arrival can provide very accurate estimations over long distances; however, they require very precise time synchronisation between receivers. For applications where receivers are closely spaced within a few meters of each other, nanosecond time synchronisation is required.

The concept behind phase difference of arrival is similar to that previously describe for angle of arrival however the angle of arrival is estimated via phase differences between antennae instead of power. Due to the nature of the system, they only work for one incoming signal, whilst the phase measurement could be noisy providing errors in the result.

To determine the most efficient localisation system for the radio telemetry tag presented in Chapter 2, comparisons were made between each system to determine the most suitable for our application. Three key parameters were considered for the system:

maximum detection range, accuracy of the location estimation and the ability to have a compact system capable of being mounted to a UAV for moveable long-range tracking.

As the frequency and transmission power of the tag have increased and decreased respectively in comparison to commercially available tags [82], the link budget between the transmitter and receiver has significantly decreased, reducing the detection range. The implementation of an antenna array with high gain could be used to provide an increased detection range between Tx and Rx. Potential applications rely on monitoring flower to flower visitations from the tagged bee which could be separated by a few meters or less. By increasing the accuracy of localisation, the system would be able to provide a higher resolution, providing more meaningful tracking data. Table 3.2 summarises the advantages and disadvantages of each system:

To achieve the requirements listed above, the angle of arrival was deemed to be the most suitable as a single directional antenna provides an increased gain compared to omnidirectional approaches, whilst the accuracy of the system is contingent upon the design. The possibility of increased accuracy could also be obtained with the implementation of multiple receivers. The mechanical or electrical scanning of the antenna, along with antenna placement, however, has to be considered in order to provide reasonable detection coverage.

Table 3.2: Advantages and disadvantages of localisation systems for radio telemetry applications

Positioning scheme	Advantages	Disadvantages
Received signal strength	• Simple configuration • Possibility to be compact and portable	• Requires omnidirectional antennae for the required coverage and position estimates • Attenuation in signal leads to large errors in bearing estimation • Single antenna and receiver can only detect proximity
Angle of arrival	• Use of mechanical or electrical scanning can mean an operational system capable of position estimates with a single antenna • Typically uses antenna array which will increase gain of the receiver	• Susceptible to multipath effects • Inability to have near isotropic coverage due to mechanical and electrical scanning limitations.
Time difference of arrival	• Omnidirectional coverage or directional depending on antenna type • Highly precise positioning if suitable synchronisation can be achieved	• Requires the use of multiple antennae and receivers with adequate separation • Nanosecond synchronisation required for receiver a few meters apart, which is costly and difficult to achieve
Phase difference of arrival	• Compatible with a single antenna array and beamforming	• Only suitable for a single incoming signal • Phase measurements can be affected by noise

3.2 Mechanical scanning vs electronic scanning for AoA estimation

Mechanical beam scanning has been implemented for several applications, which are mainly used in satellite communication and radar applications [158]. Figure 3.1 outlines a typical mechanical beam steering system consisting of a directional antenna and steerable unit.
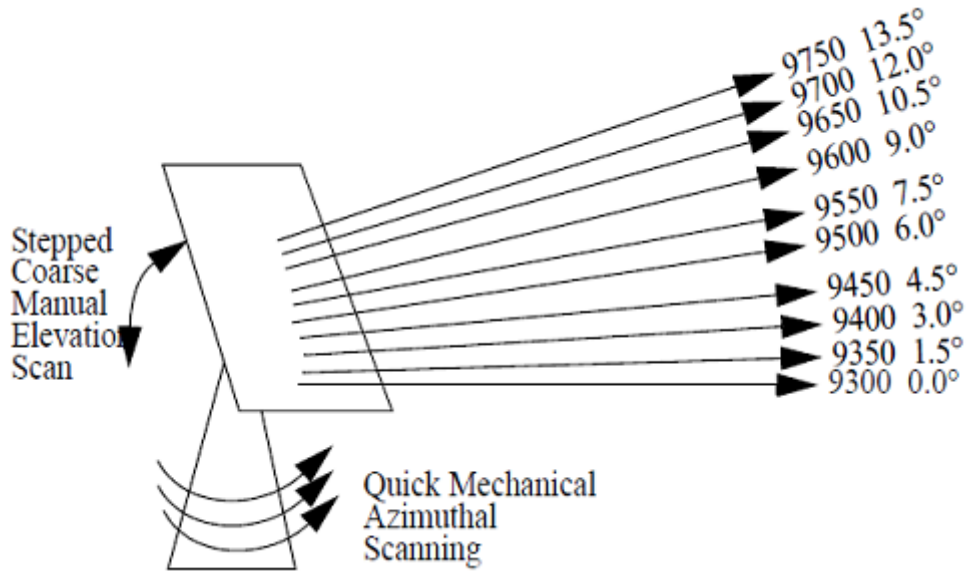
Fig 3.1: Mechanical beam steering system [159]

Since applications involve satellite communication and radar applications, a high gain is required for the antenna as it is required to operate at 10's of Kilometres. The size of the antenna is the main drawback for mechanical scanning systems. A large motor is typically required to change the direction of the antenna, thus limiting the scan speed to the speed of the motor, which can often be seconds to perform a full scan. Secondly, scanning is only performed in a single plane, this results in careful design of the antenna to provide satisfactory coverage of the sensing environment or communication system. Fan beam antennae are used to overcome this problem due to the properties of the antennas radiation pattern which is depicted in Figure 3.2. A large beam width in the elevation plane allows for sufficient coverage whilst scanning is performed in the azimuth plane in which the antenna is sufficiently more directional as shown by the E-Plane beam width.
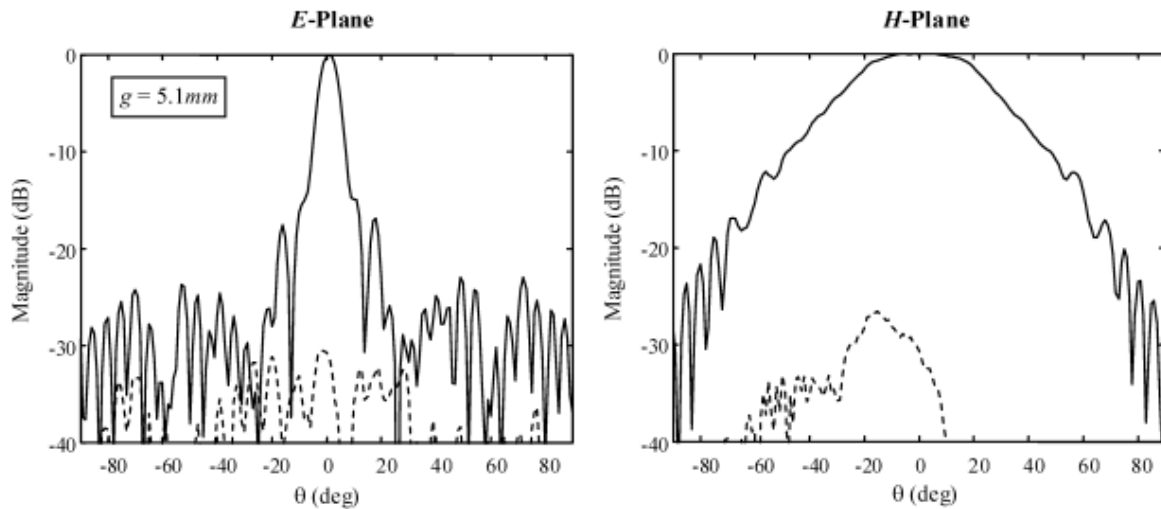
Fig 3.2: Radiation pattern of fan beam antenna for E and H plane [160].

Mechanical scanning is advantageous for such applications as 360° scanning in the azimuth plane can be achieved. For applications such as localisation and tracking, the inability to obtain a directional elevation plane limits the sensitivity and accuracy of the tracking system. To overcome this, hybrid systems have been introduced whereby the antenna is mechanically scanned in azimuth and the elevation plane is scanned electronically [161].

Electronic scanning is often achieved using phased array antennae, often requiring a phase shifter at each element, leading to high financial costs when a large number of antenna elements are required. Frequency scanned antennae have also been implemented as a low-cost solution, whereby each element in the array is frequency sensitive. The change in frequency provides a change in phase to each element scanning the beam. Figure 3.3 shows examples of a phased array antenna and frequency-scanned antenna.
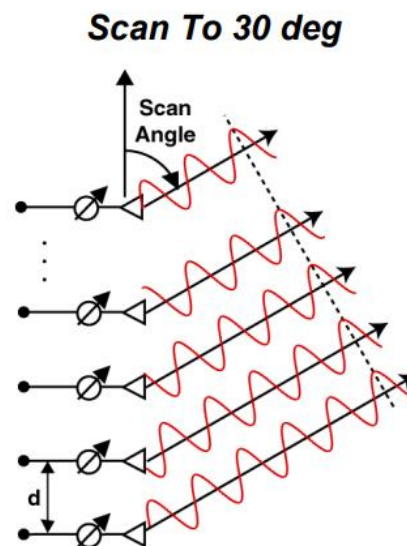
Fig 3.3: Electronic beam steering system demonstrating phased array antenna [162].

For electronic beam steering, greater flexibility can be achieved in scanning potential of azimuth and elevation, as each element is adaptively controlled to create a beam in the desired locations. The scan speed is now limited to the response time of the phase shifters, which can be in the order of microseconds. Whilst much faster scanning times can be achieved electronically, the coverage of the antenna is significantly lower than mechanical scanning. Typically 120° can be achieved in azimuth and elevation planes [163], due to the spacing between the elements and change in antenna aperture at higher scan angles, leading to extremely low efficiencies.

Table 3.3 summarises the advantages and disadvantages of mechanical vs electronic beam scanning

Table 3.3: Summary of comparisons between mechanical and electronic scanning

Scanning mechanism	Advantages	Disadvantages
Electronic	• Ability to scan in azimuth and elevation planes • Fast scanning capability dependent upon phase shifter response time • Ability to have side lobe suppression	• High costs • Limited scanning range • Deformation of antenna pattern as scan angle increases
Mechanical	• Low cost • Simple implementation • Large scanning coverage	• Difficult to scan in elevation plane • Slow scanning speed

Whilst electronic scanning presents drawbacks with scanning range, +/- 60° scanning capability in azimuth and elevation planes can be achieved, such coverage would be sufficient providing careful consideration of antenna placement. For applications involving beehive/nest monitoring or foraging activity, the antenna could be placed outside the hive or above the flowers. For long range tracking, the scanning range limitations could be overcome by mounting the antenna facing directly to the ground. Since the ability to scan in azimuth and elevation is critical to the accuracy of the tracking system, electronic scanning was chosen.

3.3 Phased array antenna theory and design

Phased array antennas can be defined as multiple stationary antenna elements, which apply varied phase or time delay at the input to each element in order to scan the antenna beam to specified angles in space. The primary reason for implementing phased array antennae is the ability to produce a directive beam that can be repositioned electronically.

To demonstrate the principle of operation, an N-element phased array antenna is depicted in Figure 3.4, in which identical antenna elements are equally spaced with spacing equal to d. We assume for the following discussion that the phased array antenna is operating in the receiver case, however, due to the reciprocity principle the discussion could be extended to the transmitter side.
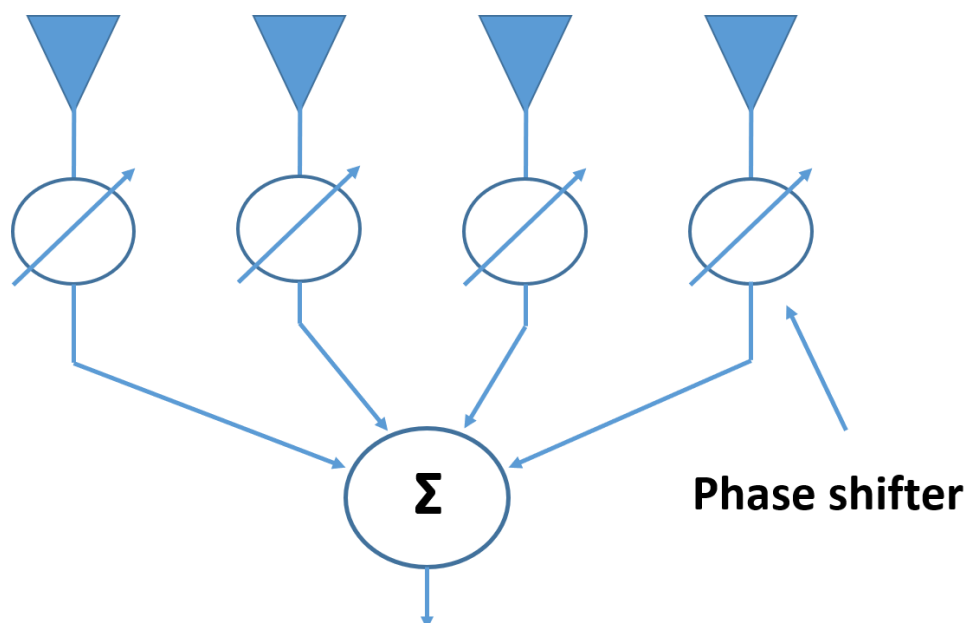
Fig 3.4: Block diagram on N-element phased array antenna

The individual signals at each element are manipulated by incorporating small time delays to control the phase at each element before combining all the signals together at the output. The phase difference is related to the path difference, x, between two adjacent beams. Equation 3.1 explains how the ratio of phase difference, φ (0 to 2π) should be equal to the ratio of path difference to wavelength.

$$\frac{2\pi}{\varphi} = \frac{\lambda}{x} \tag{3.1}$$

Additionally, the path difference is:

$$x = dsin(\theta_s) \tag{3.2}$$

Where θ_s is the desired angle of steering. Combining equations 3.1 and 3.2 the required phase difference between each element can be expressed as:

$$\Delta\boldsymbol{\phi} = \frac{2\pi dsin(\theta_s)}{\lambda} \tag{3.3}$$

The following equation applies to a linear array, which is only capable of scanning a single plane. For a planar array, that can scan both azimuth and elevation plane the complexity significantly increases. Figure 3.5 demonstrates a 4 x 4 element planar array where the elements are arranged into a matrix (labelled numbers indicate rows and columns). We can now express the desired direction of the beam in polar co-ordinates (θ_s, ϕ_s) for azimuth and elevation planes, respectively.

For a planar array, the relative phase difference between the antenna elements is expressed as:

$$\Delta\phi = k(rd_r sin\phi + cd_c sin\theta) \tag{3.4}$$

Where $k = \frac{2\pi}{\lambda}$ and r and c are defined as the row and column number of the element, whilst d_r and d_c are the separations between elements in azimuth and elevation plane respectively.
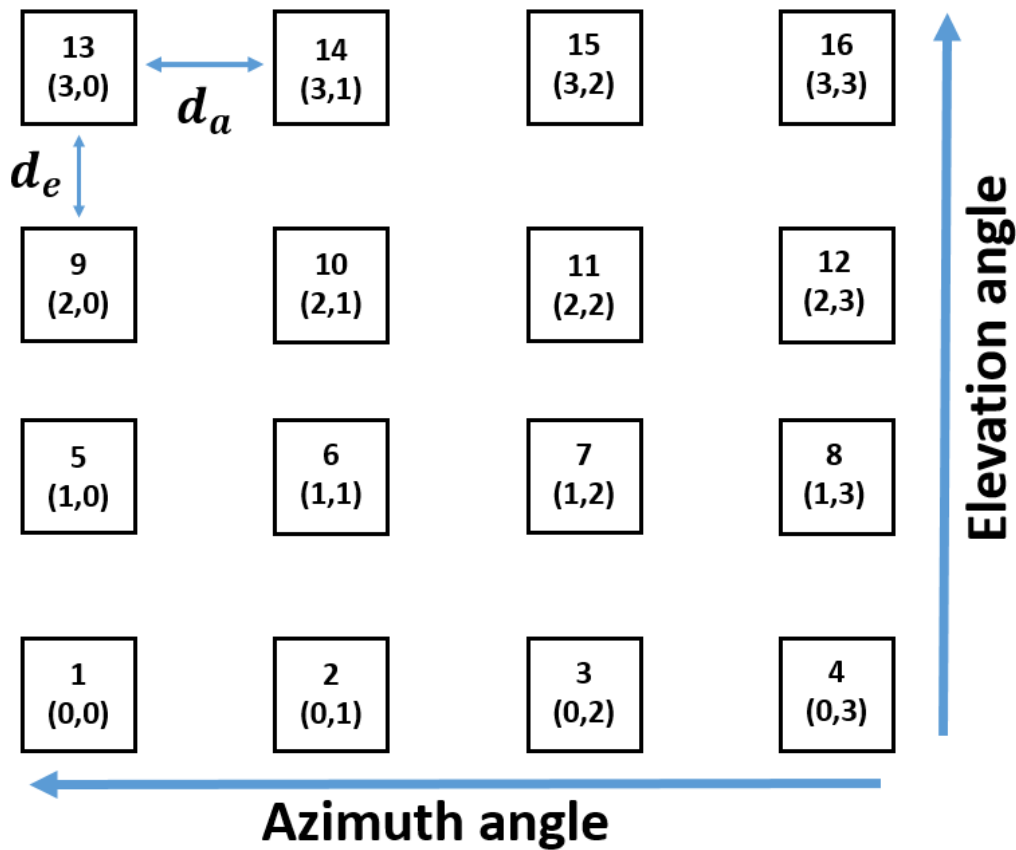
Fig 3.5: Planar array element configuration

A phased array antenna typically comprises a feeding network and phase shifters [164]. The phase shifters are responsible for forming the beam direction of the array by controlling the input phase to each element. The feeding network can be described as a multiport power divider circuit to link multiple antenna elements to a single port.

Generally, the most practical in terms of implementation is the constrained feed which consists of a feed line and passive elements to distribute the power to each element [162]. The constrained feed can further be separated into two categories, which are series and parallel fed (Figure 3.6), in which the input is connected to a receiver system.

Series fed designs rely on feeding the element from one end to the other with the input signal, which are coupled serially to each individual antenna element. Due to this property the phase shifters have a cumulative aspect resulting in relaxation of the design constraints for the phase shifter as the phase tuning range required will be significantly less compared to a parallel design. For antenna arrays with a large number of elements, a series feed can become problematic as the cumulative relationship also applies to the loss through the phase shifters.

(a)

(b)
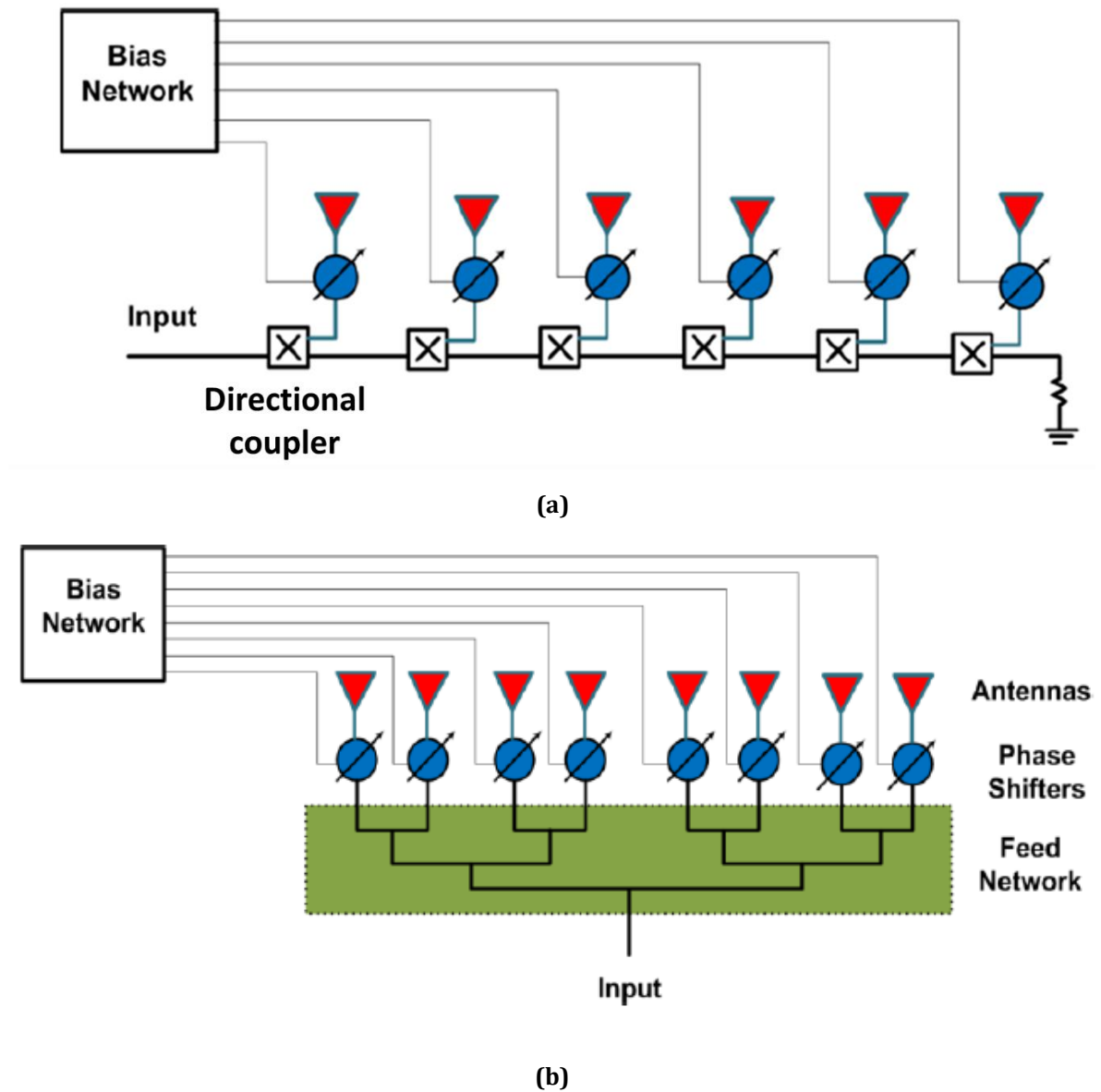
Fig 3.6: Constrained feed for phased array antenna when fed (a) in series, (b) in parallel [162]

Parallel designs comprise a corporate tree network of power dividers to disaggregate the input signal. The phase shifters are not cumulative due to their position in the feeding network meaning that they require a high phase tuning range. For these designs 2^N elements are preferred where N is the number of elements. For both series and parallel designs, phase shifters can be placed at any stage of the array.

A phase shifter is defined as a two-port network responsible for changing the transmission phase angle [165]. Phase shifters have a wide range of implementations and can be controlled magnetically, mechanically, and electrically using analogue signals or digital bits.

For mechanical phase shifters, the turning on a dial will adjust the phase from the input to output. Magnetically controlled phase shifters rely on voltages applied to ferrite material such as yttrium iron garnet (YIG) to achieve a phase shift [166]. Electrically controlled phase shifters can be analogue or digital. Analog phase shifters provide a continuously tuneable and variable phase by a varying voltage [167]. These types of devices are often implemented with tuning diodes, which have a varying capacitance with voltage. Digital phase shifters have a small number of binary states with a designated phase shift. 360 degrees is often divided into the number of available bits. The highest order bit is 180 degrees, the next 90 degrees and the relationship continues thus as the number of bits increases. A six-bit digital phase shifter would provide a least significant bit of 5.625 degrees. Table 3.4 summarises the advantages of using analogue and digital phase shifters

Table 3.4: Advantages of analogue and digital phase shifters

Analogue phase shifters	Digital phase shifters
• Can achieve a lower loss in comparison to digital phase shifters • Cost of fabrication and parts are cheaper, but assembly can be difficult	• Easier to assemble • More uniform performance due to the precise phase difference between each bit • Can operate over a higher bandwidth

3.3.1 Phase shifter design

To allow for flexibility in the antenna and feeding networks design, analogue phase shifters with 360° phase shift were implemented. As the aim of the phased array antennae is to locate the position of a tagged bee emitting at 5.8 GHz, high bandwidth operation was not required, and therefore, analogue phase shifters were selected for their lower loss and cheaper fabrication. As a single-phase shifter is required at the input to each antenna element, the system would be costly when using a directional antenna with high gain in a digital system.

The two most common implementations of analogue phase shifters are the loaded transmission line approach and reflection type phase shifters. The latter employs a four port coupler and two reactive variable loads [168]. Loaded transmission lines consist of periodically loaded transmission lines with varactors [169]. Figure 3.7 demonstrates the schematic for a loaded transmission line and reflective type phase shifter approaches, whilst Figure 3.7c demonstrates a phase shift by sweeping the capacitance between 0.1 – 5pF. The phase shift is achieved by applying a variable voltage

which changes the capacitance of the varactor. The change in capacitance modifies the reactance of the circuit, thus providing a phase shift dependent upon the capacitance of the varactor diode (Equation 3.8). For proof of concept a frequency of 1 GHz was chosen.

(a)

(b)

(c)

(d)
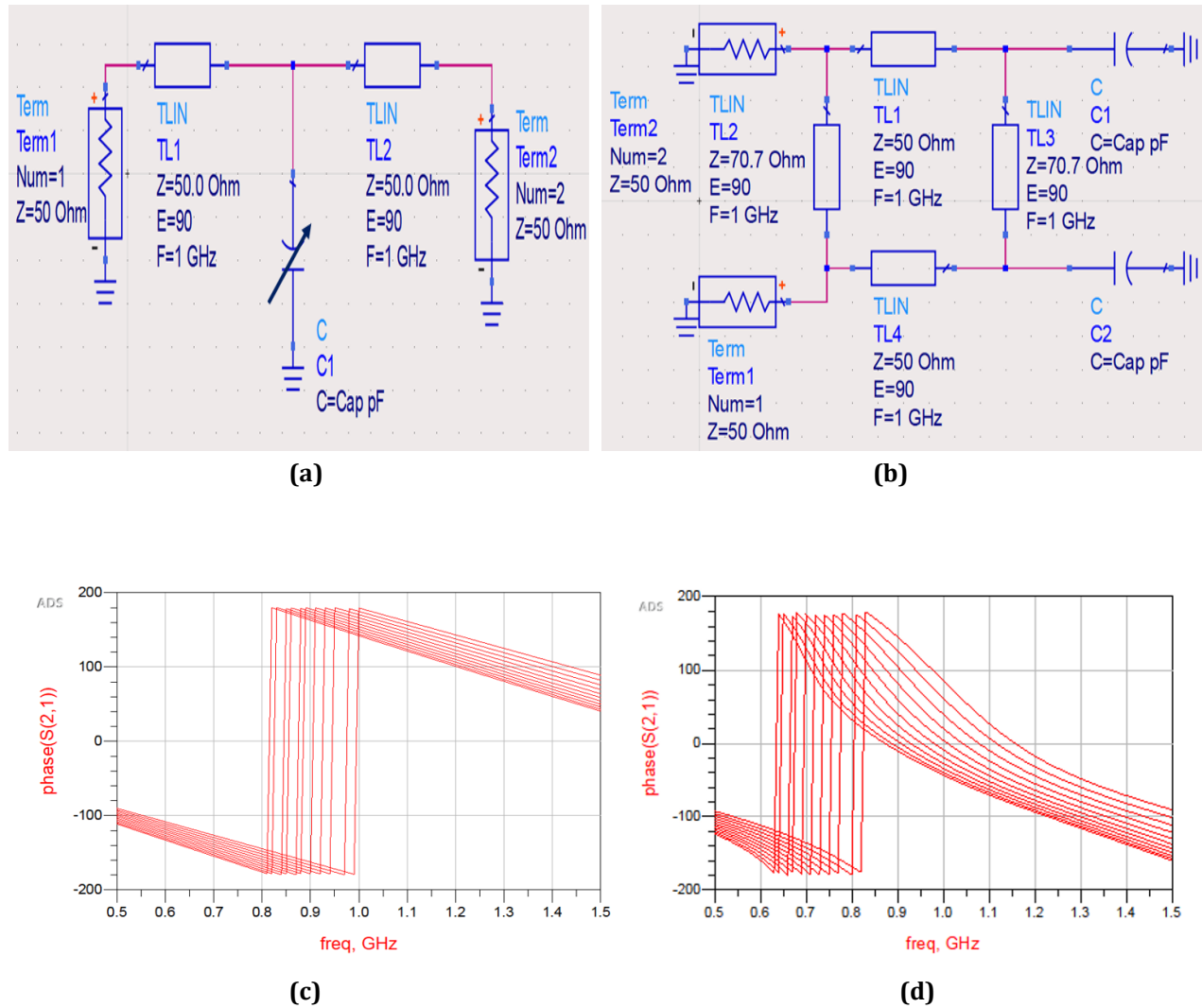
Fig 3.7: Schematic for (a) loaded transmission line (b) reflective type phase shifters (c) change in phase with varying capacitance for loaded transmission line (d) change in phase with varying capacitance for reflection type phase shifter.

A 360° phase shift can be achieved with both designs, however, due to the matching at input/output ports and compactness, the reflective type phase shifter offers an acceptable compromise [167]. To guarantee a 360°, two series resonant loads (complex load) are placed in parallel configuration as shown in Figure 3.9a. Also depicted in Figure 3.9a is a conventional branch line coupler, which is typically used to divert a fraction of the signal from one transmission line to another. When a complex load is applied to the through and coupled ports of the coupler, all the power entering the input is directed to the output with a change in phase dependent upon the reactance of the complex load.

Varactor diodes are implemented where the two inductors (L_1 and L_2) are chosen, such that series resonance is achieved with the maximum and minimum values of the varactor (C_{min} and C_{max}). The phase shift of each resonance is 0°, meaning the design guarantees 360° when the inductance values satisfy the following equation to allow for series resonance.

$$L_{1,2} = \frac{1}{\omega_0^2 C_{min,max}} \qquad (3.5)$$

Where ω_0 is the centre frequency, resonance occurs at the low and high voltage bias of the chosen varactor, which gives a circuit reactance of X_L and X_H respectively. The reactance range between high and low bias is given by:

$$\Delta X = \frac{1}{\omega_o C_{min}} - \frac{1}{\omega_o C_{max}} \qquad (3.6)$$

Parallel resonance is achieved between the two series points where the two reactance's are equal and opposite. This occurs with an equal parallel resistance:

$$R_p = \frac{1}{8} \frac{(\Delta X)^2}{r} \qquad (3.7)$$

Where r is the corresponding loss resistance. We can define the total phase shift by finding the relationship between the parallel resistance, loss resistance and the reactance's at high and low bias. The total phase shift is given as:

$$\phi = 2 \frac{\Delta X}{\sqrt{r\,R_p}} \qquad (3.8)$$

An initial prototype was constructed using FR-4 substrate $\varepsilon_r = 4.3$ and varactor diodes, with $C_{min} = 0.15pF$ and C_{max} = 1pF. Considering a centre frequency of 5.8 GHz, and the above parameters $L_{1,2}$ was calculated to be 5.02 nH and 0.73 nH, respectively. Each transmission line of the coupler is a quarter wavelength in length. Figure 3.8 illustrates a circuit diagram and the simulated phase shift of the coupler using an advanced design system.
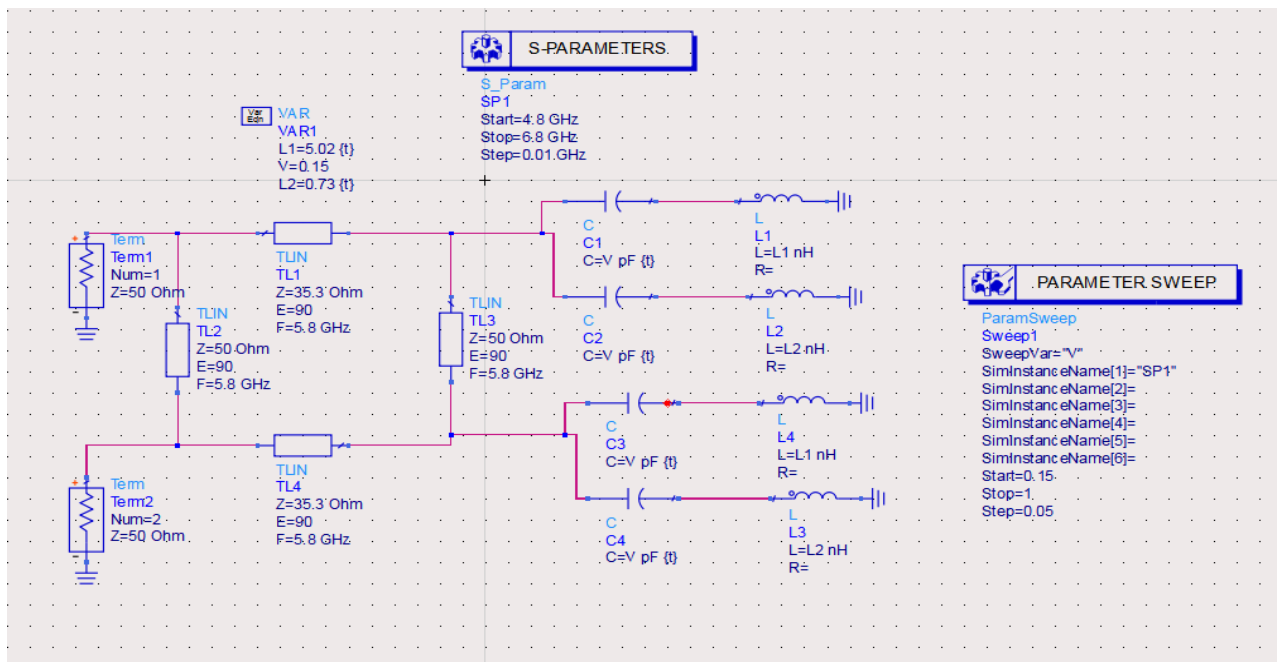
(a)
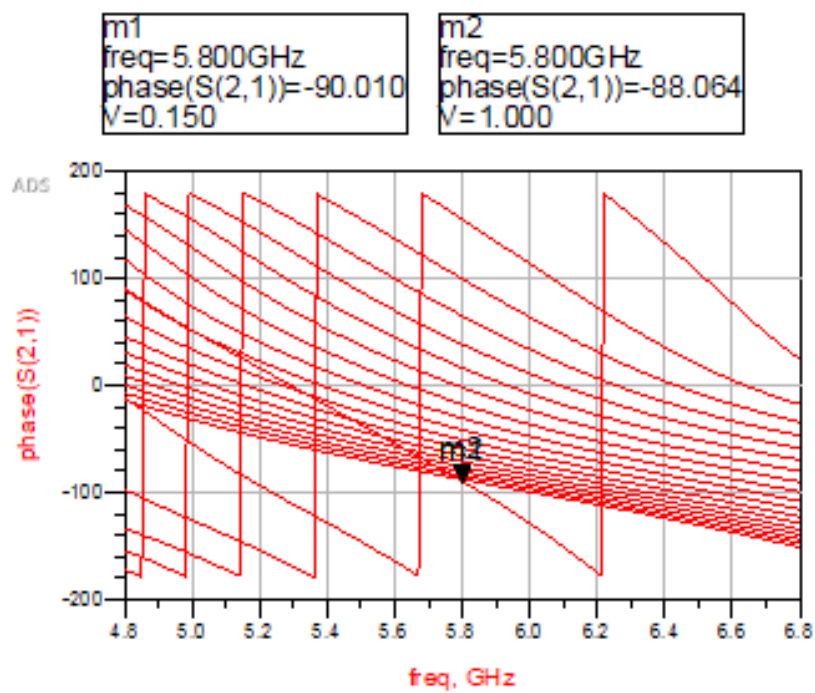
(b)

Fig 3.8: (a) Reflection type phase shifter with complex load modelled in ADS for a varactor diode with capacitance range between 0.15pF and 1 pF (b) Simulated phase shift with series resonance occurring at around 0°.
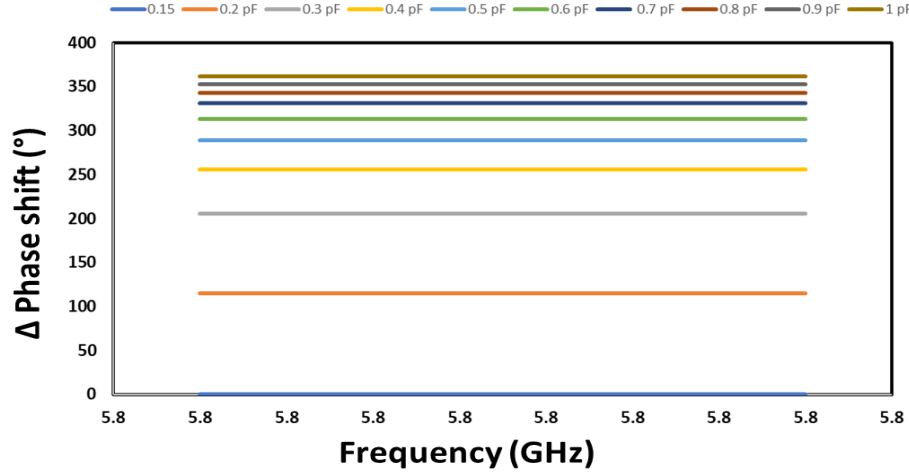
Fig 3.9: Delta phase shift at 5,8GHz with 0.15pF acting as reference value

The simulation allows for rapid modelling of the proposed phase shifter and verification that 360° phase shift could be achieved for the calculated series LC resonant circuits. As the dielectric constant and thickness of the phase shifter substrate were known the values proposed in the above circuit can be converted into a microstrip circuit and modelled in the CST studio suite.

Matching the coupler consists of two quarter wavelength lines at 50Ω and quarter wavelength lines at 35.3Ω [39]. To calculate the impedance, Equations 3.9 – 3.12 were used where W is the microstrip width, H is the substrate thickness and ε_r is the dielectric constant of the material [170]:

If $(\frac{W}{H}) < 1$:

$$\varepsilon_{eff} = \frac{\varepsilon_r+1}{2} - \frac{\varepsilon_r-1}{2}\left(\frac{1}{\sqrt{1+12\left(\frac{H}{W}\right)}} + 0.04(1 - (\frac{W}{H}))^2\right) \tag{3.9}$$

$$Z_0 = \frac{60}{\sqrt{\varepsilon_{eff}}}\ln\left(8\left(\frac{H}{W}\right) + 0.25\right) \tag{3.10}$$

If $(\frac{W}{H}) > 1$:

$$\varepsilon_{eff} = \frac{\varepsilon_r+1}{2} - \frac{\varepsilon_r-1}{2\sqrt{1+12\left(\frac{H}{W}\right)}} \tag{3.11}$$

$$Z_0 = \frac{120\pi}{\sqrt{\varepsilon_{eff}}\left((\frac{W}{H})+1.393+\frac{2}{3}\ln(\frac{W}{H}+1.444)\right)} \tag{3.12}$$

Based on the above calculations and FR-4 with a thickness of 0.8mm the calculated microstrip widths were 1.625 and 2.6mm, respectively. To reduce the

reflection loss, a step-up matching network was employed for each complex load, whilst the inductance was calculated with the following equation:

$$L_{ms} = 0.0508L \left(\ln\left(\frac{2L}{W+H}\right) + 0.5 + 0.2235\left(\frac{W+H}{L}\right) \right) \qquad (3.13)$$

Where L_{ms} is the inductance of the microstrip in microhenries and L is the length of the microstrip. Figure 3.10 shows the calculated values from Figure 3.9 converted in a 3D microstrip model.
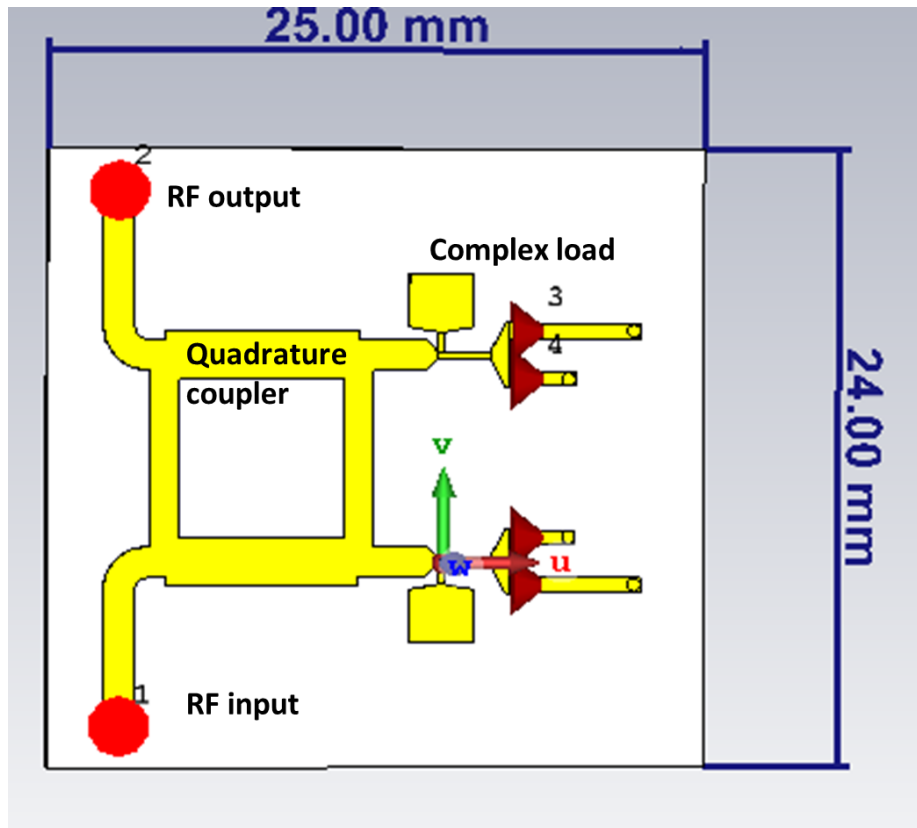
Fig 3.10: Microstrip modelled phase shifter operating at 5.8 GHz

The varactor diodes are modelled as a discrete port in which a schematic co-simulation is run in which the discrete ports are modelled as capacitors with a parametric sweep performed between $C_{min} = 0.15pF$ and $C_{max} = 1pF$. Figure 3.10 shows the simulation set up alongside the 3D simulated phase vs capacitance response in which 360° phase tuning can be achieved.

As the simulation produced satisfactory results for our design criteria, the next step was to fabricate the prototype phase shifter. Fr4 with 35µm copper cladding was obtained, along with PCB transfer paper. The 3D design was converted into an image in which the 2D projection of the device were printed onto the transfer paper using a laser printer. Placing the transfer paper onto the Fr4 and applying heat at 180° for several

minutes allows for the transfer of the structure onto the copper cladding as shown in Figure 3.14.

(a)

(b)
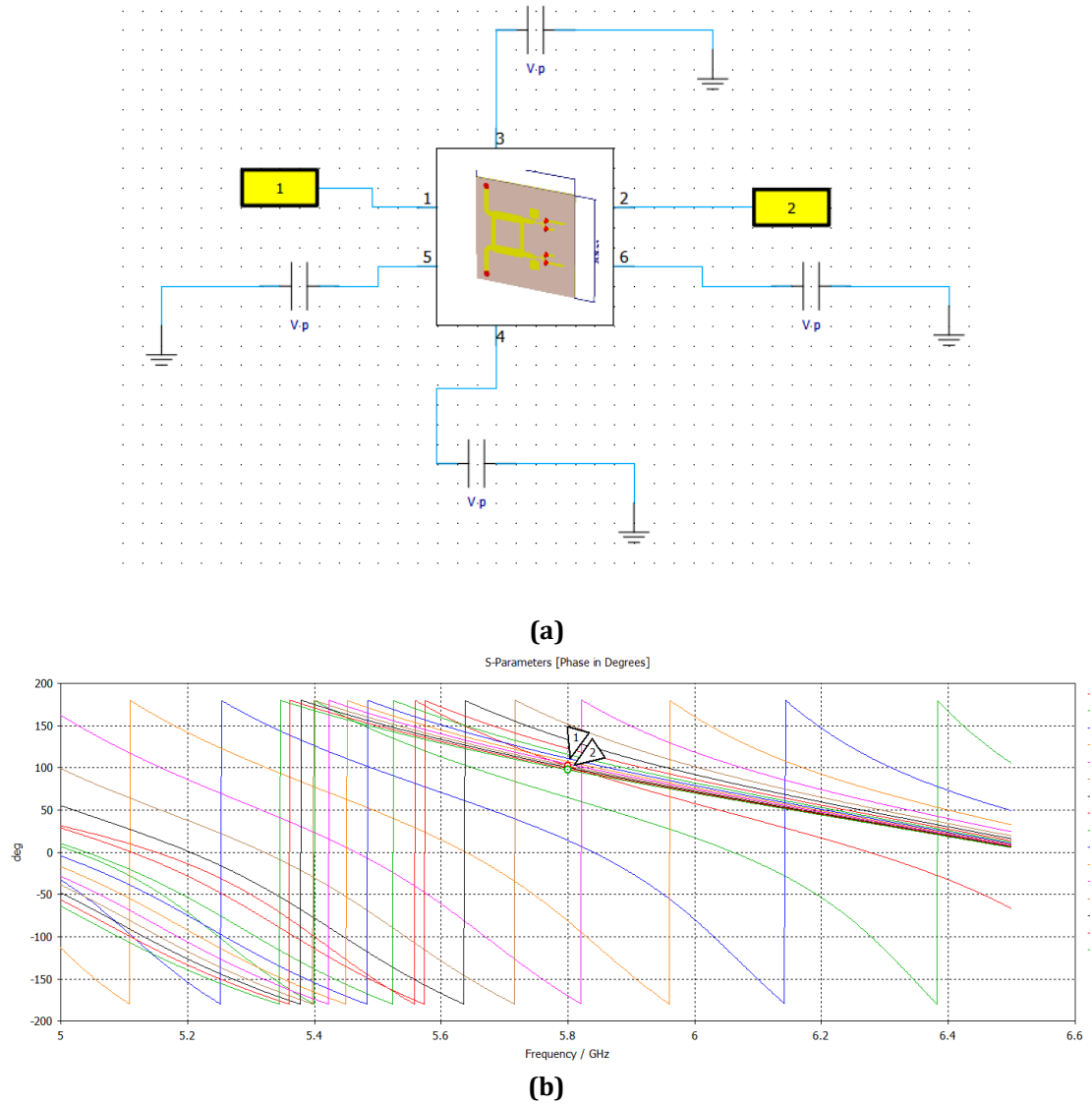
Fig 3.12: (a) Co-simulation of phase shifter with changing capacitance between $C_{min} = 0.15pF$ and C_{max} = 1pF. (b) Simulated phase shifts where 1 = C_{min} and 2 = C_{max} (c) delta phase shift at 5,8GHz with 0.15pF acting as reference value
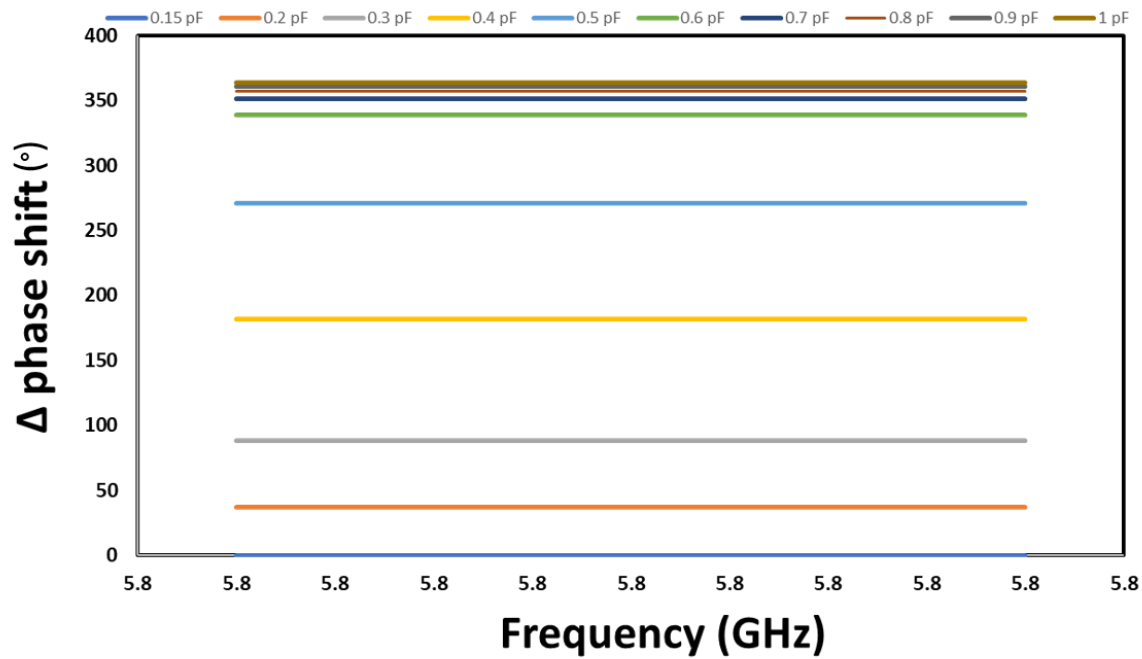
Fig 3.13: delta phase shift at 5,8GHz with 0.15pF acting as reference value
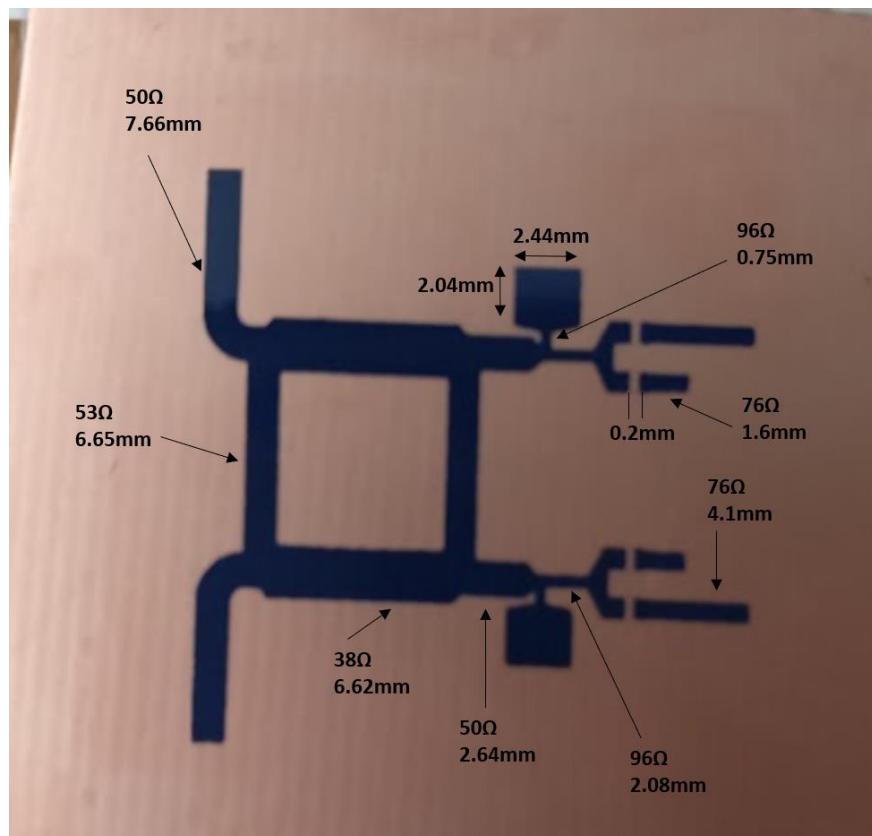
Fig 3.14: Phase shifter mask applied to copper cladding of Fr4 using heat transfer method.

Using ferric chloride ($FeCl_3$) the copper cladding could be etched away leaving the substrate and copper pattern of the mask unetched. The mask could then be removed using acetone to clean the circuit board. Using a 0.2mm drill bit, vias could be drilled into

the inductors of the complex load to connect to the ground plane with a small piece of wire. Finally, varactor diodes were soldered onto the circuit along with SMA connectors for measurements. Figure 3.15 shows the fabricated prototype of the phase shifter.
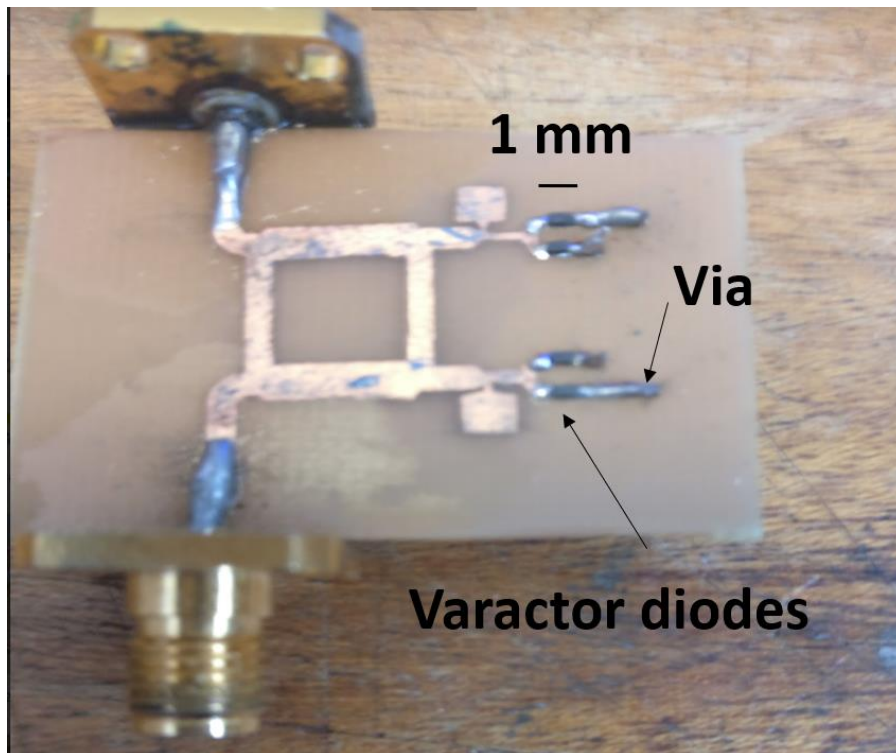
Fig 3.15 Fabricated prototype of phase shifter on Fr4 substrate.

Wires were soldered to the complex load to place the varactor didoes under reverse bias. By changing the voltage applied to them, a phase shift was observed when measuring the S21 phase using a vector network analyser. Figure 3.13a demonstrates measured and simulated return loss of the phase shifter, whilst 3.13b shows the measured phase shift. Figure 3.17 shows delta phase shift in which tracks the differences in phase in comparison to 0V bias.
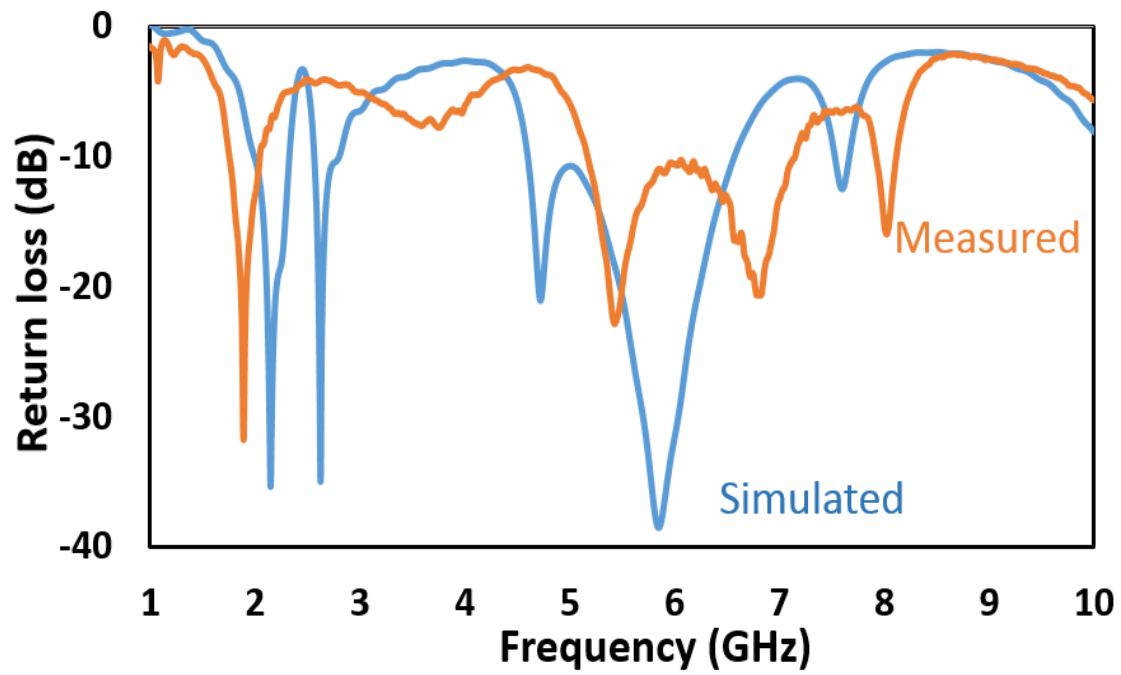
(a)
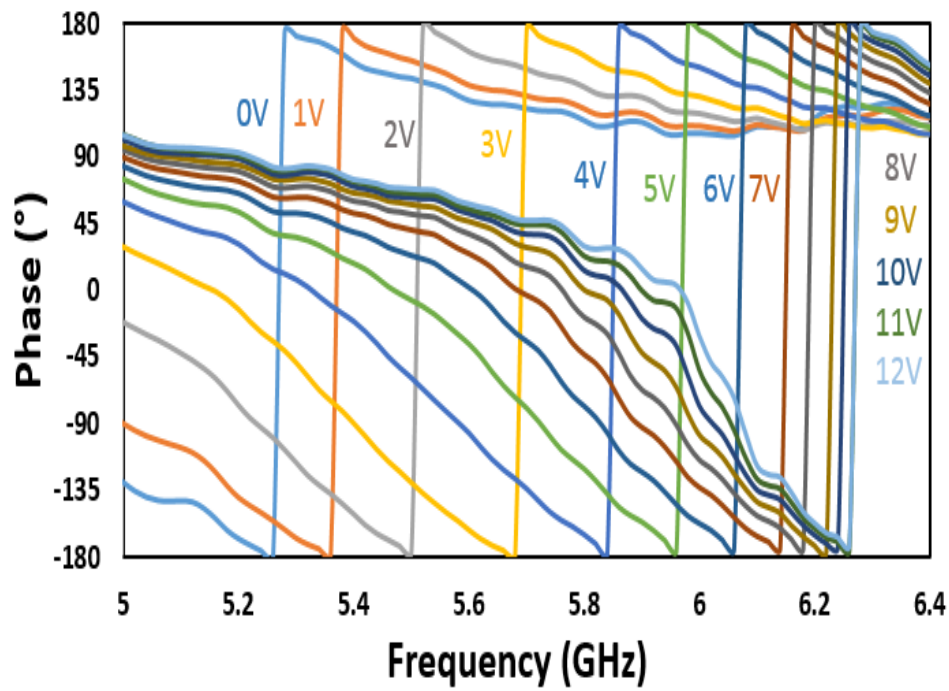
(b)

Fig 3.16: (a) Measured vs simulated results of the return loss for the phase shifter (b) measured phase shift for C_{max}, C_{min} and values in between.
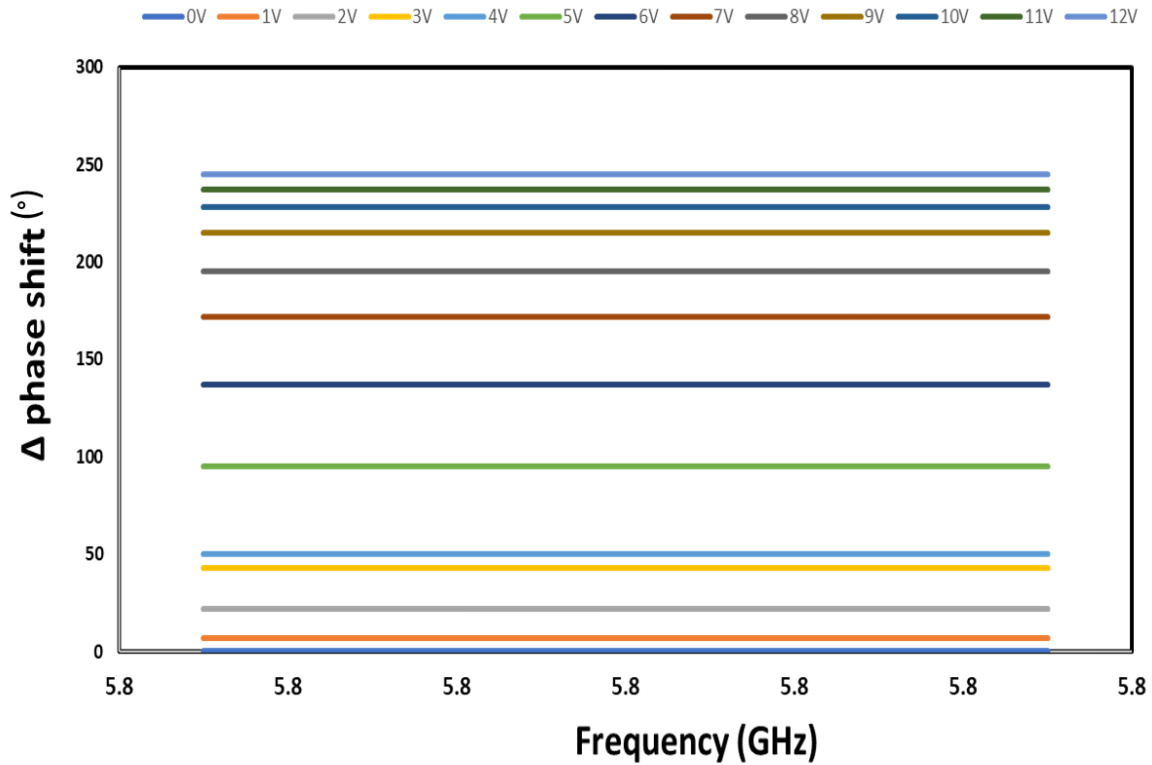
Fig 3.17: Delta phase shift at 5,8GHz with 0V acting as reference value

A slight deviation between measured and simulated results was observed. The shift in resonance is thought to be due to tolerances in fabrication and a slight change in the dielectric constant of the material, whilst the phase shift variation is due to etching the circuit, in which the inductor values were slightly modified. Nonetheless, a 300° phase tune range was achieved which provided adequate phase shift for the beam scanning application.

3.3.2 Antenna array design

Electronically scanned antenna arrays are typically limited to 120° scanning in azimuth and elevation; however, such scanning capabilities provided sufficient coverage for localisation of the radio telemetry tag. Referring back to the design criteria, the role of the antenna was to provide sufficient detection range to provide meaningful tracking data of tagged bees; ensuring accurate localisation by suppressing side lobes as much as possible and being compact enough to mount to a UAV.

To increase the gain, thus increasing the link budget of the system, an antenna array would need to be implemented, which typically consists of 2^N elements. More elements generally result in a higher antenna gain, however, since each antenna element requires an individual phase shifter, the cost of the system would significantly increase

with increased number of elements. Additionally, to perform scanning in azimuth and elevation planes a planar array needed to be employed. In order to create a compact device microstrip patch antennae were selected due to the possibility to control their wavelength with the choice of dielectric substrate [171]. By definition, the signal wavelength is:

$$\lambda = \frac{c}{f} \tag{3.13}$$

where c is the speed of light in a vacuum and f is the frequency. Utilising dielectric substrates and a microstrip antenna, the wavelength is:

$$\lambda = \frac{c}{f\sqrt{\varepsilon_{eff}}} \tag{3.14}$$

This often results in a much smaller wavelength than in free space, allowing for a much smaller antenna. Additionally, microstrip antenna arrays have a favourable fabrication process and low cost compared to other directional antennas such as Yagi and horn antennae.

Trade-offs between the antenna gain vs size vs fabrication costs lead to the onerous task of finding the optimal antenna elements. A 2x2 element planar antenna array was unable to provide sufficient gain and side lobe suppression, whilst an 8x8 element array would not be sufficiently compact to mount on a UAV and expensive to fabricate. Therefore, a 4x4-element array was chosen in an attempt to provide sufficient detection range between transmitter and receiver.

A fundamental limitation with microstrip antennae are their lower gain and narrow bandwidth [172]. Microstrip patch antennae consist of a dielectric substrate with a ground plane on the opposing side, as depicted in Figure 3.14. Multiple attempts to further increase the gain and bandwidth of patch antennas have focussed on stacked structures [173]. The use of two substrates and an air layer have shown that the gain can be increased significantly by tuning the thickness of the air layer. To investigate the benefits of stacked antenna arrays, a comparison between the performance of a single and dual layer pin fed patch antenna was drawn using CST. Figure 3.18a shows the antenna structure whilst 3.14b shows the simulated results for antenna gain and efficiency.

(a)

(b)
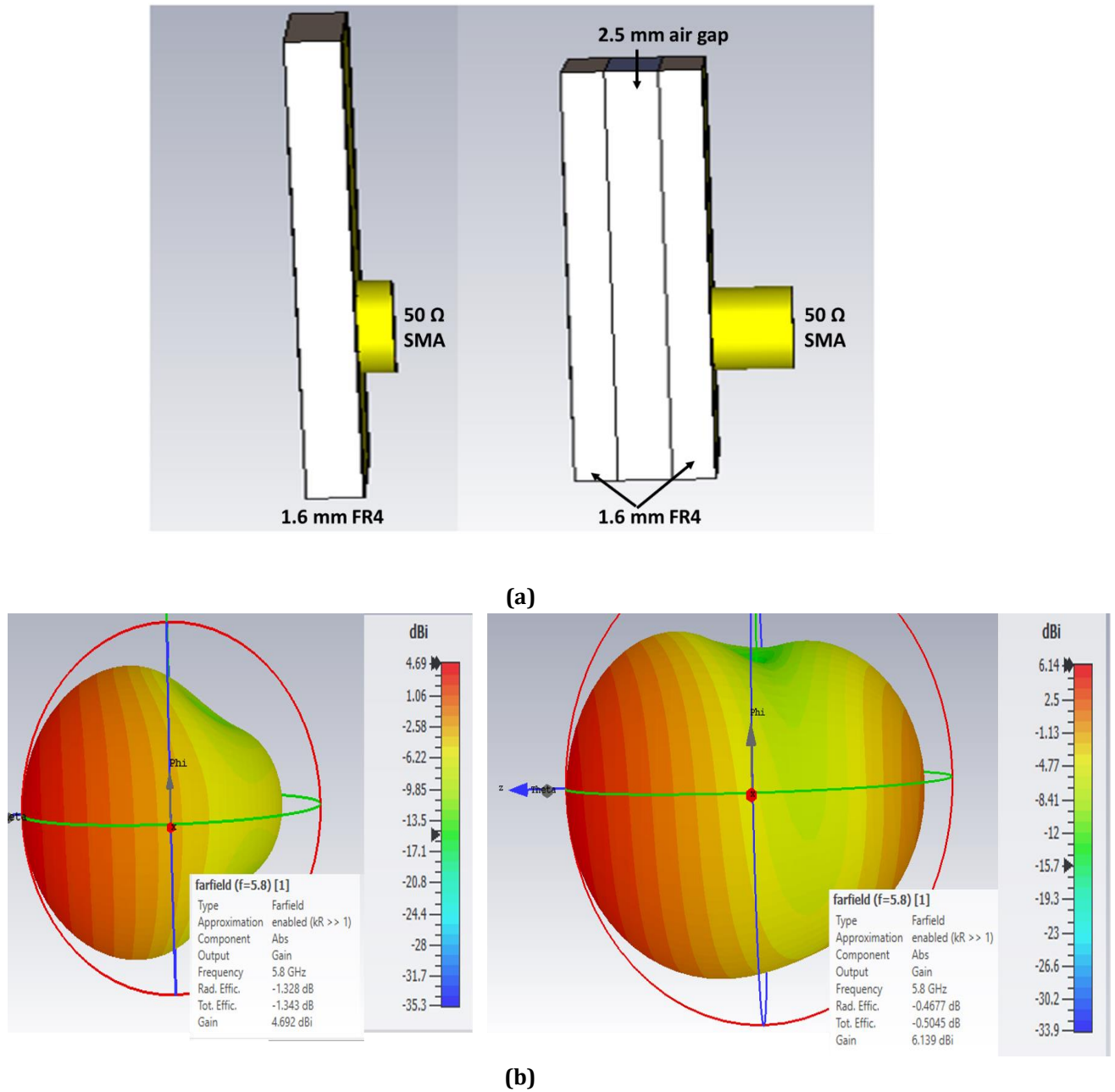
Fig 3.18: (a) Architecture for a single layer vs stacked layer pin fed patch antenna (b) gain and efficiency comparisons of stacked vs single layer patch

It can be observed in Figure 3.19 that a stacked structure is capable of providing superior gain and efficiency, thus providing a feasible solution for increasing the gain of the antenna array without the need for increasing elements. The increased thickness between antenna and ground plane can also increase the bandwidth of the antenna. When multiple layers are introduced, the geometry of the antenna has to be modified. For single layer and multilayer structures, the length and width of a patch antenna are calculated by the Equations 3.15 and 3.16 [174]:

$$Width = \frac{c}{2f_o\sqrt{\frac{\varepsilon_{eff}+1}{2}}} \qquad (3.15)$$

$$Length = \frac{c}{2f_o\sqrt{\varepsilon_{eff}}}$$ (3.16)

Where f_o is the operation frequency. As multilayer patch antennae offer superior performance over single layers in terms of gain and efficiency, the following design rules for the antenna array were set out:

- Design single element patch antenna resonating at 5.8 GHz
- Calculate appropriate spacing to eliminate any grating lobes
- Treat single element as a unit cell for frequency domain simulation. Analyse the change in active element impedance per scan angle of interest and ensure return loss greater than -10 dB for all scan angles
- Review change in active element impedance to eliminate any scan blindness
- Build full array and simulate in time domain to obtain reference solution

The first step was to design a pin fed patch antenna, which resonates at 5.8 GHz. Two Fr4 substrate layers ($\varepsilon_{r=4.3}$,$thickness = 1.6mm$) along with an air gap ($\varepsilon_{r=1}$,$thickness = 0.5mm$) where used to form the multilayer stayed substrate for the patch. Using equation 3.15 and 3.16 and, the following length and width for the patch antenna were determined to be 15.92 mm and 11 mm, respectively. Figure 3.15a shows the antenna structure, whilst 3.19 demonstrates the return loss.
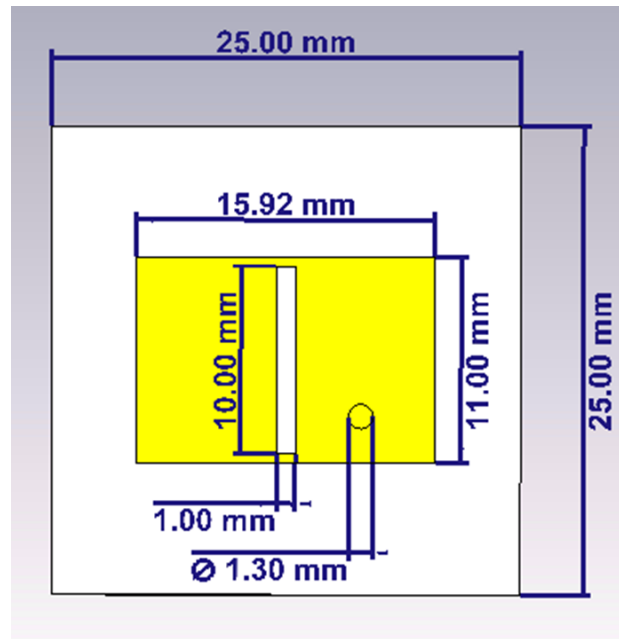
(a)
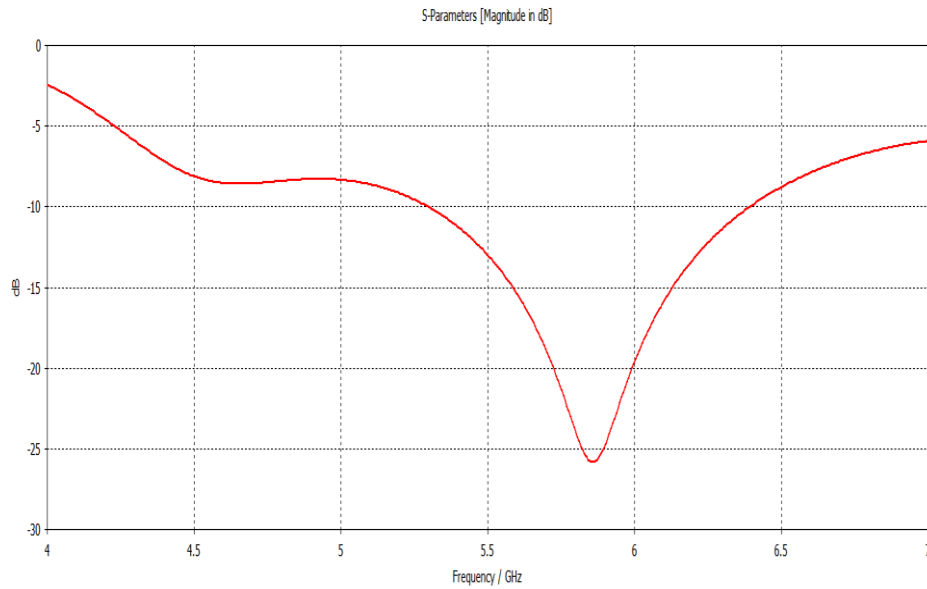
(b)

Fig 3.19: (a) Architecture for stacked layer pin fed patch antenna (b) simulated return loss for single element

Appropriate spacing was determined to prevent grating lobes at higher scan angles. Grating lobes occur when the main beam is steered too far and the main beam appears on the wrong side of the antenna with an equal amplitude to the main beam. Such a problem would completely void the system of being capable to perform AoA estimates. Grating lobes depend on the spacing between elements (d_{max}) [163] and can be:

$$d_{max} = \frac{\lambda}{1+sin\theta} \tag{3.17}$$

Figure 3.20 outlines the introduction of grating lobes at higher scan angles.
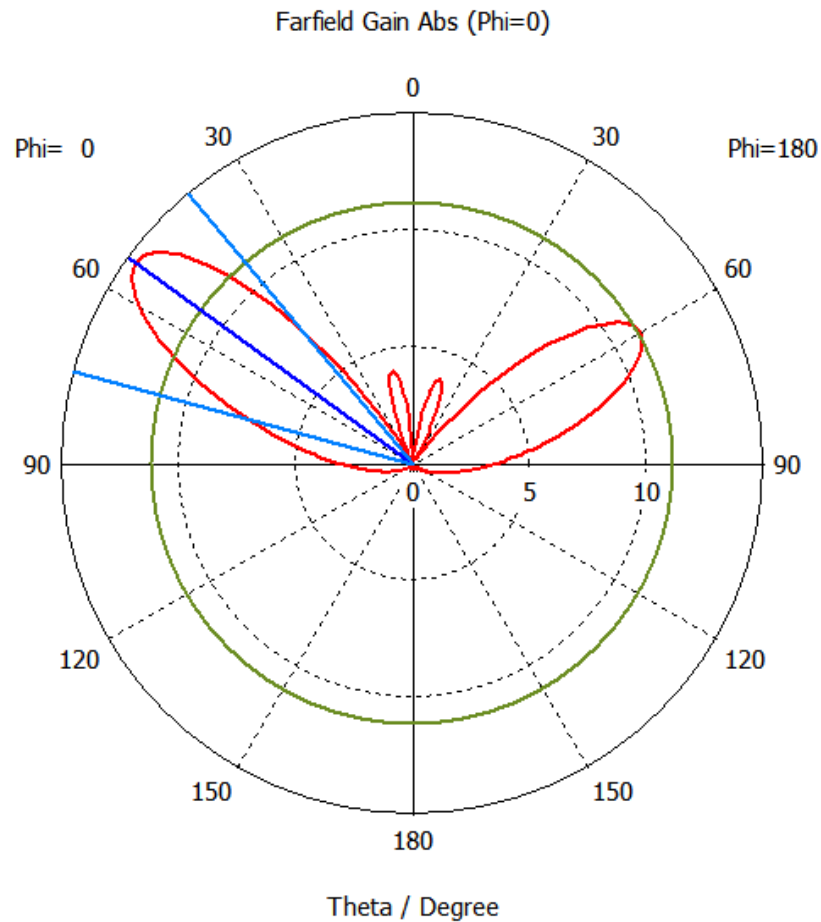
Fig 3.20: Introduction of grating lobes at higher scan angles

To comfortably achieve a scanning range of +/-50°, a maximum spacing of 0.5λ was determined from equation 3.17. A unit cell simulation considering 4x4 elements was set up as shown in Figure 3.21a, whilst 3.21b reviews the change in active element impedance. With the spacing between elements set to 0.5 λ ,it can be seen that for all angles of interest between +/-50° in azimuth and elevation, a return loss greater than -10dB can be achieved, signalling satisfactory performance for the phased array antenna in terms of its ability to receive signals at all angles of interest. Higher spacing between elements resulted in large impedance mismatch between individual elements at higher scan angles, thus, resulting in a poor return loss (>10dB).
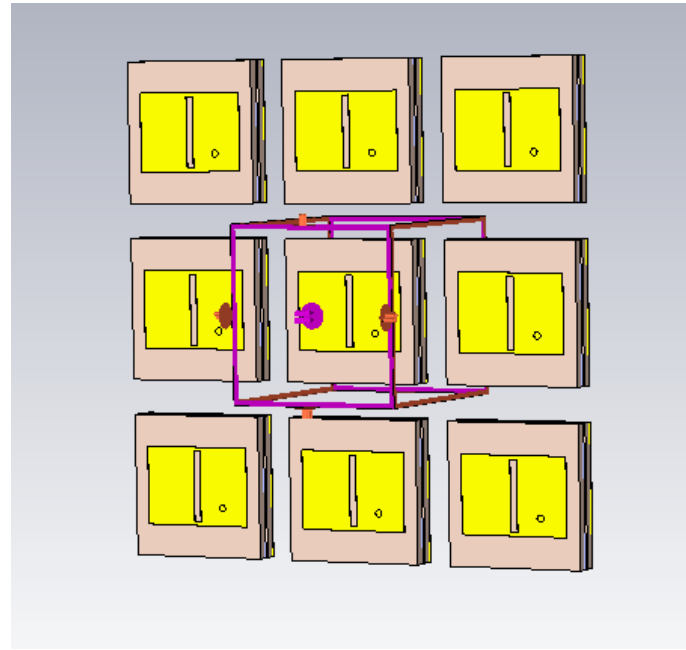
(a)
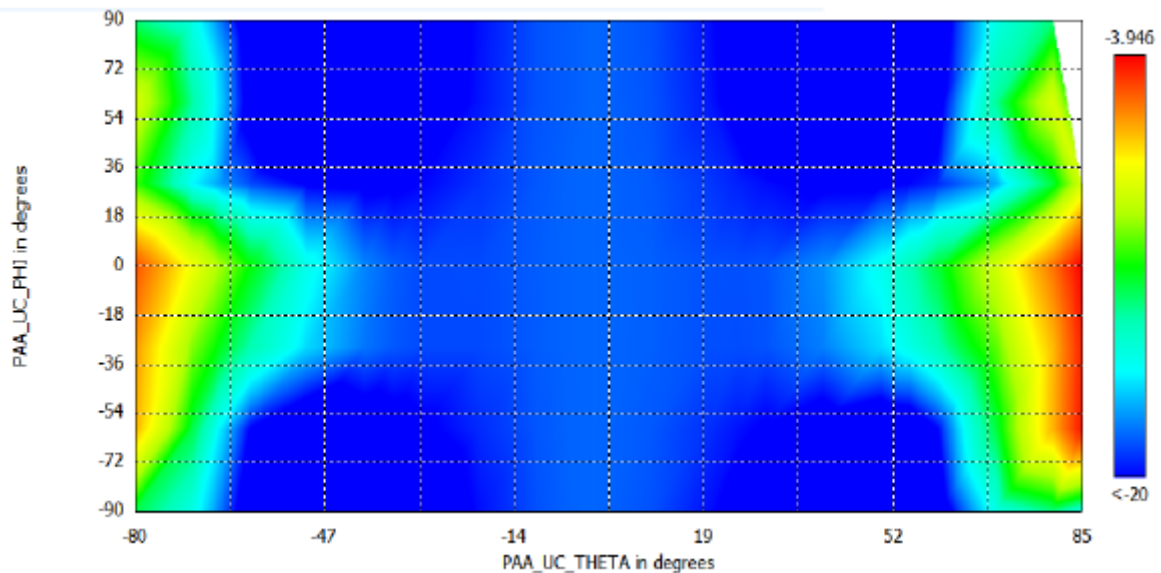
(b)

Fig 3.21: (a) Unit cell simulation set up (b) return loss for scanning azimuth and elevation

Due to the surface wave coupling which exists between each patch antenna, scan blindness can be introduced at various scan angles. We can define scan blindness as the angles in which the magnitude of the reflection coefficient is unity. In an infinite array this cannot be achieved, however, a large deviation in the input impedance can cause a significant decrease of the antenna's radiation pattern, thus outlining the importance of analysing effects from mutual coupling as shown in the simulation (Figure 3.21b).

As the effects of mutual coupling demonstrated satisfactory performance, the next stage was to build a full 3D model in order to analyse the radiation pattern and efficiency at 5.8 GHz. Firstly, it is important to study the degradation of the radiation

pattern as the scan angle increases. Figure 3.22a illustrates the 3D model created to analyse the degradation in radiation pattern with element spacing of 0.5λ, the results are displayed in Figure 3.22b. Waveguide ports were used to excite each individual antenna port in which the phase could manually be defined. Using the theory proposed in Equation 3.4, the phase shift required between elements to achieve 1° change in the beam direction was calculated to be 5°. As the proposed phase shifter can provide 300° phase shift, the system is capable of scanning its intendent range of +/-50°. Figure 3.22c shows the change in surface current between elements, showing the antennae being excited at different phases to achieve beam steering.

(a)   (b)

(c)
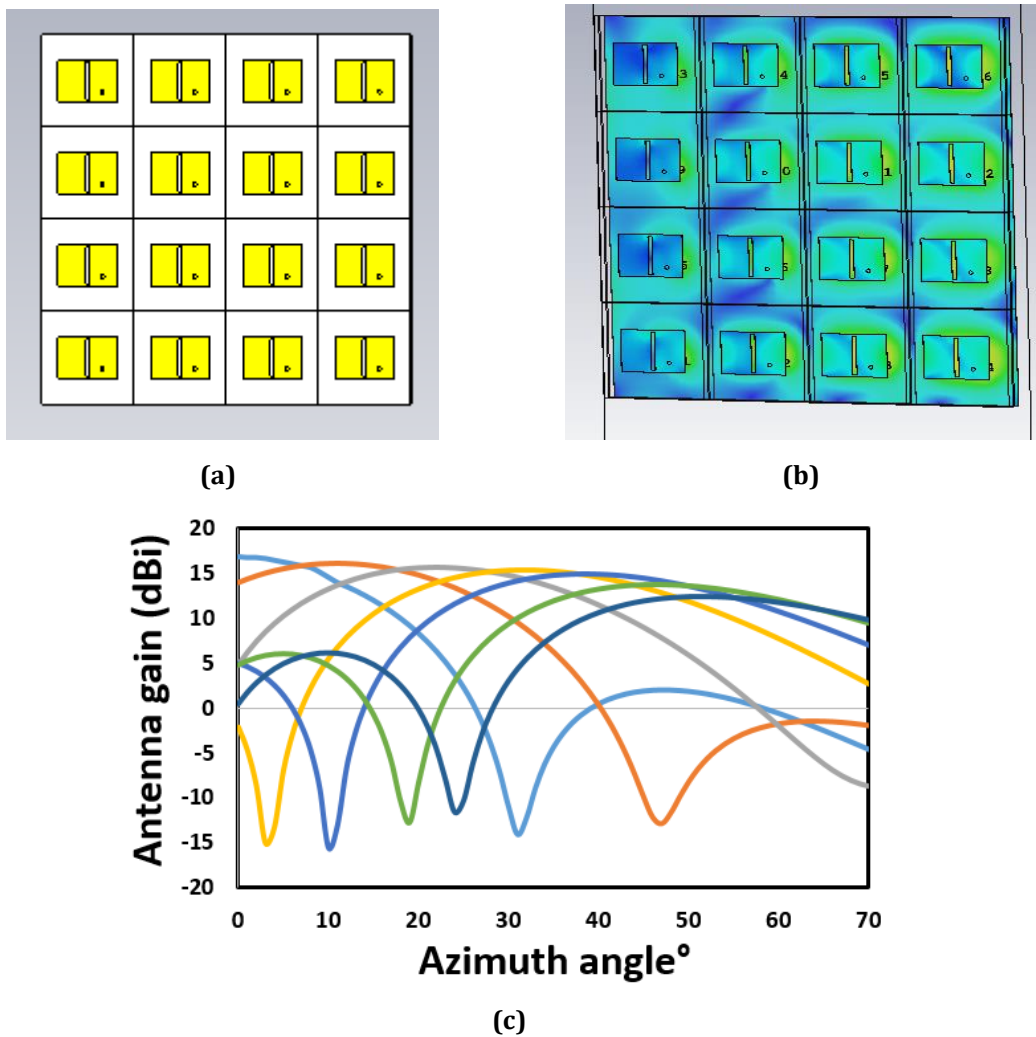
Fig 3.22 (a) Simulation model of 4 x 4 element phased array, (b) surface current distribution of phased array and (c) degradation of antenna gain with increased can angle

The gain at the broadside of the antenna is both a function of the individual element gain and the number of elements [175]. The aperture gain is calculated by:

$$G_A = 4\pi \frac{A\eta}{\lambda^2}$$

(3.18)

Where A is the aperture area and η is the efficiency. Aperture is essentially a measure of the antenna's effectiveness of receiving the power of an RF signal. As the scan angle increases, the aperture area of the antenna decreases thus providing a degradation of the gain. Typically, the gain degrades at the cosine of the scanning angle. This is shown in Figure 3.18b which simulates the scanning of the beam from broadside to 90 degrees. At 60° half power is achieved, illustrating the reason why phased array antennae are limited to a 120° scanning range.

The next step was to fabricate the antenna array as modelled in Figure 3.23a. The same fabrication process as the phase shifter was applied, and a mask of the antenna array was generated and transferred to Fr4 with a thickness of 1.6mm. An additional double sided Fr4 substrate was etched on to a single side to provide the ground plane for the antenna. An SMA connector was soldered onto the input of each antenna after drilling a hole for the signal pin to feed the radiating antenna. During soldering a 0.5mm thick foam layer was applied to the substrate's corners to ensure the target air gap was achieved. Figure 3.23 outlines the fabricated phased array alongside its measured vs simulated return loss.
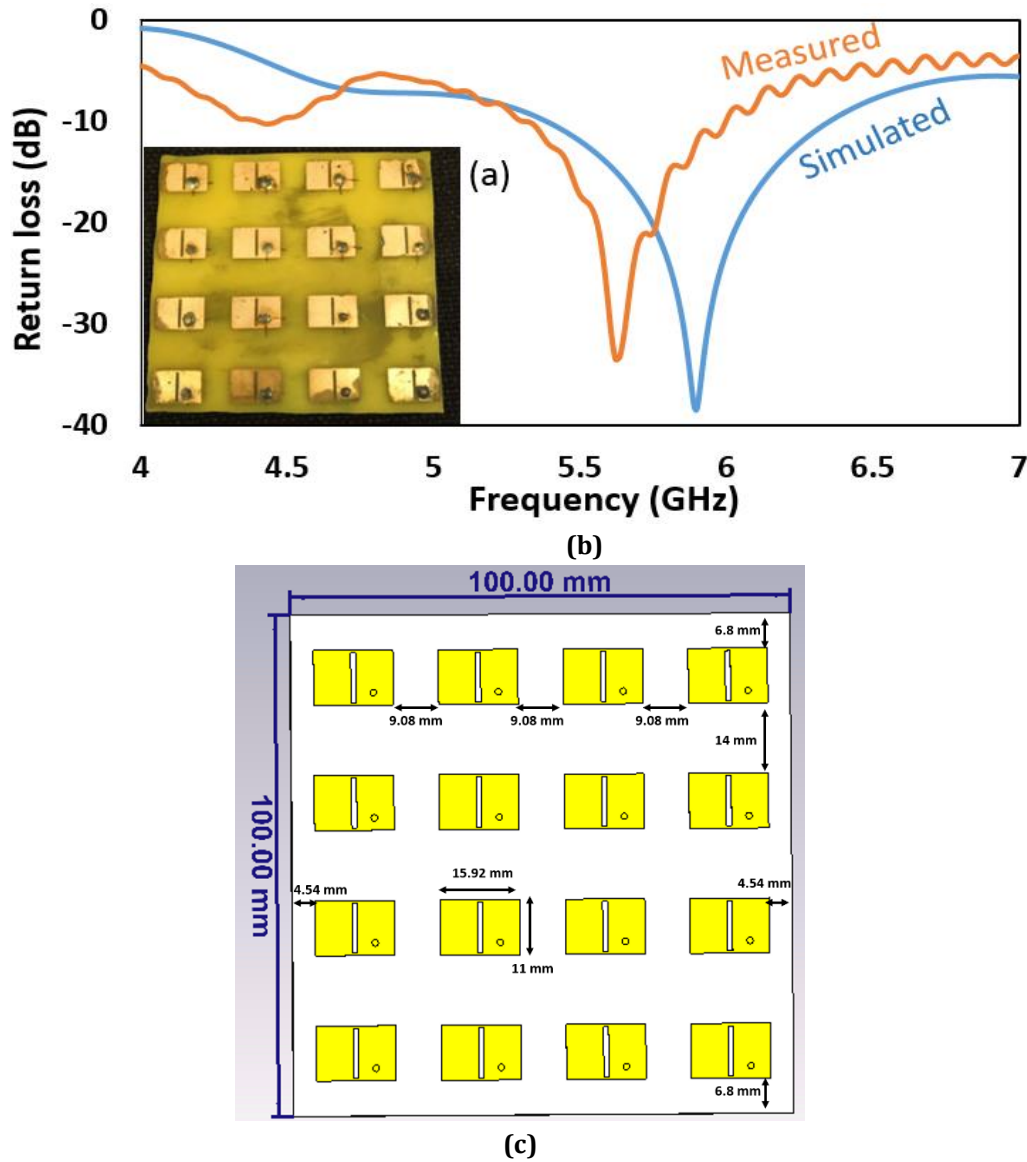
Fig 3.23: (a) Fabricated phased array antenna (b) Measured vs simulated return loss (c) diagram showing diagram of antenna size and spacing between elements

The shift in frequency is believed to be due to tolerances associated with fabrication process. Firstly, the air gap between the substrates could not be guaranteed have a uniform gap of 1.6mm throughout the antenna. Additionally, the patch antennas were fed by drilled vias to connect the signal pin of the SMA. Each SMA was hand soldered which could not be accurately simulated accounting for small variations in feed location and solder volume. The use of female SMA's to excite each antenna element allowed for easy SMA (Male SMA) attachment in which a phase shifter could be attached to each antenna element in the array as shown in figure 3.24. Using the phase vs capacitance relationship for the phase shifter (Figure 3.17) and by calculating the required phase shift for each from Equation 3.4, which was also verified in CST, the phased array could be scanned in each desired direction. (see Appendix A).
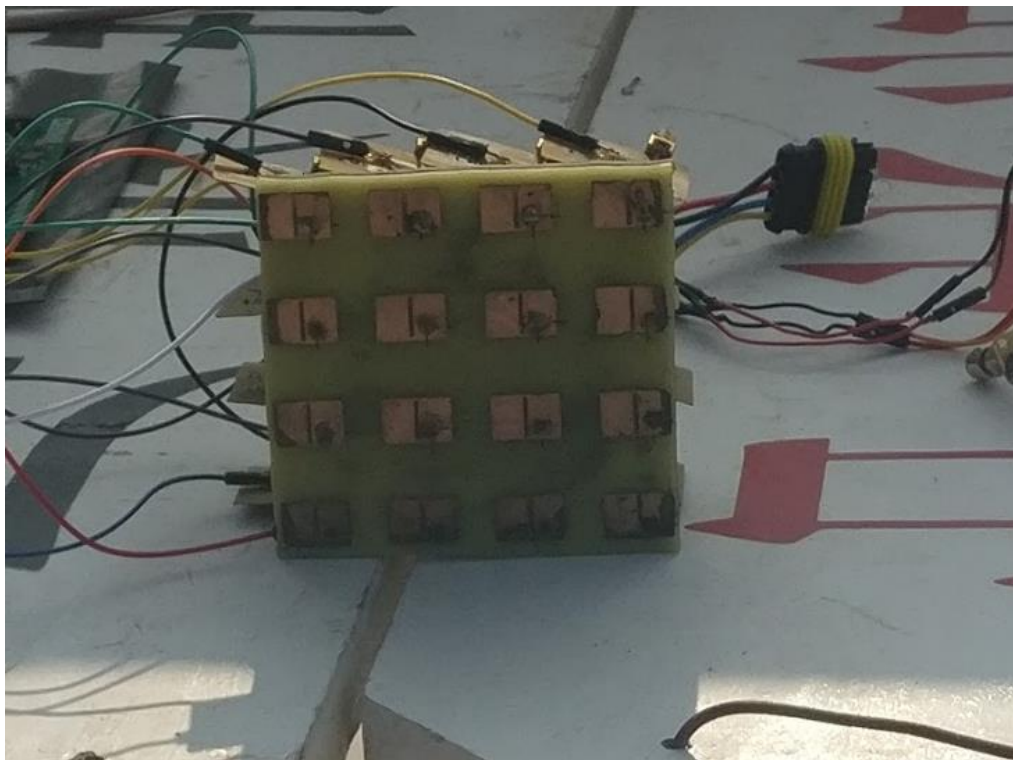
(a)
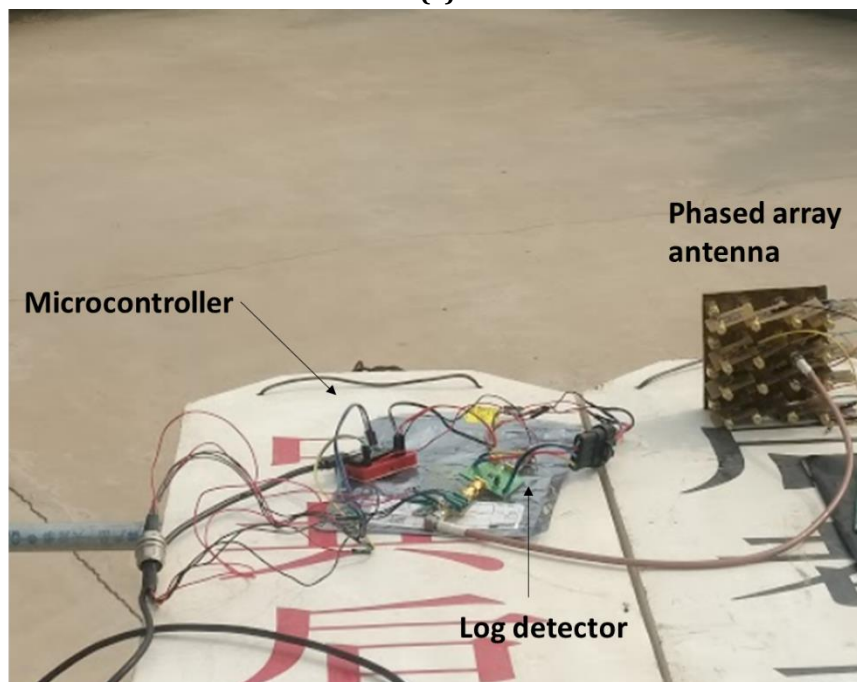
(b)

Fig 3.24: (a) Phase shifter attached to each element of the antenna array (b) Phased array antenna, microcontroller and log detector used to take received signal strength measurements

Before testing the system on tagged insects (Chapter 4), a study to determine the maximum range between the tag and the phased array at broadside and its maximum scan angle was performed. The combination of a logarithmic detector [176] and microcontroller [177] allowed for measurements of the received signal strength for the phased array antenna (Figure 3.24b). As the logarithmic detector transduces the received

signal power into a voltage, a processing unit can record the power at x meters from the antenna to determine the maximum operational range of the system. Using a handheld transmitter operating at 5.8 GHz with 11 dBm output [178], we were able to determine the received power as a function of the transmitter receiver distance (Fig 3.25). The receiver range could then be extrapolated using a power output comparable to the one generated by the bee as presented in Chapter 2. The phase array was set to scan 0° in azimuth and elevation. Walking backwards in a straight line and taking power readings every 2m, the maximum operation distance of the system was determined.
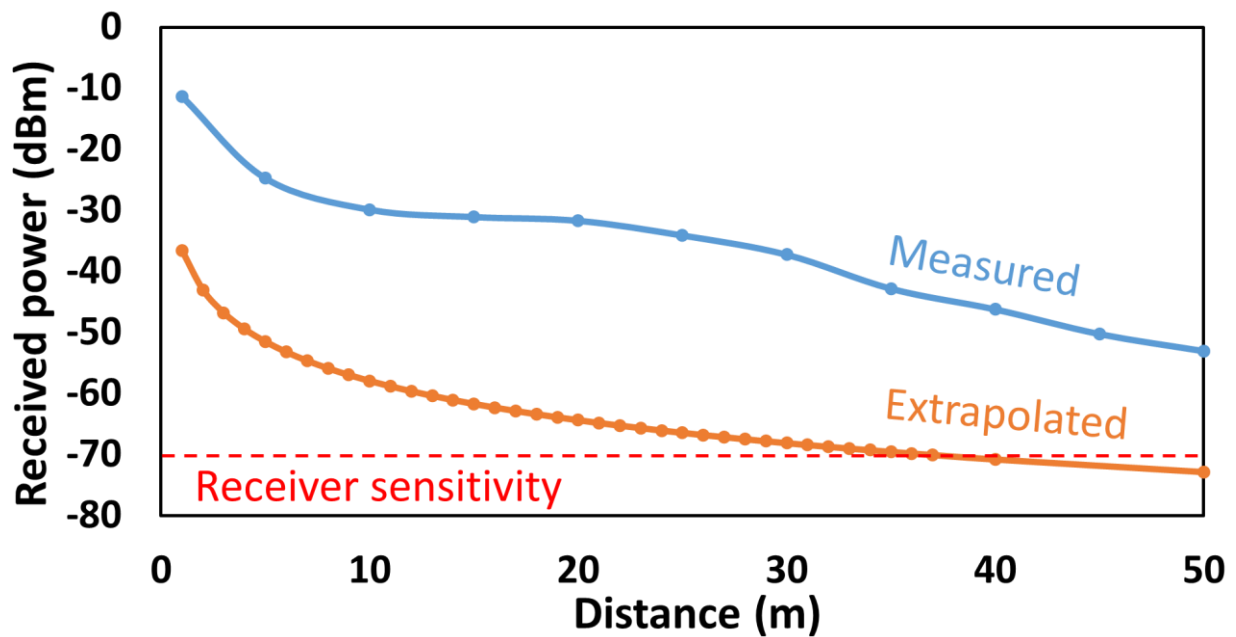
Fig 3.25: Measured received signal and the extrapolated data for Tx power comparable to the bee.

With a receiver sensitivity of -70 dBm, which corresponds to an output voltage of 2V, the receiver system is capable of operating within 20m of the hive or nest. This outlines the fundamental maximum range in which the antenna can be placed from the hive or nest. As this is the maximum distance, issues such as signal attenuation, multipath and impedance mismatch occur. Therefore, the ideal distance is recommended to be less than 20m where possible.

This chapter summarised typical positioning schemes widely implemented for the localisation of RF sources. Due to the high gain and compatibility with a single receiver, RF localisation via AoA was deemed to be the most efficient solution to our proposed problem. Comparisons between mechanically and electrically scanned antennae were drawn, in which fundamental limitations of mechanical scanning were discussed, outlining the need for an electrically scanned antenna system. Fundamental

concepts behind the design of a phased array antennae were discussed and implemented to design and fabricate a phased array antenna capable of scanning +/-50° in the azimuth and elevation plane. The effects of mutual coupling were analysed to ensure zero scan blindness, whilst optimal inter-element spacing was determined to eradicate grating lobes. Experiments were conducted to determine maximum operational range of the antenna to successfully detect tagged bees.

Chapter 4. Power based localisation system and tracking results

The following chapter discusses how the antenna designed in Chapter 3 was applied to an RF receiver system to be able to estimate the bearing of the self-powered radio telemetry tag (Chapter 2). The RF system presented herein, describes the system design, implementation and results obtained. Further comparisons are made of the systems performance with respect to current state of art.

4.1 RF system design

In order to utilise the phased array antenna for the application of AoA estimation, a RF system and microcontroller were designed and implemented for autonomous and accurate operation. The system needed to be as compact and lightweight as possible to allow for integration with a UAV. Figure 4.1 outlines a block diagram of the proposed system in which the optimal components were identified and trade-offs between device compactness and size were made.
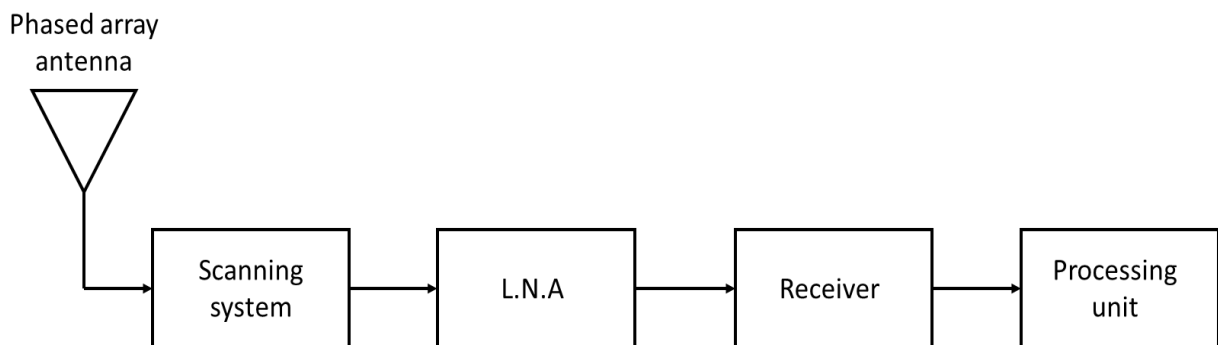
Fig 4.1: Block diagram of proposed AoA system

Whilst the antenna and scanning system have previously been proposed, a low noise amplifier (L.N.A), RF receiver and processing unit suitable for the application needed to be identified. Current available systems, [1, 2] are based on a similar approach to Figure 4.1, but operate at lower frequencies and their bulkiness significantly impairs technical integration to the drone, as well as substantial time delays for positional updates. Firstly, a suitable receiver system to detect the received signal strength is

required. The use of a spectrum analyser would allow for easy identification of the received signal strength at 5.8 GHz, however, size, sweep time and software limitations would impair the ability to have a lightweight and compact solution. Additionally, the use of a single power supply would facilitate system miniaturisation potential. The use of a logarithmic detector can be implemented to convert RF signals at the input into a proportional DC voltage at its output port. Such devices can generate a high dynamic range and conversion accuracy, whilst achieving a compact and easy to operate configuration as they require a single voltage of either 5V or 3.3V [181]. Typically, logarithmic detectors function by using a series of amplifiers and diodes. As the input power into the device is increased, the amplifiers sequentially move into saturation mode, providing clipping to the signal. As a result of clipping, an accurate approximation of the logarithm function is obtained. Figure 4.2 outlines a typical schematic of a logarithmic detector in which the output of a series of detectors are summed and converted into a voltage to drive the output port.
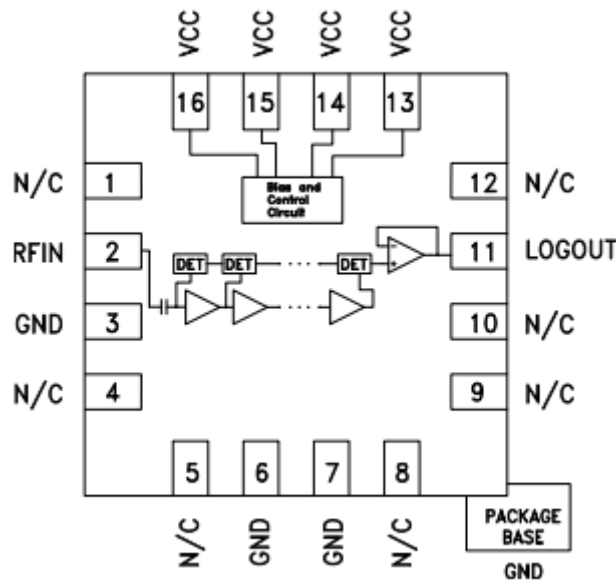
Fig 4.2: Functional diagram of logarithmic detector [176]

By connecting the array to a logarithmic detector, a voltage level can be obtained corresponding to the received power at 5.8 GHz. Due to the high dynamic range and simple operation requirements, the HMC602LP4 logarithmic detector was chosen [176]. Figure 4.3a depicts the relationship between the input RF power and output voltage of the detector, whilst Figure 4.3b illustrates Log (Vout) vs frequency over input. This highlights a disadvantage for AoA estimation, as due to the non-linearity in the receiver's response there are harmonics that can result in spurious signals of detectable power at frequencies other than 5.8 GHz. For noisy environments where interference could be present, the use

of a bandpass filter would allow the system to operate at 5.8 GHz and eliminate other harmonics.

(a)

(b)
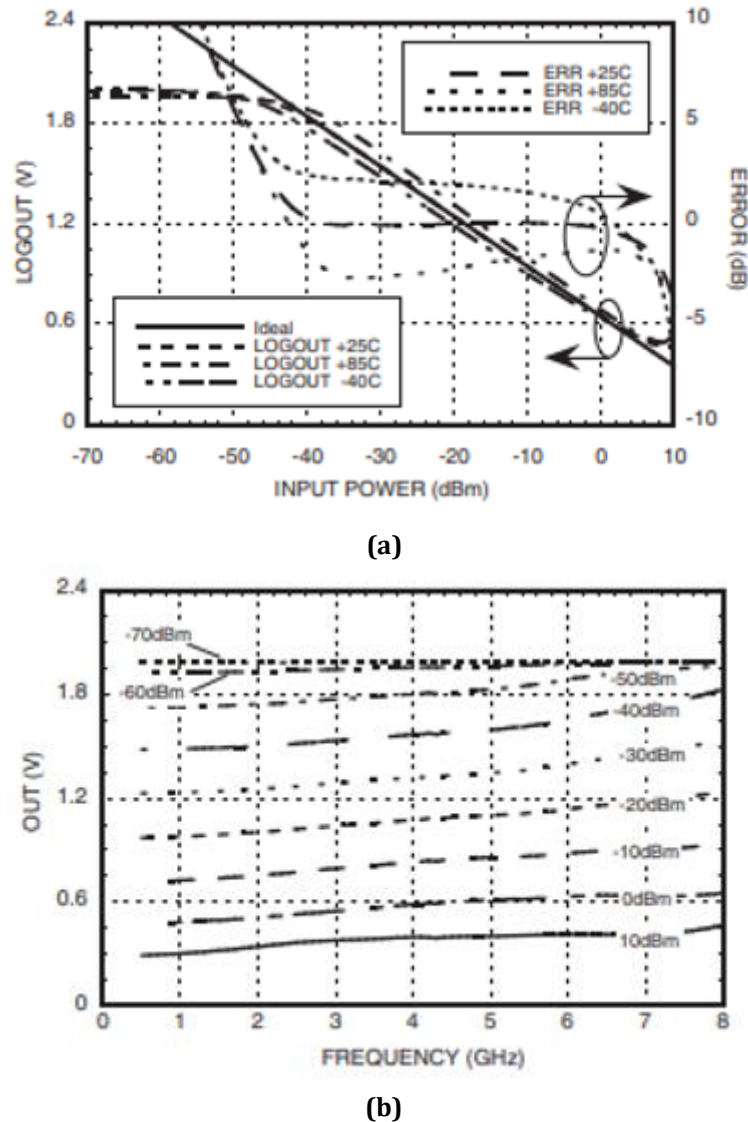
Fig 4.3: (a) LOGOUT voltage and error vs input power at 5.8 GHz (b) LOGOUT vs frequency for various input powers [176].

As discussed in Chapter 3, a 20m detection range could be achieved with a receiver sensitivity of -70 dBm, which is dictated by the chosen logarithmic detector. Typical operation and power readings are likely to take place between -50 and -70 dBm (Figure 3.2), however, Figure 4.3a shows very small voltage changes for various input powers and errors, which could lead to misleading results if the sampling from the microcontroller is unable to distinguish between the small changes. A processing unit with precise voltage sensing capabilities can be used to overcome this, whilst the implementation of an L.N.A before the receiver stage would acts as a solution as at higher power levels a greater difference between input power and output voltage is present. Low

noise amplifiers with simple configurations, ease to power from a single supply, high gain and low noise figure and widely commercially available were identified as suitable options for the receiver system [5, 6]. Consequently, typical operation can be altered such that the performance of LOGOUT vs input power is linear, producing a reduced error, leading to improved system precision. The LNA has the potential to increase operational range, allowing the implementation of a processing unit capable of precisely sensing LOGOUT.

Finally, a processing unit was required to allow for autonomous detection and AoA estimation. The processing unit needs to function using a single power supply, whilst providing voltage regulation to the 5V and 3.3V outputs for the logarithmic detector and LNA to function. The processing unit must be capable of reading the voltage from the LOGOUT port whilst continuously comparing LOGOUT at every scan angle in order to determine the highest received power, thus identifying the bearing of the tagged bee. For initial prototypes an Arduino Uno open-source microcontroller board [177] was preferred due to its compactness, single power supply compatibility, 3.3V and 5V outputs and 10 bit resolution ADC, providing a sensing capability of 0-5V with 1024 different values. The Arduino Uno is connected to a power management unit enabling the entire system to be operated using a single 7.2V LiPO battery with a 45-minute operation time, operating on a 20cm x 17cm platform with a total weight < 1Kg.

Figure 4.4 depicts the chosen logarithmic detector, which was used to transduce the received signal power into an output voltage. The voltage was fed into a processing unit where the RSSI was recorded for each scan angle of the beam. With a receiver sensitivity of -70 dBm corresponding to an output voltage of 2V, the receiver system was capable of operating within a 20m range. To eliminate possible false readings, any AOA estimate with a RSSI > 2V, corresponding to P < -70 dBm, was considered erroneous.
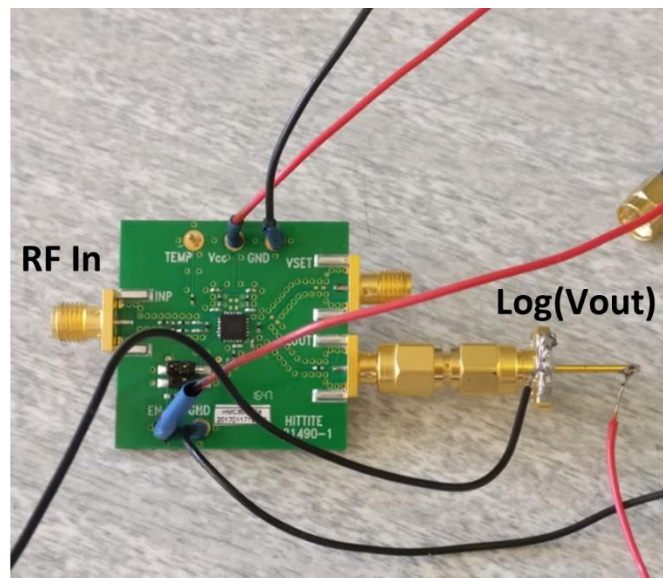
Fig 4.4: Prototype receiver unit. RF signal is fed into the device in which multiple amplifiers go into saturation depending on the input power. Output of the amplifier is then measured at LOGOUT pin.

Figure 4.5 illustrates key aspects of the code showing the voltage reading for each scan angle and using the voltage for each angle to determine the AoA. The complete script can be found in the appendix.
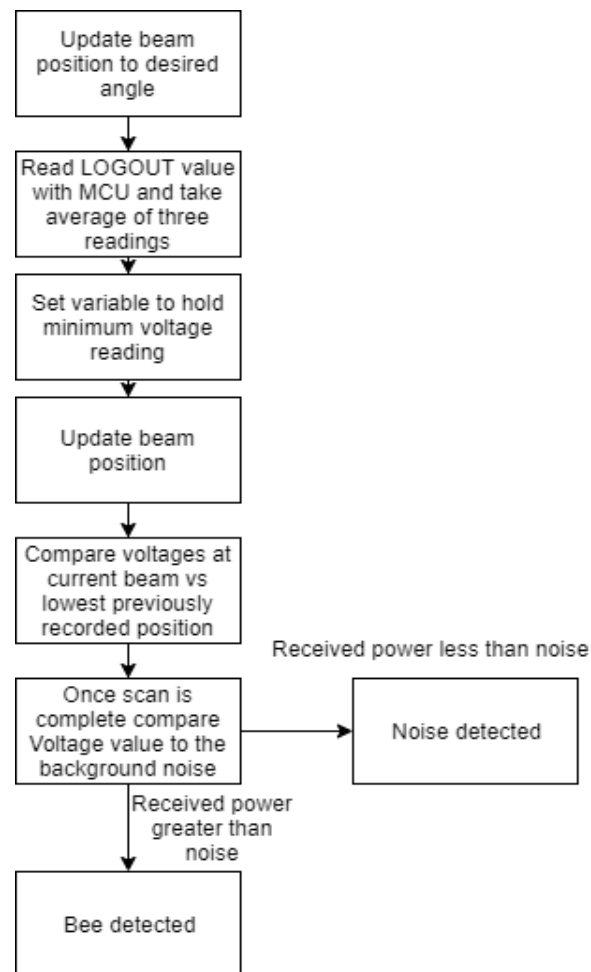
Fig 4.5: Flowchart describing how transduced voltage is processed to determine AoA estimation

Figure 4.5 demonstrates how the transduced voltage was processed and stored. The input to the processing unit from the LOGOUT pin on the logarithmic detector is, which records and sums the defined number of readings for each scan angle. The average reading is found and returned to the main loop of code. Two loops are responsible for defining the current angle of the antenna, in which the average recorded LOGOUT value is returned to and converted from a bit value to a voltage. The lowest voltage corresponds to the highest received power, therefore an 'if' statement is used to compare the current value to the previously lowest recorded voltage value to determine the values azimuth and elevation in which the highest received power was recorded (Figure 4.3).

4.2 Verifying performance of the system

To test the accuracy of the system to successfully predict the bearing of a signal, initial test was performed using a voltage-controlled oscillator emitting a 5.8 GHz source at 9.7 dB. A 30 dB attenuator allowed for a power level comparable to that of the tag output. This provided a more convenient and reliable approach for testing the system's initial performance, as the tag-signal is only generated during vibration of the thorax. Initial tests used antenna scanning in the azimuth plane, and then in both the azimuth and elevation. Due to the non-linear response of the logarithmic detector, received signal strength was measured in volts to eliminate any conversion errors.

Figure 4.6a outlines the experimental set up for testing the AoA system in which a transmitter was placed 10m away from the receiver, corresponding to an angle of 0°. The beam was scanned every 1° with the average of 3 RSSI readings prior to AOA estimation (Figure 4.5b). The results presented in Figure 4.6 depicts the system accurately estimating the location of the receiver. This was followed by correlating the received signal strength to the distance between the transmitter and receiver. A polynomial trendline was fitted to the data in order to express the relationship between LOGOUT and input power as:

$$LOGOUT\ (V) = 4E^{-6}RF_{IN}{}^3 +\ 0.000RF_{IN}{}^2 - 0.023RF_{IN} + 0.5873 \qquad (4.1)$$

By taking the lowest LOGOUT value (highest input power) and applying the value to Equation 4.1, both distance and bearing were estimated using the Friis transmission equation. Such an approach can be used to gauge estimation of the separation between Tx and Rx however, due errors associated with the RF detector readings it cannot be deemed reliable. Figure 4.6 shows the variation in signal strength for multiple readings taken at

the same location, highlighting the inaccuracies associated with distance estimation from a single receiver system. Multiple receivers with known locations allowed precise distance estimates to be determined via the bearing of each receiver.
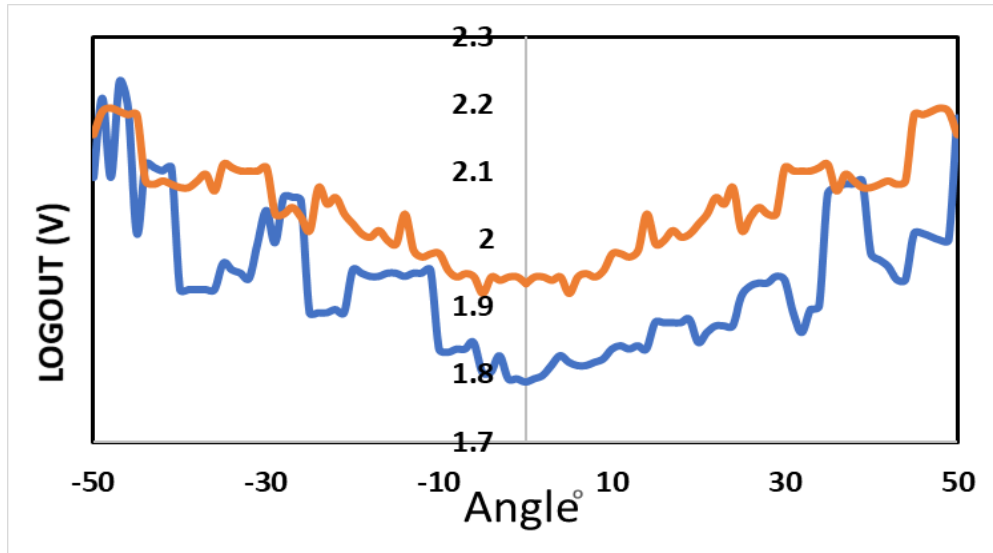
Fig 4.6: Initial test with receiver system and VCO highlighting the received signal strength displayed as an output voltage vs azimuth scan angle for an estimated AOA of 0° and the fluctuation in RSSI for repeated measurements at same angle and distance.

Further tests were conducted in which the transmitter was placed at 10° intervals scanning from -50° to 50°, in which the antenna was scanned every 1° recording received signal strength. The received signal strength for each position and angle scanned is displayed in Figure 4.7 illustrating the precision of the system to estimate the AoA of the transmitted signal.
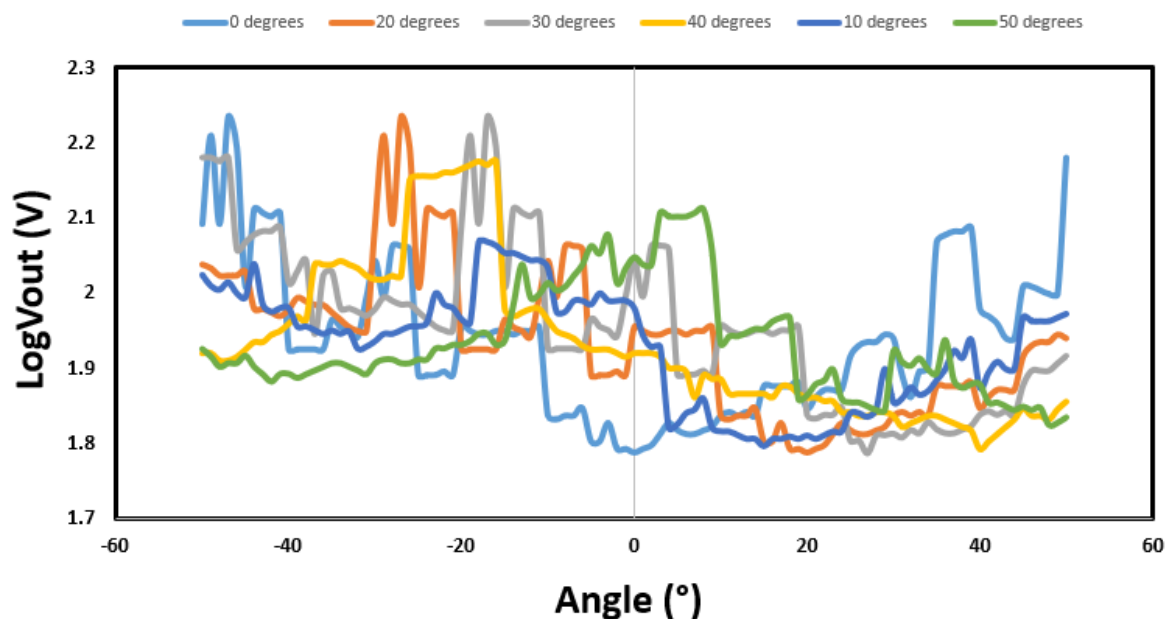
Fig 4.7: LOGOUT vs azimuth scan angle for a Tx moving from 0° to 50° with 10° increments.

After verifying the performance of the antenna scanning in the azimuth plane, additional tests were performed for both azimuth and elevations. Multiple targets were chosen in which the Tx was placed within respect to receiver system (Figure 4.8). At each location of the Tx, multiple bearing estimates were recorded and determined the maximum system error to be +/-5° (Table 4.1).

Fig 4.8: Experimental set up of testing 2D scanning capability of the system

Table 4.1: Summary of bearing estimation showing actual bearing vs recorded bearing when scanning in both azimuth and elevation planes.

Target location (Azimuth, Elevation)	Estimated reading 1	Estimated reading 2	Estimated reading 3	Estimated reading 4	Estimated reading 5
0°,0°	2°,4°	3°,4°	-2°,-5°	1°,1°	-5°,1°
-35°,0°	-33°,-5°	-34°,4°	-39°,1°	-34°,-3°	-35°,-5°

34°,25°	30°,27°	39°,27°	31°,30°	36°,30°	34°,23°
23°,25°	19°,28°	24°,27°	28°,28°	19°,23°	20°,26°
0°,25°	-4°, 30°	-5°,26°	1°,22°	-4°,28°	1°,29°
-42°,-25°	-47,-21	-42,-22	-47°,-27°	-41°,-27°	-46°,-26°

The results demonstrated a satisfactory system performance when determining the bearing of a VCO with a power level comparable to the self-powered tag. Tracking of tagged bees in controlled environment.

In order to test system's capacity to determine the bearing of a bee, a netted tunnel was constructed to allow for the tagged bee to continuously remain within a detection range of the receiver system, which was placed at various distances away from the netted tunnel (Figure 4.9).

Fig 4.9: Constructed netted tunnel to house tagged bees during experiment and experimental set up of the receiver system

A tag was attached to the thorax of a foraging bee and placed inside a netted tunnel. The phased array antenna was set to scan every 1° in azimuth and elevation. After slightly modifying the code in Figure 4.5, the azimuth and elevation results were autonomously plotted into a csv file, showing the position of the bee in real time. With the user of a spotter to confirm visually the position of the bee, the system was verified to successfully determine the tagged bee's position. Experiments were performed at distances of 10m, 15m and 20m from the receiver and centre of the tunnel. Table 4.2

shows the results at 20m, outlining the successful operation of the system within the estimated range.

Subsequently, the receiver system was placed at the end of the netted-tunnel and the same experiment was repeated to determine the potential effects of multipath (Figure 4.10). Despite scanning from -50° to 50°, the effects of any potential multipath are minimal as the bearing is always estimated within the proximity of the netted-tunnel (Table 4.3). As any non-flight movements were unable to produce a detectable signal, position was only estimated during bee flight.

Table 4.2: Recorded bearings of the tagged bee inside netted tunnel with a separation of 20m.

Bearing number	Bee Azimuth	Bee Elevation
1	2°	6°
2	-21°	-10°
3	-40°	-10°
4	-44°	-10°
5	-45°	-10°
6	-34°	-6°
7	-45°	-8°
8	37°	-10°
9	-39°	0°
10	-45°	-10°
11	-45°	-9°
12	-42°	-8°
13	-28°	-1°
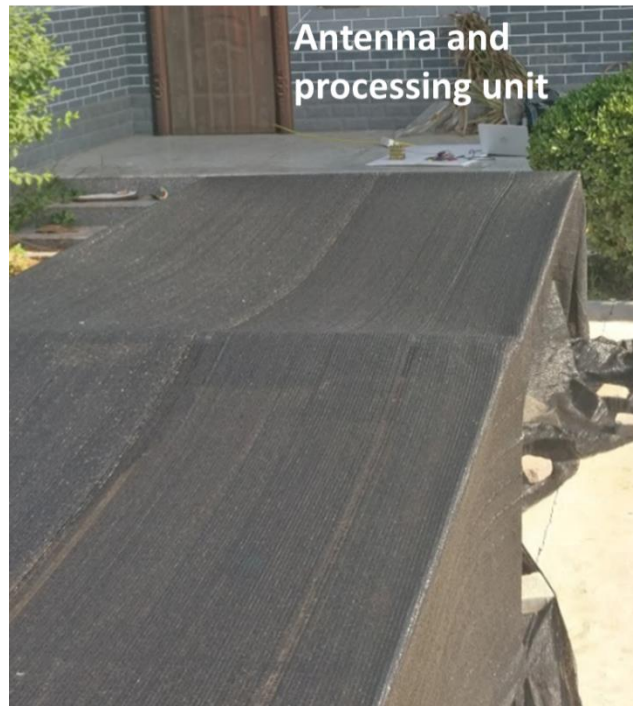
Fig 4.10: Experimental set up of the receiver system next to the netted tunnel

Table 4.3: Recorded bearings of the tagged bee inside the netted tunnel when the receiver was placed at the side of tunnel.

Bearing number	Bee Azimuth	Bee Elevation
1	-8°	-11°
2	-15°	-15°
3	-15°	-14°
4	14°	-4°
5	-1°	-15°
6	0°	-4°
7	-15°	-1°
8	-15°	-15°
9	-15°	-10°
10	15°	4°
11	-15°	-13°
12	-11°	-2°
13	15°	2°
14	-1°	-11°
15	10°	12°

4.3 Tracking of foraging bees

Further tests to monitor bumblebee movements in and out of the hive allowed for: indirect estimation of the foraging time; verification that flight direction matched the known location of a food supply and assessing the number of foraging flights a bee takes each day. The system was mounted on a static support 10m from the nest (Figure 4.11). A typical flight to and from the nest allowed recording of the azimuth/elevation coordinates and flight duration (Table 4.4). Tagged bumblebees were able to roam within the nest unhindered by the tag, in contrast to harmonic radar telemetry [9] which requires tag removal before the bee can re-enter the nest.
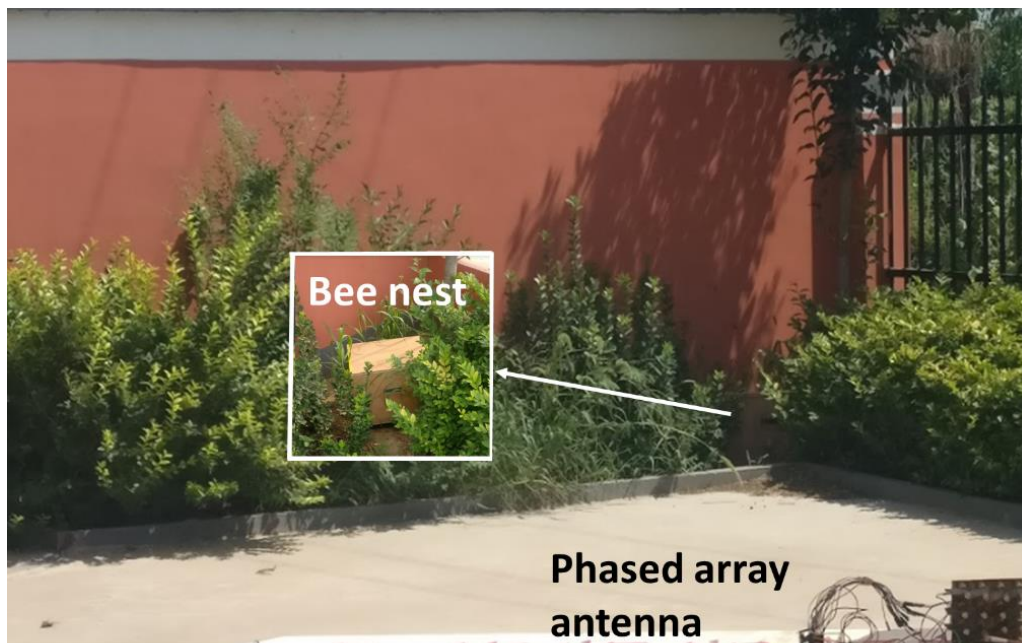
Fig 4.11: Experimental setup to monitor bumblebees entering and leaving the nest with 10m separation from the antenna array.

Table 4.4: *Recorded angular coordinates and time for tagged bee leaving and returning to hive. Time has been normalised from first recorded position*

Leaving hive			*Returning to hive*		
Time	Azimuth	Elevation	Time	Azimuth	Elevation
0 s	5°	5°	1425 s	35°	30°
3 s	-12°	17°	1428 s	12°	10°
6 s	25°	19°	1431 s	-20°	22°
9 s	No signal	No signal	1434 s	-10°	5°
Total flight time					23.9 minutes

As the current system is capable of detecting a single signal at a time, in order to obtain accurate estimation of foraging time, only a single bumblebee inside the nest was tagged during any experiment. Visual observation of the nest allowed for verification of the results, which were autonomously recorded and logged to a CSV file in real time, with a sampling rate of 30 KHz. The system was calibrated so that any background noise/signal detected when the bee was not flying within the detection of the receiver would be deemed as no recorded bearing. Figure 4.12 outlines the flights patterns of tagged bumblebees entering and leaving the nest producing a mean flight time (Table 4.5). Each coloured line represents flight trajectory of tagged bumblebees flying within detection proximity of the receiver entering and leaving the hive.
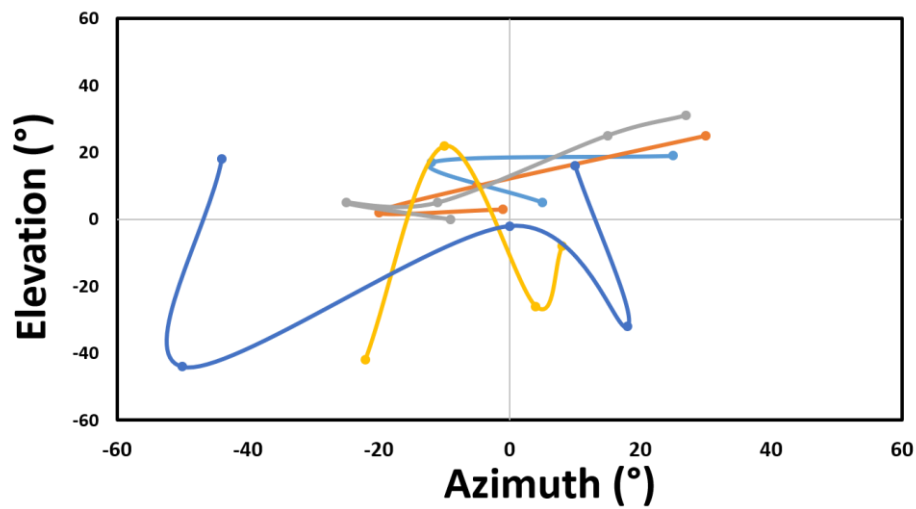
(a)
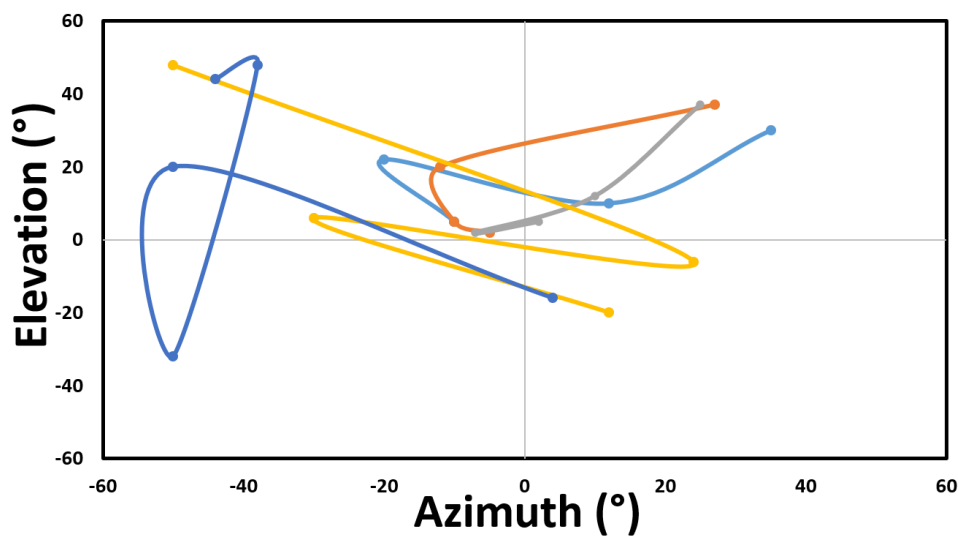
(b)

Fig 4.12: Recorded flight plans of foraging bumblebees (a) leaving and (b) returning to the hive

Although the system is currently limited to detecting and tracking a single bee at a time, current results indicate how to overcome the cm-range limitation and required transponder-nest proximity in typical radio frequency identification (RFID) data loggers [8, 9]. Additionally, the present system also demonstrated its potential for unobtrusive data logging. Unlike RFID technology, which can only determine foraging time of each bumblebee, the system here can provide additional information due to its significantly increased detection range capabilities such as verifying if the recorded flight direction matched the known location of food supplies. Figure 4.11 outlines the unobtrusive nature of the approach, as no equipment is needed to be installed into the hive. Other attempts to monitor bees entering and departing the hive/nest, have used audio signal processing. This overcomes the detection range limitations of RFID approaches, but equipment is still required to be installed on the hive or nest [100].

Table 4.5: *Recorded average foraging time of each individual tagged bumblebee*

Bee Number	Normalised foraging start time (s)	Normalised return time (s)	Total foraging time
1	0	572	9 minutes 32 seconds
2	0	120	2 minutes
3	0	525	8 minutes 45 seconds
4	0	1653	27 minutes 33 seconds
5	0	1432	23 minutes 52 seconds

The current system is limited in its placement and operation time due to the need for a laptop to log data, thus limiting the placement of the receiver system and potential applications. Whilst the Arduino processing was adequate for initial tests, its processing speed could not match the high demands of data acquisition and continuous autonomous logging. Data logging and processing capacity was explored. One application of interest was the ability of remote monitoring of flower-to-flower bee foraging in a greenhouse environment. Bumblebees are commercially used in polytunnels to provide buzz-

pollination services. There was no technology available to track and monitor bee movement in these environments. The use of multiple receiver units and an IoT data logging network [13, 14] would allow for full coverage of polytunnels which can be used to identify optimal nest placements for flower pollination.

In order to modify the system to be suitable for polytunnel monitoring, a custom 3D housing unit was printed to contain the receiver unit and placed directly above the polytunnel, reducing any potential multipath effects from the metal structures underneath the flowers. Figure 4.13 shows the receiver system placed onto the housing unit and suspended above strawberry plants within the polytunnel. The laptop was replaced with a SD card reader and portable battery pack [186], which continuously powered the system for 24 hours. The use of a 5m power cable allowed for easy replacement of the battery without having to move the receiver.

(a)

(b)

Fig 4.13: (a) Receiver system placed in custom 3D printed housing unit (b) receiver system suspended above strawberry flowers.

Multiple bumblebees were tagged before releasing them back into their nests. The receiver unit was left to autonomously run and log data for a week, and tagged bees added daily. Data logged to the SD card was loaded into a MATLAB script, which analysed and plotted all the recorded bearings from the system. Example flight paths obtained from the experiment are displayed in Figure 4.14.
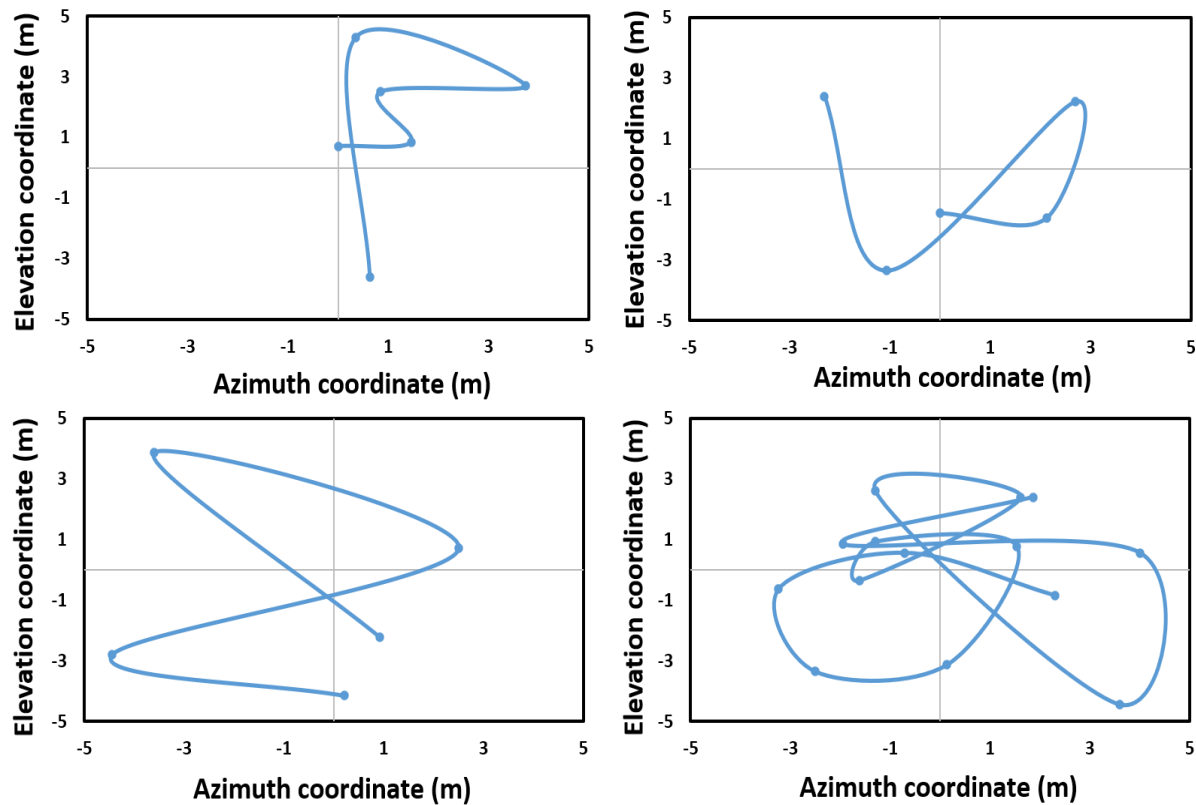
Fig 4.14: Recorded flight paths of foraging bumblebees with the recorded azimuth and elevation converted to cartesian co-ordinates

Further attempts to improve the ease of data acquisition were attempted by accessing the static receiver with a LoRa board [187]. The board was chosen due to its compatibility of 3.3V and 5V supplies to power the LNA and receiver respectively, whilst providing sufficient operation range between other receivers or base station. This allowed the processing of data in real time, rather than at given intervals typical of the SD card data logging approach. Additionally, the use of additional sensors could be employed to correlate parameters such as temperature, humidity, and lighting to monitor colony health.

4.4 Feasibility of IoT monitoring approach

In order to test the capabilities of the LoRa system, benchmark tests were performed to assess the ability to successfully transmit and receive data. A stationary transmitter was set up to send data every second. Gradually increasing the distance between Tx and Rx, the maximum transmission distance was determined (Figure 4.15). The current system utilised omnidirectional antennae for Tx and Rx, suggesting that the range could be significantly extended with aligned directional antennas.
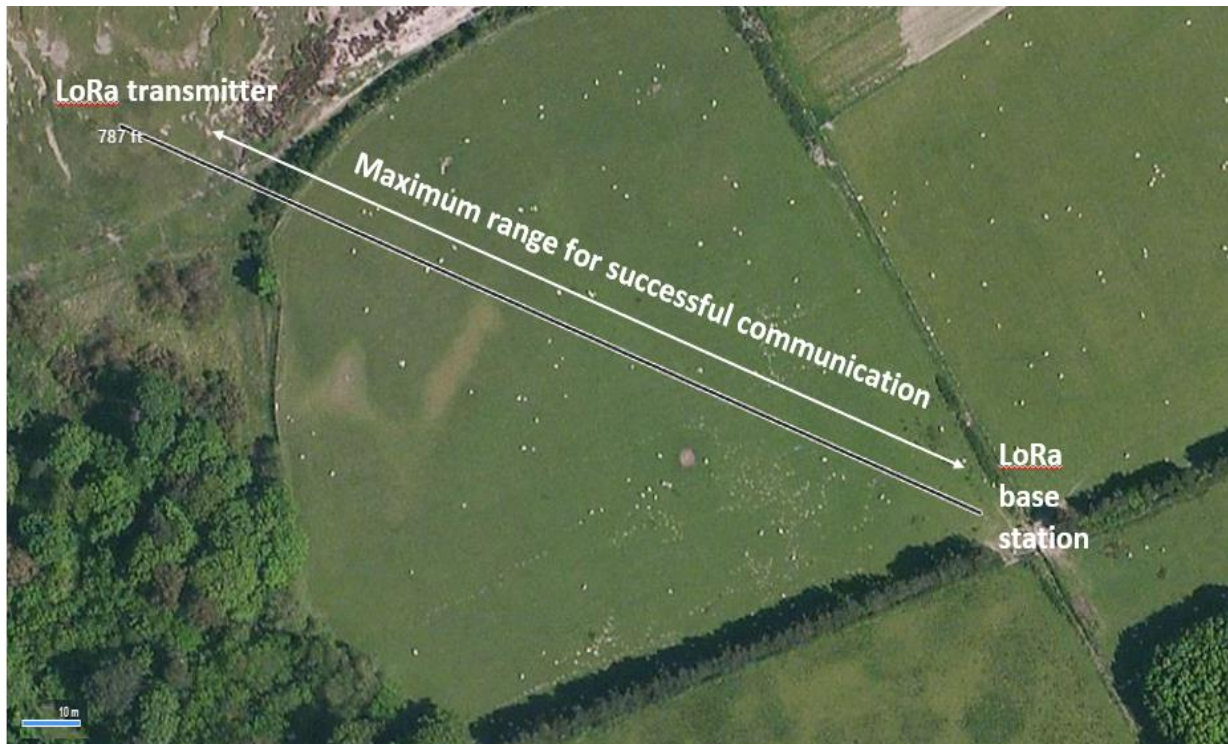
Fig 4.15: Maximum achievable separation between LoRa boards to successfully transmit and receive data

Such an approach demonstrates compatibility of the system with an IoT monitoring approach, that could potentially be applied to multiple receivers to develop a multi-sensing network. A LoRa-based processing unit could be implemented instead of the processing units previously presented in the chapter using an Arduino Uno to allow for autonomous sensing and transmission and logging of data across multiple receivers. For commercial applications in which polytunnels can be more than 100 meters long, such an approach would allow for pollination monitoring of the entire polytunnel rather than a designated area.

This chapter has discussed how the antenna array presented in Chapter 3, has been utilised inside an RF system which will calculate the bee's position from its angle of arrival. The system was initially verified using the VCO, emitting a signal at 5.8 GHz comparable to the power emitted from the self-powered tag when attached to the bee.

Tests to track the position of bees within a netted tunnel were then performed in order to verify 20m detection range and tracking capabilities. Foraging bumblebees were tracked and their foraging times and flight positions leaving and entering the nest recorded. Visual monitoring of the nest allowed the verification of corresponding time stamps. Tracking foraging activity was demonstrated over a small area within the polytunnel and logged with an SD card reader, however, the capability of covering the entire polytunnel area with an IoT monitoring approach has been explored.

Chapter 5. Integrating system to drone for autonomous tracking

This chapter addresses the need to achieve long range tracking capabilities for the system presented within Chapter 4 by integrating the current system to a UAV to achieve a moveable receiver system. The design of a custom 3D printed housing unit is presented to allow for the integration of the receiver system and UAV. The integration of the receiver system with the UAV software to facilitate communication between drone and receiver unit to achieve autonomous flight is presented. Initial experiments tracked a slow-moving target to demonstrate proof of concept. Further experiments demonstrated target detection, localisation, and autonomous movements towards the tagged bee.

5.1 Receiver integration to UAV

There is limited potential to manually edit and implement flight controls and software of most commercially available UAVs. The capability to integrate customised sensors and equipment is limited to very few models [1, 2]. UAVs present as either multi-rotor or fixed-wing [3, 4]. Fixed-wing UAVs would be advantageous to use as they require significantly less energy to stay airborne [192] and thus can maintain longer flight duration. However, the need for continuous movement and a large turning circle undermines the tracking system's capacity to maintain the detection range between Tx and Rx. Multi-rotors are able to hover and precisely move in any direction, but require greater energy consumption to remain airborne resulting in flight times of ~30 minutes [193]. Due to their ability to hover and quickly change direction, multirotor UAVs are favourable for the application of following a moving target within a limited detection range. Whilst multiple drones capable of carrying payloads commensurate with those of this study are available commercially, compatibility and integration of external sensors and drones are limited. Additional flight controllers are available, allowing developers access to open source software for autopilot applications [194]. The use of DJIs software development kits (SDKs) (Payload SDK and Mobile SDK) permits the integration of the receiver system (Chapter 4) to the Matrice series of drones [1, 8]. Due to the compatibility of integrating the receiver unit with the flight commands of the drone, along with its 1kg payload carrying capability, the DJI M200 was chosen for this study.

A compact housing unit was designed and fabricated using 3D printing to allow for the integration of the receiver unit to the drone (Figure 5.1 and figure 5.12). Consideration was given to the design of the housing unit to distribute the weight of the receiver system to minimise impact on flight capabilities. Placement of the device is critical as safety features such as collision avoidance sensors need to remain unobstructed and operational. The space vacated by the camera was replaced with the antenna. Figure 5.1 outlines the design of the 3D printed housing secured to each leg of the drone.

Due to the size of the structure, the housing unit was printed in three parts and connected together via screws. The two side units are multifunctional and were designed to meet the following criteria:

- Securely hold the payload in place during flight with minimal risk of the payload disconnecting from the done
- Providing sufficient area for additional components of the receiver system such a microcontroller, L.N.A and logarithmic detector.

The central part was responsible for housing the antenna unit and was designed for the sole purpose of securely holding the antenna array in place and ensuring it remained stable during flight, which is additionally highlighted in figure 5.10, where the antenna rests against small slots. The combination if all three parts successfully allowed for the drone to safely carry the payload whilst additionally being located in a manner which does not block critical safety functions integrated to the drone such as collision detection sensors.

To allow for efficient integration of receiver system and UAV, the phased array antenna was modified to reduce device volume and weight [193]. The previous antenna presented in Chapter 3 relied on the integration of each antenna element with a single-phase shifter via SMA connector. This contributed significantly to device weight, adding an additional 210 grams to the drone payload weight. Figure 5.1 depicts the phased array antenna when placed on the drone, highlighting space inefficiencies and payload weight approaching capacity. The integration of the phase shifters to antenna array in a single structure would allow for over 200 grams of payload weight reduction, increasing the potential max flight time of the drone per flight.

Fig 5.1: 3D printed housing unit for AoA system with integration of components to 3D printed unit

Substrate selection of both antenna and phase shifter elements currently limits further miniaturisation. Due to the structure of the quadrature coupler, requiring quarter wavelength lines, the overall size of the structure was incompatible to integrate into a feeding network without exceeding appropriate spacing between elements (D=0.5λ). The increased spacing between elements would lead to potential scan blindness and grating lobes [163] whilst additionally resulting in an antenna size which could not fit on the drone. To maintain a compact structure, the feeding network substrate material was selected with a much higher dielectric constant (Rogers TMM 10i ε_r = 9.8) than the antenna substrate (Rogers TMM 4 ε_r = 4.5). The significantly lower loss tangent associated with the substrates could also potentially lead to increased antenna efficiency [196]. Figure 5.2 and figure 5.3 outlines the design and simulated results of the modified phase shifter on Rogers TMM 10i substrate with a 1.27 mm thickness.

Whilst the quarter wavelength was 6.24mm for the FR-4, the implementation of Rogers TMM 10i reduced the quarter wavelength to 4.13mm. The total length and width of the device has been significantly reduced. The reduced dimensions of the phase shifter allow for the output port to directly excite the antenna via a slot. A slot is cut into the substrate and ground plane of the phase shifter and antenna, perpendicular to the feed of the microstrip line. The fields of the microstrip line directly excite the slot (Figure 5.5).
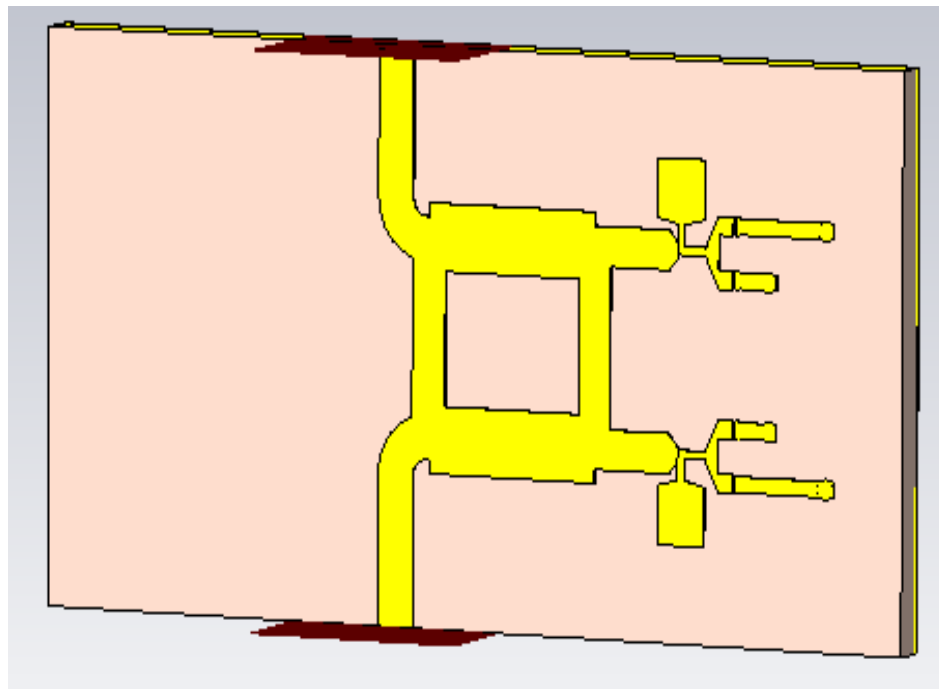
(a)
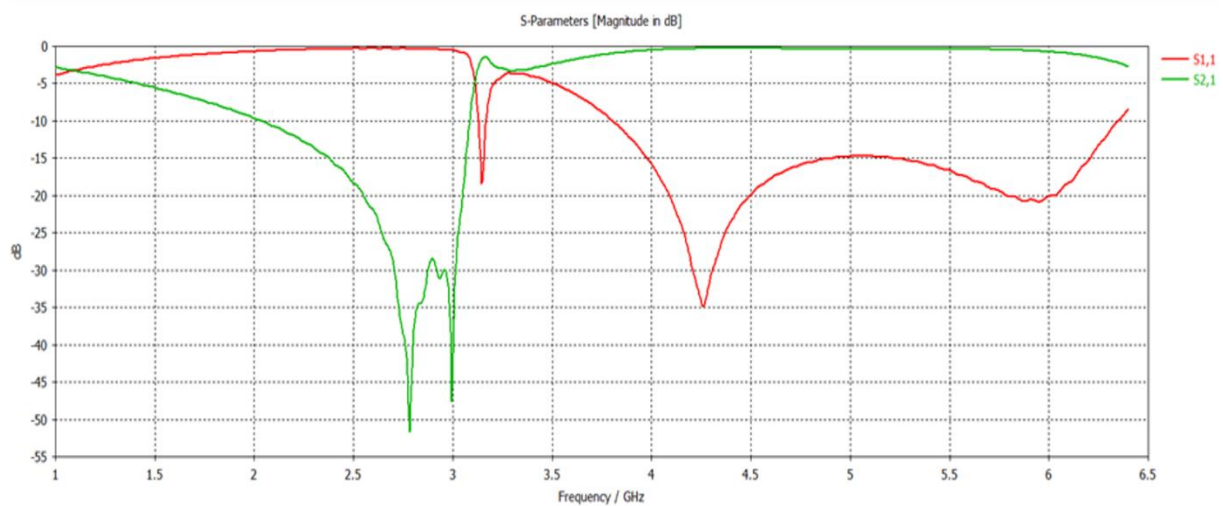
(b)

Fig 5.2: (a) Phase shifter design on Rogers TMM 10i substrate (b) simulated S-parameters (dB) of quadrature coupler
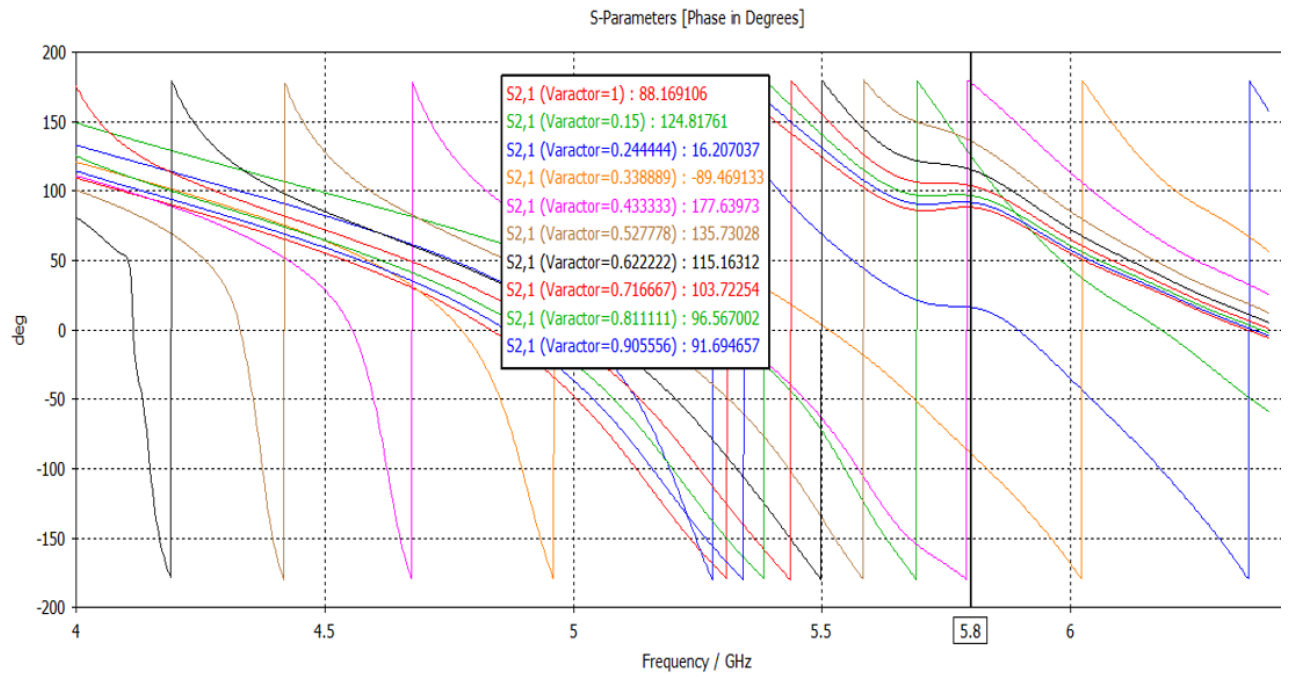
(c)
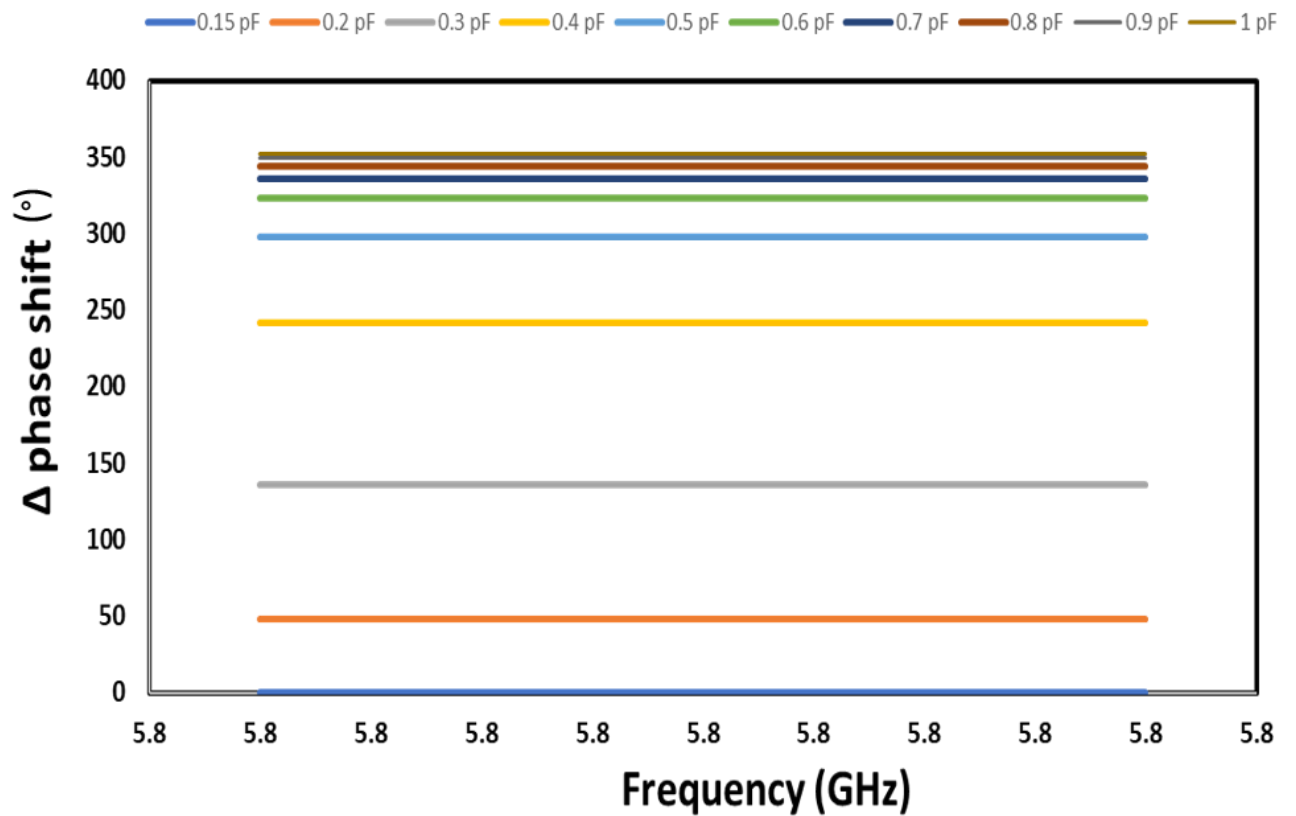
(d)

Fig 5.3: (a) Phase shift between input port and output port with a load variation of 0.15-1 pF (b) delta phase shift with load of 0.15 pF acting as reference

(a)

(b)
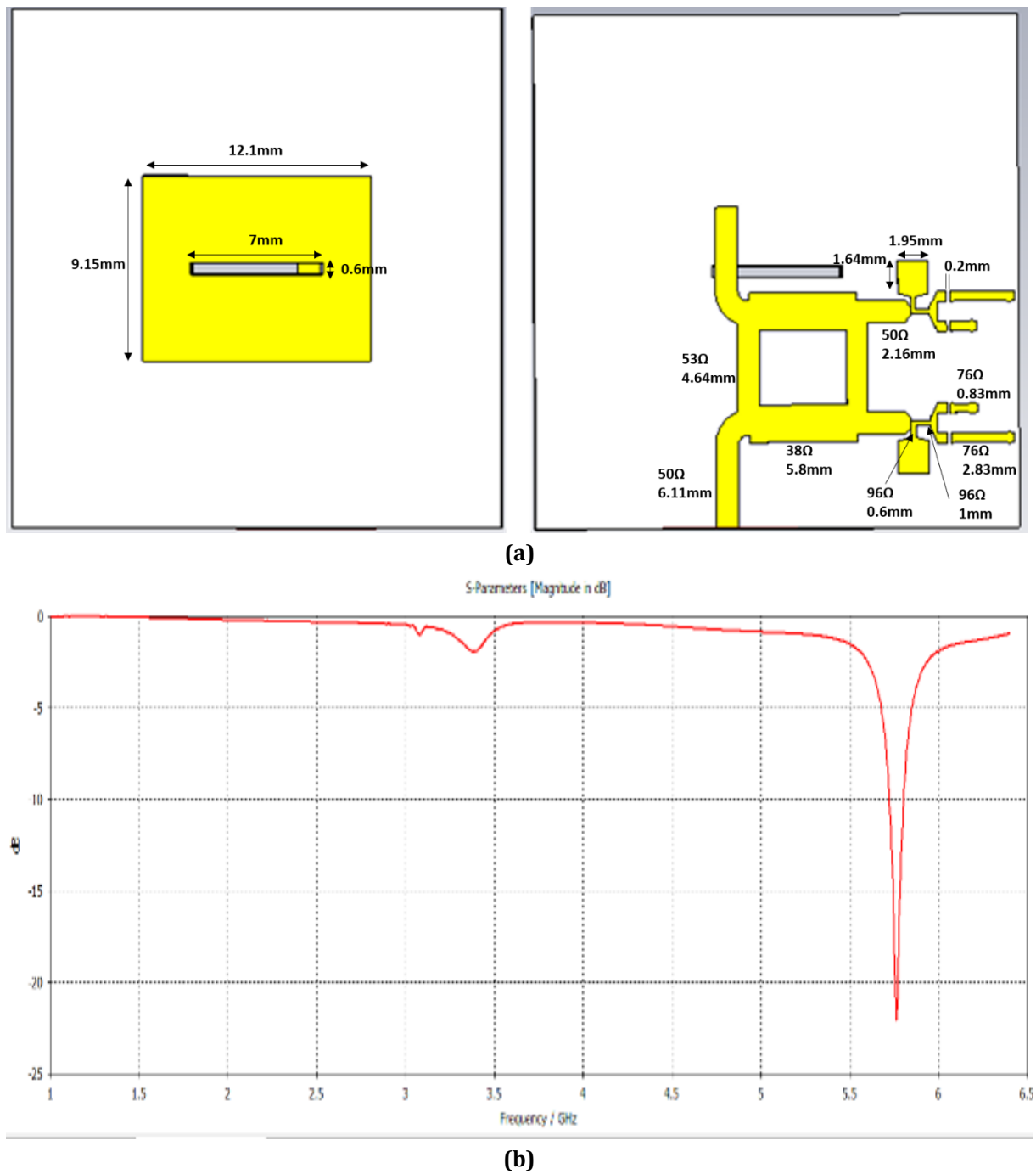
Fig 5.4: (a) Slot fed patch antenna using microstrip line of phase shifter as the feed (b) simulated S-parameters (dB) of patch antenna

(a)

farfield (f=5.8) [1]

Type	Farfield
Approximation	enabled (kR >> 1)
Component	Abs
Output	Gain
Frequency	5.8 GHz
Rad. Effic.	-1.077 dB
Tot. Effic.	-1.473 dB
Gain	4.711 dBi

(b)
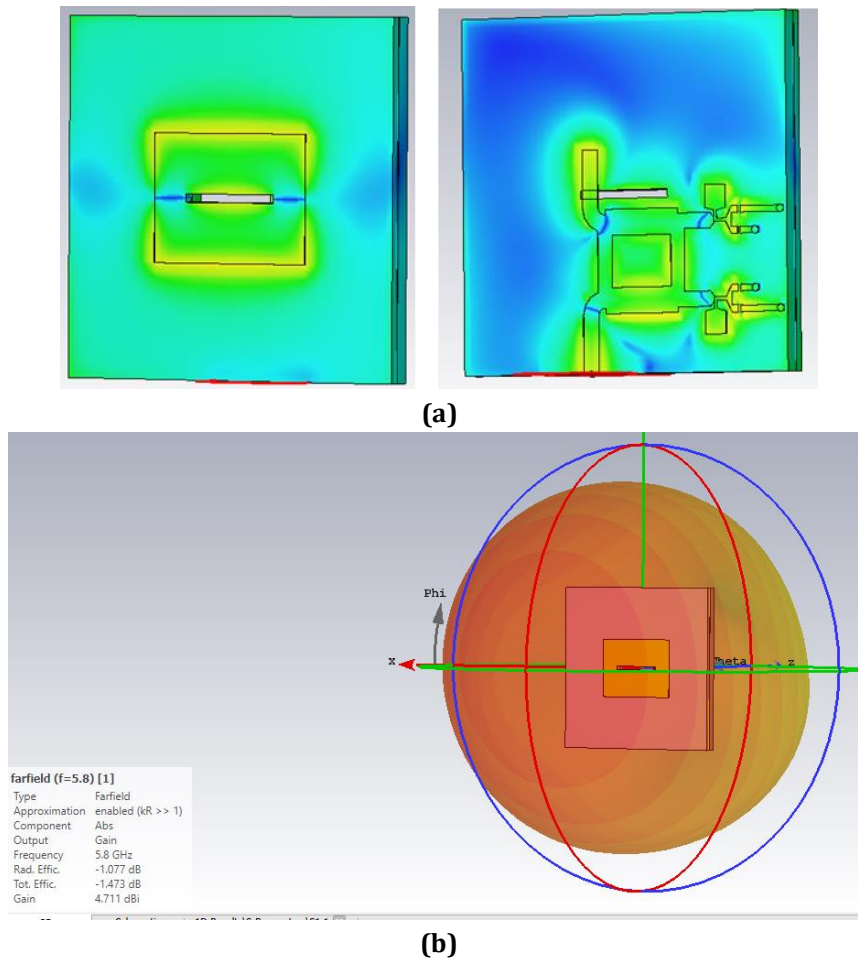
Fig 5.5: (a) Electric field of antenna showing microstrip line directly exciting the slot antenna (b) radiation pattern and efficiency of antenna.

The antenna offers acceptable return loss of -22 dB, whilst offering a gain and efficiency of 4.771 dBi and -1.473 dB, respectively. The next step in the design process was to review the change in the active element impedance vs scan angle for a 4x4 array with an element spacing of D=0.5λ.

A feeding network was designed to allow for excitation of the 4 x 4 array from a single feeding point. Using Wilkinson power dividers [39], an initial feeding network was constructed for a 2x2 array as depicted in Figure 5.6.
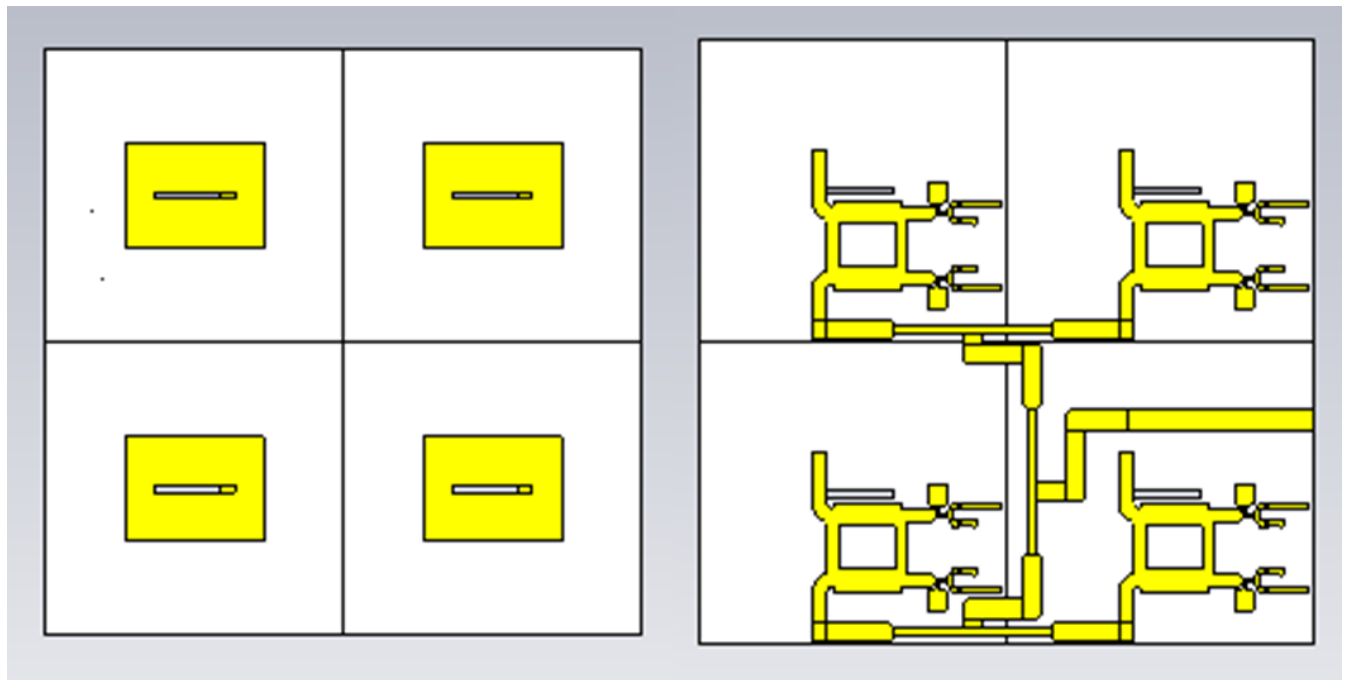
(a)
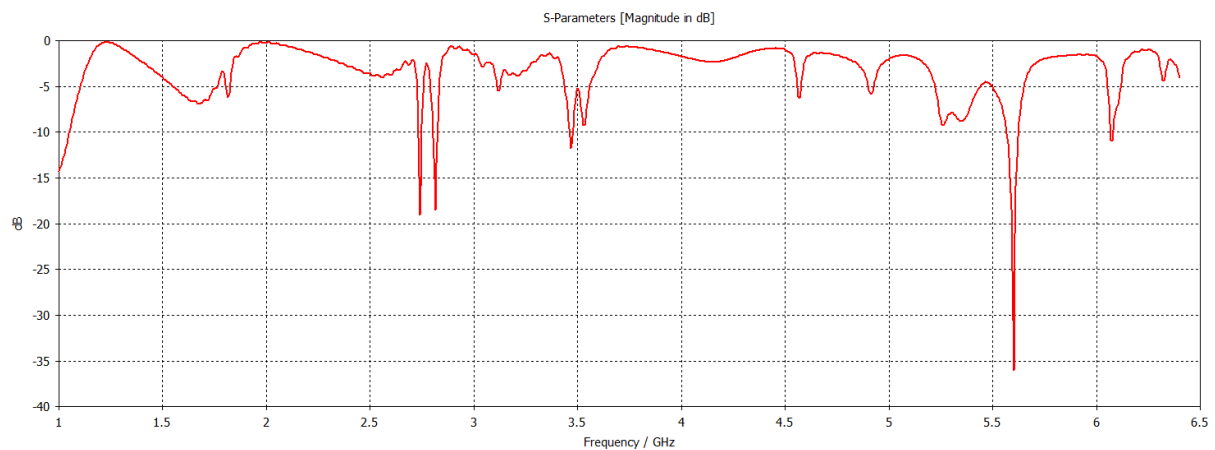
(b)

Fig 5.6: (a) 2 x 2 element antenna array and (b) simulated return loss performance

The design of 2 x 2 element antenna array in Figure 5.4 was expanded for a 4 x 4 array (Figure 5.7a). A central feeding point ensured that each phase entering each phase shifter was identical and the phase shift excited each element from the phase shifter alone.

The simulation addresses the return loss of the antenna array to ensure resonance at 5.8 GHz. The gain and efficiency are additionally monitored to ensure sufficient operational distance between Tx and Rx of the system can be achieved. Finally, the surface current is monitored to ensure the phase shift at each element is solely down to the reactance of the phase shifter.

(a)

(b)
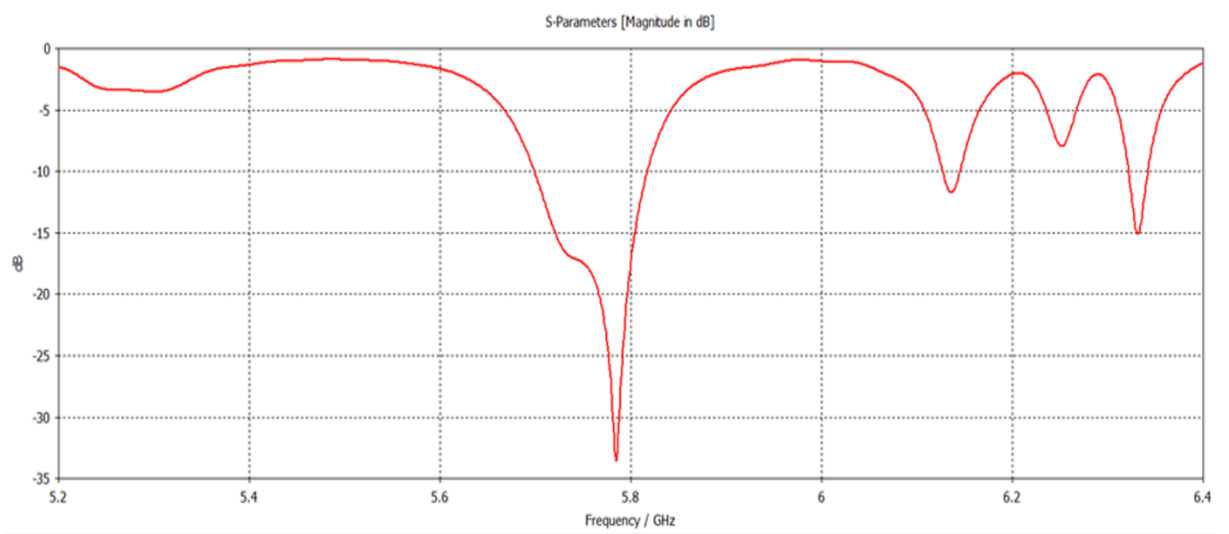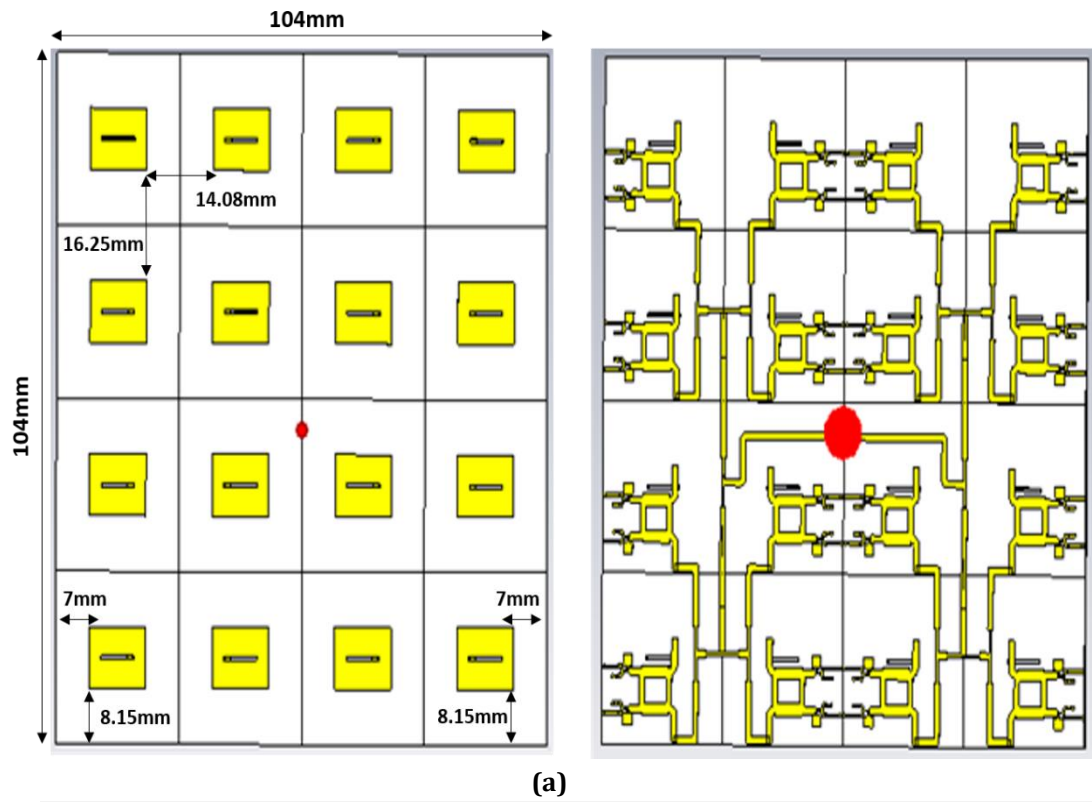
Fig 5.7: (a) 4 x 4 element array with microstrip feeding network (b) simulated return loss of 4 x 4 array

farfield (f=5.8) [2]

Type	Farfield
Approximation	enabled (kR >> 1)
Component	Abs
Output	Gain
Frequency	5.8 GHz
Rad. Effic.	-1.754 dB
Tot. Effic.	-1.836 dB
Gain	14.47 dBi
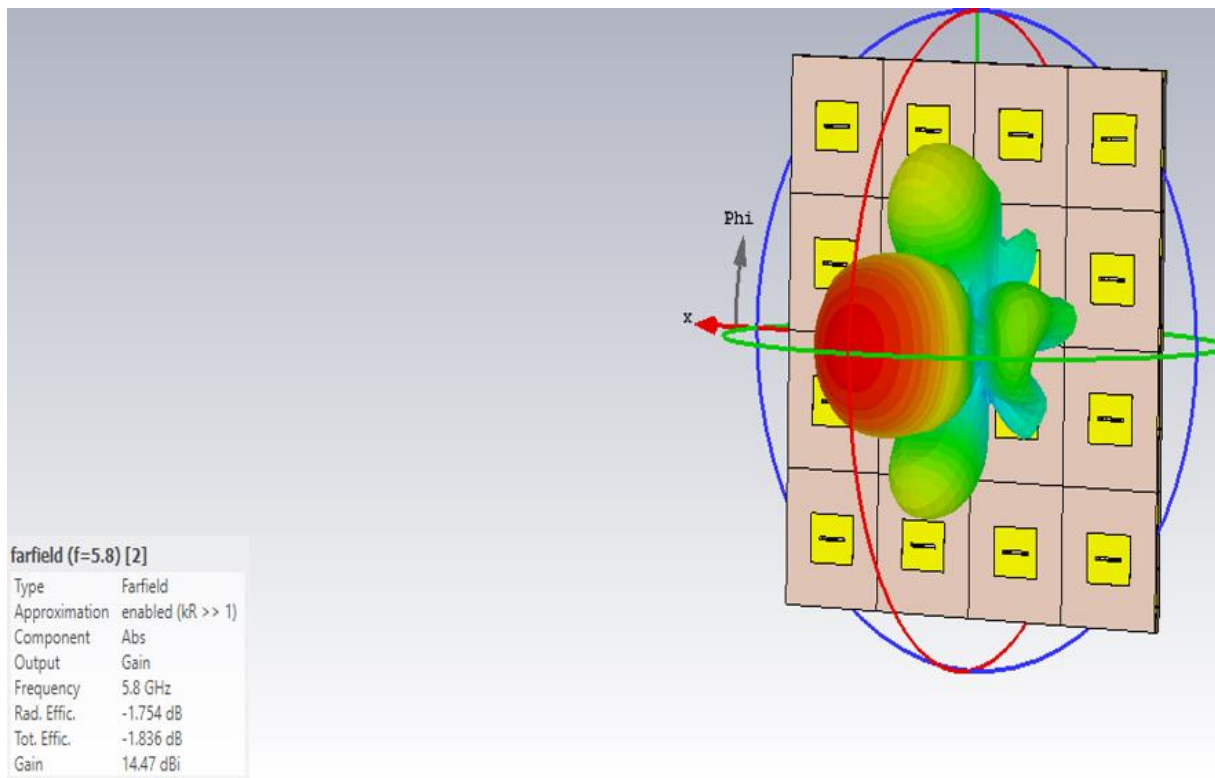
(a)
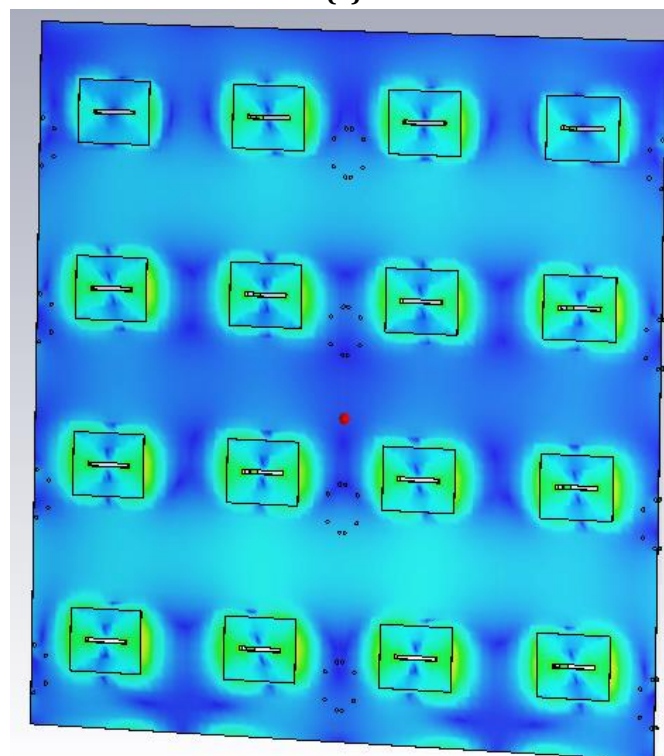
(b)

Fig 5.8: (a) simulated radiation pattern and antenna efficiency (b) Surface current distribution of each antenna element in the array with equal phase shift

The antenna array was fabricated by applying a mask to the substrates and etching using ferric chloride. Holes were drilled into the substrate to allocate the complex

load of the phase shifter in which vias were connected to the ground plane and varactor diodes were soldered to each phase shifter. Coaxial cable was then used to connect an SMA connector to the centre of the feed and ground plane (Figure 5.9).
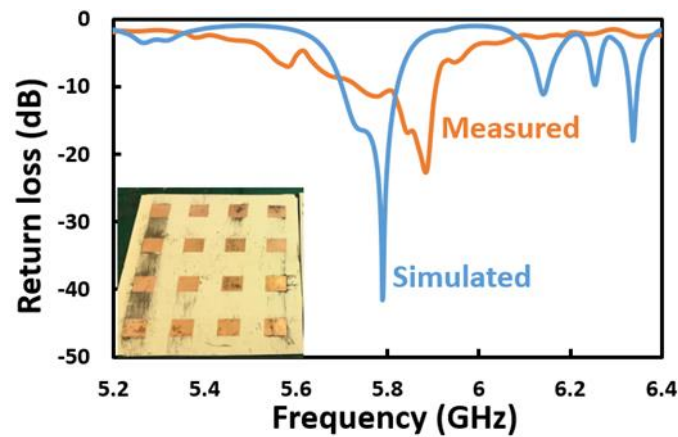
Fig 5.9: Fabricated phased array antenna and measured vs simulated return loss for the microstrip antenna array.

Tracking tests were performed with the fabricated antenna to verify its performance (Figure 5.10). A tagged bee was placed into a clear plastic box and was placed 1 meter away from the antenna, which scanned from -50° to 50° in azimuth and elevation. Table 5.1 summarises the estimated bearing of the bee for multiple readings outlining the system's ability to accurately determine the location of the bee.

Fig 5.10: Experimental set up of antenna system and receiver placed 1m away from tagged bee inside box and antenna scanned from -50° to 50° in azimuth and elevation

Table 5.1: Recorded bearing of bee tagged inside box

READING NUMBER	AZIMUTH (°)	ELEVATION (°)
1	2	-12
2	2	-10
3	4	-8
4	-2	-10
5	0	-10
6	-3	-11
7	4	-8

5.2 Processing AOA data to create co-ordinate

The inbuilt SDK allows for the connection of our processing unit to the drone via serial Universal Asynchronous Receiver/Transmitter (UART) communication, facilitating full integration of the receiver system and drone (Figure 5.11).
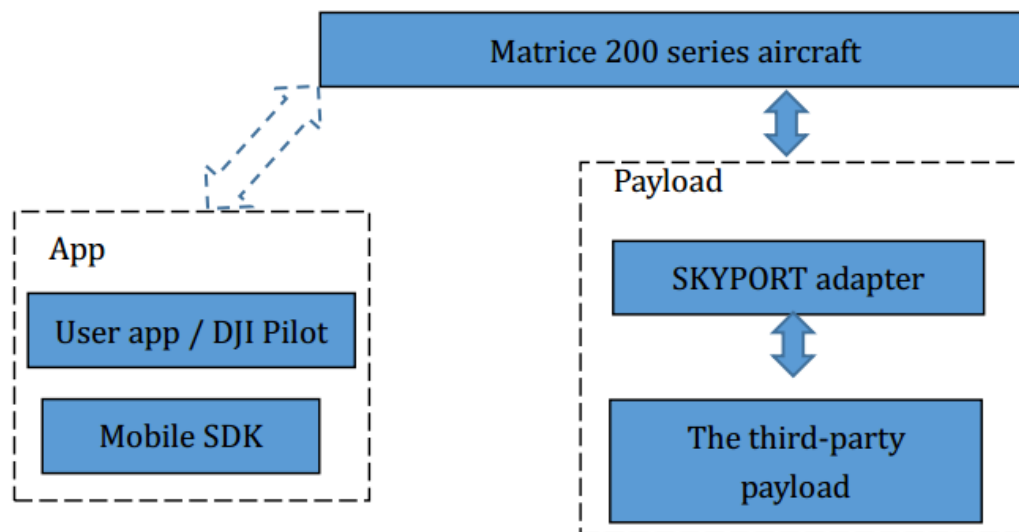
Fig 5.11: Payload SDK architecture [197].

The receiver system is defined as the third-party payload, which is linked to the drone via a STM32F407VGTx microcontroller [198] enabling UART communication with the receiver system and sky port connection via a ribbon cable (Figure 5.12).
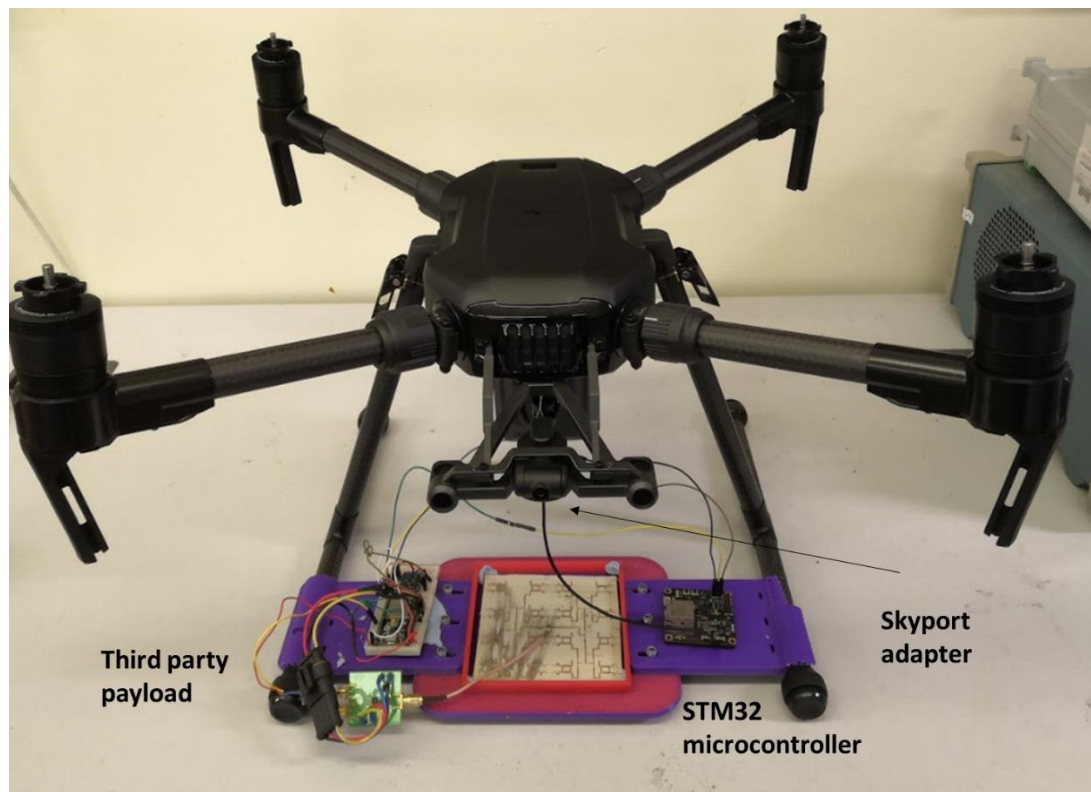
Fig 5.12: Payload SDK implementation on Matrice 200 drone.

The UART link sends all captured data from the AOA estimation to the drone's processing unit. The data is then stored into a frame, encrypted for easy identification of the start and end of a data sequence, and transmitted to a remote base station via the drone inbuilt communication system. Such step was necessary as the payload sdk obtains communication APIs for upstream and downstream communication. By passing the data to the mobile sdk, the flight control components could be utilised. The AOA estimation was determined from decoding the incoming data of the bee's bearing and location relative to the drone. The bearing was transmitted back to the drone as a command to update its position. To further illustrate this concept each step will be reviewed with supporting figures to outline the process. Figure 5.13 shows snippets of the receiver code with calculates the azimuth and elevation position and encodes the data.

Fig 5.13: Processing unit code, which calculates the azimuth and elevation value before encoding them into a string.

To encode the data an identifier is placed at the start of the sequence with the value 500. The azimuth value is placed into the string with another identifier. If the azimuth value is negative a 1 is the next value, likewise if the value is positive a 2 is placed after the 99-value followed by the bearing. The same method is repeated for the elevation value (Figure 5.14).

Fig 5.14: Encoded data along with its azimuth and elevation representation.

The data is transferred to the drone at a rate of 5 Hz. This is required as during the transmission and receiving of data must be sent at a rate of between 5 – 25 Hz, otherwise the drone will behave as if connection has been lost and simply hover *in situ*. The data from the third-party sensor network is passed through the drone via connection to the sky port adapter via a STM32F407VGTx microcontroller. Synchronisation between the third-party processing unit and the sky port adapter is difficult to realise due to the absence of a real-time clock. The processing unit and STM32 microcontroller data is stored as an 18-bite value. This ensures that a full nine bites encoded sequence with azimuth and elevation data will be present for decoding. The 18 bites value is finally stored as a string and transmitted to the mobile app (Figure 5.15).

```
┌─────────────────────┐
│ Create variable of 18│
│ bits to be able to read│
│ at least one complete│
│ encoded message     │
└─────────────────────┘
          │
          ▼
┌─────────────────────┐
│ Assign variable to  │
│ read the store the  │
│ transmitted data from│
│ figure 5.13         │
└─────────────────────┘
          │
          ▼
┌─────────────────────┐
│ Use payload SDK     │
│ functions to push the│
│ transmit the variable│
│ to mobile sdk       │
└─────────────────────┘
          │
          ▼
┌─────────────────────┐
│ Read next variable  │
│ containing Azimuth  │
│ and elevation       │
│ positions           │
└─────────────────────┘
          │
          ▼
┌─────────────────────┐
│ Transmit new data to│
│ mobile sdk and      │
│ repeat              │
└─────────────────────┘
```
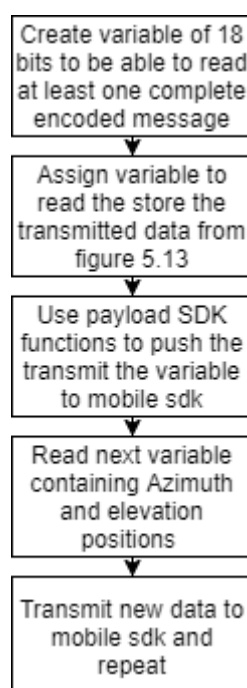
Fig 5.15: PSDK code is responsible for storing incoming data into 18 bites before transferring to the mobile app.

The incoming data is stored as variable myReturn, before a type conversion is required to be compatible with transferring the data to the mobile app. Finally, the function PsdkAppFunc_TransferToApp transfers the data to the mobile app. The mobile SDK [199], allows customised mobile apps to be developed to suit the need of the user and includes multiple integral features required for our applications such as: high and low level flight control, aircraft state through sensor data, obstacle avoidance, mission control to autonomously set waypoints and drone status information such as battery levels. To implement the app into our application two methods were trialled. Both work from the same principle to calculate the position of the bee (Figure 5.16), however, how the system processes and acts on the data is implemented differently.
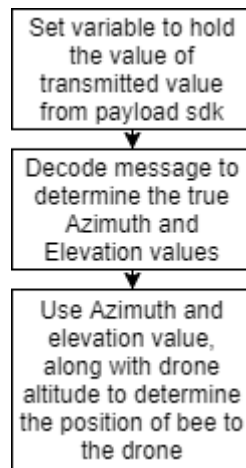
Fig 5.16: Method for determining bee position with respect to the drone.

The azimuth and elevation values are stored as variable coords [0] and coords [1] respectively. Using the altitude of the drone, the horizontal and vertical position of the bee relative to the drone can be determined. Finally, the variable tYaw is used to calculate the angle difference between the face of the drone and the bee in order to determine the new direction to which the drone must self-orientate. As we have previously demonstrated, estimating distance between Rx and Tx is not a reliable method to accurately predict distance. Assuming the bee to be the maximum possible distance away from the receive would allow for elimination in the drone undercompensating its positional updates. Any error associated with distance estimation could lead to the bee flying outside of the detection cone.

The first autonomous flight method followed the target by continuously adding waypoints to the mission flight. The idea relied on utilising functions prebuilt into the SDK such waypoint functions [200] built into the mobile sdk and customising them for the application. The data transferred from the drone to app was received, decoded, and logged in real-time (figure 5.17).

```
Update movement: Success
Azi = -25.0, Ele = 15.0
Yaw: -60.117516
Loc: ( 53.229459770314456, -4.12326487998704)
Alt: 1.0


Update movement: Success
Azi = 0.0, Ele = 15.0
Yaw: 0.0
Loc: ( 53.22946472705875, -4.123275715331181)
Alt: 1.0
```

Fig 5.17: Receiving data from receiver unit and decoding to estimate azimuth and elevation values for the target bee

By implementing the code shown in Figure 5.16, the distance between the drone and bee in x and y values can be determined, which were further converted to latitude and longitude coordinates.

The change in latitude and longitude was then applied to the current latitude and longitude to create a target position for the drone. The drone would follow the command and autonomously move towards (Figure 5.18). Figure 5.18 demonstrates the implementation of the tracking code in which a waypoint mission is defined, and the values are continuously updated in an attempt to autonomously follow the bearing of the target.
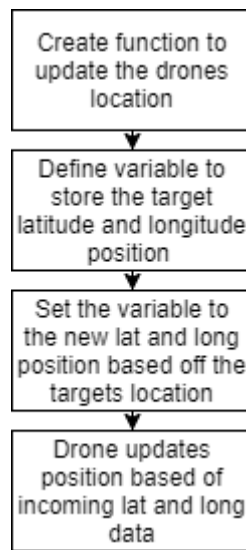
Fig 5.18: Using the change in latitude and longitude to calculate the position of the bee in latitude and longitude

Figure 5.19 shows the user interface which shows easy user operation with the addition of buttons to start and stop each functions as well as a log file which records all the recorded data from the receiver into a txt file which allows for further analysis of flight data after the simulated flights.
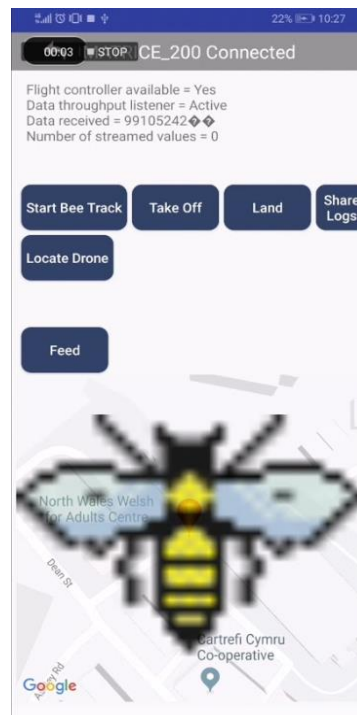
Fig 5.19: User interface of tracking code showing ease of operation

The functionality of the app was tested for any potential flaws before testing in a real environment using the DJI flight simulator. The azimuth and elevation of the bee was defined to be a random number between -50° and 50° in which the flight logs could later be compared to the flight path to confirm successful autonomous tracking (Figure 5.20).

Whilst the simulation was critical for proof of concept studies, flaws were identified which could significantly affect the system's ability to successfully track bees. Honeybees are known to fly up to 8m/s [201], however for waypoint flight the drone is unable to match the requirements of rapidly updating due to the waypoint function itself. Waypoints operate as a predefined flight path which cannot be stopped mid-operation. In order to start a new positional update, the last task must be completed in full. This means that any swift change in direction from the bee would likely result in the loss of signal due to delays in the drone's reaction time. Consequently, an alternative method without the reaction time limitations was required.

(a)
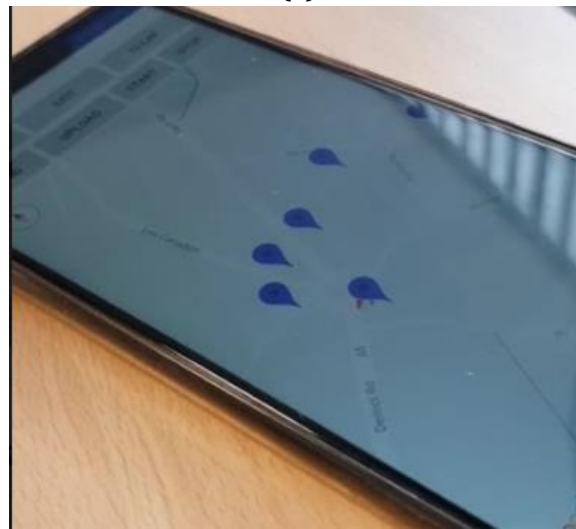
(b)

Fig 5.20: (a) Experimental set up of simulation model in which the drone is connected to a PC to simulate flight behaviour. (b) recorded flight path of autonomous test flight following its own waypoints based on the random values returned by the processing unit.

Human control flight to follow the signal is inherently limited by the operator's ability, however the use of virtual sticks addresses this issue. Virtual sticks are commands built into the mobile sdk which simulate manual flight by updating the drones pitch, roll and yaw [202]. By defining the required roll, pitch and yaw values, autonomous flight which resembles manual flight can be achieved.

Figure 5.21demonstrates the principle of autonomous virtual stick flight. The azimuth and elevation value are evaluated and converted into an angle difference between the drone and bee, along with a distance with the following equations:

```
┌─────────────────────┐
│   Define variables to│
│   represent the virtual│
│   stick movement of │
│   pitch, roll , yaw and│
│        throttle      │
└─────────────────────┘
           │
           ▼
┌─────────────────────┐
│   Implement mobile  │
│ sdk function to define│
│   the required flight│
│      control data    │
└─────────────────────┘
           │
           ▼
┌─────────────────────┐
│    Based on the     │
│   calculated bearing │
│   between bee and    │
│    drone, update the │
│    yaw accordingly so│
│   the drone faces the│
│        target        │
└─────────────────────┘
           │
           ▼
┌─────────────────────┐
│   Once complete,    │
│  increase throttle to│
│    move towards      │
│       bearing        │
└─────────────────────┘
           │
           ▼
┌─────────────────────┐
│   Once new position │
│   is calculated,    │
│   update yaw value  │
│   accordingly and   │
│        repeat        │
└─────────────────────┘
```

Fig 5.21: Implementation of virtual sticks with mobile sdk

The advantage of such an approach is that the drone operates each position update in two steps. Firstly, it updates its yaw to turn towards the bearing. Once the drone has updated its bearing, it will swiftly move forwards before receiving the next positional update. The new bearing will be calculated in which the drone will stop moving in a straight line and move towards a target. Implementing the same experimental set up as Figure 5.18, but replacing the waypoint operation with the virtual sticks, the drone attempted to follow a preprogramed flight route of a zig-zag line (Figure 5.22).
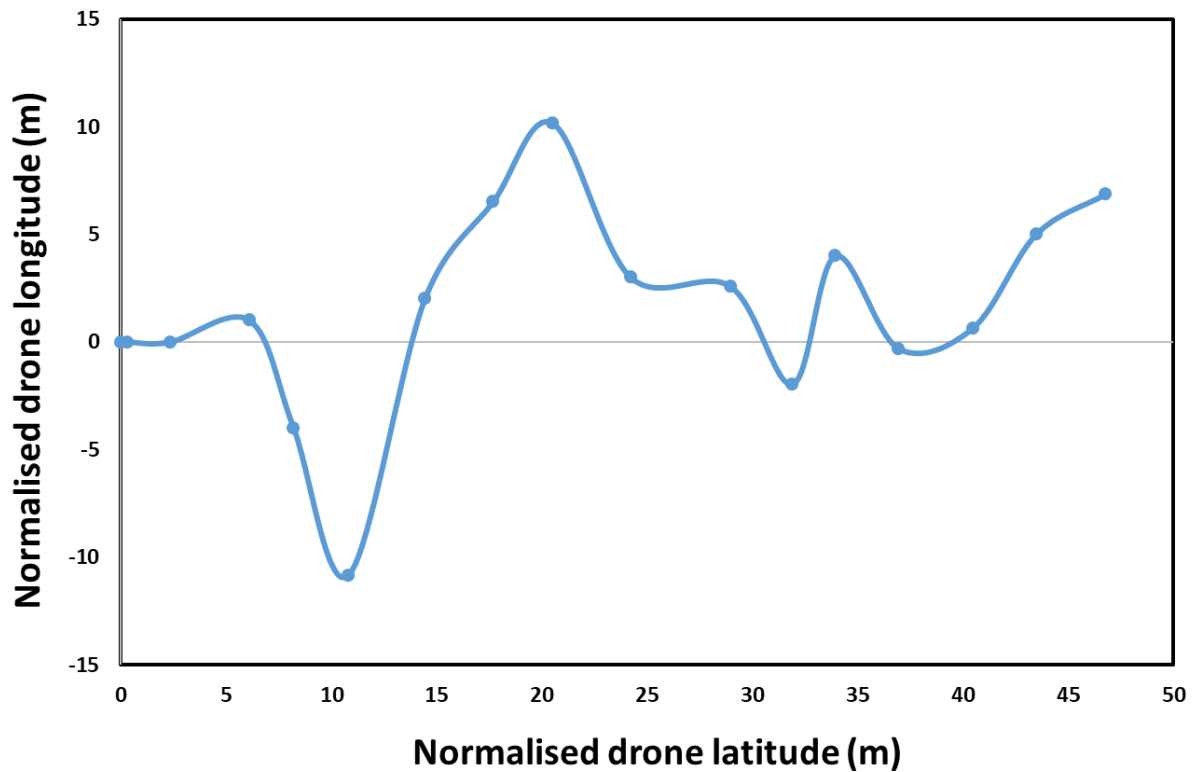
Fig 5.22: Simulated flight trajectory of the drone following a pre-programmed flight path

5.3 Autonomous tracking results

To test the accuracy of the system's ability to autonomously track targets, multiple experiments were defined to test the long-range tracking capabilities of the system. Firstly, the drone was set to a speed of approximately 2m/s to track moving students in a field. The student was equipped with a VCO transmitting at 5.8 GHz with a transmitted power of around -20 dBm and allowed to roam around a field in which the drone would follow. The bearing of the student calculated from the processing unit was fed to the app in which a positional update command (i.e turn x degrees and move forwards until next update) is transmitted back to the drone. The RSSI was condensed into a heat map, which displayed the estimated AOA in real time (Figure 5.23).
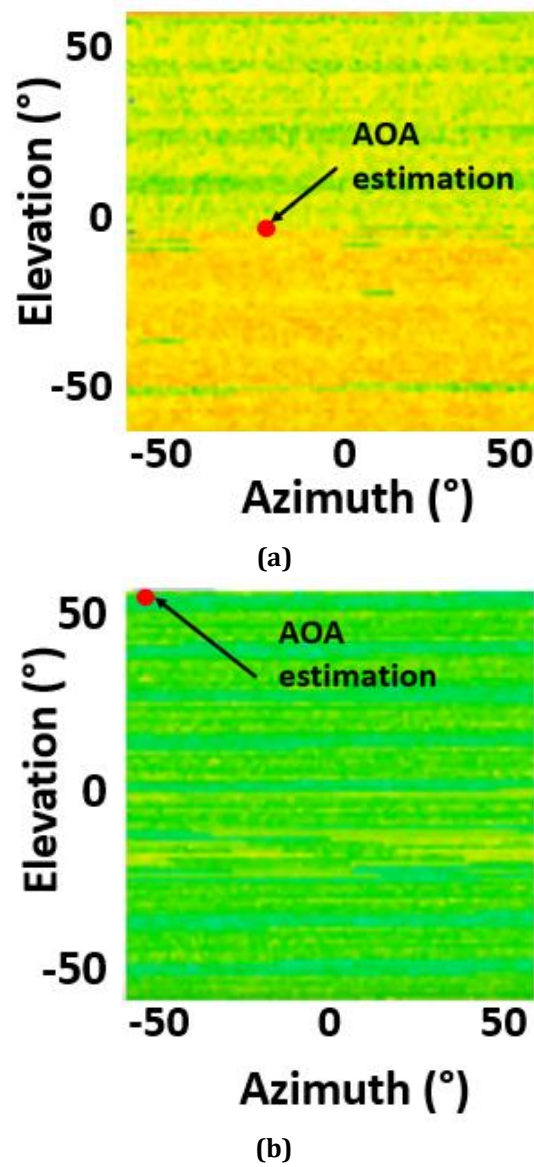
Fig 5.23: Real-time heat map outlining AOA estimates for the target's position.

Tracking tests were performed in which the drone's flight path followed the tag emitter and recorded both a linear and zig zag trajectory with an acceptable margin of error (+/-5°). The margin of error can be explained by the drone being programmed to simultaneously update its roll, pitch, and yaw, generating a deviation between the target and drone's path.
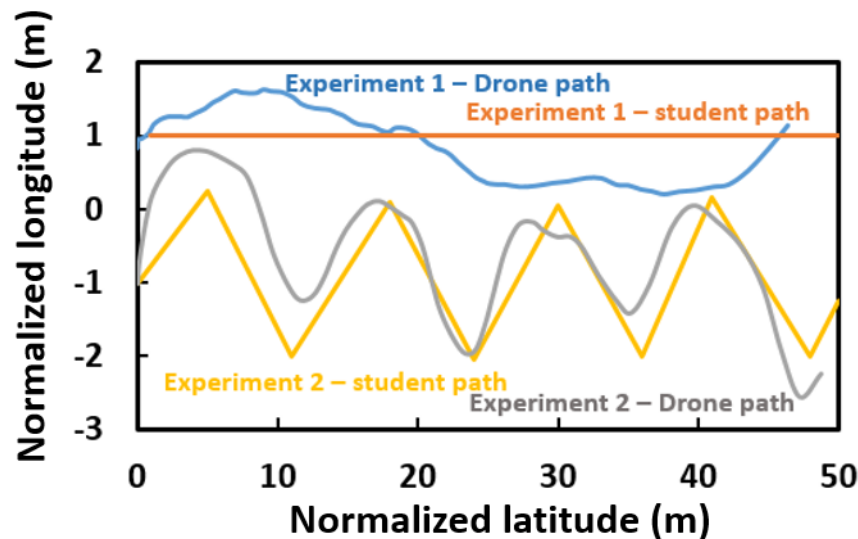
Fig 5.24: Update in drone's position whilst autonomously tracking student walking in designated paths with a handheld VCO.

Whilst the preliminary tests were limited to a 50 m range and up to 25% of typical bee flight speed, they suggest that long range tracking capabilities can be achieved with this approach providing the drone can maintain its distance within the detection area of the antenna.

The next step was to test the system with tagged bumblebees. The autonomous tracking performance involved releasing tagged bees in a plastic, semi-transparent container 25x15x10 cm³. The drone hovered at 15m altitude at several locations with horizontal projection ≤ 20m from the tagged bees. When the bee flapped its wings inside the box, the system was able to locate the target and autonomously move towards the location of the tagged bee. The drone updated its bearing and the internal log readings were plotted for two representative experiments (Figure 5.23).

Prior to the experiment, the received signal strength was calibrated so that any background reading was treated as no recorded bearing. This was an important step as the device's operation is contingent upon vibrations from the bee's thorax. Any readings during stationary activities (i.e. grooming and walking) would consist solely of background signals which would result in erroneous trajectories of the tracking drone, additionally resulting in the drone flying out of detection range of the tagged bee. To alleviate this issue calibration of the system is performed to determine the power level of background noise. The system is then accordingly updated to treat incoming signals with power levels within close approximation of the background noise as false readings.
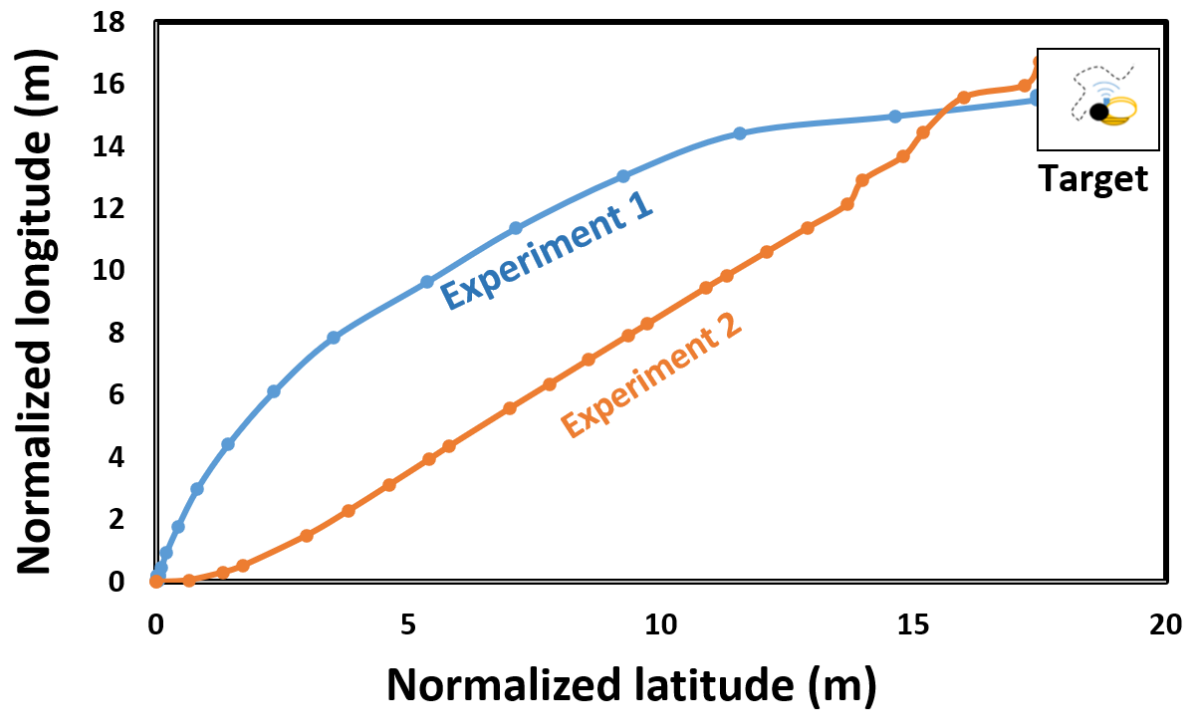
Fig 5.25: Update in drone's position over time, whilst autonomously tracking tagged bee flapping inside plastic container.

To conduct the experiment the bees were placed inside a semi-transparent container 25x15x10 cm^3, whilst the drone hovered at 15m in altitude and within the detection area of the bee when emitting a signal. The setup is displayed in figure 5.26

Fig 5.26: Experiment to test long-range bee tracking capabilities of autonomous system

5.4 Discussion and applications

Long range tracking studies of tagged bees were attempted whilst often achieving a relatively small autonomous tracking distance, however long-range tracking capabilities were demonstrated with a much slower target (moving student). Various drawbacks of the system have been identified which are capable of causing the error observed in tracking capabilities. Firstly, the acceleration of the drone to reach max flight speed introduces a lag between the bee and drone. This effect is critical for initial tracking as the drone must quickly determine the position of the bee and move towards its location before the bee flies outside of the detection range. Any delay in determining the direction, processing time and acceleration is likely to contribute to the drone lagging behind the bee. The delay between readings is then likely to lead to the loss of signal between drone and bee, resulting in the drone hovering in place. Additionally, the +/-5° angle of arrival error between Tx and Rx has been typically measured with a stationary target. During the scanning of azimuth and elevation, the tagged bee will be moving, which is likely to affect the angle vs RSSI scan. This ultimately determines the bearing of the target. The greater the AoA error, the less consistent the flight plan will be, as the drone will misestimate the bee's exact bearing. An accumulation of error could result in the bee eventually moving outside the detection range before the drone has had time to adjust its course. To achieve consistent long-range tracking capabilities with tagged insects, various approaches are being pursued which are highlighted within the future works. The approaches include machine learning to attempt to accurately predict the foraging behaviour and flight patterns to update the drone's position, increasing the processing speed of the system to attempt to minimise the lag between the drone and tagged insect.

The results presented in this chapter provide proof of concept of the autonomous tracking system, by demonstrating tracking capabilities with tagged bees and moving students, however, there are several system applications suitable for the study of bee movement, behaviour, and foraging. For example, the system described in this chapter would allow the tagging of wild foraging bumblebees and locating their nest sites. Similarly, locating Queen over-wintering sites are problematic as they are often hidden in field margin grass tufts or boundary walls. Their location and discovery in the spring is critical to understanding the impacts of neonicotinoid pesticides on their over-wintering survival. This application could also be extended to Asian Hornets by locating nest sites [203]. The autonomous tracking system presented here offers opportunities to monitor bee movement, behaviour, and foraging. Additionally, applications could extend, to the

monitoring of bees within the hive, however, such an approach is would currently be problematic due to the requirement of thorax vibrations to generate a signal. The limitation of signals would provide a limited resolution, however a possible application could be the monitoring a presence of the queen inside a hive, which has recently been explored by implementing radar approaches [204]

The chapter has discussed the integration of the tracking system with a UAV to achieve autonomous long-range tracking. In order to allow for efficient integration of drone and receiver, significant weight reduction was needed which was achieved using a stacked microstrip array with phase shifters integrated into the arrays feeding network. The system architecture has been discussed in which the AoA estimate was encrypted and transmitted to a mobile base station before a bearing and positional update was transmitted to the drone to update its yaw and pitch. Proof of concept was provided by demonstrating long-range tracking of a slow-moving student equipped with a 5.8 GHz VCO, whilst the concept was later demonstrated in tagged bees enclosed within a confined space. Current limitations of the system have been discussed which currently restrict the tracking capabilities of the drone, however, providing the issues can be overcome, the system has a vast amount of applications that it could be utilised for.

Chapter 6. Conclusion and future works

This chapter forms a review of the most important findings within the thesis. Current commercially available technology for radio telemetry studies are limited to larger insects due to the larger size of the tag, which mainly comprises of a small battery. Chapter two of the thesis focusses on addressing limitations associated the size and weight of radio telemetry tags by replacing the battery with a compact piezoelectric energy harvester capable of scavenging energy from the vibrations of insect flight. The increase of operational frequency additionally reduces the size and weight of the tag, however, consequently reduces the detection range between transmitter and receiver.

Chapters three and four address how the signal emitted from the self-powered radio telemetry tag can be detected and tracked via AoA estimates from the received signal strength. The use of an autonomously scanned antenna system allows for continuous non-obtrusive data collection from a single receiver without the need of human operation, thus, eliminating any human error associated with current state of the art techniques. The tracking of foraging bees within an enclosed netted tunnel and foraging environments was successfully demonstrated. The increased operational frequency of the system (5.8 GHz) in comparison to commercially available systems (300 MHz) allowed for substantial size reduction of the receiving antenna, thus allowing integration of the compact receiver system within commercial polytunnel. Such study is the first of its kind known to the author.

The increase in frequency and limitation in maximum harvestable power from the insect were shown to significantly reduce the link budget of the radio telemetry system in comparison to commercial systems. Chapter 5 focuses on demonstrating proof of principle of autonomous tracking with long range tracking capabilities. Previous radio telemetry studies utilising UAVS have been presented in which positional updates can take up to 60 seconds per reading. The use of a phased array antenna allows for significantly faster update times. Long range tracking capabilities was successfully demonstrated tracking slow moving targets.

The thesis focuses on adapting current radio telemetry systems to be capable of operating autonomous, and capable of being attached to the world's most economically beneficial insect, the honeybee. The results presented within the chapters act as a proof

of concept with potential for a range of applications within academic and commercial environments. Suggestions for future work are also given.

6.1 Vibration powered radio telemetry tag

Current radio telemetry technology is too cumbersome to be employed on tracking honeybees. This is because the on-board battery contributes most of the bulk mass of the tag. This can be eliminated via utilisation of the bees' own vibrational energy. The self-powered tag reduced the transmitter weight sufficiently to allow honeybees to fly. Current commercially available tags weight between 200 – 300mg whilst the tag presented within the thesis weighs 35 mg. The weight opens up a variety of insects that can be tracked that previously could not be due to limitations in the weight and size of the tag.

Due to the simple design, ease of fabrication and high voltage output, piezoelectric materials were chosen as they offer easy integration to small structures whilst providing high power output compared to electromagnetic and electrostatic devices.

An analysis of piezoelectric energy harvesting identified the need for a non-resonant energy harvesting approach due to the broadband wing beat frequency associated with bees. A solution to provide sufficient power output across the frequency range involved exciting the tip of the beam from the vibrations generated by the thorax. Utilising a finite element model, the trade-offs between device weight vs power output allowed the maximisation of energy harvester power output whilst minimising the weight of the energy harvester.

The design and fabrication of an initial prototype ~130 mg was demonstrated, which was used on larger species of bees (carpenter bees), whilst subsequent integration of a flexible substrate reduced the size and mass of the tag (~35 mg). Initial tests were performed to examine how the electromagnetic effects of the bee affected antenna and system performance.

Initial tests verified the transmission of a signal at 5.8 GHz using a spectrum analyser outlining successful operation of the self-powered transmitter tag, and thus providing proof of concept for the proposed design.

6.2 Localisation system calculating bees position based on AoA

Current radio-telemetry systems are generally inefficient as they require a user to determine the angle of arrive. Autonomous systems rely on utilising multiple receiver units equipped with omnidirectional antennas; however, the low gain of the antennas would result in insufficient detection range between transmitter and receiver. Additionally, the requirement of multiple receivers would not be compatible to integrate to a drone.

An analysis of methods for the localisation of RF signals was developed whereby a power based AoA was identified as the optimal technique requiring only a single antenna to determine the location of the signal. Further reviews of AoA using directional and omnidirectional antennas were conducted. Directional antennas were identified as a critical component of the system due to their higher gain which results in a significant detection range increase.

Power-based AoA systems can be used through either mechanical scanning or electronically with the implementation of a phase-shift to each element of an antenna array. Limitations in scanning in both azimuth and elevation planes highlighted the need for electronic scanning which can be used via an analogue and digital approach. A 4 x 4 element patch antenna array, capable of scanning +/-50° in azimuth and elevation, was designed and presented, whilst a reflection-type phase-shifter capable of 360° was presented to each element to provide the beam steering.

To determine the location of the RF signal, an LNA, logarithmic detector and microcontroller amplified, detected, recorded, and processed the incoming signal power level to determine the angle at which the maximum signal strength was received. Initial tests proved a system accuracy of +/- 5°.

The fabrication and testing of a slot fed phased array with phase shifters integrated into the feeding network was presented, which significantly decreased the weight of the receiver The results highlighted the capability of implementing phased array antennas in a compact design capable of UAV integration.

6.3 Autonomous tracking of tagged bees

The overall system operation was verified in two stages. Firstly, stationary testing verified the system's capacity to detect and track tagged bees. Using a netted tunnel to control the space in which flight occurred, tests confirmed the system's ability to detect

and determine the AoA of the signal within a 20m range. Further tests were then performed in which bumblebees were captured, tagged, and placed back in their nest. By visually monitoring the nest, the time of leaving and returning to the hive was determined. This was then compared to the data logged from the system to verify its ability to unobtrusively monitor the in goings and out goings of a foraging bumblebee. Commercial applications were demonstrated by monitoring a section of strawberry plants within a commercial polytunnel. Results show the successful detection of the signal. The received power at each angle of interest is processed to determine the bearing of the bee which can be used to monitor its foraging activity between flowers.

The final phase of the research focussed on the integration of the receiver unit to a UAV for long-range tracking. The system architecture to achieve autonomous flight based on AoA readings used virtual sticks to mimic manual flight controls. Bees were placed within small plastic containers, within the detection range of a hovering drone. The drone autonomously moved towards the target, thus verifying system functionality. The challenges of tracking fast moving targets flying outside the detection range of the drone, can lead to flaws within the system. Long range tracking capabilities were demonstrated with slow moving students equipped with an attenuated 5.8 GHz VCO emitting a power comparable to that of the tag, thus proving proof of concept.

6.4 Future works

Given further time, various RC values would be tested within the transmitter circuitry to determine the optimal pulse rate for autonomous tracking. Whilst faster pulses would be unable to accumulate as much energy, resulting in a smaller detection range between Tx and Rx, the increased frequency of bearings could help the drone remain within the detection range whilst providing more flight data points. Further work to improve the processing power and speed of the receiver system to match the faster pulses would additionally need to be addressed. Slower pulses would allow for an increase in the transmitted power, which would extend the detection range allowing the drone could hover and detect at a higher altitude. Consequently, the detection cone of the scanning system would increase the probability of the bee remaining within the detection range of the drone.

Additionally, further work would focus on developing a more accurate mechanical model of the of the piezoelectric cantilever, thus, allowing for a more accurate

approximation of the power output to be obtained. A two-body model considering the vibrations for the attachment rig and bee will be developed rather than assuming the support structure is rigid.

The next stage of research would focus on methods to distinguish between multiple signals, allowing the tracking of multiple tagged bees without them crossing paths. The current system would only identify the bee with the highest received power. A review of technologies to encode and decode signals would be required.

Additional work would look at further testing of the tag and receiver system in a lab environment to further understand the tags consistency and power output. The use of hexbugs [205] could be used to mimic the vibrations of bee flight whilst autonomously moving in random directions. Such an approach would act as an intermediate study of the tag and receiver's performance in a lab environment, additionally eliminating the complexities associated with testing the tag on live bees.

The phased array antenna is exposed to harsh conditions during its operational lifetime such as high winds, temperature, and humidity. As the phase shift relies on the capacitance of the varactor diode, environmental variables can potentially modify the capacitance of the complex load. The work would look at monitoring the reliability of the voltage vs capacitance relationship of the varactor diode over time. This would allow the identification of the maximum operation lifespan of the antenna. Further work to design and fabricate packaging for the antenna array could additionally extend the operational lifespan.

Additional focus will look at achieving consistent long-range tracking capabilities via the use of an artificial intelligence. The receiver system will not only have the capability to sense and estimate the insects' location, but to additionally predict the insects likely flight plans and smoothly tether the drone to the RF signal source to minimise the lag between drone and insect. Additionally, the use the multiple receivers combined together with an algorithm could be used increased spatial resolution in single insect tracking.

REFERENCES

[1]   C. A. Hallmann *et al.*, "More than 75 percent decline over 27 years in total flying insect biomass in protected areas," *PLoS One*, vol. 12, no. 10, 2017.

[2]   B. J. Cardinale *et al.*, "Citation for the published paper : Publishing Group . Epsilon Open Archive http://epsilon.slu.se Biodiversity loss and its impact on humanity," pp. 59–67, 2012.

[3]   F. Isbell *et al.*, "Linking the influence and dependence of people on biodiversity across scales," *Nature*, vol. 546, no. 7656, pp. 65–72, 2017.

[4]   S. A. Corbet, I. H. Williams, and J. L. Osborne, "Bees and the pollination of crops and wild flowers in the european community," *Bee World*, vol. 72, no. 2, pp. 47–59, 1991.

[5]   K. Stein *et al.*, "Bee pollination increases yield quantity and quality of cash crops in Burkina Faso, West Africa," *Sci. Rep.*, vol. 7, no. 1, pp. 1–10, 2017.

[6]   R. Winfree, J. R. Reilly, I. Bartomeus, D. P. Cariveau, N. M. Williams, and J. Gibbs, "Species turnover promotes the importance of bee diversity for crop pollination at regional scales," *Science (80-.).*, vol. 359, no. 6377, pp. 791–793, 2018.

[7]   S. R. Leather, "'Ecological Armageddon' – more evidence for the drastic decline in insect numbers," *Ann. Appl. Biol.*, vol. 172, no. 1, pp. 1–3, 2018.

[8]   G. Vogel, "Where have all the insects gone?," *Science (80-.).*, vol. 356, no. 6338, pp. 576–579, 2017.

[9]   W. Daniel Kissling, D. E. Pattemore, and M. Hagen, "Challenges and prospects in the telemetry of insects," *Biol. Rev.*, vol. 89, no. 3, pp. 511–530, 2014.

[10] J. Fischer, T. Müller, A. K. Spatz, U. Greggers, B. Grünewald, and R. Menzel, "Neonicotinoids interfere with specific components of navigation in honeybees," *PLoS One*, vol. 9, no. 3, pp. 1–10, 2014.

[11] C. Botías *et al.*, "Neonicotinoid Residues in Wildflowers, a Potential Route of Chronic Exposure for Bees," *Environ. Sci. Technol.*, vol. 49, no. 21, pp. 12731–12740, 2015.

[12] K. von Frisch, *The dance language and orientation of bees*. Cambridge: Harvard Univ. Press., 1967.

[13] T. Seeley, *Honeybee democracy*. Prinbceton, Oxford: Princeton University Press, 2011.

[14] C. Grüter and W. M. Farina, "The honeybee waggle dance: can we follow the steps?," *Trends Ecol. Evol.*, vol. 24, no. 5, pp. 242–247, 2009.

[15] R. Menzel, R. J. De Marco, and U. Greggers, "Spatial memory, navigation and dance behaviour in Apis mellifera," *J. Comp. Physiol. A Neuroethol. Sensory, Neural, Behav. Physiol.*, vol. 192, no. 9, pp. 889–903, 2006.

[16] R. Menzel, J. Fuchs, A. Kirbach, K. Lehmann, and U. Greggers, "Navigation and Communication in honeybees," in *Honeybee Neurobiology and Behavior*, Springer, 2012, pp. 103–116.

[17] D. Goulson, "Call to restrict neonicotinoids Science transcends cultures in Taiwan," *Science (80-.).*, vol. 360, no. 6392, 2018.

[18] A. Sobhakumari, R. Poppenga, and S. Tawde, *Avian Taxicology*. Vetinary Toxicology, 2018.

[19] T. Blacquière, G. Smagghe, C. A. M. Van Gestel, and V. Mommaerts, "Neonicotinoids in bees: A review on concentrations, side-effects and risk assessment," *Ecotoxicology*, vol. 21, no. 4, pp. 973–992, 2012.

[20] M. Henry *et al.*, "A common pesticide decreases foraging sucess and survival in Honey Bees," *Science*, vol. 336, no. April, pp. 3–5, 2012.

[21] R. J. Gill, O. Ramos-Rodriguez, and N. E. Raine, "Combined pesticide exposure severely affects individual-and colony-level traits in bees," *Nature*, vol. 491, no. 7422, pp. 105–108, 2012.

[22] L. Bortolotti, R. Montanari, J. Marcelino, P. Medrzycki, S. Maini, and C. Porrini, "Effects of sub-lethal imidacloprid doses on the homing rate and foraging activity of honey bees," *Bull. Insectology*, vol. 56, no. 1, pp. 63–67, 2003.

[23] C. Porrini, P. Medrzycki, R. Montanari, L. Bortolotti, A. G. Sabatini, and S. Maini, "Effects of imidacloprid administered in sub-lethal doses on honey bee behaviour. Laboratory tests," *Bull. Insectology*, vol. 56, no. January, pp. 59–62, 2003.

[24] J. W. Chapman, V. A. Drake, and D. R. Reynolds, "Recent Insights from Radar Studies of Insect Flight," *Annu. Rev. Entomol.*, vol. 56, no. 1, pp. 337–356, 2011.

[25] R. Menzel *et al.*, "A common frame of reference for learned and communicated vectors in honeybee navigation," *Curr. Biol.*, vol. 21, no. 8, pp. 645–650, 2011.

[26] U. Greggers, C. Schöning, J. Degen, and R. Menzel, "Scouts behave as streakers in

honeybee swarms," *Naturwissenschaften*, vol. 100, no. 8, pp. 805–809, 2013.

[27] S. Wolf *et al.*, "So near and yet so far: Harmonic radar reveals reduced homing ability of nosema infected honeybees," *PLoS One*, vol. 9, no. 8, 2014.

[28] D. MASCANZONI and H. WALLIN, "The harmonic radar: a new method of tracing insects in the field," *Ecol. Entomol.*, vol. 11, no. 4, pp. 387–390, 1986.

[29] M. Beekman and F. L. W. Ratnieks, "Long-range foraging by the honey-bee, Apis mellifera L.," *Funct. Ecol.*, vol. 14, no. 4, pp. 490–496, 2000.

[30] D. Psychoudakis, W. Moulder, C. C. Chen, H. Zhu, and J. L. Volakis, "A portable low-power harmonic radar system and conformal tag for insect tracking," *IEEE Antennas Wirel. Propag. Lett.*, vol. 7, pp. 444–447, 2008.

[31] M. E. O'Neal, D. A. Landis, E. Rothwell, L. Kempel, and D. Reinhard, "Tracking insects with harmonic radar: A case study," *Am. Entomol.*, vol. 50, no. 4, pp. 212–218, 2004.

[32] J. R. Riley and A. D. Smith, "Design considerations for an harmonic radar to investigate the flight of insects at low altitude," *Comput. Electron. Agric.*, vol. 35, no. 2–3, pp. 151–169, 2002.

[33] H. M. Aumann, "Comments on 'a high-range-accuracy and high-sensitivity harmonic radar using pulse pseudorandom code for bee searching,'" *IEEE Trans. Microw. Theory Tech.*, vol. 61, no. 12, p. 4285, 2013.

[34] N. Tahir and G. Brooker, "Recent developments and recommendations for improving harmonic radar tracking systems," *Proc. 5th Eur. Conf. Antennas Propagation, EUCAP 2011*, pp. 1531–1535, 2011.

[35] J. R. Riley, A. D. Smith, D. R. Reynolds, and A. S. Edwards, "Tracking bees with harmonic radar," *Nature*, vol. 379, no. 6560, p. 29, 1996.

[36] D. Milanesio, M. Saccani, R. Maggiora, D. Laurino, and M. Porporato, "Design of an harmonic radar for the tracking of the Asian yellow-legged hornet," *Ecol. Evol.*, vol. 6, no. 7, pp. 2170–2178, 2016.

[37] P. H. Jau *et al.*, "Signal processing for harmonic pulse radar based on spread spectrum technology," *IET Radar, Sonar Navig.*, vol. 8, no. 3, pp. 242–250, 2014.

[38] Z. M. Tsai *et al.*, "A high-range-accuracy and high-sensitivity harmonic radar using pulse pseudorandom code for bee searching," *IEEE Trans. Microw. Theory Tech.*, vol. 61, no. 1, pp. 666–675, 2013.

[39] D. . Pozar, *Microwave Engineering*. Toronto: Wiley, 1998.

[40] A. Singh and V. M. Lubecke, "Respiratory monitoring and clutter rejection using a CW doppler radar with passive RF tags," *IEEE Sens. J.*, vol. 12, no. 3, pp. 558–565, 2012.

[41] N. Tahir and G. Brooker, "Millimetre wave band unbiased harmonic transponder," *Int. Conf. Infrared, Millimeter, Terahertz Waves, IRMMW-THz*, pp. 1–2, 2012.

[42] S. Cheng, P. Hallbjörner, and A. Rydberg, "Array antenna for body-worn automotive harmonic radar tag," *Eur. Conf. Antennas Propagation, EuCAP 2009, Proc.*, pp. 2823–2827, 2009.

[43] B. G. Colpitts and G. Boiteau, "Harmonic radar transceiver design: Miniature tags for insect tracking," *IEEE Trans. Antennas Propag.*, vol. 52, no. 11, pp. 2825–2832, 2004.

[44] G. Charvat, E. Rothwell, and L. Kempel, "Harmonic Radar Tag Measuremnt and Characterization," in *IEEE Antennas and Propagation Society International Symposium*, 2003, no. 1, pp. 179–191.

[45] R. . Hansen, "Fundamental limitations in antennas," *Proc. IEEE*, vol. 69, no. 2, pp. 170–182, 1981.

[46] K. Rasilainen and V. V. Viikari, "Transponder Designs for Harmonic Radar Applications," *Int. J. Antennas Propag.*, vol. 2015, 2015.

[47] D. Dardari, "Detection and accurate localization of harmonic chipless tags," *EURASIP J. Adv. Signal Process.*, vol. 2015, no. 1, 2015.

[48] M. A. Flemming, F. H. Mullins, and A. W. Watson, "Harmonic radar detection systems," in *Internation conference radar*, 1977, pp. 552–554.

[49] J. L. Woodgate, J. C. Makinson, K. S. Lim, A. M. Reynolds, and L. Chittka, "Life-long radar tracking of bumblebees," *PLoS One*, vol. 11, no. 8, pp. 1–22, 2016.

[50] J. L. Osborne *et al.*, "A landscape-scale study of bumble bee foraging range and constancy, using harmonic radar," *J. Appl. Ecol.*, vol. 36, no. 4, pp. 519–533, 1999.

[51] E. A. Capaldi *et al.*, "Ontogeny of orientation flight in the honeybee revealed by harmonic radar," *Nature*, vol. 403, no. 6769, pp. 537–540, 2000.

[52] D. Milanesio, M. Saccani, R. Maggiora, D. Laurino, and M. Porporato, "Recent upgrades of the harmonic radar for the tracking of the Asian yellow-legged hornet,"

Ecol. Evol., vol. 7, no. 13, pp. 4599–4606, 2017.

[53] R. Maggiora, M. Saccani, D. Milanesio, and M. Porporato, "An Innovative Harmonic Radar to Track Flying Insects: the Case of Vespa velutina," *Sci. Rep.*, vol. 9, no. 1, pp. 1–10, 2019.

[54] J. W. Lee, H. Kwon, and B. Lee, "Design consideration of UHF RFID tag for increased reading range," *IEEE MTT-S Int. Microw. Symp. Dig.*, pp. 1588–1591, 2006.

[55] M. Donelli and M. Manekiya, "Development of environmental long range RFID sensors based on the modulated scattering technique," *Electron.*, vol. 7, no. 7, 2018.

[56] J. Wang, J. Zhang, I. Nsdi, and J. Wang, "Pushing the Range Limits of Commercial Passive RFIDs This paper is included in the Proceedings of the," *Nsdi*, 2019.

[57] M. Pahl, H. Zhu, J. Tautz, and S. Zhang, "Large scale homing in honeybees," *PLoS One*, vol. 6, no. 5, pp. 1–7, 2011.

[58] P. de Souza *et al.*, "Low-cost electronic tagging system for bee monitoring," *Sensors (Switzerland)*, vol. 18, no. 7, pp. 1–21, 2018.

[59] E. J. H. Robinson, F. D. Smith, K. M. E. Sullivan, and N. R. Franks, "Do ants make direct comparisons?," *Proc. R. Soc. B Biol. Sci.*, vol. 276, no. 1667, pp. 2635–2641, 2009.

[60] A. H. Easton and D. Goulson, "The Neonicotinoid Insecticide Imidacloprid Repels Pollinating Flies and Beetles at Field-Realistic Concentrations," *PLoS One*, vol. 8, no. 1, pp. 8–11, 2013.

[61] D. E. Silcox, J. P. Doskocil, C. E. Sorenson, and R. L. Brandenburg, "Radio frequency identification tagging: A novel approach to monitoring surface and subterranean insects," *Am. Entomol.*, vol. 57, no. 2, pp. 86–93, 2011.

[62] C. W. Schneider, J. Tautz, B. Grünewald, and S. Fuchs, "RFID tracking of sublethal effects of two neonicotinoid insecticides on the foraging behavior of Apis mellifera," *PLoS One*, vol. 7, no. 1, pp. 1–9, 2012.

[63] X. He, W. Wang, Q. Qin, Z. Zeng, S. Zhang, and A. B. Barron, "Assessment of flight activity and homing ability in Asian and European honey bee species, Apis cerana and Apis mellifera, measured with radio frequency tags," *Apidologie*, vol. 44, no. 1, pp. 38–51, 2013.

[64] P. Nunes-Silva *et al.*, "Applications of RFID technology on the study of bees," *Insectes Soc.*, vol. 66, no. 1, pp. 15–24, 2019.

[65] P. Tenczar, C. C. Lutz, V. D. Rao, N. Goldenfeld, and G. E. Robinson, "Automated monitoring reveals extreme interindividual variation and plasticity in honeybee foraging activity levels," *Anim. Behav.*, vol. 95, pp. 41–48, 2014.

[66] A. Decourtye *et al.*, "Honeybee tracking with microchips: A new methodology to measure the effects of pesticides," *Ecotoxicology*, vol. 20, no. 2, pp. 429–437, 2011.

[67] A. Van Geystelen, K. Benaets, D. C. de Graaf, M. H. D. Larmuseau, and T. Wenseleers, "Track-a-Forager: a program for the automated analysis of RFID tracking data to reconstruct foraging behaviour," *Insectes Soc.*, vol. 63, no. 1, pp. 175–183, 2016.

[68] U. Engelke, H. Hutson, H. Nguyen, and P. De Souza, "MelissAR: Towards augmented visual analytics of honey bee behaviour," *Conf. Hum. Factors Comput. Syst. - Proc.*, vol. 07-12-May-, pp. 2057–2063, 2016.

[69] S. E. Barlow, M. A. O'Neill, and B. M. Pavlik, "A prototype RFID tag for detecting bumblebee visitations within fragmented landscapes," *J. Biol. Eng.*, vol. 13, no. 1, pp. 1–6, 2019.

[70] M. Molet, L. Chittka, R. J. Stelzer, S. Streit, and N. E. Raine, "Colony nutritional status modulates worker responses to foraging recruitment pheromone in the bumblebee Bombus terrestris," *Behav. Ecol. Sociobiol.*, vol. 62, no. 12, pp. 1919–1926, 2008.

[71] K. Ohashi, D. D'Souza, and J. D. Thomson, "An automated system for tracking and identifying individual nectar foragers at multiple feeders," *Behav. Ecol. Sociobiol.*, vol. 64, no. 5, pp. 891–897, 2010.

[72] F. Craighead and J. Craighead, "Tracking Grizzly Bears," *Bioscience*, vol. 15, no. 2, pp. 88–92, 2016.

[73] W. W. Cochran and R. D. Lord, "A Radio-Tracking System for Wild Animals," *J. Wildl. Manage.*, vol. 27, no. 1, p. 9, 1963.

[74] R. MACKAY, "Galapagos tortoise and Marine Iguana Deep Body Temperatures Measured by radio Telemtry," *Nature*, vol. 204, no. 4956, pp. 355–358, 1964.

[75] S. J. Cooke *et al.*, "Biotelemetry: A mechanistic approach to ecology," *Trends Ecol. Evol.*, vol. 19, no. 6, pp. 334–343, 2004.

[76] S. Levett and S. Walls, "Tracking the elusive life of the Emperor Dagonfly Anax imperator Leach," *J. Br. Dragonfly Soc.*, vol. 27, no. 1, pp. 59–68, 2011.

[77] C. D. Kelly, L. F. Bussière, and D. T. Gwynne, "Sexual selection for male mobility in a

giant insect with female-biased size dimorphism," *American Naturalist*, vol. 172, no. 3. pp. 417–423, 2008.

[78]   D. . Gilmer, L. . Cowardin, R. . Duval, L. . Mechlin, C. . Schaiffer, and V. . Kuechle, *Procedures for the use of aircraft in wildlife biotelemetry studies*. U.S. Fish and Wildl. Serv. Resour. Publ, 1981.

[79]   P. J. Seddon and R. F. Maloney, "Tracking wildlife radio-tag signals by light fixed-wing aircraft," *Depattment Conserv. Tech. Ser. 30*, no. October, pp. 1–23, 2004.

[80]   N. Duda *et al.*, "Bats: Adaptive ultra low power sensor network for animal tracking," *Sensors (Switzerland)*, vol. 18, no. 10, 2018.

[81]   Lotek.com,   "No   Title,"   2019.   [Online].   Available: www.lotek.com/products/nanotags.

[82]   I. A. T. Systems, "Fish and Wildlife VHF Transmitter Series," 2019. [Online]. Available: www. atstrack.com/tracking-products/transmitters.

[83]   M. Wikelski *et al.*, "Large-range movements of neotropical orchid bees observed via radio telemetry," *PLoS One*, vol. 5, no. 5, pp. 5–10, 2010.

[84]   G. F. Dubois, V. Vignon, Y. R. Delettre, Y. Rantier, P. Vernon, and F. Burel, "Factors affecting the occurrence of the endangered saproxylic beetle Osmoderma eremita (Scopoli, 1763) (Coleoptera: Cetoniidae) in an agricultural landscape," *Landsc. Urban Plan.*, vol. 91, no. 3, pp. 152–159, 2009.

[85]   M. Wikelski, D. Moskowitz, J. S. Adelman, J. Cochran, D. S. Wilcove, and M. L. May, "Simple rules guide dragonfly migration," *Biol. Lett.*, vol. 2, no. 3, pp. 325–329, 2006.

[86]   C. Watts, R. Empson, D. Thornburrow, and M. Rohan, "Movements, behaviour and survival of adult Cook Strait giant weta (Deinacrida rugosa; Anostostomatidae: Orthoptera) immediately after translocation as revealed by radiotracking," *J. Insect Conserv.*, vol. 16, no. 5, pp. 763–776, 2012.

[87]   R. S. Pasquet *et al.*, "Long-distance pollen flow assessment through evaluation of pollinator foraging range suggests transgene escape distances," *Proc. Natl. Acad. Sci. U. S. A.*, vol. 105, no. 36, pp. 13456–13461, 2008.

[88]   M. Hagen, M. Wikelski, and W. D. Kissling, "Space use of bumblebees (Bombus spp.) revealed by radio-tracking," *PLoS One*, vol. 6, no. 5, 2011.

[89]   P. J. Kennedy, S. M. Ford, J. Poidatz, D. Thiéry, and J. L. Osborne, "Searching for nests

of the invasive Asian hornet (Vespa velutina) using radio-telemetry," *Commun. Biol.*, vol. 1, no. 1, 2018.

[90]   "Day 2 on the front line fighting Asian hornets in Jersey," *Somerset Beekeepers association*,   2019.   [Online].   Available: https://www.somersetbeekeepers.org.uk/members-blog/day-2-on-the-front-line-fighting-asian-hornets-in-jersey.

[91]   R. Dudley, "Extraordinary flight performance of orchid bees (Apidae: Euglossini) hovering in heliox (80% He/20% O2)," *J. Exp. Biol.*, vol. 198, no. 4, pp. 1065–1070, 1995.

[92]   E. A. Capaldi and F. C. Dyer, "The role of orientation flights on homing performance in honeybees," *J. Exp. Biol.*, vol. 202, no. 12, pp. 1655–1666, 1999.

[93]   D. Goulson and J. C. Stout, "Homing ability of the bumblebee Bombus terrestris (Hymenoptera: Apidae)," *Apidologie*, vol. 32, no. 1, pp. 105–111, 2001.

[94]   L. McKendrick *et al.*, "Microsatellite analysis supports the existence of three cryptic species within the bumble bee Bombus lucorum sensu lato," *Conserv. Genet.*, vol. 18, no. 3, pp. 573–584, 2017.

[95]   S. Le Conte, S. Vaiedelich, J. H. Thomas, V. Muliava, D. de Reyer, and E. Maurin, "Acoustic emission to detect xylophagous insects in wooden musical instrument," *J. Cult. Herit.*, vol. 16, no. 3, pp. 338–343, 2015.

[96]   S. S. Greenleaf, N. M. Williams, R. Winfree, and C. Kremen, "Bee foraging ranges and their relationship to body size," *Oecologia*, vol. 153, no. 3, pp. 589–596, 2007.

[97]   L. Mei *et al.*, "Agricultural pest monitoring using fluorescence lidar techniques Feasibility study," *Appl. Phys. B Lasers Opt.*, vol. 106, no. 3, pp. 733–740, 2012.

[98]   E. R. Mullen, P. Rutschman, N. Pegram, J. M. Patt, J. J. Adamczyk, and Johanson, "Laser system for identification, tracking, and control of flying insects," *Opt. Express*, vol. 24, no. 11, p. 11828, 2016.

[99]   D. Heise, Z. Miller, E. Harrison, A. Gradisek, J. Grad, and C. Galen, "Acoustically Tracking the Coming and Goings of Bumblebees," in *IEEE Sensor Applications Symposium*, 2019, pp. 1–6.

[100] S. Ferrari, M. Silva, M. Guarino, and D. Berckmans, "Monitoring of swarming sounds in bee hives for early detection of the swarming period," *Comput. Electron. Agric.*,

vol. 64, no. 1, pp. 72–77, 2008.

[101] J. A. Shaw *et al.*, "Polarization lidar measurements of honey bees in flight for locating land mines," *Opt. Express*, vol. 13, no. 15, p. 5853, 2005.

[102] J. R. Hagler and C. G. Jackson, "Methods For Marking Insects : Current Techniques and Future Prospects," *Annu. Rev. Entomol.*, vol. 46, no. 1, pp. 511–543, 2001.

[103] G. Pyke, H. Pulliam, and E. Charnov, "Optimal Foraging: A Selective Review of Theory and Tests," *Q. Rev. Biol.*, vol. 52, no. 1, pp. 137–154, 1977.

[104] C. Guédot, J. Bosch, and W. P. Kemp, "Relationship between body size and homing ability in the genus Osmia (Hymenoptera; Megachilidae)," *Ecol. Entomol.*, vol. 34, no. 1, pp. 158–161, 2009.

[105] H. Weimerskirch, F. Bonadonna, F. Bailleul, G. Mabille, G. Dell'Omo, and H. P. Lipp, "GPS tracking of foraging albatrosses," *Science (80-.).*, vol. 295, no. 5558, p. 1259, 2002.

[106] J. C. Evans, S. R. X. Dall, M. Bolton, E. Owen, and S. C. Votier, "Gemeinsame nahrungssuche bei krahenscharben: GPS ortung zeigt, dass sich vogel benachbarter kolonien nahrungsgebiete teilen," *J. Ornithol.*, vol. 157, no. 1, pp. 23–32, 2016.

[107] R. Silva, I. Afán, J. A. Gil, and J. Bustamante, "Seasonal and circadian biases in bird tracking with solar GPS-tags," *PLoS One*, vol. 12, no. 10, pp. 1–19, 2017.

[108] B. Habib, S. Shrotiya, K. Sivakumar, P. Sinha, and V. Mathur, "Three decades of wildlife radio telemetry in India: a review," *Anim. Biotelemtry*, vol. 2, no. 1, p. 4, 2014.

[109] M. Takeuchi, S. Matsuzawa, K. Tairaku, and C. Takatsu, "Piezoelectric generator as power supply for RFID-tags and applications," *Proc. - IEEE Ultrason. Symp.*, pp. 2558–2561, 2007.

[110] M. M. Snowdon, J. Horne, B. Gyr, and Y. Jia, "Feasibility of vibration energy harvesting powered wireless tracking of falcons in flight," *J. Phys. Conf. Ser.*, vol. 1052, no. 1, 2018.

[111] D. R. Patton, D. W. Beaty, and R. H. Smith, "Solar Panels : An Energy Source for Radio Transmitters on Wildlife," *J. Wildl. Manage.*, vol. 37, no. 2, pp. 236–238, 2019.

[112] S. C. Chang, F. M. Yaul, F. O. Sullivan, D. M. Otten, J. H. Lang, and E. Initiative, "Harvesting Energy from moth vibrations during flight," *Int. Work. Micro*

Nanotechnologies Power Gener. Energy Convers. Appl., pp. 3–6, 2009.

[113] E. E. Aktakka, H. Kim, and K. Najafi, "Energy scavenging from insect flight," *J. Micromechanics Microengineering*, vol. 21, no. 9, 2011.

[114] H. Li *et al.*, "An Energy Harvesting Underwater Acoustic Transmitter for Aquatic Animals," *Sci. Rep.*, vol. 6, no. August, pp. 1–9, 2016.

[115] L. Capineri, L. Masotti, V. Ferrari, D. Marioli, A. Taroni, and M. Mazzoni, "Comparisons between PZT and PVDF thick films technologies in the design of low-cost pyroelectric sensors," *Rev. Sci. Instrum.*, vol. 75, no. 11, pp. 4906–4910, 2004.

[116] Y. Lu, F. Marty, D. Galayko, J.-M. Laheurte, and P. Basset, "A MEMS EVEH-Assisted Long-Range RFID Tag System for Applications with Low-Frequency Vibrations," *Proceedings*, vol. 1, no. 10, p. 582, 2017.

[117] Y. Chen, D. Liu, S. Wang, Y. Li, and X. Zhang, "Self-powered smart active RFID tag integrated with wearable hybrid nanogenerator," *Nano Energy*, vol. 64, p. 103911, 2019.

[118] R. Kays *et al.*, "Tracking animal location and activity with an automated radio telemetry system in a tropical rainforest," *Comput. J.*, vol. 54, no. 12, pp. 1931–1948, 2011.

[119] K. Stark, G. Jackson, and J. Lyle, "Tracking arrow squid movements with an automated accoustic telemtry system," *Mar. Ecol. Prog. Ser.*, vol. 299, pp. 167–177, 2005.

[120] W. W. Cochran, D. Warner, J. Tester, and V. Kuechle, "Automatic Radio-Tracking System for Monitoring Animal Movements," *Bioscience*, vol. 15, no. 2, pp. 98–100, 1965.

[121] R. Kenward, *A manual of wildlife radio tagging*. Boston, Mass: AP Professional, 2001.

[122] S. W. Searcy, J. K. Schueller, Y. H. Bae, and B. A. Stout, "Measurement of agricultural field location using microwave frequency triangulation," *Comput. Electron. Agric.*, vol. 4, no. 3, pp. 209–223, 1990.

[123] D. Doak, "Spotted Owls and Old Growth Logging in the Pacific Northwest," *Conserv. Biol.*, vol. 3, no. 4, pp. 389–396, 1989.

[124] K. J. Krizman, T. E. Biedka, and T. S. Rappaport, "Wireless position location: Fundamentals, implementation strategies, and sources of error," *IEEE Veh. Technol.*

Conf., vol. 2, pp. 919–923, 1997.

[125] M. Malajner, P. Planinsic, and D. Gleich, "Angle of arrival estimation using RSSI and omnidirectional rotatable antennas," *IEEE Sens. J.*, vol. 12, no. 6, pp. 1950–1957, 2012.

[126] H. C. Chen, T. H. Lin, H. T. Kung, C. K. Lin, and Y. Gwon, "Determining RF angle of arrival using COTS antenna arrays: A field evaluation," *Proc. - IEEE Mil. Commun. Conf. MILCOM*, pp. 1–6, 2012.

[127] E. Neill and P. Jansen, "Ground-based radio tracking: a best practice protocol," *Terr. Ecosyst. Unit, Sci. Capab. Gr.*, 2014.

[128] C. Real Ehrlich and J. Blankenbach, "Indoor localization for pedestrians with real-time capability using multi-sensor smartphones," *Geo-Spatial Inf. Sci.*, vol. 22, no. 2, pp. 73–88, 2019.

[129] R. Boddington, "An Analysis of Triangulation Techniques for Radio-Telemetry An Analysis of Triangulation Techniques for Radio-Telemetry," no. February 2017, 2018.

[130] M. W. Shafer, G. Vega, K. Rothfus, and P. Flikkema, "UAV wildlife radiotelemetry: System and methods of localization," *Methods Ecol. Evol.*, vol. 10, no. 10, pp. 1783–1795, 2019.

[131] P. Soriano, F. Caballero, and A. Ollero, "RF-based particle filter loclization for wildlife tracking using an UAV," in *IEEE Intelligence and saftey for robotics*, 2009, pp. 239–244.

[132] O. M. Cliff, R. Fitch, S. Sukkarieh, D. L. Saunders, and R. Heinsohn, "Online localization of radio-tagged wildlife with an autonomous aerial robot system," *Robot. Sci. Syst.*, vol. 11, 2015.

[133] H. Van Nguyen, M. Chesser, L. P. Koh, S. H. Rezatofighi, and D. C. Ranasinghe, "TrackerBots: Autonomous unmanned aerial vehicle for real-time localization and tracking of multiple radio-tagged animals," *Journal of Field Robotics*, vol. 36, no. 3. pp. 617–635, 2019.

[134] W. K. G. Seah, A. E. Zhi, and H. P. Tan, "Wireless Sensor Networks Powered by Ambient Energy Harvesting (WSN-HEAP) - Survey and challenges," *Proc. 2009 1st Int. Conf. Wirel. Commun. Veh. Technol. Inf. Theory Aerosp. Electron. Syst. Technol.*

Wirel. VITAE 2009, pp. 1–5, 2009.

[135] K. Tutuncuoglu and A. Yener, "Optimum transmission policies for battery limited energy harvesting nodes," *IEEE Trans. Wirel. Commun.*, vol. 11, no. 3, pp. 1180–1189, 2012.

[136] A. Nechibvute, A. Chawanda, and P. Luhanga, "Piezoelectric Energy Harvesting Devices: An Alternative Energy Source for Wireless Sensors," *Smart Mater. Res.*, vol. 2012, pp. 1–13, 2012.

[137] D. Shen, "Piezoelectric Energy Harvesting Devices for Low Frequency Vibration Applications," *Thesis*, p. 195, 2009.

[138] S. Rafique, *Piezoelectric Vibration Energy Harvesting: Modelling & Experiments*. Springer, 2017.

[139] C. Wei and X. Jing, "A comprehensive review on vibration energy harvesting: Modelling and realization," *Renewable and Sustainable Energy Reviews*. 2017.

[140] S. Boisseau, G. Despesse, and B. Ahmed, "Electrostatic Conversion for Vibration Energy Harvesting," *Small-Scale Energy Harvest.*, pp. 1–39, 2012.

[141] S. Moheimani and A. Fleming, *Piezoelectric Transducers For Vibration Control and Damping*. 2006.

[142] C. Wei and X. Jing, "A comprehensive review on vibration energy harvesting: Modelling and realization," *Renew. Sustain. Energy Rev.*, vol. 74, no. February, pp. 1–18, 2017.

[143] R. Hosseini and M. Hamedi, "Resonant frequency of bimorph triangular V-shaped piezoelectric cantilever energy harvester," *J. Comput. Appl. Res. Mech. Eng.*, vol. 6, no. 1, pp. 65–73, 2016.

[144] D. D. S. Marinho, F. R. Pinto, and E. R. Baptista, "Piezoelectric effect as an energy generator : A describal historic of its performance," vol. 6495, no. 11, pp. 228–232, 2019.

[145] "No Title," 2020. [Online]. Available: www.piezo.com.

[146] M. W. Barsoum, *Fundamentals of Ceramics*. IOP Publishing Ltd, 2003.

[147] S. Priya *et al.*, "A Review on Piezoelectric Energy Harvesting: Materials, Methods, and Circuits," *Energy Harvest. Syst.*, vol. 4, no. 1, pp. 3–39, 2017.

[148] H. S. Kim, J. H. Kim, and J. Kim, "A review of piezoelectric energy harvesting based on vibration," *Int. J. Precis. Eng. Manuf.*, vol. 12, no. 6, pp. 1129–1141, 2011.

[149] S. Priya and D. J. Inman, *Energy Harvesting Technologies*. Springer.

[150] M. J. Guan and W. H. Liao, "Characteristics of energy storage devices in piezoelectric energy harvesting systems," *J. Intell. Mater. Syst. Struct.*, vol. 19, no. 6, pp. 671–680, 2008.

[151] S. P. Machado, M. Febbo, C. D. Gatti, and J. M. Ramirez, "Non-resonant energy harvester with elastic constraínts for low rotating frequencies," *J. Phys. Conf. Ser.*, vol. 922, no. 1, 2017.

[152] A. Frey, J. Seidel, M. Schreiter, and I. Kuehne, "Piezoelectric MEMS energy harvesting module based on non-resonant excitation," *2011 16th Int. Solid-State Sensors, Actuators Microsystems Conf. TRANSDUCERS'11*, pp. 683–686, 2011.

[153] J. R. Coelho, "The Effect of Thorax Temperature on Force Production during Tethered Flight in Honeybee (Apis mellifera) Drones , Workers , and Queens," *Physiol. Zool.*, vol. 64, no. 3, 1991.

[154] "PMEG4002EL data sheet." [Online]. Available: https://docs.rs-online.com/a49e/0900766b80b367e2.pdf.

[155] B. Naef-Daenzer, D. Früh, M. Stalder, P. Wetli, and E. Weise, "Miniaturization (0.2 g) and evaluation of attachment techniques of telemetry transmitters," *J. Exp. Biol.*, vol. 208, no. 21, pp. 4063–4068, 2005.

[156] "2390A Series Spectrum Analyser." .

[157] A. K. Lenske and J. J. Nocera, "Field test of an automated radio-telemetry system: tracking local space use of aerial insectivores," *J. F. Ornithol.*, vol. 89, no. 2, pp. 173–187, 2018.

[158] I. Uchendu and J. Kelly, "Survey of beam steering techniques available for millimeter wave applications," *Prog. Electromagn. Res. B*, vol. 68, no. 1, pp. 35–54, 2016.

[159] Centre for severe weather research, "The DOWs," 2019. [Online]. Available: http://www.cswr.org/contents/aboutdows.html.

[160] X. Wu and J. J. Laurin, "Fan-beam millimeter-wave antenna design based on the cylindrical Luneberg lens," *IEEE Trans. Antennas Propag.*, vol. 55, no. 8, pp. 2147–2156, 2007.

[161] Y. A. Litinskaya, A. M. Alexandrin, K. V. Lemberg, S. V. Polenga, and Y. P. Salomatov, "Phased array antenna with combined electronical and mechanical beam steering for satellite networks," *2013 Int. Sib. Conf. Control Commun. SIBCON 2013 - Proc.*, pp. 1–3, 2013.

[162] D. Ehyaie, "Novel Approaches to the Design of Phased Array Antennas," 2011.

[163] R. J. Mailoux, *Phased Array Antenna Handbook*. Wendt Library, 1994.

[164] R. Kronberger, T. Knie, R. Leonardi, U. Dettmar, M. Cremer, and S. Azzouzi, "UHF RFID localization system based on a phased array antenna," *IEEE Antennas Propag. Soc. AP-S Int. Symp.*, pp. 525–528, 2011.

[165] C. C. Cheng, C. H. Ko, A. Morris, and G. M. Rebeiz, "A very low loss L.9-2.1 GHz RF MEMS phase shifter," *IEEE MTT-S Int. Microw. Symp. Dig.*, pp. 2–4, 2012.

[166] Y. Kang, "HIGH-POWER FAST RF FERRITE PHASE SHIFTER."

[167] M. A. El-Tanani and G. M. Rebeiz, "C-band low-loss phase shifter >360° for WLAN applications," *Proc. 37th Eur. Microw. Conf. EUMC*, no. October, pp. 1503–1506, 2007.

[168] O. D. Gurbuz and G. M. Rebeiz, "A 1.6-2.3-GHz RF MEMS reconfigurable quadrature coupler and its application to a 360° reflective-type phase shifter," *IEEE Trans. Microw. Theory Tech.*, vol. 63, no. 2, pp. 414–421, 2015.

[169] F. Ellinger, H. Jäckel, and W. Bächtold, "Varactor-loaded transmission-line phase shifter at C-band using lumped elements," *IEEE Trans. Microw. Theory Tech.*, vol. 51, no. 4 I, pp. 1135–1140, 2003.

[170] Pasternack, "Microstrip Calculator." .

[171] M. I. Nawaz, Z. Huiling, M. S. S. Nawaz, K. Zakim, S. Zamin, and A. Khan, "A review on wideband microstrip patch antenna design techniques," *ICASE 2013 - Proc. 3rd Int. Conf. Aerosp. Sci. Eng.*, pp. 42–49, 2013.

[172] Yongxi Qian, D. Sievenpiper, V. Radisic, E. Yablonovitch, and T. Itoh, "A novel approach for gain and bandwidth enhancement of patch antennas," pp. 221–224, 2002.

[173] R. D. Trivedi and V. Dwivedi, "Stacked microstrip patch antenna: Gain and bandwidth improvement, effect of patch rotation," *Proc. - Int. Conf. Commun. Syst. Netw. Technol. CSNT 2012*, pp. 45–48, 2012.

[174] B. S. A. I. Sandeep, "Design and simulation of micro strip patch array antenna for wireless DESIGN AND SIMULATION OF MICROSTRIP PATCH ARRAYANTENNA FOR WIRELESS COMMUNICATIONS AT 2 . 4 GHZ," vol. 3, no. November 2012, pp. 1–5, 2014.

[175] P. W. Hannan, "The Element-Gain Paradox for a Phased-Array Antenna," *IEEE Trans. Antennas Propag.*, vol. 12, no. 4, pp. 423–433, 1964.

[176] "HMC602LP4." [Online]. Available: https://www.analog.com/media/en/technical-documentation/data-sheets/hmc602.pdf.

[177] "Arduino Uno." [Online]. Available: https://store.arduino.cc/arduino-uno-rev3.

[178] "HMC358MS8G." [Online]. Available: https://www.analog.com/media/en/technical-documentation/data-sheets/hmc358.pdf.

[179] "Biotracker VHF Receiver." [Online]. Available: https://www.lotek.com/products/biotracker-vhf-receiver/.

[180] "No Title." [Online]. Available: https://atstrack.com/tracking-products/receivers.aspx.

[181] "No Title." [Online]. Available: https://www.analog.com/en/parametricsearch/11409.

[182] "Low noise amplifiers." [Online]. Available: https://www.analog.com/en/parametricsearch/10675.

[183] "Low noise amplifiers."

[184] M. Lee, J. Hwang, and H. Yoe, "Agricultural production system based on IoT," *Proc. - 16th IEEE Int. Conf. Comput. Sci. Eng. CSE 2013*, pp. 833–837, 2013.

[185] M. S. Mekala and P. Viswanathan, "A novel technology for smart agriculture based on IoT with cloud computing," *Proc. Int. Conf. IoT Soc. Mobile, Anal. Cloud, I-SMAC 2017*, pp. 75–82, 2017.

[186] B. Goradiya and H. Pandya, "Real time Monitoring & Data logging System using ARM architecture of Raspberry pi & Ardiuno UNO," *Ijves.Com*, vol. 04, no. July, pp. 513–517, 2013.

[187] "RAK811 LoRa / LoRaWAN module." [Online]. Available: https://uk.pi-

supply.com/products/rak811-lora-lorawan-module.

[188] "Matrice 200 Series." [Online]. Available: https://www.dji.com/uk/matrice-200-series.

[189] "Intel Falcon 8+ series." [Online]. Available: https://www.intel.co.uk/content/www/uk/en/products/drones/falcon-8.html.

[190] E. Capello, A. Scola, G. Guglieri, and F. Quagliotti, "Mini quadrotor UAV: Design and experiment," *J. Aerosp. Eng.*, vol. 25, no. 4, pp. 559–573, 2012.

[191] M. Hwangbo, J. Kuffner, and T. Kanade, "Efficient two-phase 3D motion planning for small fixed-wing UAVs," *Proc. - IEEE Int. Conf. Robot. Autom.*, no. April, pp. 1035–1041, 2007.

[192] M. A. Boon, A. P. Drijfhout, and S. Tesfamichael, "Comparison of a fixed-wing and multi-rotor UAV for environmental mapping applications: A case study," *Int. Arch. Photogramm. Remote Sens. Spat. Inf. Sci. - ISPRS Arch.*, vol. 42, no. 2W6, pp. 47–54, 2017.

[193] "Matrice 200 series specs." [Online]. Available: https://www.dji.com/uk/matrice-200-series/info#specs.

[194] "pixhawk flight controllers." [Online]. Available: https://pixhawk.org/.

[195] "Matrice 600 series." [Online]. Available: https://www.dji.com/uk/matrice600.

[196] L. Chandra Paul, "The Effect of Changing Substrate Material and Thickness on the Performance of Inset Feed Microstrip Patch Antenna," *Am. J. Networks Commun.*, vol. 4, no. 3, p. 54, 2015.

[197] "Payload SDK." [Online]. Available: https://developer.dji.com/payload-sdk/.

[198] "STM32F4DISCOVERY." [Online]. Available: https://www.st.com/en/evaluation-tools/stm32f4discovery.html.

[199] "Mobile SDK." [Online]. Available: https://developer.dji.com/mobile-sdk/.

[200] "Creating a MapView and Waypoint Application." [Online]. Available: https://developer.dji.com/mobile-sdk/documentation/ios-tutorials/GSDemo.html.

[201] A. M. Wenner, "The flight speed of honeybees: a quantitative approach," *J. Apic. Res.*, vol. 2, no. 1, pp. 25–32, 1963.

[202] "Virtual Sticks." [Online]. Available: https://developer.dji.com/mobile-sdk/documentation/ios-tutorials/SimulatorDemo.html.

[203] F. Requier *et al.*, "Predation of the invasive Asian hornet affects foraging activity and survival probability of honey bees in Western Europe," *J. Pest Sci. (2004).*, vol. 92, no. 2, pp. 567–578, 2019.

[204] A. E. S. Cunha, J. Rose, J. Prior, H. M. Aumann, N. W. Emanetoglu, and F. A. Drummond, "A novel non-invasive radar to monitor honey bee colony health," *Comput. Electron. Agric.*, vol. 170, no. August 2019, p. 105241, 2020.

[205] "HEXBUG Micro Robotic Creatures | HEXBUG", Hexbug.com, 2020. [Online]. Available: https://www.hexbug.com/?__store=hexbuguk&__from_store=hexbug.

Appendix A Collaborations

This appendix details work which was performed in collaboration with the University of Guelph and China Agricultural University. In Summer 2018, the research group visited Dr Nigel Raines lab at Guelph university. During this time, we were able to extensively evaluate the effect of the tag on the behaviour of the bee. Figure 2.24 depicts 3D printed tags comparable to the weight of the fabricated tags which were mounted to the thorax of the bee. The aim was to validate that flying insects that can power the tag can also fly and behave normally with the tag attached and the following methodology was flowed:

1. Catch relevant insect and assign to either control or treatment
2. Chill insect to make marking easier
3. Control add an opalith, Test add a tag
4. Allow 10min for recovery
5. Transfer to flight cage and observe behaviour for 10 min

During the ten-minute monitoring period the bee was recorded for one of four activities. The activities monitored were testing, walking, grooming, and flying. Table A:1 shows a summary of the following experiment.

**Table A.1:** Summary of the behavioural data collected during the experiment

species	opolithor/ tag	weight (g)	intertag width	obersvational file name	Species	any flight	notes on flight- when provoked	prop_time_rest	prop_time_walk	prop_time_groom	prop_time_fly	NOTE: all tag
b.impatients	opolith	0.172	3.92mm	control bumblebee 26	bumblebee	no	no motivaton to fly	0.495343866	0	0.504656134	0	
b.impatients	opolith	0.185	3.93mm	control bumblebee 29	bumblebee	no	no motivaton to fly	0.057138201	0.942861799	0	0	
apis mellifera	opolith	0.204	4.1mm	control drone 14	drone	no	no motivaton to fly	0.519538982	0.431843675	0.048617343	0	
apis mellifera	opolith	0.216	4.6mm	control drone 16	drone	no	no motivaton to fly	0.349316422	0.540811191	0.023187327	0.086634793	
apis mellifera	opolith	0.21	4.6mm	control drone 17	drone	no	no motivaton to fly	0.649793447	0.309344398	0.040862155	0	
apis mellifera	opolith	0.224	4.43mm	control drone 19	drone	no	no motivaton to fly	0.638927835	0.348090562	0.012981604	0	
apis mellifera	opolith	0.216	4.41mm	control drone 20	drone	no	no motivaton to fly	0.762489985	0.184771655	0.05273836	0	
apis mellifera	opolith	0.104	3.01mm	control honeybee 35	honeybee	no	no motivaton to fly	0.585896835	0.23945425	0.174648915	0	
apis mellifera	opolith	0.098	3.31mm	control honeybee 37	honeybee	no	no motivaton to fly	0.022232028	0	0.977767972	0	
b. bimac	opolith	0.206	4.24 mm	control bumblebee 1	bumblebee	yes	normal	0.049160989	0.810087177	0.099437109	0.041314725	
b.impatients	opolith	0.206	3.99mm	control bumblebee 11	bumblebee	yes	normal	0.989769162	0.010230838	0	0	
b.impatients	opolith	0.185	4.48mm	control bumblebee 27	bumblebee	yes	normal	0.683830382	0.071734789	0.051727466	0.192488302	
b.impatients	opolith	0.144	3.3mm	control bumblebee 3	bumblebee	yes	normal	0.803733356	0.128575496	0.046393099	0.021269416	
b.impatients	opolith	0.172	4.26mm	control bumblebee 31	bumblebee	yes	normal	0.856832349	0	0	0.142965636	
b.impatients	opolith	0.13	3.5mm	control bumblebee 33	bumblebee	yes	normal	0.141352881	0.029259476	0.829387643	0	
b.impatients	opolith	0.138	3.12mm	control bumblebee 5	bumblebee	yes	normal	0.349316422	0.540811191	0.023187327	0.086634793	
b.bimac	opolith	0.236	4.68mm	control bumblebee 9	bumblebee	yes	normal	0	1	0	0	
apis mellifera	opolith	0.2	4.40mm	control drone 24	drone	yes	normal	0.596226111	0.394438704	0.004661011	0.004669593	
apis mellifera	opolith	0.071	2.91mm	control honeybee 7	honeybee	yes	normal	1	0	0	0	
b. bimac	tag	0.227	3.94mm	test bumblebee 12	bumblebee	no	does not fly well- can fly without tag	0.172724628	0.327385445	0.499889927	0	
b.impatients	tag	0.137	4.19mm	test bumblebee 25	bumblebee	no	no motivaton to fly	0.706012883	0.07210223	0.221884886	0	
b.impatients	tag	0.17	4.07mm	test bumblebee 28	bumblebee	no	cannot sustain flight	0.717465509	0.141558066	0.140976425	0	
b.impatients	tag	0.145	3.45mm	test bumblebee 30	bumblebee	no	did no fly willingly	0.010268555	0.989731445	0	0	
b.impatients	tag	0.155	3.75mm	test bumblebee 32	bumblebee	no	hovered over ground for short period	0.732776207	0.267223793	0	0	
b.impatients	tag	0.159	3.53mm	test bumblebee 4	bumblebee	no	maybe glue on wingbase	1	0	0	0	
b.impatients	tag	0.089	2.95mm	test bumblebee 6	bumblebee	no	did not fly when given opportunity-wings stuck together at back	0	0.990548427	0.009451573	0	
apis mellifera	tag	0.193	4.65mm	test drone 13	drone	no	no motivaton to fly	0.60761182	0.39238818	0	0	
apis mellifera	tag	0.222	4.9mm	test drone 15	drone	no	wouldn't fly (not sure if he can)	0.049781821	0.950218179	0	0	
apis mellifera	tag	0.196	1.67mm	test drone 18	drone	no	no motivaton to fly	0.714765375	0.089151353	0.196083272	0	
apis mellifera	tag	0.208	4.31mm	test drone 21	drone	no	no motivaton to fly	0.841895391	0.016326381	0.141778227	0	
apis mellifera	tag	0.228	5mm	test drone 23	drone	no	no motivaton to fly	0.369299832	0.004706507	0.62599366	0	
apis mellifera	tag	0.091	3.27mm	test honeybee 38	honeybee	no	can fly without tag	0.082474038	0.173077724	0.744448238	0	
b.bimac	tag	0.208	3.78mm	test bumblebee 10	bumblebee	yes	normal	0	0.028920718	0.960843197	0.010236085	
b.bimac	tag	0.202	3.95mm	test bumblebee 2	bumblebee	yes	normal	0	0	1	0	
b.impatients	tag	0.15	3.82mm	test bumblebee 34	bumblebee	yes	can fly but struggles with lift	0.172418745	0	0.827581255	0	
apis mellifera	tag	0.207	3.93mm	test drone 22	drone	yes	normal	0.000138127	0.695500734	0.068432579	0.235928506	
apis mellifera	tag	0.116	3.58mm	test honeybee 36	honeybee	yes	a little difficult	0.748358356	0.130720358	0.120921286	0	
apis mellifera	tag	0.104	3.42mm	test honeybee 40	honeybee	yes	removed tag and could fly	0	0.053834582	0.916849893	0.029315525	
apis mellifera	tag	0.109	2.84mm	test honeybee 8	honeybee	yes	laboured- hovered over ground	0	0.180374754	0.819625246	0	

The test was performed observed the flight behaviour for Bumblebees, Honeybee drones and Honeybee workers. Table A:2 shows the mean time spent for each activity with and without the tag attached.

Table A.2: Comparison of behaviours for each Bee with and without control

comparison of behaviours	mean				SE			
	prop_time_resting	prop_time_walking	prop_time_grooming	prop_time_flying	prop_time_resting	prop_time_walking	prop_time_grooming	prop_time_flying
Bumblebee Control	0.412983859	0.380726471	0.193489692	0.012794952	0.08775305	0.099051544	0.099120368	0.009174473
Bumblebee Treatment	0.47114068	0.422030712	0.106828608	0	0.117517642	0.126855716	0.052005519	0
Drone Control	0.637472425	0.130101965	0.158449256	0.073893025	0.133065398	0.08437139	0.134488235	0.033008999
Drone Treatment	0.244348001	0.037171888	0.716774096	0.001706014	0.290451653	0.027562361	0.128022402	0.001706014
Honeybee Control	0.53207537	0.464812901	0.00155367	0.001556531	0.059985488	0.1123793	0.139106906	0.039016038
Honeybee Treatment	0.187124121	0.265107607	0.481457251	0.066311008	0.187078081	0.145806414	0.22444374	0.056959826

The following comparisons in behaviour could then be compared directly with the control (without tag) against the treatment (with tag). Figure A:1a shows the comparison for Bumblebees whilst additionally showing the results for Honeybee males (Figure A:1b) and Honeybee workers (A:1c). The control is represented by the blue bar whilst orange represents the treatment.
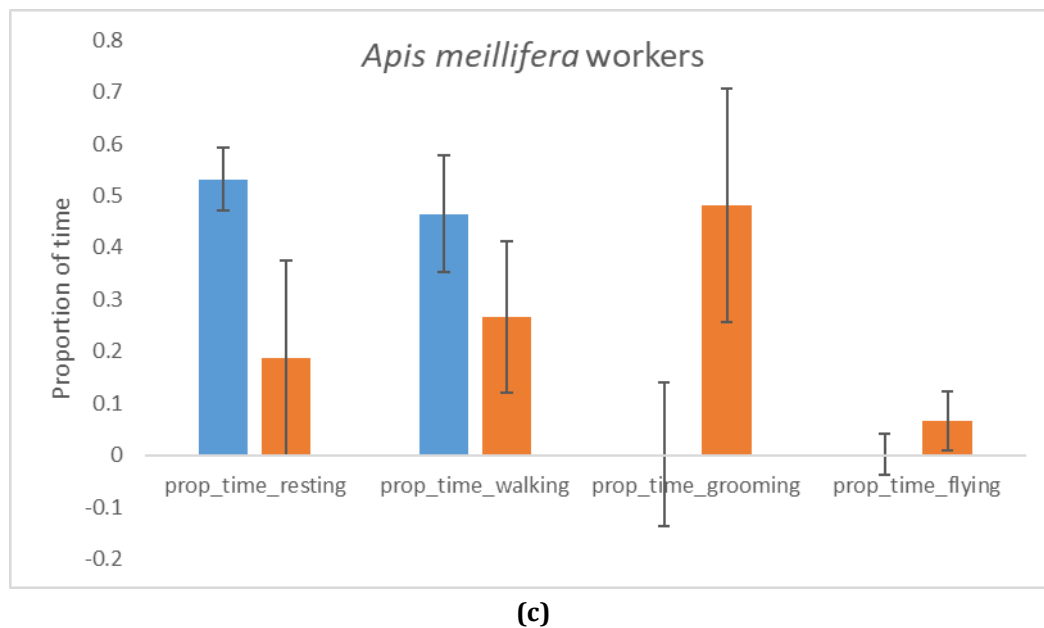

(a)

(b)

(c)
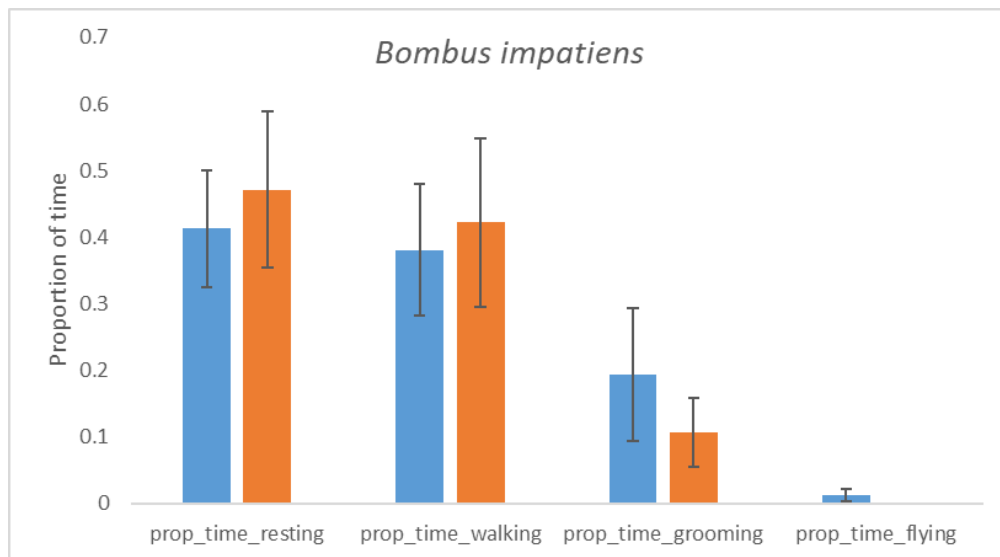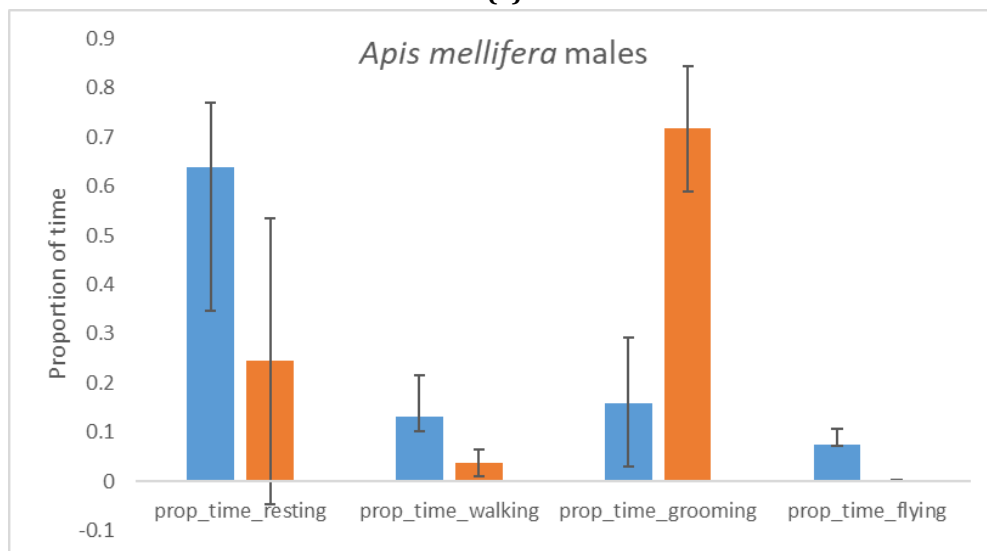
Fig A:1: Comparisons between behaviours of control b (blue) and treatment (orange) for (a) Bumblebees, (b) Honeybee males and (c) Honeybee workers.

Additionally, the group visited China Agricultural University in a collaborative project to validate the operation of the system. The results from the collaboration are presented within the majority of Chapter 4. Preliminary validation was performed with the use of a voltage-controlled oscillator with power levels comparable to that of the tag and placed at known locations and the received signal strength was evaluated vs scanning angle of the antenna array. The results and mapping of the antennas scanning angle can be found within the shared folder placed below the paragraph.

(https://drive.google.com/open?id=1iSZ6npCGn7OGoZD33avDsHMAay9TIRuD)

Finally, in Summer 2019 our group collaborated with S&A produce in order to demonstrate tracking within a polytunnel in order to monitor the pollination of their crops. Figure 4.13 demonstrates the experimental set up in which the antenna and receiver system was mounted above strawberry flowers. The received signal strength was continuously compared vs scan angle to detect and located a tagged bee flying within proximity before writing the data to a SD card. The raw data can additionally be found within the google drive folder. The data is processed using the MATLAB script parser.m to find instances in which a signal was detected.

APPENDIX B Drone Tracking Code and Data

The system presented in Chapter 5 relies on the ability to promptly transmit and evaluate the data obtained from the tracking system. The system involves the integration of the receiver system with the drone via DJI's payload software development kit. Unfortunately, due to licensing agreements the code cannot be made available in the appendix however the segment is responsible for reading the encrypted data from the receiver system and transmitting it to a mobile device connected to the receiver. The mobile software development kit is responsible for the flight controls of the drone and converts the encrypted positional data from the receiver into a direction for the drone to autonomously travel towards. Initial snippets of key aspects of the code are presented in figure 5.14 and 5.16 which show how the position of the bee was determined and updating the drone's position, respectively. The application is also designed to monitor key aspects of the drone's flight capabilities such as signal strength, battery life, GPS signal and flight mode. The application was built using java and the full build and code can be found in the following shared folder (https://drive.google.com/open?id=1qlj_3VMz6FPT3juGBDLDKnKRs644LBl7).

Chapter 5 concludes by presenting two forms of autonomous tracking with the UAV in which the results are presented in figures 5.22 and 5.23. The targets position is originally stored as a latitude and longitude position in the flight logs before being normalised into meters. The raw data for each individual flight and stored within the flight logs are found within the following folder (https://drive.google.com/open?id=1qlj_3VMz6FPT3juGBDLDKnKRs644LBl7)